Università degli Studi di Napoli Federico II

Dottorato di Ricerca in Fisica

Ciclo 36°

Coordinatore: Prof. Vincenzo Canale

Probing Star-forming Environments with Gamma-ray and Neutrino Astronomy

Settore Scientifico Disciplinare: FIS/02

Dottorando

Antonio Ambrosone

Coordinatore

Prof. Gennaro Miele

Dr. Antonio Marinelli

Anni: 2020/2023

Abstract

In this thesis, we investigate extragalactic star-forming environments such as Starburst Galaxies (SBGs) and Star-forming Galaxies (SFGs) as potential gamma-ray and neutrino factories, both as diffuse and as point-like emitters. In particular, using the state-of-the-art modelling of the CR transport inside Starburst Nuclei (SBNi), we develop a data-driven blending of spectral index to quantitatively assess the diffuse gamma-ray and neutrino fluxes of these sources. We find that this new scenario can account for a sizeable part of IceCube diffuse measurements, while consistent with the current gamma-ray limits from non-blazar sources. We also estimate the neutrino budget of local (known) SBGs, pointing out KM3NeT/ARCA as a crucial probe for the star-forming activity of these sources. Indeed, we also report dedicated analysis on behalf of the KM3NeT collaboration, evaluating for the first time, the expected quasi-differential sensitivity and discovery potential, analysing also local SBGs. We have also performed a forecast analysis for the Cherenkov Telescope Array (CTA), simulating mock data sets for SBNi demonstrating that the future telescope is going to indirectly probe CR transport mechanisms inside these sources, having also important implications for neutrino astronomy. We have also exploited such a forecast in order to conduct a beyond standard model study to constrain exotic interactions between light Dark Matter (DM) particle and protons.

Finally, we also analyse, in the light of the latest IceCube results, galactic star-forming environments as quasi-diffuse neutrino emissions. We utilize the concept of discovery horizon for a high-energy neutrino telescope in order to show that the current IceCube discovery potential cannot disentangle a true diffuse neutrino emission from a quasi-diffuse neutrino emission from galactic pevatrons. Nonetheless, we show that the upcoming KM3NeT/ARCA will have the capability of probing Young Massive Stellar Clusters (YMSCs) and Hypernovae.

Contents

Chapter 1

Introduction

In 1912 Victor Hess fortunately discovered Cosmic Rays (CRs) by analyzing how the γ radiation changed as a function of the distance from the ground [1]. Since then, the origin of these particles has been one of the most important conundrum of modern physics, although we have gain a lot of information about them. In particular, they are charged particles with energies with a very wide energy range $\sim [10^2, 10^{11}]\,\mathrm{GeV}$ [2]. Most of these particles up to $\sim 1\,\mathrm{PeV}(10^6\,\mathrm{GeV})$ are believed to originate within our own galaxy [2]. In fact, they are supposed to be powered by supernova explosions where a lot of the realised energy goes to accelerating electrons, protons and also heavier elements [2]. This picture can also be indirect probed by gamma-ray and neutrino experiments, in the framework of the multi-messenger astronomy. Indeed, interactions between CRs and the interstellar medium particles n_{ISM} copiously produce charged and neutral pions which in turn decay in gamma-rays and neutrinos (see for instance [3] or even the following chapters). Therefore, measurements of galactic emission of gamma-rays and neutrinos are the smoking guns of the existence of galactic source of cosmic rays. The Fermi-LAT collaboration has confirmed this picture after the 21 month of data taking [4]. On the other hand, it is important to stress that gamma-rays can also be produced by leptonic processes such as bremsstrahlung and Inverse Compton scattering processes and so they do not clearly demonstrate the existence of galactic sources able to emit and accelerate high-energy protons up to $\sim$ PeVs energies [2]. Neutrinos, actually, are the natural smoking gun for hadronic processes and potentially demonstrating the existence of high-energies protons and heavier nuclei inside the Milky way. The IceCube Neutrino Observatory ([5]) has recently measured with a $\sim 4.5\,\sigma$ significance, the diffuse neutrino flux produced in the galactic plane of the Milky Way [6]. These measurements demonstrate that star-forming environments such as supernovae ex-

plosions (SNe) are emitters of high-energy particles such as CRs, gamma-ray and neutrinos. By contrast, for higher energies $E \gtrsim 10^6\,\mathrm{PeV}$, CRs are expected to be powered by extra galactic sources, whose sources are yet to be discovered. The main difficulty is given by the fact that CRs get deflected by magnetic field, due to electromagnetic interactions, and so their measured direction does not correspond to the direction of the source which powered them. As a result, in order to pinpoint these sources, indirect measurements are needed. Also in this case, the multi-messenger astronomy framework is a fundamental tool in order to discover the origin of high-energy CRs. Indeed, The Fermi-LAT and the IceCube collaboration has respectively measured the extra-galactic component of the diffuse gamma-rays and neutrino emissions throughout the all sky (see [7] for the gamma-rays and [5, 8–10] for neutrinos) whose emission are not completely known. What we know for the moment is that Blazars are expected to dominate the extragalactic gamma-ray background (EGB) flux measured by Fermi-LAT [11–13], even though many analyses have demonstrated that these sources do not contribute to the diffuse neutrino measurements (see [14–17]) for instance). An important class of astrophysical sources which can be emitters of gamma-rays neutrinos and CRs is: Star-forming and Starburst Galaxies (SFGs and SBGs). In fact, these sources manifest star-forming activity [18] with a star formation rate as high as $10^2 - 10^3$ the star formation rate of the Milky Way [18], which from the observational point of view, it is traced by infrared luminosity [19–21]. Therefore, they are expected to produce gamma-rays and neutrinos with a flux much higher than the Milky-Way. Up to this moment, only a dozen of these sources have been detected by the Fermi-LAT telescope to be GeV gamma-ray emitters by the Fermi-LAT telescope (see for instance [19]). The GeV luminosity correlates with the infrared luminosity [19–21], reinforcing the idea that star-forming processes are responsible for such emissions. Furthermore, M82 and NGC253 have also been detected as TeV gamma-ray emitters [22, 23]. Furthermore, the Auger collaboration has find compelling evidence of a correlation between SBGs with high-energy cosmic-rays [24, 25].

All of these means that SFGs and SBGs are regarded to be perfect laboratories for multi-messenger studies. In particular, in this thesis, we exploit the state-of-the-art CR transport modelling inside SFGs and SBGs in order to quantitatively assess the gamma-ray and neutrino budget of these sources. We study both the diffuse fluxes (the totality of gamma-rays and neutrinos emitted by all SFGs and SBGs distributed in the Universe) and the flux of the known local sources. We also investigate how different cosmic-rays transport models impact the gamma-ray and neutrino observations from local SBGs, quantifying, using only public information, the potentiality of the Cherenkov Telescope Array (CTA) [26] to detect local SBGs. We also exploit

the nature of CR transport inside SBGs in order to perform a beyond standard model study, probing the properties of light Dark Matter (DM) particles showing, for the first time, how to use the gamma-ray data of SBGs to probe DM-protons interactions.

Last but not least, we explore the capability of the upcoming KM3NeT/ARCA neutrino detector [27] to trace TeVs neutrinos from star-forming environments, encompassing both diffuse and point-like signals. We introduce, for the first time for the KM3NeT/ARCA detector, the 90% C.L. quasi-differential sensitivity for 10 years of the full detector operation, considering the whole energy range observable by KM3NeT/ARCA (100 GeV-100 PeV) and selecting upgoing track-like as well as all-sky cascade-like events. We also compute the sensitivity for several equatorial declinations, focusing also on some particular Starburst Galaxies sources, such as NGC 1068, the Small Magellanic Cloud (SMC) and Circinus Galaxy. The present analysis demonstrate that KM3NeT/ARCA will be fundamental in strengthening the observations of the IceCube experiment and also in connecting the star formation processes with the high-energy neutrino production, within a few years of operation in full configuration.

The Thesis is organised as follows: Chapter 2 is dedicated to the astrophysical definition of SBGs, the tracers of the star formation activity and the description of the local SBGs discovered by the Fermi-LAT telescope. Chapter 3 is dedicated to the role of SBGs to the diffuse gamma-ray and neutrino measurements. In chapter 4, we quantify the neutrino fluxes of local SBGs and we perform a statistical forecast for current and future neutrino telescopes to further constrain their physical parameter space. In chapter 5, we discuss the implications for different CR transport models in the cores of SBGs and perform a statistical forecast for the CTA telescope in order to not only to simulate future measurements but also to quantify the potentiality of the future telescope to disentangle between different CR transport models. In Chapter 6, we exploit the models developed for the non-thermal emissions of SBGs in order to perform a beyond standard model study: constraining Dark Matter and proton interactions by distortion to the gamma-ray fluxes. Chapter 7 is dedicated to galactic neutrino emission and, in particular, on the contribution of the quasi-diffuse neutrino emission from a template of a neutrino source distribution along the galactic plane. This allows us to probe and restrict the parameter space of galactic star-forming environments. In chapter 8, we provide details about Cherenkov neutrino telescopes in order to clarify details used throughout the thesis about neutrino telescopes. In this chapter, we also describe the KM3NeT/ARCA expected geometry and Monte Carlo simulation pipeline. In the following chapter (9), we perform a sensitivity analysis for the KM3NeT/ARCA detector, determining the quasi-differential sensitivity both for diffuse and point-like (and extended) emis-

sions. In particular, for the first time, we show the quasi-differential sensitivity for the expected detector using a maximum binned likelihood ratio method. We also uses these expectations to quantify the potentiality of this detector to trace TeV neutrinos from local SBGs. Finally, in chapter 10, we draw the conclusions of all these studies.

Chapter 2

Starburst Galaxies

Star formation (SF) not only underlies the origin of planets and starts, but it is also an important regulator of the galaxy formation and evolution [28]. Therefore, it comprises a lot of processes and it is difficult to find descriptive path between a specific type of galaxy and a Starburst Galaxy in the literature [29]. In general, SBGs are galaxies, that for a certain period, present an efficiency of the star formation higher than other catalogued galaxies (at least of an order of magnitude) [29]. As a result, the quantity of gas in these galaxies is very high and it gets depleted due to the star forming activity [29] in a timescale which can be as long as $\sim 10^6\,\mathrm{yr}$ [30]. The star formation rate (SFR) of these sources is generally of the order of $\sim 10 - 100\,\mathrm{M_\odot\,yr^{-1}}$ [18, 20, 21, 29–32], which is at least an order of magnitude higher than the star formation rate of the Milky way $\sim 1\,\mathrm{M_\odot\,yr^{-1}}$ [29, 33]. The star forming regions of SBGs usually coincide with the Starburst Nuclei (SBNi) extending up to hundreds of parsecs of the core of these galaxies [31, 32]. Furthermore, the high star formation rate mirrors a high far infrared (FIR) luminosity [31, 34], which in turns to a high supernova rate $\mathrm{R_{SN}} \sim 0.1 - 1\,\mathrm{yr^{-1}}$ [31]. Therefore, these sources are expected to be guaranteed emitters and accelerators of high-energy CRs at least up to $\sim 1 - 10\,\mathrm{PeV}$ [20, 21, 31, 32].

2.1 Tracers of the Star Formation

There are several tracers of the star formation rate, namely there are several ways to quantitatively infer the star formation rate of a galaxy. Indeed, the full electromagnetic spectrum has been used for years in order to quantify star formation estimators: X-rays, ultraviolet (UV), the optical and infrared (IR) as well as the radio with both continuous and line emissions [35].

This is simply due to the fact that both the starlight of young stars and the reprocessed light by interstellar gas and dust can be observed through the indicated electromagnetic bands [29].

2.1.1 Ultraviolet Light

The importance of the UV light as a tracer of SBGs has been demonstrated by the International Ultraviolet Explorer (IUE) satellite, which have operated for twenty years [29]. In fact, young stars predominantly emit light in the UV range ($\lambda \lesssim 0.3\,\mu$m) [35] for a timescale of $\sim 10{-}100\,\mathrm{M\,yr}$ depending of their O or B type [29, 35]. As a result, this kind of emission is a powerful probe of the star formation rate over a very large timescale. Indeed, assuming a star formation rate constant over a period of time $100\,\mathrm{M\,yr}$, the UV luminosity (L) of the stars can be converted in the SFR as [35]

$$\dot{\mathrm{M}}_*[\mathrm{M}_\odot\,\mathrm{yr}^{-1}] = 3.0 \cdot 10^{-47}\,\lambda \cdot \mathrm{L}(\lambda) \tag{2.1}$$

where λ is the wavelength of the radiation in $\mathring{\mathrm{A}}$ and $\mathrm{L}(\lambda)$ is the radiation luminosity expressed in $\mathrm{erg\,s}^{-1}$ [35]. The calibration factor $3.0 \cdot 10^{-47}$ (this factor also encodes the change of the unity) has a 15% of uncertainty and it is also dependent on the timescale of the SFR constancy [35].

The brightest point of using this approach in order to estimate the SFR is that the UV light can be relatively easily measured also for high-redshift galaxies [29]. One of the instruments which measured and catalogued the UV light of galaxies, for almost 20 years of galaxies, has been the International Ultraviolet Explorer (IUE) satellite [29].

Another way to target SFR using UV light as a probe, is using the UV absorption lines formed in the ISM [29]. These lines are detectable in SBGs and specially in local galaxies and give a lot of information about gas profiles, kinematics, its ionization state and also the optical depth. For instance, they show that very fast outflows which can reach velocity $\sim 10^3\,\mathrm{Km\,s}^{-1}$ (see [29, 35] for further details). In other words, the UV absorption lines test stellar feedback and ISM enrichment rather than provide a quantitative estimation of the star formation rate, although even these processes play important roles in the evolution of a galaxy such as a SBG. The main problem of tracing the SFR with UV is given by the presence of the dust [35]. In fact, the dust attenuates the UV light, thereby making 2.1 over optimistic and in need for corrections [35].

2.1.2 Infrared Light

The dust absorbs the UV light produced by the stars and in generally it re-emits it at higher wavelengths (IR wavelengths) [28, 29, 35]. In particular, IR light peaks at $\lambda \sim 60\,\mu\,\mathrm{m}$ for dust which re-emits light from young stars and between $100\,\mu\,\mathrm{m} \lesssim \lambda \lesssim 150\,\mu\,\mathrm{m}$ [35]. As a result, the IR emission ($5 - 1000\,\mu\,\mathrm{m}$) can be used as a tracer for the star formation rate [35]. If we consider the total infrared luminosity L(TIR) between ($5 - 1000\,\mu\,\mathrm{m}$), the SFR can be estimated by [20, 35]

$$\dot{\mathrm{M}}_*[\mathrm{M}_\odot\,\mathrm{yr}^{-1}] = 1.7 \cdot 10^{-10}\,\epsilon \mathrm{L(TIR)}[\mathrm{L}_\odot] \tag{2.2}$$

where the SFR is measured in $\mathrm{M}_\odot\,\mathrm{yr}^{-1}$ and $L(\mathrm{TIR})$ is measured in solar luminosities $\mathrm{L}_\odot$. $\epsilon \simeq 0.79$ is a factor which depends on the initial mass function (IMF) [20, 21]. Eq. 2.2 is used especially for sources with a very intense IR luminosity as a proxy of the SFR, but it presents different limitations: 1) not all the UV light emitted by stars is reprocessed in IR light by dust. 2) The dust heating produced by multiple-age stellar populations has the effect of producing a thermal equilibrium IR spectral energy distribution (SED) rather than a single temperature modified black-body spectrum (see for more details [29] or even [28]). Furthermore, ϵ, depending on the IMF, changes as a function of the stellar population in galaxies and it might lead to a relatively large systematic uncertainty on the SFR [28]. As a result, in order to overcome these issues, for more precise estimates on the SFR, is to combined IR and UV observations [28]. In practice, the UV luminosities gets corrected as [28]

$$\mathrm{L_{UV}(Corr)} = \mathrm{L_{UV}} + \eta \mathrm{L_{IR}} \tag{2.3}$$

where L are the monochromatic luminosities defined as $\nu \mathrm{L}(\nu)$ [20, 28] and η is a factor which usually depends on the wavelength of the IR luminosity [28]. One of the most common correction uses the GALEX FUV (far ultraviolet $\lambda = 155\,\mathrm{nm}$) and the total IR luminosity [28]. In this case, for instance, $\eta = 0.46$ (see also [36] for further details). On the contrary, as a proxy of the IR luminosity, it can be used the luminosity at $\lambda = 25\,\mu\mathrm{m}$. In fact, the star formation rate can consequently be estimated also by [20, 21, 28, 36]

$$\log\dot{\mathrm{M}}_*[\mathrm{M}_\odot\,\mathrm{yr}^{-1}] = \log\big(\mathrm{L_{FUV}} + 3.98\mathrm{L}_{25\,\mu\mathrm{m}}\big)[\mathrm{erg\,s}^{-1}] - 43.35 \tag{2.4}$$

Eq. 2.4 is one of the most important equation when it comes to estimating the SFR of galaxy and in particular of a SBG, although there might be other estimators of the SFR.

2.1.3 Other Tracers of the Star Formation

The IR light cannot trace the SFR of a source, if its dust content is pretty low [28]. This is specially the case for galaxies with a low SFR [37–39]. Therefore, other tracers are needed for such sources. For instance, the centimeter-wavelength radio continuum emission can be used as a proxy for the SFR, because of its tight correlation with the IR luminosity [28] (see also for further details [40]). The reason is that radio emission should be mainly powered by synchrotron emission by electrons accelerated and produced by SNRs [28, 40]. Consequently, a decrease in the dust, it leads to a decrease also in the radio luminosity emitted by synchrotron processes [28, 40]. The corrected luminosity in this case can be expressed as [28, 36]

$$\mathrm{L_{FUV}(corr)} = \mathrm{L_{FUV}} + 7.2 \cdot 10^{14}\,\mathrm{L(1.4\,GHz)} \tag{2.5}$$

where $\mathrm{L(1.4\,GHz)}$ is expressed in $\mathrm{erg\,s^{-1}\,Hz^{-1}}$ [28]. The final calibration for the SFR is (see Table 1 in Ref. [28] for more details)

$$\log\dot{\mathrm{M}}_*[\mathrm{M_\odot\,yr^{-1}}] = \log\big(\mathrm{L_{FUV}} + 7.2 \cdot 10^{14}\,\mathrm{L(1.4\,GHz)}\big)[\mathrm{erg\,s^{-1}}] - 43.35 \tag{2.6}$$

Also other wavelengths have been used as a proxy for the SFR, such as the x-rays. In fact, when there is no AGN accretion disk related activity, the x-rays fluxes are dominated by supernovae and supernovae remnants, thereby they correlated with fresh star formation [28]. However, there is no calibration with the SFR derived from first principle, so it is generally phenomenologically derived. On the other hand, Ref. [41] (see also [42]) has proposed that SFR is traced by the HCN luminosity, according to ([42])

$$\dot{M}_*[\mathrm{M_\odot\,yr^{-1}}] = 1.8 \cdot 10^7 \frac{\mathrm{L_{HCN}}}{10^3\,\mathrm{Km\,pc^2\,s^{-1}}} \tag{2.7}$$

Ref. [41] has proposed the ratio between $\mathrm{L_{HCN}}$ and $\mathrm{L_{CO}}$ as a proxy for SBGs, in particular when $\mathrm{L_{HCN}/L_{CO}} \approx 0.1 - 0.25$. The physical reason for this calibration is given by the fact that HCN is associated with a high gas dense region and star forming processes [43]. All of the above-mentioned equations are used to effectively define what a SBG is and to quantify its SFR. However, this kind of classification, as will we see in the next chapter, does not capture one of the non-thermal property of SBGs: confining high-energy CRs inside their nuclei. As a result, following Ref. [32], in this thesis we use an effective definition of SBG as a source which effectively confine CRs and a star-forming galaxy, a galaxy which has a finite confinement power

over CRs (see the following chapters for more details).

2.2 Kennicutt-Schmidt Relation

There is an important empirical relationship between the star formation rate and the gas density of a SBG [28, 44–46]. From a qualitative point of view, a region with a very intense star forming activity is a region full of gas, thereby leading to a somewhat proportionality between these quantities. Schmidt in 1959 (see [47] and [48]) proposed that the star formation surface density is a power-law of the gas density of the same region [28, 44–46]

$$\Sigma_{\rm SFR} = A\Sigma_{\rm gas}^{n} \tag{2.8}$$

This power-law holds for over five orders of magnitude in gas density [46]; in other words, it works both for normal galaxies, starforming galaxies as well as the ultraluminous SBGs. Data are well fitted with a power-law whose slope is $n = 1.50 \pm 0.02$ [46], which is a bit softer than the previous estimation of $n = 1.40$ [28, 44, 45]. From Eq. 2.8, we understand why the higher the star formation rate the higher the gas density of galaxy becomes. If, for simplicity, we assume that a sample of galaxy has a circumnuclear SBG region of radius $R \sim 200 - 500\,{\rm pc}$ [28, 32, 44–46] and that for a $\dot{M}_* = 5\,{\rm M}_\odot\,{\rm yr}^{-1}$ for $n_{\rm ISM} = 175\ {\rm cm}^{-3}$ (see Chapter 4 for more details and also Ref. [32] for details about this benchmark), then we can rewrite

$$\frac{\dot{M}_*}{5\,{\rm M}_\odot\,{\rm yr}^{-1}} = \left(\frac{n_{\rm ISM}}{175\,{\rm cm}^{-3}}\right)^{3/2} \tag{2.9}$$

Eq. 2.9 can be inverted in order to estimate the gas density in a Star forming region when it is know its SFR (see chapter 4 where we use this relation). This demonstrate how the gas density is linked to the sta formation rate of a SBG.

2.3 Phenomenological Properties of Local SFGs and SBGs

In this section, we analyze the properties of local (known) SFGs and SBGs. For the moment, a dozen of SBGs have been measured as a gamma-ray emitter by Fermi-LAT [19]. Tab. 2.1 summarizes the properties of such a galaxy sample.

M 82 and NGC 253 are two nuclear SBGs which have been detected as hard power-law between $0.1 - 100\,{\rm GeV}$ (with a spectral index respectively of $\gamma = 2.14$ and $\gamma = 2.10$ [19]).

Galaxy	D(Mpc)	$\log(L_\gamma)[0.1-100]\,\mathrm{GeV}$	$\log(L_{IR}/L_\odot)$	$\dot{M}_*[M_\odot\,yr^{-1}]$
M 82	3.53	40.19	10.75	10.4
NGC 253	3.56	40.12	10.56	5.03
ARP 220	80.9	42.36	12.20	214
ARP 299	46.8	41.46	11.86	97
NGC 4945	3.72	40.28	10.44	1.22
NGC 1068	10.1	40.96	11.00	22.7
NGC 2146	17.2	40.81	11.10	14.0
NGC 2403	3.18	39.17	9.17	0.37
NGC 3424	25.6	41.10	10.27	1.59
M 31	0.77	38.21	9.37	0.26
M 33	0.91	38.30	9.14	0.29
SMC	0.060	37.10	7.85	0.027
LMC	0.050	37.77	8.72	0.20
Circinus	4.21	40.18	10.22	2.05

Table 2.1: Summary of the main properties of the local SFGs and SBGs discovered as GeV photon emitters. Data taken from Refs. [20, 21].

Furthermore, these two sources are the only SBGs which have been detected as TeV gamma-ray emitters. In particular, M 82 by the VERITAS telescope [22] and NGC 253 by the HESS telescope [49], confirming them as emitters of high-energy photons with hard spectra. ARP 220 is an ultra-luminous infrared galaxy (ULIRG), defined as sources a IR luminosity $L_{IR} \gtrsim 10^12\,L_\odot$ (see [50] for more details), and it represents the most distance ULIRG ever measured as a GeV emitter. This source also host an AGN inside so it is possible that it gives a non-negligible contribution to its gamma-ray spectrum. In fact, Ref [19] has confirmed that it stands above the calorimetric limit (see chapter 4 for details). ARP 299 is another powerful galaxy with a SFR of the order of $\sim 100\,M_\odot\,yr^{-1}$, although it has been discovered as a source in recent times and it spectral SED presents a lot of uncertainty. Ref. [51] has recently discovered, with 14 years of Fermi-LAT data, that IRAS13052-5711 may be a new GeV photon emitters. Furthermore, the authors propose that such emission might be caused by SBG activity, making IRAS13052-5711 potentially the most distant SBG recorded as GeV emitters thus far. However, this source seems to substantially exceed the calorimetric limit conditions and so it is well possible that this emission is not caused by SBG activity. Moreover, the source is spatially very near to another source (angular distance of 0.094° [51]), making this gamma-ray emission still controversial. NGC 1068 is one of prototypical SBG with a high SFR ($\sim 20\,M_\odot\,yr^{-1}$). It also present a very massive black hole in its core with a strong AGN activity, although the steady gamma-ray emission measured by Fermi-LAT seems to confirm SBG activity as its origin (see chapter 4 a more detailed discussion about this source). Also, NGC 3424, NGC 2146, NGC 4945 and Circinus galaxy have been detected as GeV emitters, although with hints of variability of this

flux. Consequently, their AGN activity might well contribute to such emissions. Finally, the local group of galaxies near the Milky-way, M 31, M 33, the Small Magellanic Cloud (SMC) and the Large Magellanic Cloud (LMC) have been detected as steady gamma-ray emitters. Even though their intrinsic luminosities are pretty low, their gamma-ray flux are pretty high given their vicinity to our galaxy. SMC, LMC and M 31 have also been detected as extended sources [19].

this sample is still limited compared with other astrophysical sources such as Blazars, impeding to draw robust conclusions on the general properties of SBGs. Nonetheless, it clearly demonstrates that SFGs and SBGs are able to emit non-thermal radiation like GeV photons and in some cases TeV photons. As a result, they are bound to produce and accelerate high-energy CRs in their nuclei. In the next chapters, we are going to build a model in order to quantify the theoretical budget for these kinds of emissions for these sources.

Chapter 3

Starburst Galaxies Role on Diffuse Gamma-ray and Neutrino Emissions

In this chapter, we discuss the role of starburst galaxies (SBGs) on the diffuse gamma-ray and neutrino observations and the importance for a more complete catalogue of sources in the gamma-ray range in order to get a precise evaluation of their spectra. The chapter is based on our analysis published in Ref. [52].

3.1 Introduction

In this chapter, we discuss the contribution of starburst galaxies to the high-energy neutrino spectra obtained by the IceCube Neutrino Observatory after a decade of data taking [8, 9, 53–57]. Indeed, these observations clearly reveal the presence of high-energy neutrino emitters in the Universe. At the moment, there are only two clear indications of point-like sources: a powerful blazar, TXS0506+056 [58](possible source of the 290 TeV track-like event IC170922A and the TeV neutrino flare measured in 2014/15 [59]) and a starburst galaxy with a AGN activity, NGC 1068 [60]. By contrast, the galactic contribution to these observations is strongly constrained to be less than 10% [61–65], pointing towards a extra-galactic dominance of such emissions. Several models and source classes have been proposed in order to explain these data. For instance, Refs. [66–70] have fitted the electromagnetic spectrum of TXS0506+056 and tried to assess the hadronic component for this cosmic-ray "accelerator" during the neutrino observations. Nonetheless, the IceCube collaboration has performed a dedicated stacking analysis which has constrained the contribution of 2LAC blazars (belonging to the 2nd Fermi-LAT AGN catalog)

to less than 27% of the HESE neutrino flux, when taking into account an unbroken power-law, $\Phi_\nu(E_\nu) \propto E_\nu^{-2.5}$ [14] (see also [15–17]). However, since such a limits weaken when assuming a harder power-law [14, 59], these sources are allowed to account for the diffuse neutrino flux above 200 TeV [71, 72]. The lack of spatial and temporal correlations between high-energy neutrinos and known gamma-ray sources has also led to upper limits on other classes of astrophysical objects [73–77]. For example, gamma-ray bursts [78] have been constrained to contribute up to a few % to the diffuse neutrino flux [79–82]. Moreover, the analyses [83–85] have pointed out that starforming (SFGs) and starburst (SBGs) galaxies, where neutrinos and gamma-rays are produced in hadronuclear proton-proton interactions [86], cannot be the dominant source of the whole TeV-PeV diffuse neutrino, because they would exceed the actual limits of the of the extragalactic gamma-ray background (EGB) measured by Fermi-LAT [7] principally attributed to blazars. Hence, the origin of high-energy neutrinos is still unclear. All these constraints, along with the tension among different IceCube data samples, point towards the presence of multiple different components in the diffuse neutrino flux [87–90]. Many analyses have also highlighted a tension between the diffuse neutrino and gamma-ray data, especially driven by the large neutrino flux observed below 100 TeV [91–96]. This has triggered the scientific community to investigate hidden cosmic-ray accelerators with a highly suppressed gamma-ray emission [96–103], invisible decay of active neutrinos [104, 105] and leptophilic decaying dark matter [106–108] (see [109–112] for more recent analyses on dark matter neutrino signals).

Despite the existing limits, starburst galaxies (SBGs) are well-motivated candidates for the diffuse neutrino flux, since they are guaranteed high-energy cosmic-ray "reservoirs" with enough interstellar gas to be considered as good calorimeters. Observed and catalogued mostly through their infrared emission, denoting an intense star formation rate, gamma-ray observations for few of them point out their capability to emit non-thermal component above the TeV energy. The possibility of confining cosmic-rays in a core with the high-density interstellar matter guarantees an effective hadronic contribution to the observed gamma-ray emission. However, the gamma-ray observations from these galaxies are available just from few of them, confirming their low luminosity at high energy and making it difficult to assess an exhaustive prediction of the neutrino counterpart. Refs. [31, 32, 113] have recently reexamined the neutrino and gamma-ray emissions from SBGs pointing out that these sources can indeed account for most of the IceCube through-going muon neutrino flux at hundreds of TeVs in agreement with gamma-ray data. In particular, Ref.s [31, 32] have proposed a prototype-based method to compute the cumulative neutrino and gamma-ray fluxes emitted from the SBGs population. In this approach, the galaxy M82

is considered as a reference SBG for setting the physical parameters such as supernovae rate, magnetic field, velocity of the wind, density of the interstellar medium. Most importantly, Ref.s [31, 32] assume that the cosmic-ray spectrum injected in all the SBGs is fixed to be a power-law with spectral index of 4.2 [1] and cut-off energy of 100 PeV. Although this scenario provides a good description of the through-going muon neutrino flux, the astrophysical neutrino flux below 100 TeV remains still unexplained. Moreover, at higher neutrino energies, a contribution from blazars to the diffuse neutrino flux is physically motivated [71].

In this analysis, we relax the assumption of a single power-law and consider a more realistic scenario where the cosmic-ray spectra of each starburst galaxy can have different spectral indexes. In particular, we go through the recent study [19] that considers ten years of Fermi-LAT data for a sample of 12 starforming galaxies making a statistical analysis with the spectral features of these astrophysical objects. Differently from [31, 32], we take into account the distribution of spectral indexes from this sample and consider it as representative of the whole SBGs population. Such a data-driven blending of spectral indexes has the remarkable results of increasing the neutrino flux at 100 TeV without enlarging the gamma-ray flux below 1 TeV. This is the multi-messenger requirement to potentially explain IceCube low-energy events and alleviate the tension between neutrino and gamma-ray data. To further investigate this result, we perform a multi-messenger likelihood analysis of the extragalactic gamma-ray background (EBL) measured by Fermi-LAT and the neutrino flux observed by IceCube, considering both the contributions of SBGs and blazars. For the latter, we follow the model [71] that, using the TXS0506+056 as a standard candle, describes the neutrino and electromagnetic emission satisfying the IceCube stacking limit [14]. For both the two classes of sources, we include the secondary gamma-ray emission from electromagnetic cascades using the public code γ-`Cascade` [114]. Regarding neutrino data, we examine the latest 7.5-year HESE data [8] as well as the 6-year high-energy cascade ones which probe the neutrino emission at lower neutrino energies [9]. In order to analyze the whole EGB spectrum, we also take into account the diffuse gamma-ray emission from radio galaxies dominating the Fermi-LAT observations below 1 GeV [11]. Along with the three overall normalizations for the SBGs, blazars and radio galaxies components, we leave as a free parameter the maximal energy reached by the cosmic rays accelerated from supernovae remnants (SNRs) inside of the nucleus of starburst galaxies. In this analysis, we focus on the differences obtained with the two different models for the SBG emission: the standard prototype approach resulting in a single power-law behavior and the more realistic data-driven blending of spectral indexes. We

[1] It is important to remark that, in general, when we are referring to the spectral index, we usually refer to the index of high-energy protons.

find that, independently of the data-sets considered in the multi-messenger analysis, the former is more constrained by data and implies an almost negligible SBG contribution to the diffuse neutrino flux. On the other hand, the latter is in better agreement with data and a sizeable SBG neutrino component is allowed at 100 TeV. Moreover, the SBG model with blending generally requires a cut-off energy smaller than few tens of PeV, in agreement with the expected SNRs acceleration description for SBGs [83, 84, 115] (see below for further discussion) and with an expected dominant neutrino emission from blazars above 200 TeV [71, 116]. Finally, we point out that our model for the SBG component is can account for the 40% (50%) of the total 7.5-year HESE neutrino events at 95.4% (99.7%) confidence level, while being compatible with the existing limits on the non-blazar EGB component and on the contribution of nearby SBGs to the diffuse neutrino flux [75, 117–120].

3.2 Cosmic-Ray Transport in a Single Starburst Galaxy

SBGs are endowed with a high star formation rate (SFR), which can as high as($\psi \sim 10 - 100$ $M_\odot$ yr^{-1}) [18]. Consequently, the rate of supernovae explosions is pretty enhanced with respect to the one of normal galaxies such as the Milky Way, leading to an abundance of cosmic-ray accelerators as well as a higher density of interstellar gas which represents the target for inelastic collision of accelerated particles. Since interstellar gas efficiently absorbs star emission and re-emits it in the infrared (IR) band [121], the IR emission of SBGs, usually $10 - 100$ times greater than normal galaxies [113], can be considered a good tracer for the SFR. These characteristics, in principle, favour the production of high-energy gamma-rays and neutrinos through the hadronic proton-proton interaction and explain the *almost linear* relation between gamma-ray luminosity and infrared emission observed by [121]. Beside an interstellar medium density of $n_{\rm ISM} \sim 10^2$ cm^{-3}, these sources present also a strong magnetic field ($10^2 - 10^3 \mu$G) [18] which plays an important role in the CR confinement. In fact, as explained by Ref. [31, 32], a regime of strong turbulence lead to a small diffusion coefficient throughout the galactic plane and this makes the role of diffusion very marginal in SBG environments. Furthermore, the episodes usually occur in small circumlinear regions within the SBGs, which are called starburst nuclei (SBNi). In particular, SNRs are expected to inject a massive amount of gas and this becomes a supersonic wind flow [122, 123]. Hence, winds and turbulence play a decisive role in the motion and interaction of CRs. If these high-energy CRs are confined inside the central part of these galaxies, SBGs may be thick enough to efficiently produce neutrinos and non-thermal radiation.

This calorimetric condition can be expressed by

$$T_{\rm loss} \leq T_{\rm esc}\,, \tag{3.1}$$

where $T_{\rm loss}$ is the typical CR timescale for interactions and $T_{\rm esc}$ is the timescale taken for a CR to escape the source. Many authors focused on CR spectral features of SBGs [31, 113, 124–133] inferring that CR electrons are well confined inside SBNs, while the calorimetric condition for high-energy protons strictly depends on the ISM density and the wind flow velocity inside a SBG (see also [32]). In this thesis, we follow [31] to describe CR timescales. We consider the SBNi are spherical regions with the advection time $T_{\rm adv} = R/v_{\rm wind}$ depending on the radius (R) of this region and on the wind velocity ($v_{\rm wind}$). On the other hand, for the time loss of CR we take into account proton-proton (p-p) interactions, ionization and Coulomb interactions, even though for $E > 1\,\mathrm{GeV}$ the $p-p$ timescale dominates over the others (see appendix A for details about the actual formulae used). We describe CR diffusion using the quasi-linear theory framework, where the diffusion coefficient is related to the power spectrum of the magnetic field irregularities, which describes how the magnetic field strength varies at different spatial scales. In particular, we choose a Kolmogorov-like scenario, assuming a density of the magnetic field $F(k) \propto k^{-d+1}$ with $d = 5/3$ and a regime of strong turbulence inside the SBN [31, 32]. These assumptions lead to a diffusion coefficient $D(p) \propto p^{1/3}$, which implies $T_{\rm diff}(E) \propto E^{-1/3}$. For a magnetized fluid the Kolmogorov scenario should in principle be replaced by the Kraichnan model [134] for turbulence. However, as shown by [31, 32], the diffusion timescale is always larger than all the other timescales, so that the details of the turbulence model do not influence our conclusions. The escape time $T_{\rm esc}$ in Eq. (3.1) is given by

$$T_{\rm esc} = \left(\frac{1}{T_{\rm adv}} + \frac{1}{T_{\rm diff}}\right)^{-1}. \tag{3.2}$$

For SBG typical values ($R \sim 10^2$ pc and $v_{\rm winds} \sim 10^2 - 10^3$ km/s, see [18]), we have that $T_{\rm adv} \sim 10^5 - 10^6$ yr. On the other hand, the high level of turbulence and interstellar medium density makes the diffusion timescale much greater than this timescale (see [31]); consequently, escape phenomena are principally dominated by advection and therefore $T_{\rm esc} \simeq T_{\rm adv}$. The timescale $T_{\rm loss}$ depends on the proton energy and in particular, for energies much greater than the proton mass, it is mainly driven by the timescale of p-p interactions. As shown in [31], $T_{\rm loss}$ usually becomes less than advection timescale for energy higher than 10 TeV. On the other hand, electrons are always confined inside the SBN and therefore, they always lose efficiently

their energy. The most convenient way to study the CR distribution (high-energy protons and primary electrons) inside SBNs is to use the leaky-box model equation

$$F_{p,e} = Q_{p,e}\left(\frac{1}{T_{\rm adv}} + \frac{1}{T_{\rm loss}} + \frac{1}{T_{\rm diff}}\right)^{-1}, \tag{3.3}$$

where $F_{p,e}$ and $Q_{p,e}$ are respectively the distribution function and the injection rate of protons and electrons. Eq. (3.3) physically represents the balance between the injection and CRs loss terms. Indeed, the high ISM density, from one hand, fuels the star forming activity and at the same time, it is heated by supernovae explosions. Hence, a balance between the injection and the winds phenomena is expected in a generic SBN. The injection of CRs arises directly from SNRs, consequently $Q_{p,e}(p, \mathcal{R}_{\rm SN}, \alpha, p^{\rm max})$ depends both on the rate of supernova explosions $\mathcal{R}_{\rm SN}$ and on the spectral shape originated in a single SNR. In particular, it is assumed to be a power-law with spectral index α and high-energy cut-off.[2] For protons, we have

$$Q_p(p, \mathcal{R}_{\rm SN}, \alpha, p^{\rm max}) = \frac{\mathcal{N}_p\, \mathcal{R}_{\rm SN}}{V_{\rm SBN}} p^{-\alpha} e^{-p/p^{\rm max}}\,, \tag{3.4}$$

where $V_{\rm SBN}$ is the volume of the starburst nucleus, the cut-off energy $p^{\rm max}$ is taken to be a free parameter in the range 1-100 PeV, and the normalization $\mathcal{N}_p$ is fixed by requiring that each supernova releases into CRs only a fraction $\xi = 0.1$ of its total explosion kinetic energy $E_{\rm SN} = 10^{51}$ erg. Hence, we consider the following constraint on the cosmic-ray spectrum:

$$\int_0^\infty 4\pi\, p^2\, T(p)\, \left(\frac{V_{\rm SBN}}{\mathcal{R}_{\rm SN}} Q_p(p)\right) {\rm d}p = \xi\, E_{\rm SN}\,, \tag{3.5}$$

with $T(p)$ being the single particle kinetic energy. For primary electrons, we take

$$Q_e(p, \mathcal{R}_{\rm SN}, \alpha) = \frac{\mathcal{N}_e\, \mathcal{R}_{\rm SN}}{V_{\rm SBN}} p^{-\alpha} e^{-(p/p_e^{\rm max})^2}\,, \tag{3.6}$$

with $p_e^{\rm max} = 10$ TeV and $\mathcal{N}_e = \mathcal{N}_p/50$ according to [31, 32].

3.3 Secondary Particle Production

Neutrinos and gamma-rays are mainly produced inside the SBNs through charged and neutral pion decays ($\pi \to \mu\, \nu_\mu$, $\mu \to e\, \nu_e\, \nu_\mu$ and $\pi_0 \to 2\gamma$) (produced in pp interactions). To determine the pion injection rate Q_π, we assume that any produced pion carries a fixed fraction of the

[2] Throughout the chapter, we consider natural units for which the cut-off momentum and the cut-off energy coincides in the highly relativistic regime.

kinetic energy of the high-energy proton ($K_\pi \simeq 0.17$) [135]. Under this assumption, we have

$$Q_\pi(E_\pi) = \left. \frac{c\, n_{\rm ISM}}{K_\pi} \sigma_{pp}\left(E'\right) n_p\left(E'\right) \right|_{E'=m_p+E_\pi/K_\pi} , \tag{3.7}$$

where σ_{pp} is the proton-proton cross-section, n_p denotes the energy distribution function of injected high-energy protons obtained by solving the leaky-box model equation, and m_p is the proton mass. The secondary electron (and positron) injection term is given by [31]

$$q_e(E_e) = 2\int_{E_e}^{+\infty} Q_\pi(E_\pi) f_e(E_e/E_\pi) dE_\pi \tag{3.8}$$

where $f_e(x)$ is defined in Appendix A. Then, we compute the neutrino production rate Q_ν from pion decays as

$$Q_\nu(E_\nu) = 2\int_0^1 \left(\frac{f_{\nu_e}(x) + f_{\nu_\mu^1}(x) + f_{\nu_\mu^2}(x)}{3} \right) Q_\pi\left(\frac{E_\nu}{x}\right) \frac{{\rm d}x}{x} , \tag{3.9}$$

where the function $f_\nu(x)$ encode the probability distribution according to which neutrinos carry a fraction of the pion energy (see appendix A for the formulae of these functions). We directly take into account the effect of neutrino oscillations changing the flavour ratio (1:2:0) at the source into (1:1:1) at the Earth; by virtue of the low magnetic fields inside the SBN, we only consider a pion beam flavor composition for the neutrino fluxes. Hence, the single flavour neutrino flux at the Earth is given by

$$\phi_\nu(E,z) = \frac{V_{\rm SBN}}{4\pi\, d_c^2(z)} Q_\nu\left(E(1+z)\right) , \tag{3.10}$$

where $d_c(z)$ is the co-moving distance between the source and the Earth as a function of the redshift z. To compute the gamma-ray emissivity, defined as the number of photons produced per unit energy, time, and solid angle ϵ_γ, we account for to the dominant pion decay component the bremsstrahlung, synchrotron and inverse Compton scattering (ICS) photons emitted by both primary and secondary electrons as explained by [31]. In particular, for the pion decay component

$$4\pi\epsilon_\gamma(E) = 2\int_{E_{\rm min}}^{+\infty} \frac{Q_\pi(E_\pi)}{\sqrt{E_\pi^2 - m_\pi^2 c^4}} dE_\pi \tag{3.11}$$

where $E_{\rm min} = E + m_\pi^2 c^4/(4E)$. For bremsstrahlung, we have

$$4\pi\epsilon_\gamma = \frac{n_{\rm ISM}\sigma_{\rm bremc}}{E} \int_E^{+\infty} n_e(E_e) dE_e \tag{3.12}$$

where $\sigma_{\rm brem} \simeq 3.4 \cdot 10^{-26}\,{\rm cm}^2$. For the inverse compton scattering emissivity, to simplify the calculation and to avoid the double integration over the electron and the photon energies, we replace the physical target of photons by an effective monochromatic spectrum centered around the peak energy $\simeq 0.1\,{\rm eV}$ of the photon target and normalized to the same total energy density $U_{\rm rad}$. This procedure is pretty similar to the one implemented by Ref. [31]. We verified that we obtained the same results. Nonetheless, as already explained by Ref. [31], this leads to an uncertainty of a factor 2 to IC emissivity which is acceptable since SBNi are predominantly hadronic.

$$4\pi\epsilon_\gamma(E) = \frac{3\sigma_{\rm T}}{4}\,\frac{U_{\rm rad}}{\epsilon_{\rm peak}^2}\int_{p_{\rm min}(E,\epsilon_{\rm peak})}^{\infty} f_e(p)\left(\frac{m_e}{E_e}\right)^2 G(q,\Lambda) 4\pi p^2 {\rm d}p\,, \tag{3.13}$$

with $p_{\rm min}(E,\epsilon_{\rm peak})$ being the momentum corresponding to the electron energy

$$E_e = \frac{E}{2}\left[1 + \big(1 + \frac{m_e^2 c^4}{E\,\epsilon_{\rm peak}}\big)^{1/2}\right] \tag{3.14}$$

and also [31]

$$q = \frac{E}{(E_e - E)\Lambda} \tag{3.15}$$

where Λ and $G(q,\Lambda)$ are defined in appendix A. An important process to be taken into account is the internal absorption of gamma-rays after collision with the low-energy photons (optical and IR photons) present in the Starburst Nuclei. Over each line of sight, parametrized by the path length s, the intensity $I(E,s)$ of gamma radiation obeys the transport equation

$$\frac{{\rm d}I}{{\rm d}s}(E,s) = \epsilon(E) - I(E,s)\,\eta(E)\,, \tag{3.16}$$

where $\epsilon(E)$ is the gamma-ray emissivity and $\eta(E)$ is the absorption coefficient, which can be written as $\eta(E) = \int \sigma_{\gamma\gamma}(E,E') n_{\rm bkg}(E'){\rm d}E'$: here $\sigma_{\gamma\gamma}(E,E')$ is the photon-photon cross-section for photons of energies E and E' and $n_{\rm bkg}(E')$ is the background photon density at low energies. For this work, we choose the M82 best-fit background spectrum reported by [31] for the background spectrum. After averaging over every lines of sight, we obtain the following internal absorption function of the gamma-ray flux at energy E:

$${\rm Abs}(E) = \frac{3}{2\eta(E)R}\left[\frac{1}{2} - \frac{1 - e^{-2R\eta(E)}(1 + 2R\eta(E))}{4R^2\eta(E)^2}\right]\,, \tag{3.17}$$

where R is the radius of the SBG. Hence, this computation of the gamma-ray flux at Earth can be resumed by:

$$\begin{aligned}\phi_\gamma(E,z) =& \frac{V_{\rm SBN}}{4\pi\, d_c^2(z)} Q_\gamma\left(E(1+z)\right) \\ & \times \mathrm{Abs}\left(E(1+z)\right)\, e^{-\tau_{\gamma\gamma}(E,z)}\,,\end{aligned} \tag{3.18}$$

where $\tau_{\gamma\gamma}$ represents the absorption term from CMB and EBL [136, 137]. Furthermore, we also take into account electromagnetic cascades using the public code γ–`Cascade` [114].

It is worth noticing that the calorimetric condition given by Eq. (3.1) significantly affects the spectrum of expected neutrinos and gamma-rays [32]. In fact, we have that $Q_{\nu,\gamma} \propto Q_\pi \propto n_{\rm ISM}\,\sigma_{pp}\,F_p$ and F_p principally depends on the minimum timescale in Eq. (3.3). In particular, we get

$$Q_{\nu,\gamma} \propto \begin{cases} Q_p & \text{Calorimetric Scenario} \\ c\, n_{\rm ISM}\,\sigma_{pp} Q_p\, \frac{R}{v_{\rm wind}} & \text{Wind Scenario} \end{cases} \tag{3.19}$$

This equation highlights that in the calorimetric scenario the gamma-ray and neutrino emission from a SBG is weakly dependent on the physical parameters of the source. Indeed, in this scenario we are able to quantify the hadronic emission with three main quantities: $\mathcal{R}_{\rm SN}$, α and $p^{\rm max}$. Furthermore, it is expected to be a tight connection between $\mathcal{R}_{\rm SN}$ and the star formation rate (SFR) ψ, since for each supernovae remnants an equivalent mass of $\simeq 100\,{\rm M}_\odot$ is considered to be injected [31]. As a result:

$$\frac{\dot{M}_*}{1\,{\rm M}_\odot\,{\rm yr}^{-1}} = 100 \frac{\mathcal{R}_{\rm SN}}{1\,{\rm yr}^{-1}} \tag{3.20}$$

for the rest of the work we describe the emission of the SBGs through: ψ, α and $p^{\rm max}$. This is a crucial observation, because the calorimetric approximation allows us to neglect all the structural details of the sources and consequently, just like in Ref. [32], it is possible to fix all the other parameters such as the magnetic field, the velocity of the wind, the density of the interstellar medium, to the values of a benchmark galaxy, which is M82 in our case. Tab. 3.1 summarizes the structural parameters considered (see also [32]).

Parameters	value
R (pc)	250
B μG	200
$n_{\rm ISM}\,({\rm cm}^{-3})$	100
$v_{\rm wind}\,({\rm Km\,s}^{-1})$	700
$U_{\rm rad}\,({\rm eV\,cm}^{-3})$	2500

Table 3.1: Summary of the structural parameters used for the prototype starburst galaxy.

Before discussing in the next section the computation of the cumulative diffuse neutrino and gamma-ray fluxes from the population of SBGs through the spectral index blending, let us comment on the maximum proton energy expected in SBNs, which is here considered as free parameter in the following multi-messenger likelihood analysis. The possibility for the SNR shock to accelerate CRs up to the knees energy is still an open question. Generally, the Sedov phase is reached at late times, when the maximum energy is too low and the spectrum at very high energies is very steep [138] (see also Chapter 7 for further discussion on this topic). An estimation of the maximal energy reached in a SN type Ia or type II shock can be written as [83, 84, 115]:

$$p^{\rm max} \approx 3.1 \text{ PeV} \left(\frac{n_{\rm ISM}}{1 \text{ cm}^{-3}}\right)^{-1/3} \left(\frac{B}{10^{-3.5} \text{ G}}\right) \times \left(\frac{E_{\rm ej}}{10^{51} \text{ erg}}\right)^{1/3} \left(\frac{v_{\rm ej}}{10^{9} \text{ cm/s}}\right)^{1/3}, \tag{3.21}$$

where B is the magnetic field, $E_{\rm ej}$ is the ejected energy and $v_{\rm ej}$ is the ejected velocity. This means that $p^{\rm max}$ can reach values as high as $\sim 1\,$PeV for typical values of SBNi [83]. On this regard recent observations of possible Galactic Pevatrons with Cherenkov gamma-ray telescopes [139, 140], in the Milky Way, rise up the question about the hadronic or leptonic origin of this emission when related to a SNR. The confirmation of the first hypothesis would be an experimental proof that SNR shock can accelerate CRs up to few PeVs of energy. It has also been proposed that at high redshift hypernovae could be more present than supernovae and therefore, the energy and particle velocity injected could be higher than the typical values used above and this would increase $p^{\rm max}$ to $\sim$ 10 PeV [83]. Another possibility to obtain higher values of $p^{\rm max}$ up to $10-100$ PeV [83, 84] is given by higher values of magnetic field ($1-30$ mG) which may be typical values for some SBGs (see [18]). In this work, we do not need to evoke these particular scenarios since our analysis favors $p^{\rm max}$ of the order of few PeVs from the SNR shocks inside the selected sample of SBGs. On the other hand, the introduction of SBGs as potential emitters of ultra-high-energy (UHE) cosmic-rays requires a completely different hypothesis for the physical processes responsible of that emission (see [141–143] for further details). Between them: extremely fast spinning young pulsars [144], newly born magnetars [145], gamma-ray bursts (GRBs) events [146] or tidal disruption events (TDEs) caused by super massive black holes [147]. All these processes can occur inside of a SBGs even though their inclusion here is behind the scope of this work.

3.4 Diffuse neutrino and gamma-ray fluxes

In this section, we discuss the diffuse gamma-ray and neutrino fluxes. Firstly, the diffuse spectrum is given by the sum over all SBGs in the Universe. Therefore, a realistic computation should both account for the distribution of these sources throughout redshift and how the individual properties of each source change throughout the source class. For the actual calculation, we follow the approach put forward to [32]. In particular, we use the method of the star formation rate function to describe the number of starburst galaxies in the Universe. The SFR evolution with redshift indeed provides a lot of information about the distribution of the galaxies in the Universe and the high SFR of a generic SBG makes it a perfect tracer for identifying these objects. We consider the modified Schecter function $\Phi_{\rm SFR}(z,\psi)$ reported by [32], which has been obtained by fitting in the redshift interval $0 \leq z \leq 4.2$ the IR+UV data of a Herschel Source sample [148] after subtracting the AGN contamination [149]. Such a function represents the number of SBGs per unit of Universe's co-moving volume and logarithmic SFR ψ (see Appendix B for further details of Ref. [32]). As pointed out in [32], it is then possible to define through the Kennicutt relation [44, 45] an effective threshold value $\psi_* = 2.6\ {\rm M}_\odot\ {\rm yr}^{-1}$ for the star formation rate above which a generic galaxy can be considered as an efficient calorimeter. Indeed, only those SBGs that can be regarded as astrophysical reservoirs substantially contribute to the diffuse very-high energy (VHE) flux. Some important comments are in order to justify this approach: while a $R \simeq 200\,{\rm pc}$ is consistent and tuned for local known SBGs, we know that the vast majority of stars in the Universe do not form galaxies with radii of 200 pc. Furthermore, SBGs constitute only a small part of the total SFR of the Universe (see [150] for more details about this). However, this mainly come from the fact that, from the observational point of view, SBGs are classified by their IR emission being above some threshold [32]. However, in this thesis, we define a SBG using their non-thermal emission properties; in other words their ability to confine high-energy CRs [32]. For such galaxies, the description of a dense core region whose density is related to the SFR via the Kennicut relation [44, 45] should be realistic. Therefore, since our focus is mainly to obtain a realistic estimate of the diffuse gamma-ray and neutrino flux, rather than a detailed description of the galaxy structure, we believe a more detailed modeling would be beyond the scope of this thesis. Moreover, as discussed in the previous section, in the calorimetric scenario the neutrino and gamma-ray fluxes do not depend on the structural parameters of the starburst galaxy, but rather on the SFR and on the CR spectral shape parametrized by the spectral index α and the cut-off energy $p^{\rm max}$ (see Eq. (3.4)).

On the other hand, in the present chapter, each starburst galaxy is allowed to have different

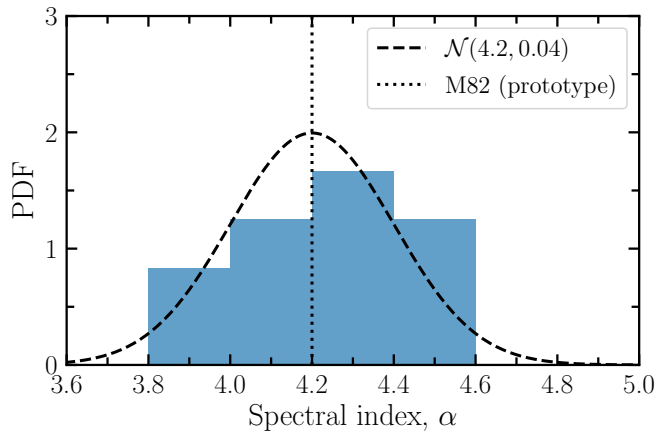

Figure 3.1: Number of observed SBGs with different spectral indexes α according to the analysis [19]. The dashed line shows the underlined Gaussian probability distribution function with mean $\mu_\alpha = 4.2$ and variance $\sigma_\alpha^2 = 0.04$ used in the present analysis. The vertical dotted line displays the spectral index of M82 generally adopted as prototype [32].

values for the individual parameters describing its emission. This is the main novelty with respect to the one reported by [32], where instead all the SBGs have been assumed to have the same properties of the prototype galaxy. In particular, because of the discussion of the previous section, we focus on the range of possible spectral indexes α originated in the core of a SBG. Therefore, the diffuse differential neutrino and gamma-ray fluxes are given by

$$\begin{aligned}\Phi_{\nu,\gamma}^{\rm SBG}(E, p^{\rm max}) = \int_0^{4.2} {\rm d}z \int_{\psi_*}^{\infty} {\rm d}\log \dot{M}_* \, \frac{c\, d_c(z)^2}{H(z)} \\ \times \, \Phi_{\rm SFR}(z, \dot{M}_*) \left\langle \phi_{\nu,\gamma}\big(E, z, \dot{M}_*, p^{\rm max}\big) \right\rangle_\alpha ,\end{aligned} \tag{3.22}$$

where $H(z) = H_0 \sqrt{\Omega_M (1+z)^3 + \Omega_\Lambda}$ is the Hubble parameter with $H_0 = 67.74$ km s^{-1}Mpc^{-1}, $\Omega_M = 0.31$ and $\Omega_\Lambda = 0.69$, and $\langle \phi_{\nu,\gamma} \rangle_\alpha$ is the emitted neutrino and gamma-ray fluxes averaged over the distribution of spectral indexes. We have

$$\left\langle \phi_{\nu,\gamma}\big(E, z, \dot{M}_*, p^{\rm max}\big) \right\rangle_\alpha = \int {\rm d}\alpha \, \phi_{\nu,\gamma}\big(E, z, \dot{M}_*, \alpha, p^{\rm max}\big) \, p(\alpha) \, , \tag{3.23}$$

where $p(\alpha)$ describes the blending of spectral indexes and the quantities $\phi_{\nu,\gamma}$ are given in Eq.s (3.10) and (3.18) once $\mathcal{R}_{\rm SN}$ is substituted with $\dot{M}_*$. The prototype model delineated by [32] can be simply recovered by taking $p(\alpha) = \delta(\alpha - \alpha_{\rm M82})$ with $\alpha_{\rm M82} = 4.2$. To constrain the distribution $p(\alpha)$, we instead consider a sample of sources as representative of all the SBGs. In particular, we consider the 12 SFG and SBGs observed in gamma-rays for which the photon spectral index Γ have been inferred by a fitting procedure with a power-law function [19, 151].

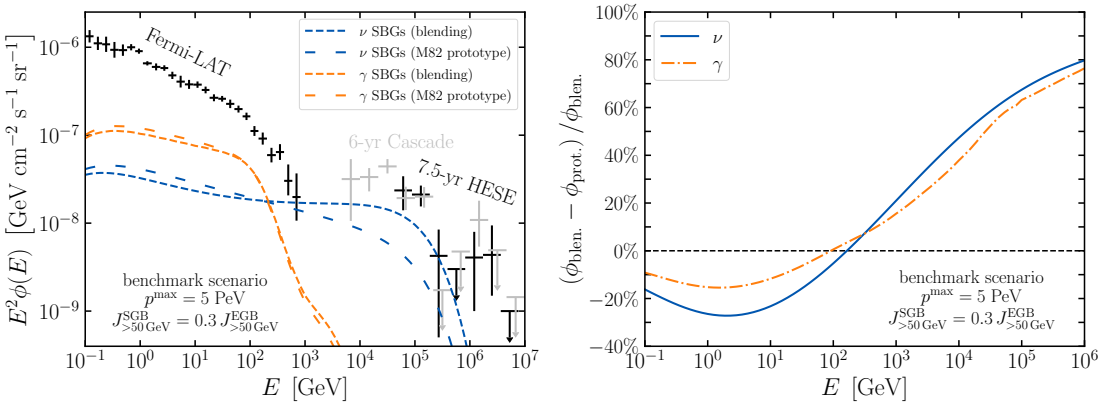

Figure 3.2: *Left:* comparison between the diffuse emission of starburst galaxies modeled with the blending of spectral indexes (short-dashed lines) and with the assumption of M82 as prototype [32] (long-dashed lines) for the benchmark case with $p^{\max} = 5$ PeV. The normalization of the SBG emission is fixed to account the 30% of the total EGB integrate flux above 50 GeV (see Eq. (3.24)). The blue (orange) color corresponds to the neutrino (gamma-ray) flux. *Right:* Relative difference of the two different SBG modelings with blending (blen.) and prototype (prot.) for the diffuse neutrino (blue solid line) and the gamma-ray (orange dot-dashed line) fluxes as a function of energy. Below (above) the horizontal dashed line, the blending of the spectral indexes leads to a lower (higher) flux.

Bearing in mind that $\phi_\gamma \propto Q_\pi \propto E^2 Q_p \propto E^{-\alpha+2}$, we can infer the values of α by taking $\Gamma + 2$. We report the different values of the spectral indexes obtained from [19] in the histogram of Figure 3.1. Hence, we assume a Gaussian distribution $\mathcal{N}(\alpha|\mu_\alpha, \sigma_\alpha^2)$ for the blending of spectral indexes, whose mean and variance are deduced by this source catalog. We have $\mu_\alpha = 4.2$ and $\sigma_\alpha^2 \simeq 0.04$.

We emphasize that, due to the limited number of SBGs in the sample we are considering, it is difficult to draw robust conclusions on the distribution of the spectral indexes. In particular, with this low statistics, the estimated distribution will depend on the statistical approach with which the data are treated. We have also tested other data-driven approaches than the Gaussian fit to the observation: for example, assuming as a distribution a superposition of Gaussian functions for each measurement[3] or replacing the α-integral in Eq. (3.23) with an average over the measured spectral index values. In the former case, we have found no significant differences with respect to blending approach defined in Eq. (3.23). In the latter, the number of neutrino HESE events accounted for by SBGs reduces by about 70%. Hence, different statistical data-driven methodologies could lead to different results. In this sense, only an increase in the statistical sample of observed SBGs or in the precision of the measurements could provide definite results.

In order to highlight the effect of having a spectral index blending rather than a fixed power-

[3]This substantially amounts to a kernel density estimation with a Gaussian kernel and a width equal to the experimental uncertainty on each measurement.

law according to the M82 prototype, we show in the left panel Figure 3.2 the neutrino (blue lines) and gamma-ray (orange lines) fluxes obtained with the two approaches for the benchmark case of $p^{\rm max} = 5$ PeV. The normalization $N_{\rm SBG}$ of the SBG emission is determined so that the SBG gamma-ray flux accounts for the 30% of the total EGB integrated flux $J^{\rm EGB}_{>50\ {\rm GeV}} = 2.4 \times 10^{-9}{\rm ph/cm^2/s/sr}$ [7]. A fraction of 0.3 is indeed compatible with the limits affecting the non-blazar component of the EGB above 50 GeV [12, 13]. Hence, we require

$$J^{\rm SBG}_{>50\ {\rm GeV}} = N_{\rm SBG} \int_{50\ {\rm GeV}}^{820\ {\rm GeV}} \Phi^{\rm SBG}_{\gamma}(E_\gamma) {\rm d}E_\gamma = 0.3\, J^{\rm EGB}_{>50\ {\rm GeV}}\,, \tag{3.24}$$

which is satisfied for $N_{\rm SBG} \simeq 0.73$. The comparison between the two approaches is made clearer in the right plot of Figure 3.2 where we report the relative difference between the two neutrino and gamma-ray fluxes. The spectral index blending results in the flux having a complex convex structure than a simple power-law due to the contribution of spectra which are harder than the "average" spectral index, leading to a reduction of the neutrino and gamma-ray emission at low energies ($E \lesssim 10^3$ GeV), while for higher ones the fluxes are greater. Remarkably, while the neutrino diffuse flux calculated using the M82 prototype model is almost negligible when compared to the IceCube 7.5-year HESE and 6-year cascade data, the spectral index blending allows for a large neutrino flux around 100 TeV. Moreover, in this benchmark scenario a cut-off energy of $p^{\rm max} = \mathcal{O}$(PeV) is enough to account for a considerable part of the astrophysical SED measured by IceCube, bypassing the need of SNR shock that can accelerate CR up to energies of the order of 10^2 PeV. By contrast, the gamma-ray contribution remains almost unchanged due to the contribution of electromagnetic cascades. Even though the direct spectrum of photons produced by the blending has a lower normalization than the prototype for energies below 10^3 GeV, the electromagnetic cascade contribution is higher because more photons are available for reprocessing. This leads to a compensation of contributions, resulting in an almost-unaltered spectrum. It should be noticed that this compensation is partially due to the internal absorption phenomena that suppress the gamma-ray flux before they escape the source. Hence, the more realistic model based on the spectral index blending has the potentiality to reduce the existing tension of the hadronic production scenario with diffuse neutrino and gamma-ray data. In particular, the spectral index blending allows starburst galaxies to account for ~ 26 neutrino events ($\sim 25\%$) of the 7.5-year HESE data.[4] In comparison, the standard prototype-based model saturating the non-blazar EGB component provides only 8 ($\sim 8\%$) of the 7.5-year HESE data.

[4]For the same benchmark scenario, the alternative data-driven approach based on the average over the measured spectral indexes values predicts an SBG contribution of $\sim 18\%$ to the 7.5-year HESE data.

In any case, other sources are in general required to account for the whole diffuse neutrino flux.

Before discussing the multi-messenger analysis we have performed, several comments are in order: our approach delineated in Eq.s (3.22) and (3.23) could be in principle extended to the other parameters describing the SBG emission. Regarding the parameter $p^{\rm max}$, however, no direct measurements of the cut-off energy exist for this class of sources and therefore a data-driven distribution for this parameter cannot be inferred. On the other hand, several measurements have been carried out for example to infer the magnetic field B inside the starburst nucleus. According to the analysis [18], the observational estimates for the magnetic field range from tens to thousands μG. However, we have checked that the magnetic field has a very marginal impact on the neutrino and gamma-ray fluxes as expected in the calorimeter scenario. Indeed, the magnetic field only affects the diffusion time $T_{\rm diff}$ that is in general much higher than the other timescales involved [31, 32]. As a result, larger values for the magnetic field than our benchmark of $B = 200$ μG would slightly increase the neutrino flux at high energies where $T_{\rm diff} \sim T_{\rm adv}$. Furthermore, other parameters such as the density of the interstellar medium only affect the normalization of the neutrino flux without changing its spectral shape. The same effect is also produced by taking different values for the threshold star formation rate ψ_*. Indeed, as shown in Ref. [32], the diffuse fluxes asymptotically scale as $\Phi_{\nu,\gamma} \propto \psi^{0.4}$. Therefore, to account for the effect of all these parameters, we simply introduce the overall normalization $N_{\rm SBG}$ as free parameter in the multi-messenger analysis discussed in the next section.

3.5 Multi-messenger analysis

In order to quantitatively discuss the role of starburst galaxies in the production of astrophysical neutrinos, we perform a statistical multi-messenger analysis which takes into account both neutrino and gamma-ray data. In particular, we analyze two neutrino IceCube data samples: the 7.5-year HESE data [8] and the 6-year high-energy cascade data [9]. The former contains neutrino events of all flavours with track and shower topologies above 60 TeV. The latter, instead, only includes shower-like events (mostly electron and tau neutrino flavours) and characterizes the diffuse neutrino flux down to few TeV thanks to the smaller background contamination. Concerning gamma-ray data, we examine the extragalactic gamma-ray background (EGB) measured by Fermi-LAT [7]. Most of the EGB spectrum is accounted by for resolved and unresolved blazars, while the contribution of other sources is in general sub-dominant [11–13]. Therefore, in addition to the starburst galaxies, we take into account other classes of sources contributing to the neutrino and gamma-ray skies. In particular, we have:

- **Neutrinos**
  - **Starburst galaxies**: the modeling of the neutrino flux from starburst galaxies has been detailed in the previous sections. In particular, the shape of the SBG spectrum strongly depends on the maximum energy $p^{\max}$ of the cosmic protons in the galaxy;
  - **Blazars:** for this subclass of Active Galactic Nuclei, we follow [71] where the blazar neutrino flux has been computed by assuming the baryonic loading directly linked to the blazar sequence trend [152] and taking the same blazar distribution as used by [11]. An early use of the blazar sequence is reported in [153]. In [71], three different models for the blazar neutrino flux are provided according to different assumptions on the baryonic loading. We have checked that our results do not depend on the particular blazar model considered. Therefore, in the following we just use as a benchmark the "scenario 1" (see Figure 5 in [71]) where the baryonic loading is assumed to be constant (see also [154]). In any case, as will be clear in the following, we check that in our best-fit scenarios the blazar neutrino component is always compatible with the IceCube stacking limit [14].
- **Gamma-rays**
  - **Starburst galaxies**: the gamma-ray flux from starburst galaxies has been discussed in the previous sections;
  - **Blazars:** we include in this class the diffuse gamma-ray flux from BL Lacs and Flat Spectrum Radio Quasars. This contribution has been estimated by [11]. However, this estimate does not take into account the contribution of electromagnetic cascades to the diffuse flux. For this reason, we have integrated the use of the γ-Cascade code to obtain the diffuse blazar flux, using the best-fit values for the Luminosity-Dependent Density Evolution (LLDE) model provided by [11], together with the contribution of electromagnetic cascades. We find that the latter can enlarge the diffuse blazar spectrum by even 20%, causing significant changes in the multi-messenger analysis;
  - **Radio galaxies:** we take their contribution to the EGB from [11] (see also [155, 156]). In these works, Radio galaxies provide a large gamma-ray flux below 1 GeV. It is worth noticing that for the sake of simplicity we do not consider a relevant contribution from Radio Galaxies to the neutrino flux, in agreement with analyses like [157]. However, recent works like [158] have proposed radio galaxies to be an important source of

high-energy neutrinos. Hence, a negligible high-energy neutrino emission from these sources should be regarded as an assumption of this analysis.

For both the neutrino and the gamma-ray components, we perform a maximum likelihood analysis using a chi-squared likelihood. For the neutrino data, we use the following chi-squared function:

$$\chi^2_\nu = \sum_i \left(\frac{\Phi^{\rm IC}_{\nu,i} - N_{\rm Blazars}\Phi^{\rm Blazars}_{\nu,i} - N_{\rm SBG}\Phi^{\rm SBG}_{\nu,i}(p^{\rm max})}{\sigma^{\rm IC}_{\nu,i}} \right)^2 , \tag{3.25}$$

where $\Phi^{\rm IC}_{\nu,i}$ is the diffuse single-flavour flux observed by IceCube in each energy interval i with uncertainties $\sigma^{\rm IC}_{\nu,i}$, whereas $\Phi^{\rm Blazars}_{\nu,i}$ and $\Phi^{\rm SBG}_{\nu,i}$ are the neutrino flux of blazars and SBG sources, respectively. The neutrino chi-squared function depends on three free parameters: the maximum proton energy $p^{\rm max}$ in each starburst galaxy, and the two normalizations $N_{\rm SBG}$ and $N_{\rm Blazars}$ for the cumulative contributions of the starburst galaxies and the blazar sources, respectively, which represent two overall factors that multiply the fluxes. The normalization $N_{\rm SBG}$ is mainly related to the efficiency of SNRs energy release ξ (see Eq. (3.5)), while it very slightly depends on the threshold value ψ_* of the SFR above which the SBG can be considered an efficient calorimeter (see Eq. (3.22)). Both theoretical arguments and numerical simulations show that the normalization $N_{\rm SBG}$ can be expressed in terms of the physical parameters as

$$N_{\rm SBG} = \left(\frac{\xi}{0.1}\right) \left[1.47 - 0.32 \left(\frac{\psi_*}{1\ {\rm M}_\odot\ {\rm yr}^{-1}} \right)^{0.4} \right] . \tag{3.26}$$

Due to the very mild dependence on ψ^*, the determination of $N_{\rm SBG}$ through our likelihood analysis amounts roughly to a determination of the SNRs efficiency ξ. For the gamma-ray data, we follow the analyses [11, 94, 95] based on a chi-squared function. In particular, we consider two independent normalizations for the blazar component $N_{\rm Blazars}$ and for the radio galaxies component $N_{\rm RG}$. In [11] a prior distribution was obtained for the cumulative normalization of the whole astrophysical flux by averaging the theoretical uncertainties on the predictions for the flux over the energy range of interest. For this work, we proceed along similar lines, separately averaging the theoretical uncertainties of the radio galaxies and blazar fluxes. In this way we obtain the following chi-squared for the gamma-rays

$$\begin{aligned} \chi^2_\gamma = & \sum_i \frac{1}{{\sigma^{\rm EGB}_{\gamma,i}}^2} \left(\Phi^{\rm EGB}_{\gamma,i} - N_{\rm RG}\Phi^{\rm RG}_{\gamma,i} - N_{\rm Blazars}\Phi^{\rm Blazars}_{\gamma,i} + \right. \\ & \left. - N_{\rm SBG}\Phi^{\rm SBG}_{\gamma,i}(p^{\rm max}) \right)^2 + \\ & + \left(\frac{N_{\rm Blazars} - 1}{\sigma_{\rm Blazars}} \right)^2 + \left(\frac{N_{\rm RG} - 1}{\sigma_{\rm RG}} \right)^2 \end{aligned} \tag{3.27}$$

where the quantities $\Phi_{\gamma,i}^{\rm EGB}$ are the EGB data with uncertainties $\sigma_{\gamma,i}^{\rm EGB}$, while $\Phi_{\gamma,i}^{\rm RG}$, $\Phi_{\gamma,i}^{\rm Blazars}$ and $\Phi_{\gamma,i}^{\rm SBG}$ are respectively the radio galaxies, blazar and SBG contributions to the EGB. The last two terms are the priors that take into account the uncertainty on the normalization of the two non-SBG components: the average uncertainties are estimated to be $\sigma_{\rm Blazars} = 0.26$ and $\sigma_{\rm RG} = 0.65$ [11].

Differently from the more recent analysis [95], we take into account a further prior distribution from the estimate of [13] that $0.68^{+0.09}_{-0.08}$ of the EGB above 50 GeV consists of resolved point sources. We compute the fraction of the total blazar diffuse flux that originates from resolved blazars, defined as the blazars with a total flux larger than 10^{-8} ph/cm^2/s according to [11]. Averaging this fraction over the energy range above 50 GeV, we find that 81% of the blazar flux above 50 GeV is composed of point sources. Assuming that most of the point sources detected in the EGB above 50 GeV are blazars, we obtain that $0.84^{+0.11}_{-0.10}$ of the EGB above 50 GeV is composed of blazars. Furthermore, we calculate the blazar gamma-ray flux normalisation which corresponds to such values and therefore we add the following positional prior contribution

$$\chi^2_{\rm pos} = \left(\frac{N_{\rm Blazars} - 0.80}{0.11} \right)^2 \tag{3.28}$$

to the chi-squared for the integrated contribution of blazars above 50 GeV, where the 10% of uncertainty in Eq. (3.28) comes from the uncertainty of the blazar contribution over 50 GeV calculated by [13]. It is worth noticing that such a pull term is consistent with the similar one in Eq.s (3.27) once the contribution of electromagnetic cascades is neglected as done originally in Ref. [11]. The multi-messenger analysis is therefore performed by combining the three chi-squared functions as

$$\chi^2_{\nu+\gamma}(N_{\rm RG},\, N_{\rm Blazars},\, N_{\rm SBG},\, p^{\rm max}) = \chi^2_\nu + \chi^2_\gamma + \chi^2_{\rm pos}\,, \tag{3.29}$$

which is a function of four free parameters $N_{\rm RG}$, $N_{\rm Blazars}$, $N_{\rm SBG}$ and $p^{\rm max}_{\rm SBG}$. In the next section, we discuss the main results of the maximum likelihood analysis.

3.6 Results

As mentioned at the beginning of this section, we examine the IceCube 7.5-year HESE and the 6-year high-energy cascade neutrino data, being the latter sensitive to a wider energy range. For each of the two neutrino data-sets we consider as gamma-ray counterpart the whole Fermi-LAT

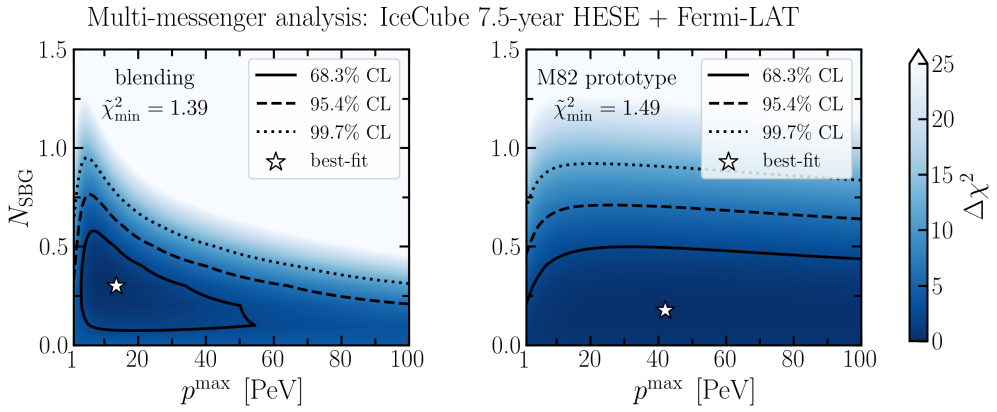

Figure 3.3: Profile likelihoods for the SBG parameters obtained in the multi-messenger analysis of IceCube 7.5-year HESE neutrino data and Fermi-LAT gamma-ray data with energy above 0.1 GeV. The left (right) panel corresponds to the blending (M82 prototype) model for the SBG emission. The solid, dashed and dotted lines represent the likelihood contours at 68.3% CL, 95.4% CL and 99.7% CL, respectively. The white stars display the best-fit points. The full set of likelihood contour plots is reported in Appendix C.

EGB spectrum above 0.1 GeV. We explore the four-dimensional parameter space by means of the profile likelihood method on the quantity $\Delta\chi^2 = \chi^2_{\nu+\gamma} - \min \chi^2_{\nu+\gamma}$ representing the inverse of the log-likelihood ratio. In agreement with the Wilks' theorem, we assume that the distribution of $\Delta\chi^2$ is a chi-squared distribution with a number of degrees of freedom equal to the number of free parameters. In the following discussion, we mainly aim at highlighting the differences in the results obtained with the two different models for the SBG emission: the one based on the data-driven blending of spectral indexes (hereafter dubbed as "blending") and the one already adopted in the literature and based on the prototype method resulting in a single power-law neutrino flux (hereafter dubbed as "M82 prototpye").

In Figures 3.3 and 3.4 we report the results for the SBG parameters, $p^{\rm max}$ and $N_{\rm SBG}$, in case of the two neutrino data sample considered. The plots show the two-dimensional profile likelihood ratios when the remaining free parameters ($N_{\rm Blazars}$ and $N_{\rm RG}$) are considered as nuisance parameters (see Appendix C for the complete set of two-dimensional profile likelihoods). The different contours delimit the regions at 68.3%, 95.4% and 99.7% confidence level (CL) according to a chi-squared distribution with two degrees of freedom. The best-fit points are depicted by the white stars. In the figures, the left and right panels refer to the SBG models "blending" and "M82 prototype", respectively. We find substantially different results in correspondence of the two SBG models. Remarkably, in the case of IceCube HESE data (Figure 3.3), the blending of spectral indexes allows for a preference of a non-zero SBG contribution at slightly more than 1σ. Moreover, the SBG maximum energy is constrained to be smaller than about 50 PeV at

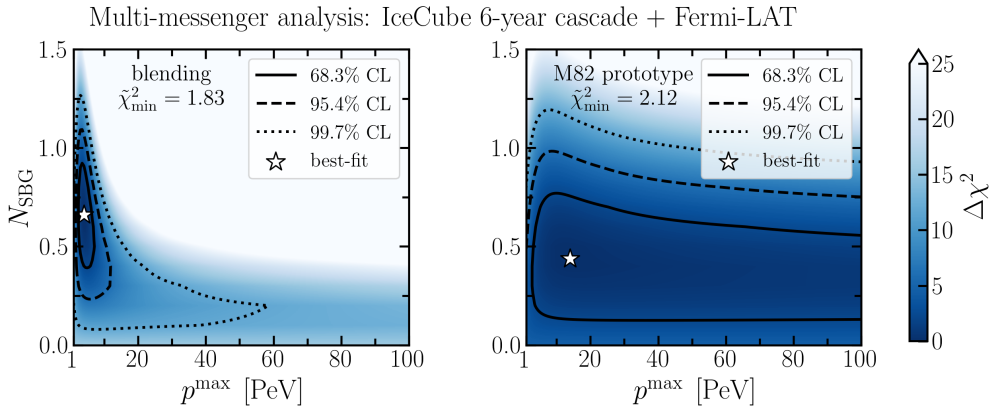

Figure 3.4: Profile likelihoods for the SBG parameters obtained in the multi-messenger analysis of IceCube 6-year cascade neutrino data and Fermi-LAT gamma-ray data with energy above 0.1 GeV. The left (right) panel corresponds to the blending (M82 prototype) model for the SBG emission. The solid, dashed and dotted lines represent the likelihood contours at 68.3% CL, 95.4% CL and 99.7% CL, respectively. The white stars display the best-fit points. The full set of likelihood contour plots is reported in Appendix C.

68.3% CL. On the other hand, the prototype-based model with a single power-law behaviour is instead disfavoured by data, implying the presence of an upper bound on $N_{\rm SBG}$ and consequently an almost unconstrained range of values for $p^{\rm max}$. In the case of IceCube 6-year high-energy cascade data (Figure 3.4), the additional neutrino data below 100 TeV highly prefer a larger neutrino emission from starburst galaxies. For the SBG model "blending", a negligible SBG component with $N_{\rm SBG} \simeq 0$ is disfavoured at more than 3σ, and the maximum energy $p^{\rm max}$ is constrained to be smaller than 10 PeV at 95.4% CL. On the other hand, for the SBG model "M82 prototype", a preference for a non-zero SBG contribution is relaxed at slightly more than 1σ, and no upper bound for $p^{\rm max}$ is found.

In Table 3.2, we report the best-fit points of the different multi-messenger analyses, together with the reduced chi-squared values (last row). The second and third columns in each table correspond to the two different models for the SBG emission, "blending" and "M82 prototype", respectively. For both the two neutrino data samples, the former results to be in better agreement with data having smaller reduced chi-square values with respect to the latter. As expected from the previous discussion, we find that the spectral index blending allows for a lower cut-off energy $p^{\rm max}$ and a larger normalization $N_{\rm SBG}$ when compared to the prototype-based model. In all the cases, the blazar component has a normalization smaller than the one predicted by [11] ($N_{\rm Blazars} = 1$). This result is mainly driven by the inclusion of the contribution of electromagnetic cascades in the blazar diffuse gamma-ray flux. In any case, the best-fit blazars component provides the dominant contribution to the EGB above 50 GeV in agreement with

IceCube 7.5-year HESE + Fermi-LAT

	SBG model	
Parameters	Blending	M82 prototype
$p^{\max}$	13.6	42.0
$N_{\rm SBG}$	0.30	0.18
$N_{\rm Blazars}$	0.72	0.77
$N_{\rm RG}$	2.24	2.19
$\tilde{\chi}^2 = \chi^2/32$	1.39	1.49

IceCube 6-year cascade + Fermi-LAT

	SBG model	
Parameters	Blending	M82 prototype
$p^{\max}$	4.0	14.0
$N_{\rm SBG}$	0.66	0.44
$N_{\rm Blazars}$	0.59	0.68
$N_{\rm RG}$	2.24	2.15
$\tilde{\chi}^2 = \chi^2/38$	1.83	2.12

Table 3.2: Best-fit points obtained in the multi-messenger analyses of IceCube 7.5-year HESE (left) and 6-year high-energy cascade (right) neutrino data and the extragalactic gamma-ray background data measured by Fermi-LAT. The second (third) column in each table refers to the SBG model with the data-driven spectral index blending (a single power-law behaviour set by M82 prototype). The last row reports the reduced chi-squared.

the positional prior [13]. The contribution of radio galaxies is instead required to be larger than the one predicted by [11], leading to a slight tension with the corresponding prior on $N_{\rm RG}$.

The neutrino and gamma-ray fluxes corresponding to the two best-fit points for the SBG model "blending" are depicted in Figure 3.5. The contributions to gamma-ray and neutrinos are displayed in orange and blue colors, respectively. The SBG, blazars and radio galaxies components are represented by the dashed, dotted and dot-dashed curves, while the solid lines refer to the cumulative flux. For both the two neutrino data samples, starburst galaxies (where p-p interactions dominate) mainly contribute to the neutrino flux below PeV energy, while blazars (where p-γ interactions dominate) account for the PeV neutrinos in agreement with the IceCube stacking limit (shaded grey band). The neutrino data considered in the fit constrain the maximum energy in each starburst galaxy to be of the order of ~ 10 PeV. On the other hand, the main difference between the two analyses is a tendency toward a larger role of the SBG component when considering the IceCube 6-year cascade data sample. Diversely, the role of gamma-ray data is mainly to constrain the normalization of the SBG component in favour of the non-SBG ones (blazars and radio galaxies). As expected, the predicted gamma-ray spectrum is indeed almost independent from $p^{\max}$ due to the gamma-ray absorption. In the two best-fit scenarios the blazars dominate the EGB above about 1 GeV, while at lower photon energies they give way to a larger contribution from radio galaxies.

To further highlight the remarkable implications of using the spectral index blending, we

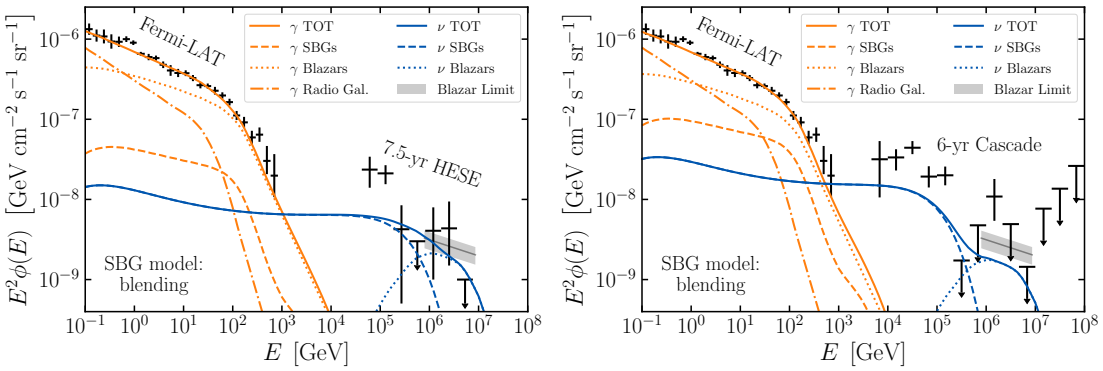

Figure 3.5: Best-fit gamma-ray (orange lines) and single-flavour neutrino (blue lines) fluxes in case of the SBG model with data-driven blending of spectral indexes. The left (right) plot corresponds to the multi-messenger analysis with IceCube 7.5-year HESE (6-year cascade) neutrino data. The dashed, dotted and dot-dashed lines correspond to the contributions of SBGs, blazars and radio galaxies, respectively. The grey area displays the IceCube stacking limit affecting the blazar component [14].

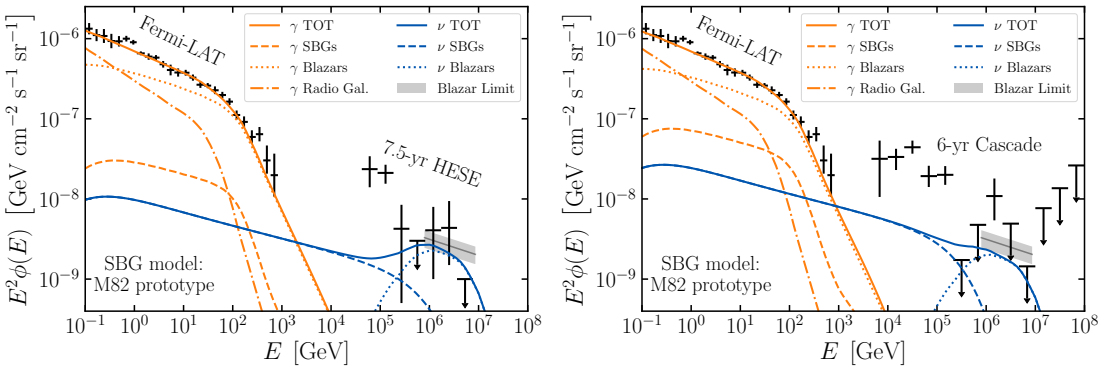

Figure 3.6: Best-fit gamma-ray (orange lines) and single-flavour neutrino (blue lines) fluxes in case of the SBG prototype-based model with a single power-law behaviour. The left (right) plot corresponds to the multi-messenger analysis with IceCube 7.5 year HESE (6-year cascade) neutrino data. The dashed, dotted and dot-dashed lines correspond to the contributions of SBGs, blazars and radio galaxies, respectively. The grey area displays the IceCube stacking limit affecting the blazar component [14].

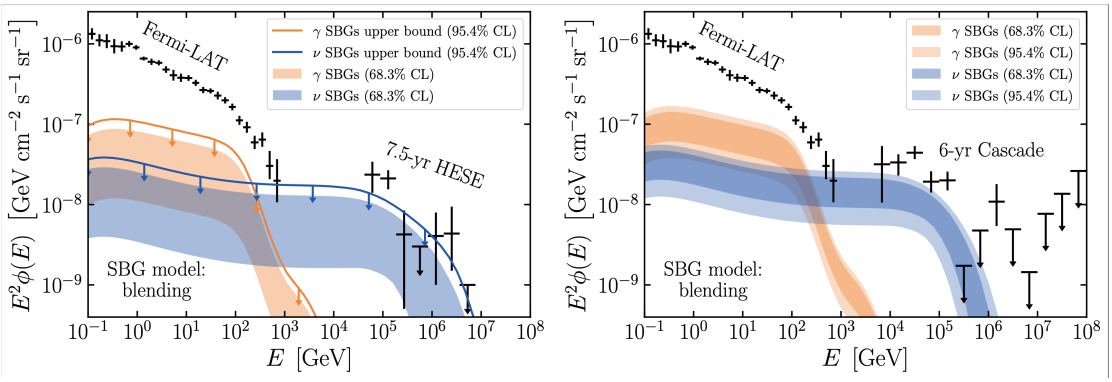

Figure 3.7: Gamma-ray (orange) and single-flavour neutrino (blue) uncertainty bands at 68.3% CL (dark colors) and 95.4% CL (light colors) for the SBG component deduced by the multi-messenger analysis in case of data-driven blending of spectral indexes. The left (right) plot corresponds to the multi-messenger analysis with IceCube 7.5-year HESE (6-year cascade) neutrino data. In the left plot, the solid lines correspond to upper bounds at 95.4% CL.

show in Figure 3.6 the best-fit gamma-ray and neutrino fluxes obtained for the SBG model "M82 prototype". As can be seen in the plots, the single power-law model is highly constrained by gamma-rays data, thus leading to an almost negligible contribution from starburst galaxies to the diffuse neutrino flux. As already shown in Figure 3.2, the assumption of a distribution for the spectral indexes causes the diffuse SBG neutrino spectrum to behave differently from a simple power-law with a higher cut-off, but rather as a more complicated function of the energy. Such a behaviour is a key feature, allowing starburst galaxies to provide a larger contribution to the neutrino flux without exceeding the corresponding EGB limits. Our results point out that the existing strong limits [83–85] affecting starburst galaxies and in general *p-p* interaction-dominated sources could be due to a too simplistic modeling of their gamma-ray and neutrino emission. On the other hand, better and more realistic models capturing the different properties of individual emitters within the same class of astrophysical sources seem to be required to explain the data and potentially alleviate the claimed tension between neutrino and gamma-ray observations.

Focusing only on the more realistic SBG model "blending", we visibly quantify the allowed SBG contribution to the gamma-ray and neutrino data in Figure 3.7. In particular, we show the 1σ and 2σ uncertainty bands at 68.3% CL for the SBG contribution to the extragalactic gamma-ray background and the diffuse neutrino flux, according to the results displayed in the left panels of Figures 3.3 and 3.4. In the left plot, the solid lines represent the upper bound on the SBG component at 95.4% CL. It is worth pointing out that a large SBG neutrino component dominating the neutrino flux below 100 TeV is therefore allowed at 2σ. This is especially true

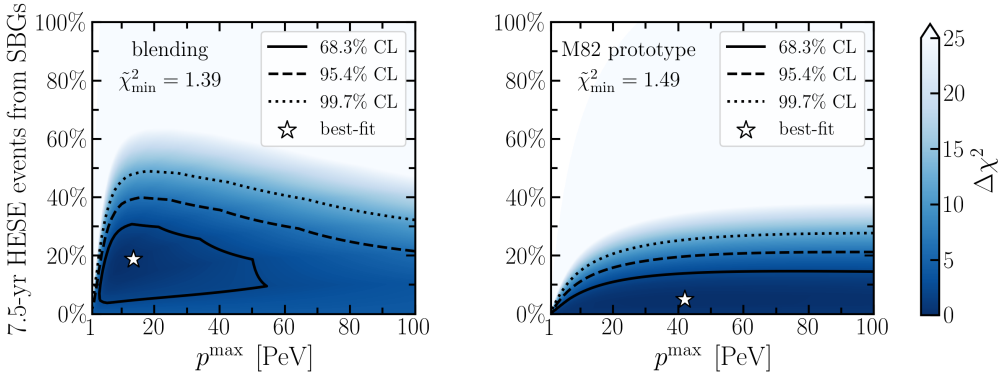

Figure 3.8: Percentage of IceCube 7.5-year HESE neutrino events above 30 TeV accounted for by starburst galaxies with blending (left plot) and M82 prototype (right plot) models. The solid, dashed and dotted lines represent the likelihood contours at 68.3% CL, 95.4% CL and 99.7% CL, respectively, according to the corresponding multi-messenger analysis (see Figure 3.3). The white stars display the best-fit points.

in case of the IceCube 6-year cascade data (right plot) for which smaller uncertainty bands are obtained. On the other hand, in neither case starburst galaxies are allowed to saturate the low-energy neutrino data.

Finally, in Figure 3.8 we report the percentage of HESE events that can be accounted for by starburst galaxies modelled with the spectral index blending (left plot) and M82-prototype (right plot). The number of neutrino events after 7.5-year of data taking is simply computed by convolving the SBG neutrino flux above 30 TeV with the HESE effective area [53]. Remarkably, in the "blending" scenario, starburst galaxies are allowed to account for the 40% ($\sim 50\%$) of the total HESE events at 95.4% (99.7%) CL. On the other hand, in the "M82 prototype" scenario, they can only explain no more than 20% ($\sim 30\%$) of HESE events at 95.4% (99.7%) CL. Such a comparison further highlights the impact of the spectral index blending in quantifying the SBGs contribution to the diffuse neutrino flux measured by IceCube. These results are in agreement with the constraints placed on the contribution to the IceCube neutrino events from nearby starforming and starburst galaxies [75, 117–120]. We find that in all the SBG parameter space explored, the contribution of nearby starburst galaxies within a distance of 250 Mpc (redshift $z \leq 0.06$) is smaller than 1%. Hence, it is worth observing that, although starburst galaxies can provide a significant contribution to the diffuse neutrino flux, other components seem to be required to fully explain the data below 100 TeV. In particular, the addition of a diffuse Galactic component as the one recently introduced by [61] and constrained by IceCube and Antares experiments [63, 64] would probably describe the portion of HESE flux at 100 TeV unfilled by the SBG "blending" scenario. Interestingly also the analyses done about the Galactic diffuse

component indicate as a preferential $p^{\max}$ at about 5 PeV, in accordance with the favourite $p^{\max}$ range obtained in this work for the SNRs inside the SBGs.

3.7 Discussion and Conclusions

The astrophysical origin of cosmic neutrinos has still not been determined, even though many candidate sources have been proposed. Therefore, it is important to understand the role that each such candidate plays. In this chapter, we have analysed the neutrino and gamma-ray hadronuclear production of SBGs. We have exploited a recent review of SBG gamma-ray spectral features, based on 12 objects, in order to go beyond the usual simplifying assumption that the diffuse flux from SBG is a superposition of identical unresolved sources and consider a distribution of SBG varying parameters. In particular, our analysis shows how the variability of the spectral index of the hadronic emission of SBGs leads to drastic changes in the expected diffuse neutrino flux. As a result, we find that the diffuse neutrino production from SBGs, at the energies observed by IceCube, under this spectral index blending assumption is larger than what would be expected for a simple power law spectrum. On the other hand, the gamma-ray production is very weakly sensitive to the introduction of the blending, allowing this larger diffuse neutrino component without exceeding the diffuse gamma-ray constraint known for this astrophysical class. In order to verify this assertion, we have proceeded to a multi-messenger statistical analysis, using the up-to-date EGB data from Fermi-LAT and the 7.5-years HESE and 6-years high-energy cascade data from IceCube. We have tested the hypothesis that these data can be explained by the simultaneous emission of the SBG component plus additional astrophysical components from blazars and radio galaxies. Moreover, differently from the previous literature, we have fully taken into account also the gamma-ray radiation produced by the electromagnetic cascades both for SBGs and blazars. At the same time, we have considered as prior information the limit of resolved sources contribution to the EGB above 50 GeV. Previous analyses, based on a single power-law assumption for the SBG flux, strongly disfavored this component in the neutrino sector, due to an overproduction of gamma-rays. We have shown that the improvement in the description of the hadronic fluxes due to the blending of spectral indexes leads to a non-vanishing best-fit SBG neutrino flux. Our analysis leads to the conclusion that SBG and blazars cannot fully explain the IceCube data while complying with the gamma-ray constraints, leaving space for another component which could possibly be associated to the diffuse Galactic neutrino emission or other extra-galactic sources.

Finally, our statistical analysis indicates as a maximal energy reached by astrophysical ac-

celerators within SBGs a value that lies below 50 PeV, reconciling this result with the physics of the potential Galactic Pevatrons. This conclusion is strongly driven by the multi-component description of IceCube data taking into account blazars and SBGs. In fact, in our benchmark scenario we assume the PeV neutrinos are mainly produced by blazars. Our results may vary depending on the specific assumptions behind the analysis, including our treatment of the EM cascades, the EBL function and our analytical modeling of SBG neutrino and gamma-ray production; more details are reported in the appendix C including the case without EM cascades. Another source of uncertainty comes from the limited number of sources in the sample which does not allow for a conclusive spectral index distribution. In this regard, future and improved γ-ray catalogue of SBGs will unveil the potential importance of the spectral index blending and its consequence for multi-messenger astronomy. Nevertheless, we are led to the conclusion that SBGs may play a rather important role in the description of IceCube and Fermi-LAT observed diffuse fluxes. In particular, the introduction of this new data-driven statistical analysis highlights how this class can be crucial to describe the low-energy part of the IceCube HESE and cascade fluxes. Future observations of the Global Neutrino Network (GNN) and in particular KM3NeT [159], Baikal-GVD [160], P-ONE [161] and IceCube-Gen2 [162] will shed more lights on this astrophysical component.

Chapter 4

Gamma-ray and Neutrino Prospects for Nearby Star-forming Galaxies

In this chapter, we assess the possibility for current and future gamma-ray and neutrino telescopes to constrain the non-thermal emissions of nearby, known SBNi. The chapter is based on the analysis published in [163].

4.1 Introduction

In the last chapter, we assessed the possibility of SBGs explaining the diffuse neutrino emissions. The rationale of the main finding is that, indeed, they can provide a non negligible contribution. However, in order to explain a sizeable portion of measured high-energy neutrino flux with SFGs and SBGs, the deep Universe must be considered up to redshift $\sim$ 4–5, because of their dimness [19, 32, 52]. In fact, the low gamma-ray luminosity of SFGs and SBGs typically represents a bound for their contribution to the observed astrophysical neutrinos as a point-like component. For the moment, as emphasized in Sec. 2.3, only a dozen of these sources have currently been catalogued as gamma-ray point-like sources using the Fermi-LAT data and only few of them have been observed through Imaging Cherenkov telescopes [19].

In this chapter, we employ a multi-messenger and multi-wavelength approach to assess the ability of current and upcoming neutrino telescopes to observe such galaxies as neutrino point-like sources. This is significantly important after the IceCube collaboration, analyzing 10-year of tracks (from April 2008 to July 2018), reported a 2.9σ excess of signal neutrino events from the direction of NGC 1068 [76]. Recently, the excess has increased to an overall significance of 4.2σ,

analyzing track events from 2011 and 2020 [60]. Even though additional Active Galactic Nuclei (AGN) activity could be present, observations like this one suggest that star-forming activity could trace the hadronic emission and produce point-like excesses in the TeV sky observed by IceCube as well as in the future skymap of the upcoming KM3NeT/ARCA and IceCube-Gen2 telescopes.

We follow the scenario described in the last chapter which consider the transport of high-energy protons and electrons in the SBNi and analyze the 10-year Fermi-LAT data provided by [19], taking into account the spectral energy distributions (SEDs) of 13 SFGs and SBGs presented in Sec. 2.3. We describe these gamma-ray observations through the hadronic and leptonic processes at work in the star-forming regions and determine the corresponding neutrino fluxes. For each source, we require the star formation rate (SFR) to be consistent with the one derived from infra-red (IR) and ultra-violet (UV) observations [20] within a maximal level of discrepancy, thus making sure that our predictions are consistent with the star forming activity of the sources. Hence, we compare the most-likely point-like neutrino flux normalizations at 1 TeV with IceCube, IceCube-Gen2, and KM3NeT sensitivities (see Figure 4.1). Besides, for the brightest sources we also show in Figure 4.2 the prospects of the Cherenkov Telescope Array (CTA).

4.2 Modelling the emission from nearby sources

In this section, we describe how we model the gamma-ray and neutrino emissions of the sources. Firstly, we make use of the same CR transport model described in the last chapter. In this context, the neutrino and gamma-ray emissions mainly depend on the gamma-ray spectral index $\Gamma = \alpha - 2$ and on the star formation rate. For the density $n_{\rm ISM}$ of the interstellar gas (target of the proton interactions), we rely on the Kennicutt relation (Eq. 2.8) [28, 45, 46].

For simplicity, we consider for all the galaxies $R_{\rm SBN} = 200$ pc, which is an average size of the circumnuclear regions [31]. By using the benchmark value $n_{\rm ISM} = 175$ cm^{-3} for $\dot{M}_* = 5$ M$_\odot$ yr^{-1} [31], by inverting Eq. 2.9, we obtain the scaling relation

$$n_{\rm ISM} = 175 \left(\frac{\dot{M}_*}{5 \text{ M}_\odot \text{ yr}^{-1}} \right)^{2/3} \text{cm}^{-3} \,. \tag{4.1}$$

For the background photon density $U_{\rm rad}$, we assume a direct proportionality to the SFR, which is expected to be tightly related to the infrared (IR) luminosity [28, 45, 46, 164–166]. In particular,

we consider the scaling relation

$$U_{\rm rad} = 2500 \left(\frac{\dot{M}_*}{5\,{\rm M}_\odot\,{\rm yr}^{-1}} \right) {\rm eV\,cm^{-3}}\,, \tag{4.2}$$

where the reference values, $U_{\rm rad} = 2500\,{\rm eV\,cm^{-3}}$ and $\psi = 5\,{\rm M_\odot\,yr^{-1}}$, are obtained from what has been inferred for M82 by [31, 32]. Such a relation is generally satisfied by high-SFR galaxies which behave as good calorimeters. On the other hand, low-SFR galaxies have been shown to deviate from the assumed linear SFR-IR relation, as also recently pointed out by [20, 37]. Nevertheless, for

these galaxies we have verified that Eq. 4.2 is a good and conservative approximation: indeed the gamma-ray emission depends only slightly on $U_{\rm rad}$ since the leptonic component is in general subdominant in our model. Moreover, a smaller value for $U_{\rm rad}$, as observed for low-SFR galaxies [20], would further reduce the leptonic production in favor of the hadronic one. Finally, for all the galaxies, we adopt the average values $B = 200$ μG [18] and $v_{\rm wind} = 500$ km/s [32] for the magnetic field and the dust-wind velocity in the SBNi, respectively.

4.3 Data Analysis

Our main purpose is to determine the high-energy neutrino emission from SFGs and SBGs based on a likelihood analysis of gamma-ray data. A crucial observation must be made: for some of these galaxies, a possible additional source of gamma-rays may be related to AGN activity [19, 167–173], which is not included in the following analysis. Thus we test the hypothesis that the observed gamma-ray SEDs are saturated by star-forming activity only, and determine the most-likely neutrino emission under this assumption. We analyze the gamma-ray SEDs of 13 galaxies observed by Fermi-LAT with 10 years of observation [19]. These data correspond to the Pass 8 data passing the quality data selection in the energy range $0.1 - 800\,{\rm GeV}$ [19]. The data reported in [19] are normalized to a constant value at an energy of 1 GeV. Therefore, we have suitably rescaled them using the reported best-fit parameters of the power-law model. Tab. 4.1 reports the scaling factor for the sources.

For M82 and NGC 253 we make also use of the data provided by VERITAS [22] and H.E.S.S. [23], respectively. For each galaxy, we pursue a Bayesian approach to assess the most-likely values for the two free parameters of the model: the star formation rate $\dot{M}_*$ and the spectral index Γ, where $\Gamma = \alpha - 2$, with α being the spectral index of injected protons and

Source	Scaling Factor
M31	0.67
NGC 253	0.88
SMC	2.89
M33	0.22
NGC 1068	0.73
NGC 2146	0.25
M82	1.15
ARP 299	0.13
NGC 4945	1.22
ARP 220	0.36
NGC 2403	0.14
NGC 3424	0.15

Table 4.1: Scaling factor from the spectra of Ref. [19].

electrons. We determine the posterior distribution as

$$p(\dot{M}_*, \Gamma|\mathrm{SED}) \propto p(\mathrm{SED}|\dot{M}_*, \Gamma)\, p(\dot{M}_*)\, p(\Gamma)\,, \tag{4.3}$$

with a Gaussian likelihood function

$$p(\mathrm{SED}|\dot{M}_*, \Gamma) = e^{-\frac{1}{2}\sum_i \left(\frac{\mathrm{SED}_i - E_i^2 \Phi_\gamma(E_i|\dot{M}_*, \Gamma)}{\sigma_i}\right)^2}\,. \tag{4.4}$$

Here, SED_i are the measured data, where i runs over the energy bins centered around the energy E_i, and σ_i are the observational uncertainties. The data are compared to the gamma-ray emission $\Phi_\gamma(E_i|\dot{M}_*, \Gamma)$ predicted by our model. We adopt the source distances provided by [20] and neglect the uncertainty on such values. For all the galaxies we consider the same uniform prior on the spectral index in the range 1.0–3.0. For the SFR, we instead adopt a different uniform prior distribution for each source. We require $\dot{M}_*$ to be consistent within a factor of 3 with the corresponding values reported in [20]. This choice is made to cover the wide variety of SFR estimates presented in the literature [19, 32, 168, 174–177] as well as to cover the distance uncertainty on these sources which is degenerate with the SFR (influencing only the spectra normalizations).

4.4 Results

The results of the analysis are summarized in Table 4.2. For M82, NGC 253, NGC 2146, NGC 2403, Circinus galaxy, M31, M33, and SMC, we find a reasonable agreement both with the data and the measured SFR values. We emphasize that in our model all the galaxies are

approximated as point-like sources with a dominant emission limited to the SBN. Hence, the SBN extension intrinsically defines the extension of the gamma-ray source emission. Most of the sources have not been resolved and therefore they are consistent with our starburst nucleus approximation. On the other hand, SMC and M31 have been observed by [19] as extended sources with an angular extension of 1.5° and 0.45°, respectively. Thus, for these sources we have also performed our analysis by assuming a different core radius in agreement with these observations (i.e. 800 pc and 3000 pc, respectively) and have obtained results similar to the ones reported in Fig. 4.1. Indeed, the most likely values of the neutrino flux normalizations change less than a factor of two, thereby making our predictions unchanged. We stress that our main goal is to assess the possibility for future neutrino telescope of singularly observing these sources, only using their gamma-ray data and the star formation rate as constraints for their neutrino emissions. In order to robustly constrain the parameters of these extended sources, it would be necessary a numerical simulation of their astrophysical environment, which we leave for future work.

Table 4.2: Results of the likelihood analysis of current gamma-ray data. The columns report the source name, the SFR prior, the most-likely values of the two parameters, the 68% maximum posterior density credible intervals of the marginal distributions, and the reduced chi-squared values considered as an estimate of the goodness of the fit.

Source	Uniform Prior $\dot{M}_*$	Most-Likely Values ($\dot{M}_*$, Γ)	68% Credible Intervals		χ^2/dof
			$\dot{M}_*$	Γ	
M82	3.0 – 30	(4.5, 2.30)	[4.3, 4.6]	[2.27, 2.33]	1.24
NGC 253	1.4 – 17	(3.3, 2.30)	[3.14, 3.40]	[2.28, 2.32]	1.32
ARP 220	60 – 740	(740, 2.66)	[492, 740]	[2.51, 2.68]	1.52
NGC 4945	0.35 – 4.15	(4.15, 2.30)	[4.05, 4.15]	[2.23, 2.32]	1.52
NGC 1068	5 – 93	(16, 2.52)	[13, 20]	[2.45, 2.65]	0.65
NGC 2146	3 – 57	(15, 2.50)	[9, 27]	[2.44, 2.88]	0.50
ARP 299	28 – 333	(28, 2.15)	[28, 200]	[1.40, 1.90] ∪ [2.77, 3.00]	0.18
M31	0.09 – 0.90	(0.34, 2.40)	[0.31, 0.40]	[2.29, 2.61]	0.52
M33	0.09 – 0.90	(0.44, 2.76)	[0.19, 0.56]	[2.57, 2.96]	0.44
NGC 3424	0.4 – 5.4	(5.4, 2.22)	[2.5, 5.4]	[1.92, 2.67]	1.63
NGC 2403	0.1 – 1.2	(0.75, 2.12)	[0.58, 0.96]	[1.92, 2.36]	0.38
SMC	0.008 – 0.090	(0.038, 2.14)	[0.037, 0.039]	[2.13, 2.16]	1.90
Circinus Galaxy	0.1 – 8.1	(6.6, 2.32)	[6.2, 7.8]	[2.15, 2.45]	0.92

For NGC 4945, NGC 3424, and ARP 220, we find a lower limit for the SFR, implying the need for additional contributions to explain their gamma-ray observations. Indeed these sources host an AGN [19, 168, 172]. A special case is ARP 299, for which we find an upper limit for the SFR. This is due to the fact that most of its the gamma-ray measurements are only flux upper

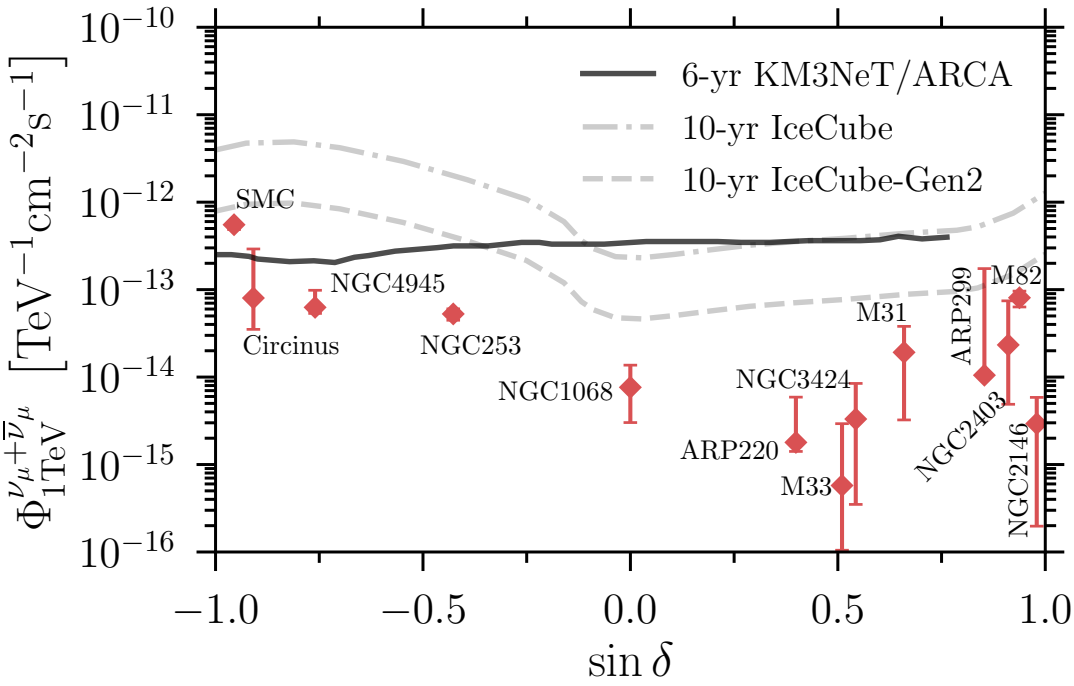

Figure 4.1: Muon neutrino flux normalizations at 1 TeV predicted by the source star-forming activity as a function of source declination. The diamonds correspond to the most-likely values of the source parameters deduced by current gamma-ray data (see Table 4.2), while the bands represent the 68% credible intervals of the marginal flux distributions. The lines shown the point-like sensitivity of different neutrino telescopes as functions of declination: 6-year KM3NeT/ARCA [179], 10-year IceCube [76], and 10-year IceCube-Gen2 estimated according to [162].

limits, thus jeopardizing the likelihood procedure, leading to a vary poor parameter constraints. Finally, for NGC 1068, we find a good agreement both with the data and the SFR value given by [20]. However, as will be discussed later, the corresponding neutrino emission predicted by our model is much lower than the one released by IceCube as a 2.9σ excess [76] and to the more recent one by Ref. [60]. Therefore, while the gamma-ray flux could well be explained by the star-forming activity of the source, the explanation of its potential neutrino emission might require an intense AGN hot corona activity [19, 170, 173, 178] (see further sections for more details).

4.5 Prospects for multi-messenger observations

The results of the likelihood analysis of current gamma-ray data are hence employed to estimate the high-energy muon neutrino flux from each source. The normalization of such fluxes at 1 TeV are shown in Figure 4.1, where the diamonds represent the predictions for the most-likely source

parameters and the bands cover the 68% interval of the marginal flux distributions. In the plot, our predictions are compared with the IceCube point-like sensitivity [76], as well as with the ones of the upcoming neutrino telescopes KM3NeT/ARCA [179] and IceCube-Gen2 with different observation times. The latter is estimated to be at least five times better than the current IceCube one [162]. Remarkably, we find that SMC could well be a perfect target for futures constraints by KM3NeT, in the assumptions that neutrinos mostly are emitted by its core. On the other hand, if the emission is more diffuse to the entire galaxy then it is needed a dedicated analysis by the collaboration (see chapter 9). This is due to the fact that the sensitivity of the detector will get worse proportionally to the angular size of the source. In particular, in a conservative approach (background-dominated data), the sensitivity will be rescaled for $\propto \frac{\sigma_{\rm ext}}{\sigma_{\rm PSF}}$, where $\sigma_{\rm ext}$ is the angular extension of the source and $\sigma_{\rm PSF}$ is the extension of the point spread function (PSF) [180]. Indeed, the median angular resolution of KM3NeT is expected to be $\simeq 0.1^\circ - 0.2^\circ$ ([159, 179]) and therefore emission from an extended source of $\sim 1^\circ$ will inevitably worsen the sensitivity of the experiment by an order of magnitude, leading to more time needed for a 90% C.L. constrain of this modelling. Also, From a theoretical point of view, it is still unclear if SMC gamma-ray data might have a leptonic contamination due to point-like source emissions such as Pulsar Wind Nebulae (PWN). Indeed, such a contamination might make the flux hard at $E_\gamma \sim 1 - 10\,\text{TeV}$. Furthermore, SMC– due to its low SFR– is likely to have a CR transport similar to the Milky-Way, namely driven by diffusion rather than advection. As a result, only future dedicated KM3NeT and CTA studies (see also the following discussion) might critically test the hadronic budget of this source, unveiling the origin of its gamma-ray spectrum. Circinus Galaxy is also potentially detectable by KM3NeT due to its location in the southern sky where the experiment has full visibility [179]. We emphasize that this source is also an AGN characterised by Seyfert-II activity, similar to NGC 1068. Indeed, such an activity might lead to an further contribution into the neutrino flux increasing the prospects of constraining this source. Although, without dedicated estimates, would be daunting to disentangle different contributions. In the northern sky, a promising source seems ARP 299 which might be within reach of IceCube-Gen2. Other galaxies such as NGC 4945, M31, NGC 2403 and M82, are instead just a factor of ~ 3 below the KM3NeT and IceCube-Gen2 point-like sensitivities within their 68% credible intervals. These considerations are likely to be representative of the real detection potential for these sources, although the experimental sensitivities are determined for an E^{-2} neutrino spectrum, and therefore the conclusions might change for softer spectra. However, as reported in Table 4.2, the most-likely spectral index for most galaxies is close to 2. Moreover, the

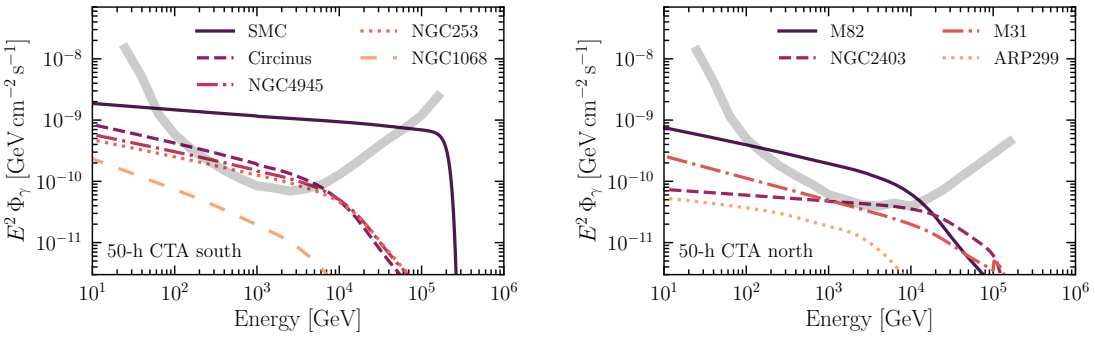

Figure 4.2: Most-likely gamma-ray spectral energy distributions of different galaxies as a function of gamma-ray energy, in agreement with their star-forming activities and current gamma-ray observations. The left (right) panel collects the galaxies of the southern (northern) sky. The thick lines show the CTA differential sensitivity for an observation time of 50 hours [26].

largest values for the neutrino flux normalization reported in Figure 4.1 are obtained in case of hard spectra, thus supporting the comparison with the reported point-like sensitivities. However, the sensitivities are obtained assuming that the sources have no high-energy cutoff. Indeed, a high-energy cut-off above hundrends of TeVs might slightly increase the sensitivity normalization given that under the same spectrum normalization, a spectrum with cut-off would induce less neutrino events into the detector, leading to slightly worse expectations.

For the brightest neutrino galaxies, we also show in Figure 4.2 the most-likely very-high-energy gamma-ray flux to be compared with the CTA differential sensitivity, for which we consider an observation time of 50 hours towards the direction of the galaxy [26]. The cutoff of the gamma-ray flux is due both to internal and external absorption. A few sources are expected to be above the CTA sensitivity in the range between 100 GeV and 10 TeV; for SMC this range might extend up to $\sim$ 100 TeV, in the same assumption discussed above. Otherwise, it will take more time for the CTA telescope to probe such high-energies from the SMC. This is particularly relevant, since one of the main limitations in our study is the lack of gamma-ray measurements in the range above 1 TeV (apart from the VERITAS and H.E.S.S. data on M82 and NGC 253). Therefore, our results suggest that CTA will allow us to draw more robust conclusions on the gamma-ray (and neutrino) production in SFGs and SBGs. It is worth emphasizing that, under the assumption of a dominant hadronic production linked to the star-forming activity, at high energies the gamma-ray and neutrino emission are directly related each other through the SFR which is derived from the UV and IR observations.

4.6 Focus on NGC 1068

NGC 1068 is a powerful starburst galaxy located at $\sim 10 - 14\,\mathrm{Mpc}$ away from the Earth at equatorial coordinates (J2000)$(40.68°, -0.01°)$ [19]. It is classified both as a starburst galaxy and as a seyfert galaxy 2, where the starburst activity is exhibited by its high star formation rate and the presence of a starburst ring [181], while the Seyfert activity is exhibited by the an active nuclei in its very core [19, 182], with a very hot corona and a dusty torus [19, 170, 173, 178, 181]. There has been also some indication of a powerful radio jet which extends up to $\sim 1\,\mathrm{Kpc}$ away from the core [181, 183] as well as the very recent detection of parsec-scale blobs in the jet in the radio band by ALMA [184]. Furthermore, Ref. [185] has reported an hint of an ultra-fast outflow (UFO) in the core of the source, analyzing X-ray blue shifted absorption lines. In this regard, Ref. [186] has studied its multi-messenger implications, showing that an UFO might contribute to the γ-ray spectrum of the source. All of these implies that a comprehensive study on NGC 1068 emissions requires many details in order to disentangle the contribution of each component in each energy band. From the phenomenological point of view, this source has been observed by Fermi-LAT [19] in the energy band $\sim [0.1 - 30]\,\mathrm{GeV}$ with actual measurements and with upper limits above this energy. Furthermore, the MAGIC collaboration has also reported strict upper limits from this source [187] strongly limiting the emission above $\sim 1\,\mathrm{TeV}$. Recently, as mentioned above, the IceCube collaboration has reported a 4.2σ excess of 79 neutrinos above the hypothesis of only-background events from the direction of NGC 1068 [60]. They inferred a very soft spectrum $\sim E^{-3.2}$ with a normalization at 1 TeV of $\phi_{\nu_\mu+\bar{\nu}_\mu} = 5 \cdot 10^{-11}\,\mathrm{TeV}^{-1}\,\mathrm{cm}^{-2}\,\mathrm{s}^{-1}$ [60]. This normalization is an order of magnitude higher than the normalization of the gamma-ray spectrum reported by Fermi-LAT and MAGIC. Therefore, the neutrinos should be emitted by a region which is gamma-ray opaque in order not to overshoot the bounds coming from the gamma-ray experiments.

Fig. 4.3 shows the gamma-ray and neutrinos predictions coming from the Starburst galaxy activity according to the analysis performed in the previous section.

In particular, on the left, the gamma-ray best-fit obtain in Sec. 4.4 is compared with Fermi-LAT data [19] and with MAGIC upper limits [187]. On the right, the corresponding 1σ most-credible band for the neutrino spectral energy distribution (SED) is compared with the 2σ confidence region published by IceCube [60]. Several comments are in order: firstly, since NGC 1068 is a full proton calorimeter, the (simplified) value of the radius $R \sim 200\,\mathrm{pc}$ has not impact in the spectrum result. Indeed, in such a regime the structure parameters of the SBG do not influence the gamma-ray and neutrino production rates. This results is also consistent with previous

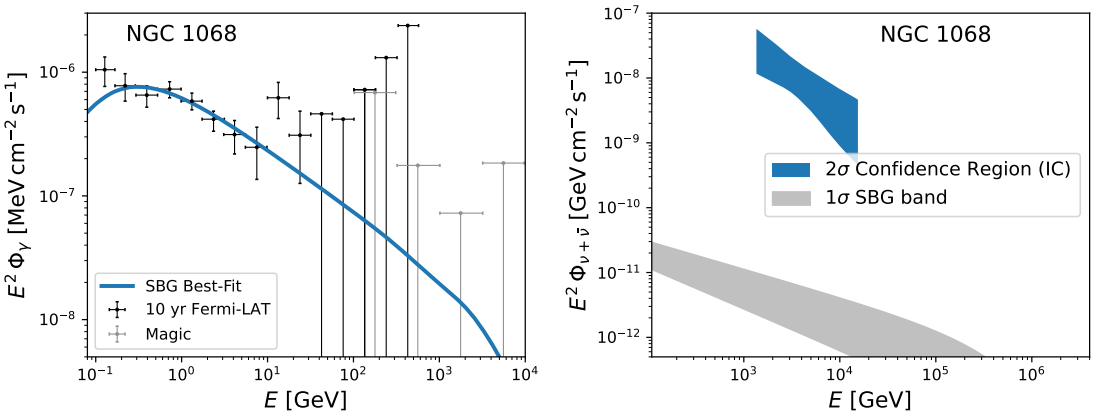

Figure 4.3: **Left:**The gamma-ray data from Fermi-LAT [19] and MAGIC upper limits [187] compared with the best-fit obtained following the analysis of Sec. 4.4. **Right:** The right panel shows the prediction of the 1σ credible intervals of the one-flavour neutrino spectrum from the SBG activity of NGC 1068 compared with the spectrum recently inferred by IceCube [60].

analyses. In fact, in Ref. [19] has been shown that NGC 1068 is at the limit of the calorimetric assumption by analyzing the correlation between IR and γ-ray luminosity. Another important point is that the Fermi-LAT gamma-ray data do not shown any time variation along 10 years of observations, pointing towards starburst activity as one of the best candidates to explain its gamma-ray data. Anyway, this argument cannot completely exclude further contamination on the gamma-ray spectrum from an UFO as well as from the jet. These components are not modelled in this work and we leave them for future investigations. Nonetheless, the neutrinos produced by the starburst activity cannot explain the excess inferred by the IceCube collaboration. Therefore, a single one-zone model is not sufficient in order to explain the multi-wavelengths observations of this source. A region which has been proposed to explain the IceCube data is the so called hot corona which surrounds the core. In this place, stochastic acceleration processes might occur, leading to protons up to $\sim 100\,\mathrm{TeV}$, with a corresponding neutrino production at TeV energies [19, 170, 173, 178, 181]. The corona is expected to be compton-thick, thereby trapping the x-ray radiation. Therefore, gamma-rays at tens of $\sim$ GeVs get reprocessed to lower energies through the Beithe-Heitler pair production [19, 170, 173, 178, 181]. This shifts the gamma-ray flux to the MeV range, where at the moment there is no experimental bounds. As a result, future and upcoming experiments will be able to shed light on the hadronic emissions of this source.

4.7 Conclusions

In the near future, upcoming neutrino telescopes will potentially observe nearby star-forming and starburst galaxies as point-like sources. In particular, they could pose a solid link between the hadronic emission of these sources, supposed to dominate the GeV-TeV gamma-rays, and the expected intense star-forming activity as obtained from IR and UV observations.

As the brightest sources predicted by our emission model are in the southern sky, a leading role will be played by neutrino telescopes located in the northern hemisphere. They include KM3NeT/ARCA as well as the planned Baikal-GVD [188] and P-ONE [161] telescopes. On the other hand, IceCube-Gen2 will have a better point-like sensitivity in the northern sky, thus remaining a crucial observer for the sources positioned in this portion of the sky. In any case, the advent of a Global Neutrino Network would be necessary to observe most of the point-like emission from SFGs and SBGs predicted in this work, by increasing the available worldwide effective volume of neutrino telescopes.

While our results are mainly derived from the star-forming activity, we cannot exclude a possible AGN emission counterpart for some of the galaxies selected. However, an additional AGN activity would typically exhibit a flaring behaviour, unless the related duty cycle is very high. Therefore, the neutrino measurements over large observational periods would be dominated by the star-forming steady component, thereby making our detection prospects more robust. In this regard, a crucial role will be also played by CTA that will potentially measure the gamma-ray emission above tens of TeV energies for some of the galaxies investigated. This will allow us to place better constraints on the sources production mechanism as well as on the parameters of the emitting SBNi.

This work indicates that the next decade will be decisive to assess whether the local star-forming activity can be a tracer of point-like neutrino production, and it highlights the importance of pivoting the presented scenarios through the low-energy thermal emissions.

Chapter 5

Probing Cosmic-Ray Transport in Starburst Galaxies with Gamma-ray and Neutrino Observations

In this chapter, we assess the possibility of current experiments as well as the prospects of future experiments to indireclty probe the cosmic-ray transport mechanisms inside local Starburst Galaxies. The chapter is based on our analysis published in Ref. [189].

5.1 Introduction

In chapter 3, we studied the implications on the diffuse gamma-ray and neutrino observations, exploiting the calorimetric behaviour of starburst galaxies. By constrast, on chapter 4, we assessed the gamma-ray and neutrino prospects for current and future experiments, using the cosmic-ray transport mechanisms following Refs. [31, 32]. However, a quantitative description of CR transport mechanisms inside SBGs is not finalized yet, since it is not completely clear how big is the fraction of cosmic rays lose their energy inside the source, producing secondary particles such as neutrinos and gamma-rays. This is because it depends on the interplay between different phenomena like diffusion, wind advection and energy losses, which are difficult to reliably model for galaxies different than the Milky Way. Different CR transport scenarios have been used to describe the observed gamma-ray emission from nearby SFGs and SBGs, trying to disentangle a calorimetric behaviour from a diffusion-dominated regime ($\tau_{\rm diff} \ll \tau_{\rm loss}, \tau_{\rm adv}$) [20, 21, 31, 37,

39, 93, 131, 132, 141, 190–194].

For instance, some models suggest Kolmogorov-like diffusion from magnetic field turbulence [31, 32, 129], others self-generated diffusion generated by the streaming instability [131, 194, 195]. Uncertainty comes also from the fraction of ionized gas, which can vary from 10^{-4} to 10^{-1} [31, 131]. This might lead to a different role for the advection phenomena, which, according to Ref [131], should predominantly affect the hot ionized gas and not the cold molecular gas.

In this framework, current measurements make it challenging to quantitatively discriminate between different scenarios, leading to a significant uncertainty in the gamma-ray and neutrino fluxes expectation from SBGs. In fact, as we saw in the previous chapters, only 13 SFGs are observed through gamma rays and just a few of them are observed at energies greater than 10 GeV [19, 20]. In fact, major discrepancies between different CR transport mechanisms arise at higher energies ($E \gtrsim 100\,\mathrm{GeV}$). This points out the importance for future gamma-ray experiments [26, 196, 197] as well as possible neutrino point-like observations [27, 60, 76, 179] to better constrain the characteristics and the CR transport scenario for the nuclei of SBGs. In this chapter, we assess the signatures of different cosmic-ray transport mechanisms on point-like and diffuse gamma-ray and neutrino contribution of SFGs and SBGs, and exploit them to understand which model can explain better the data. In particular, we consider both an advective model adopted, e.g., by [32], and the model provided by [131], which considers CR transport in the nucleus dominated by diffusion on self-induced turbulence. Following the analysis described in the previous chapter, we compare the gamma-ray predictions of the two CR transport models with 10-year Fermi-LAT data [19] as well as H.E.S.S. [23] and VERITAS [22] collaborations data for 13 known SBGs (VERITAS data are available only for M82 and H.E.S.S. data are only available for NGC 253).

We show that current data are slightly better accommodated by the model developed by [31], suggesting advection to be important for high-energy CR transport in SBNi. Then, we investigate the ability of future gamma-ray telescopes sensitive to $\mathcal{O}(10\ \mathrm{TeV})$ photons, such as CTA [26] and SWGO [196, 197], to further discriminate between the different CR transport models. We perform a forecast analysis by means of mock data generation for the most promising sources using the public instrument response functions of the CTA telescope. In particular, we determine the statistical confidence at which the diffuse-dominated model [131] might be excluded in the near future in favour of the advection-dominated one [32].[1] We report the p-values and the Bayesian factors obtained in case of Frequentist and Bayesian approaches, respectively. We

[1] By diffusion or advection dominated models, we mean that diffusion and advection are respectively the main escape processes for those particular models.

hence emphasize the importance of future gamma-ray telescopes for constraining the SFGs and SBGs emission properties.

Finally, we calculate the diffuse neutrino and gamma-ray fluxes from the whole populations of SFGs and SBGs, updating the calculation provided in chapter 3. We set the properties of all the sources, e.g. the distribution of the spectral indexes, to be consistent with the ones previously inferred by the local point-like observations. Interestingly, such a comprehensive data-driven scenario may explain 25% of the HESE neutrino flux [5] when a cut-off energy of protons of the order of 10 PeV, as well as the 33% of the Extra-galactic Gamma-ray Background (EBG) above 50 GeV [12, 13, 85, 198]. Hence, it is in agreement with the independent multi-component fit provided by [52], and it is consistent within 1σ with the gamma-ray limits on non-blazar sources [12, 13, 85, 198]. This result becomes crucial when compared to the one presented by [195], since it shows that the use of a different CR transport model for the SBG class produces different expectations in the high energy range allowing us to explain a greater portion of diffuse high-energy neutrino measurements without evading all the existing EGB bounds on non-blazar sources.

5.2 Calorimetric Fraction

In this section, we describe the models for CR transport which we consider. As mentioned in Sec. 5.1, we focus on the different phenomenologies arising from the two approaches of [31] and [131] (hereafter, model A and model B, respectively). For such a purpose, we rewrite Eq. 3.3 in terms of the so called calorimetric fraction $F_{\rm cal}$:

$$F_p(E) = Q(E) \cdot \tau_{\rm life}(E) = Q(E) \cdot \tau_{\rm pp}(E) \cdot F_{\rm cal}(E) \tag{5.1}$$

where $\tau_{\rm life}$ is the lifetime of protons inside the SBN, and $\tau_{\rm pp}$ is the pp timescale. $F_{\rm cal}$ encodes the information of the fraction of injected high-energies protons effectively producing γ-rays and neutrinos through hadronic collisions. Once again, as stressed in Chapter 3, this formalism is possible due to the steadiness expected from the long duration of the starburst activity ($\sim 10^8$ yr [30]). In general, $F_{\rm cal}$ is not only a function of the energy but also of the structure parameters and the geometry of the source. If SBGs were efficient proton calorimeters at all energy ranges, we would have $F_{\rm cal}(E) = 1$. In the following subsection, we describe separately the calorimetric fractions for model A and model B.

5.2.1 Model A

Model A corresponds to the model already implemented in chapters 3 and 4. For this model, $F_{\rm cal}$ can be expressed as

$$F_{\rm cal} = \frac{\tau_{\rm eff}(E)}{1+\tau_{\rm eff}(E)} \tag{5.2}$$

where $\tau_{\rm eff} = \tau_{esc}/\tau_{pp}$ is the dimensionless effective optical depth for protons, which represents the effective depth of the material through which a CR must pass on its way out of the SBN [131]. When p-p losses dominates $\tau_{\rm loss} \ll \tau_{\rm esc}$, $\tau_{\rm eff} \to +\infty$, leading to perfect calorimetric conditions. We emphasize that $\tau_{\rm loss}$ is totally dominated by τ_{pp} for $E > 1\,{\rm GeV}$. τ_{esc} is given by Eq. 3.2, namely by the interplay between advection phenomena which driven CRs out of the SBN in a energy-independent way and diffusion processes which driven CRs out with $E^{-1/3}$ dependency (considering a kolmogorov-like diffusion). As emphasize in chapters 3 and 4, model A is predominantly dominated by advection leading to an almost energy-independent $F_{\rm cal}$. As we will see in the following sections, this is the crucial different with model B.

5.3 Model B

Model B (see [131] for more details) considers a cylindrical geometry of the nucleus where CRs escape along the disk height (which is of the order of 10^2 pc). In this case, $F_{\rm cal}$ is given by [131]

$$F_{\rm cal} = 1 - \left[{}_0F_1\left(\frac{1}{5}, \frac{16}{25}\tau_{\rm eff}\right) + \frac{3\tau_{\rm eff}}{4M_A^3}\,{}_0F_1\left(\frac{9}{5}, \frac{16}{25}\tau_{\rm eff}\right)\right]^{-1} \tag{5.3}$$

with $M_A \simeq 2$ being the expected mach number and ${}_0F_1$ the generalized hypergeometrical function. Eq.s (5.2) and (5.3) generally give different predictions for the calorimetric fraction. In particular, under the same $\tau_{\rm eff}$, Eq. (5.3) predicts a higher calorimetric fraction than Eq. (5.2), due to pure geometrical reasons. Indeed, having more directions where to escape, model A provides a smaller calorimetric fraction than model B. Fig. 5.1 shows the exact comparison between the two calorimetric fractions as functions of $\tau_{\rm eff}$.

5.3.1 Cosmic-Rays Transport in model B

The main distinction between model A and model B resides in the fact that model B attributes diffusion processes as the primary mechanism for CR escape from SBNi. Indeed, this model neglects any advection phenomena. The reason is that the SBN should be mostly filled by cold molecular gas [131] rather than by ionized gas, which are ascribed as the responsible for

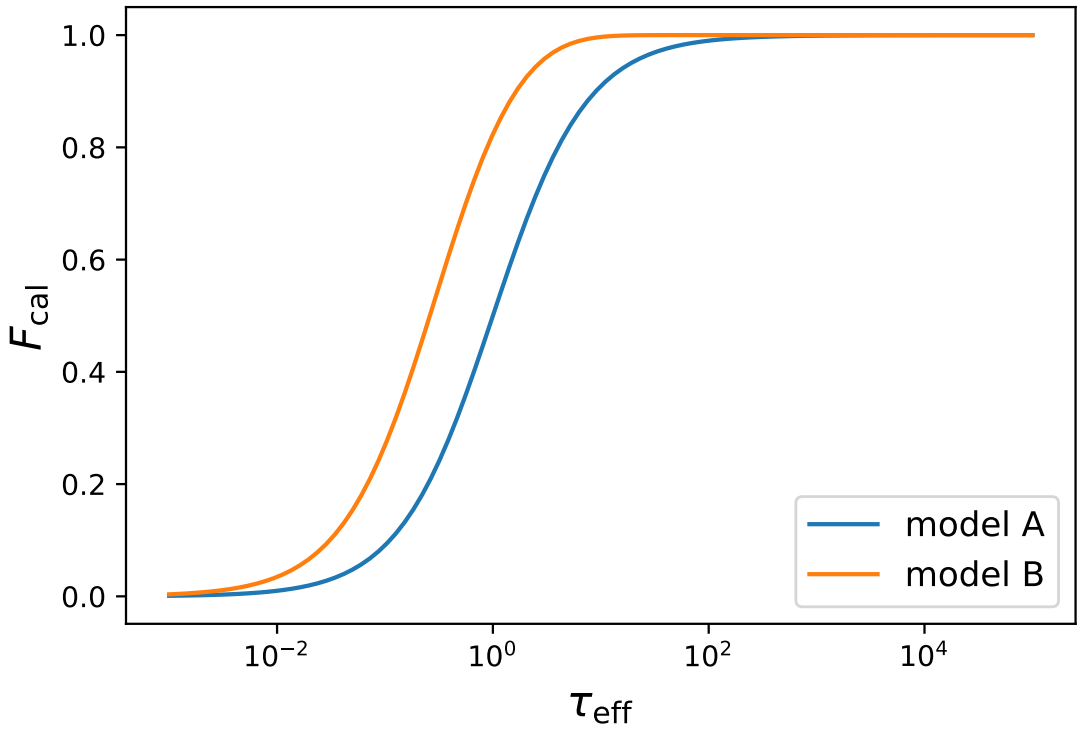

Figure 5.1: (Spherical geomtry) Model A (blue) and (cylindrical geometry) model B (orange) $F_{\rm cal}$ as functions of $\tau_{\rm eff}$.

galactic winds [131]. Indeed, Ref. [131] considers that ionized gas fraction χ is of the order of 10^{-4}. Another important difference is that CR motion is not considered by strong large-scale turbulence of the magnetic field, but rather stream along the field lines at a rate determined by the competition between streaming instability and ion-neutral damping, leading to transport via a process of field line random walk [131]. The diffusion coefficient stems from the interaction between the Alfven waves which CRs themselves generate and the streaming instability. All of these lead to important implications for CR motion above $\sim 1 - 10\,\mathrm{TeV}$.

In order to estimate the diffusive timescale, we consider the velocity of the Alfven waves as [131]

$$V_{\rm al} = \frac{\sigma_g}{\sqrt{2}\,\chi^{1/2}\,M_A} \tag{5.4}$$

where $\chi = 10^{-4}$ is the ionisation fraction and σ_g is the dispersion velocity for which we use the same scaling relation with the star formation rate reported by [195]), namely

$$\sigma_g = (32.063\,\mathrm{Km\,s^{-1}})\left(\frac{\dot{\mathrm{M}}_*}{\mathrm{M}_\odot\,\mathrm{yr}^{-1}}\right)^{0.096} \tag{5.5}$$

with a very mild dependence with the SFR. Then, we calculate the streaming velocity of CRs with energy E as

$$V_{\rm st} = \min\Bigg[c,\, V_{\rm al}\left(1 + 2.3\times10^{-3}\; c_3^{-1}\left(\frac{E}{m_p}\right)^{\Gamma-1}\left(\frac{n_{\rm ISM}}{10^3\ {\rm cm}^{-3}}\right)^{3/2} \times\left(\frac{\chi}{10^{-4}}\right)\left(\frac{\sigma_g/\sqrt{2}}{10\ {\rm km\ s}^{-1}}\right)^{-1}\right)\Bigg] \tag{5.6}$$

where m_p and c are the proton mass and the speed of light, respectively. The factor $c_3 \approx 1$ is the ratio between the number density of CRs in the middle plane in the SBG and a thousand times the number density of CRs expected in the Milky Way near the Solar circle [131].[2]. Moreover, $n_{\rm ISM}$ denotes the interstellar medium density (for SBGs $n_{\rm ISM} \sim 10^{2-3}$ cm^{-3}) and $\Gamma + 2$ is the spectral index of the proton injection spectrum. It is worth mentioning that the diffusion mechanism breaks down at high energies, where the streaming velocity becomes equal to the speed of light. In this regime, the protons start to free-stream out of the SBN. From the streaming velocity ($V_{\rm st}$) the diffusive coefficient can be calculated as

$$D = V_{\rm st}\ \cdot L_A \tag{5.7}$$

where $L_A = h/\max[1, M_A^3]$ is the turbulence length scale with h being the height of the galactic disk. Eq. 5.7 implies that the diffusion coefficient is almost constant up to $E_{\rm CR} \sim 1$ TeV, while for higher energies increases fast with the energy until $V_{st} = c$ where D returns to be constant. As we will see in the following sections have huge implications for phenomenology, since for $E_\gamma \gtrsim 100$ GeV, SBGs start losing their calorimetric behaviour. We evaluate the diffusion timescale as $\tau_{\rm diff} = h^2/D$, where we consider $h = 73$ pc for all the galaxies, consistently with the analysis presented in the previous chapter (we also discuss in Sec. 5.7 the case of varying this parameter and its impact on the following statistical analysis).

5.4 Model A vs Model B: Current Data

The models A and B, outlined in the previous section, are based on different assumptions on CRs transport, and this gives rise to differences in the gamma-ray and neutrino spectra. This is highly significant because for nearby SBGs we have available both gamma-ray data and estimates of their SFR through IR and UV data. Therefore, the comparison of the theoretical predicted gamma-ray spectra with data allows us to scrutinise whether there are observable

[2]We have verified that a slightly different value for c_3 does not significantly affect our results

Table 5.1: Results of the Bayesian inference with current gamma-ray data for models A and B. Reported are the most-likely values for the star formation rate $\dot{M}_*$ in $M_\odot\,yr^{-1}$ and the spectral index Γ, along with the reduced chi-square χ^2. The results for model A have already been reported in chapter 4.

Source	Model A		Model B	
	$(\dot{M}_*, \Gamma)$	χ^2/dof	$(\dot{M}_*, \Gamma)$	χ^2/dof
M82	(4.5, 2.30)	1.24	(3.0, 2.30)	1.88
NGC 253	(3.3, 2.30)	1.32	(2.1, 2.20)	1.95
ARP 220	(740, 2.66)	1.52	(740, 2.65)	1.53
NGC 4945	(4.15, 2.30)	1.52	(3.45, 2.40)	1.07
NGC 1068	(16, 2.52)	0.65	(12, 2.50)	0.71
NGC 2146	(15, 2.50)	0.50	(12, 2.50)	0.52
ARP 299	(28, 2.15)	0.18	(28, 2.05)	0.19
M31	(0.34, 2.40)	0.52	(0.19, 2.55)	0.46
M33	(0.44, 2.76)	0.44	(0.25, 2.89)	0.48
NGC 3424	(5.4, 2.22)	1.63	(5.4, 2.20)	1.51
NGC 2403	(0.75, 2.12)	0.38	(0.37, 2.15)	0.37
SMC	(0.038, 2.14)	1.90	(0.0149, 2.25)	5.50
Circinus	(6.6, 2.32)	0.92	(4.6, 2.30)	0.99

features characterising the CR transport inside SBGs. We here discuss such a comparison for models A and B with actual data. We calculate the gamma-ray spectrum for model B using the same procedure used for model A in chapters 3 and 4. For the data analysis, we follow the Bayesian likelihood approach put forward in chapter 4, where we fit the gamma-ray data using $(\dot{M}_*)$ and (Γ) as free parameters. The results are reported in Tab 5.1 (where we report again the results for model A presented in chapter 4, in order to make the comparison easier to follow).

For most SBGs, current data are not able to statistically discriminate between the two models, although model A generally provides slightly smaller chi-squared values. On the other hand, for M82 and NGC 253 model B is disfavoured at $\sim 2\sigma$ level. A tension at $\sim 11\sigma$ with model B is found in the case of SMC, which however is mainly driven by low-energy data. Thus, we do not consider this as a conclusive evidence in favor of model A. Indeed, as explained in the previous chapter, SMC is a particular case of bona-fide SFG [19], because of its low SFR. In fact, its low supernova explosion rate makes it more similar to a quiescent galaxy (Milky-Way like) than a SBG. This source is supposed to be dominated by Kolmogorov-like diffusion rather than self-induced diffusion or advection [21], making model B quite inapplicable to this source and the prediction of model A less optimistic. Furthermore, being a very nearby source ($D = 60\,kpc$) [20], the details of the modelling might be somewhat influential on the results, thereby making the comparison between model A and model B less robust. Nonetheless, we report the results of our analyses even for this galaxy for sake of completeness.

The importance of data above 100 GeV resides in the fact that the calorimetric fraction of

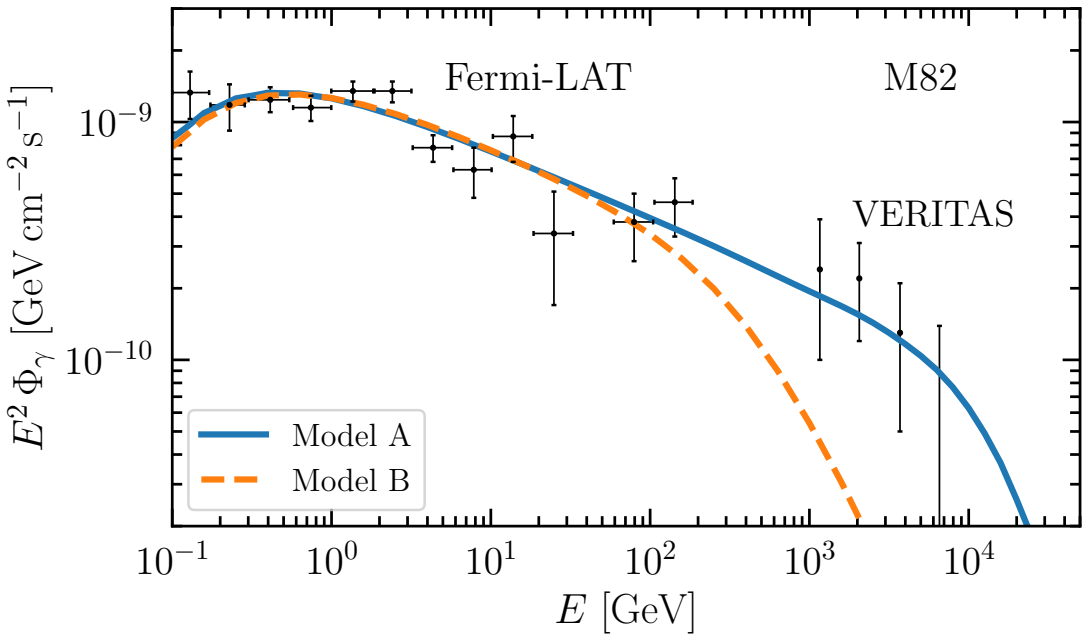

Figure 5.2: Best-fit SEDs for model A (dashed blu line) and model B (solid orange line) as inferred by Fermi-LAT data Ajello et al. [19] and VERITAS data [22].

model B rapidly drops to zero. This makes it highly difficult to accommodate high-energy data. In order to highlight this behaviour, in Fig. 5.2, we show the SED for M82 predicted by the two models in their best-fit scenario. This result is highly significant since, differently from the analysis in [131], we find that model B is not able to accommodate high-energy data for this source [22]. This suggests that the diffusive model B cannot provide a full explanation of SFGs and SBGs emission above 1 TeV.

On the other hand, it is worth noticing that the model B provides a higher calorimetric fraction for energies below 100 GeV with respect to model A. This implies that a smaller value of the SFR is required to fit the data. Therefore, sources like NGC 4945 get to be better fitted by this model because their emission can be better describe while satisfying the prior on the SFR deduced by IR and UV observations.

However, concerning the source NGC 4945, Ajello et al. [19] point out that the star-forming activity may be not responsible for the totality of its emissions due to the presence of an AGN activity. Indeed, model A cannot fully explain its gamma-ray data even with the highest value for the SFR (4.15 $M_\odot\,yr^{-1}$) as allowed by the prior, leaving room for a possible AGN component. On the contrary, this is not the case for model B which requires $\dot{M}_* = 3.45\ M_\odot\,yr^{-1}$.

The different dependence on the SFR in the two models is highlighted in Fig. 5.3, where we

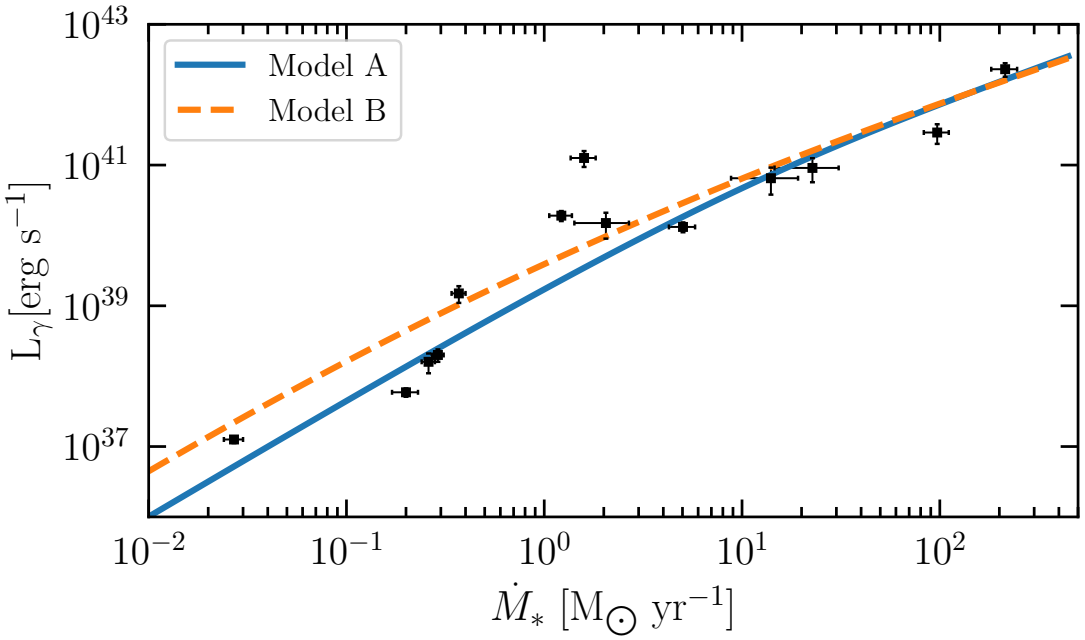

Figure 5.3: Comparison between the integrated luminosity between (0.1 − 100) GeV for (advection-dominated) model A (solid blue line) and (diffusion-dominated) model B (dashed orange line), with the corresponding measurements of the 13 galaxies analysed [20].

compare the gamma-ray luminosity L_γ (integrated between 0.1 and 100 GeV) as a function of $\dot{M}_*$. In the plot, the integrated luminosity is computed assuming a reference value of the spectral index ($\Gamma = 2.2$) for all the galaxies as in Refs. [21, 195]. However, it is worth noticing that L_γ depends only marginally on Γ. This allows for the comparison with the measurements of the individual sources even though the experimental SEDs are explained by different values for the spectral index (see Tab. 5.1). As can be clearly seen in the plot, at low SFR, the luminosity predicted by model B (dashed orange line) is higher than the one by model A. This just mirrors the higher calorimetric fraction of model B with respect to model A. On the contrary, for high values of the SFR, the two models predict the sources to be efficient calorimeters ($F_{\rm cal} = 1$), leading to the same scaling of the luminosity with the SFR.

The weak preference of current gamma-ray data for model A might already suggest the advection playing a key role as escape mechanism in SFG and SBG cores. However, more definitive conclusions might be only drawn with more gamma-ray data, especially at energies higher than 1 TeV. As will be discussed in the next section, the CR transport mechanism will be crucially probed by future gamma-ray telescopes.

5.5 Forecast for the CTA Telescope

In the last section, we discuss that gamma-ray data above $\sim 100\,\mathrm{GeV}$ might be crucial to distinguish different CR transport scenarios. In this regard, the future Cherenkov Telescope array (CTA) observatory, it is expected to have an enhanced sensitivity for photons up to $\sim 100\,\mathrm{TeV}$, thereby fundamental to probe the emission processes of nearby SBGs. In this section, we perform a quantitative forecast analysis in order to assess the ability of the future CTA telescope to discriminate between the two models of CR transport. In particular, we simulate future gamma-ray measurements using the public CTA information [26]. We make only use of the public expected instrument response functions of the detector in ideal conditions [26] to evaluate the expected number of signal n_s and background events n_b, in an observation time $T_{\rm obs}$ of 50 hours. Motivated by the results of the previous section, we assume the best-fit model A to generate CTA mock data and we determine the statistical power with which they favor model A over model B. We focus only on the local sources for which the expected SEDs are higher that the differential CTA sensitivity. According to model A which typically provides hard gamma-ray spectra, we expect that CTA telescope will observe at least four sources (see chapter 4): SMC, M82, NGC 253 and Circinus galaxy. For each of these sources, we pursue the following procedure. Firstly, we consider the sources to be in the center of the field of view the detector, in order to have the best sensitivity. Then, we bin the energy range (10^2 GeV $- 10^5$ GeV), with the same binning provided by the CTA consortium. For each source, we only consider the energy bins for which the SED is higher than the CTA sensitivity, therefore where the experiment is expected to provide actual measurements and not just upper limits. Hence, we calculate the expected number of signal events as

$$n_{\rm signal} = T_{\rm obs} \int_{\Delta E} A_{\rm eff}(E)\Phi_{\gamma,\rm A}(E)\mathrm{d}E \tag{5.8}$$

where $\Phi_{\gamma,\rm A}$ is the gamma-ray flux predicted by the best-fit model A according to present data, $A_{\rm eff}$ is the CTA effective area, ΔE is the size of the energy bin and $T_{\rm obs} = 50$ h is the time of observation. We also take into account the number $n_{\rm bkg}$ of background events associated to misidentified CRs. We remark that $n_{\rm bkg}$ only depends on the declination of the source and the opening angle $\Delta\Omega$ of the observation, driving the so called hadron-gamma separation. Considering that we expect gamma-rays mostly emitted by SBNs, we take $\Delta\Omega = \max[\Delta\Omega_{\rm res}, \Delta\Omega_{\rm SBN}]$ where $\Delta\Omega_{\rm res}$ is the CTA energy-dependent angular resolution function and $\Delta\Omega_{\rm SBN}$ represents the angular dimension of the source SBN. For all the sources except SMC (the nearest source) we

have $\Delta\Omega_{\rm SBN} < \Delta\Omega_{\rm res}$. For SMC we consider the intrinsic extension of its SBN $\Delta\Omega_{\rm SBN} = 0.38°$.

For each energy bin, we randomly generate 10^4 numbers of events $n_{\rm obs}$ by means of a Poisson distribution with a mean value of $n_{\rm tot} = n_{\rm signal} + n_{\rm bkg}$, namely $n_{\rm obs} \sim {\rm Poiss}(n_{\rm tot})$. Then, we estimate the empirical number of signal events simply as $\tilde{n}_{\rm signal} = n_{\rm obs} - n_{\rm background}$. From this quantity we can calculate the empirical $\widetilde{\rm SED}$ assuming a generic power-law flux E^{-2}. In particular, we have

$$\widetilde{\rm SED}_i = \frac{\tilde{n}_{{\rm signal},i}}{T_{\rm obs} \int_{\Delta E} A_{\rm eff}(E) \left(\frac{E}{1\ {\rm GeV}}\right)^{-2} {\rm d}E} \tag{5.9}$$

where i runs over energy bins. The reconstructed SEDs are affected by an uncertainty that can be directly estimated through the Poisson uncertainty on $n_{\rm obs}$ as

$$\frac{\Delta\widetilde{\rm SED}_i}{\widetilde{\rm SED}_i} = \frac{\sqrt{n_{{\rm obs},i}}}{\tilde{n}_{{\rm signal},i}} \tag{5.10}$$

We emphasize that in this generation of mock data we simply consider the best-fit gamma-ray flux $\Phi_{\gamma,{\rm A}}$ provided by model A with current data. Hence, we neglect the intrinsic uncertainty on the expected gamma-ray flux as provided by the posterior distribution in Eq. (4.3). We show the impact of the intrinsic uncertainty in the following section. Accounting for the intrinsic uncertainty generally leads to larger Bayes factors and smaller p-values for SMC, M82, and NGC 253. Therefore, the results presented here are reasonable conservative.

For each of the 10^4 mock data sets, we perform again the statistical analysis described in the previous section, including this time the mock data $\widetilde{\rm SED}$ along with current data. In Fig. 5.4 we show the updated best-fit scenarios for the four sources according to one realization of the CTA mock data. In particular, the solid blue (dashed orange) lines represent the best-fit SEDs according to model A (B). For M82, SMC, and NGC 253, they coincide with the one obtained with current gamma-ray data only. This stems from the fact that these sources have not only ∼GeV data which constrain their normalization (SFR), but also data above 100 GeV which constrain their shape (*i.e.* the spectral index). The only exception is Circinus Galaxy (bottom right panel) for which the current absence of data above 10 GeV leads to a different best-fit SED for model B (dot-dashed orange line referred to with "model B′"). In the plots, we also show the expected 1 yr sensitivity of the SWGO experiment [196, 197]. We emphasize that this future telescope is also expected to observe the brightest sources located in the Southern hemisphere in the $1 - 10$ TeV energy range.

We can then quantify the statistical confidence with which model B can be excluded by computing the p-value in a Frequentist approach as well as the Bayes factor $\mathcal{B}$ for the two

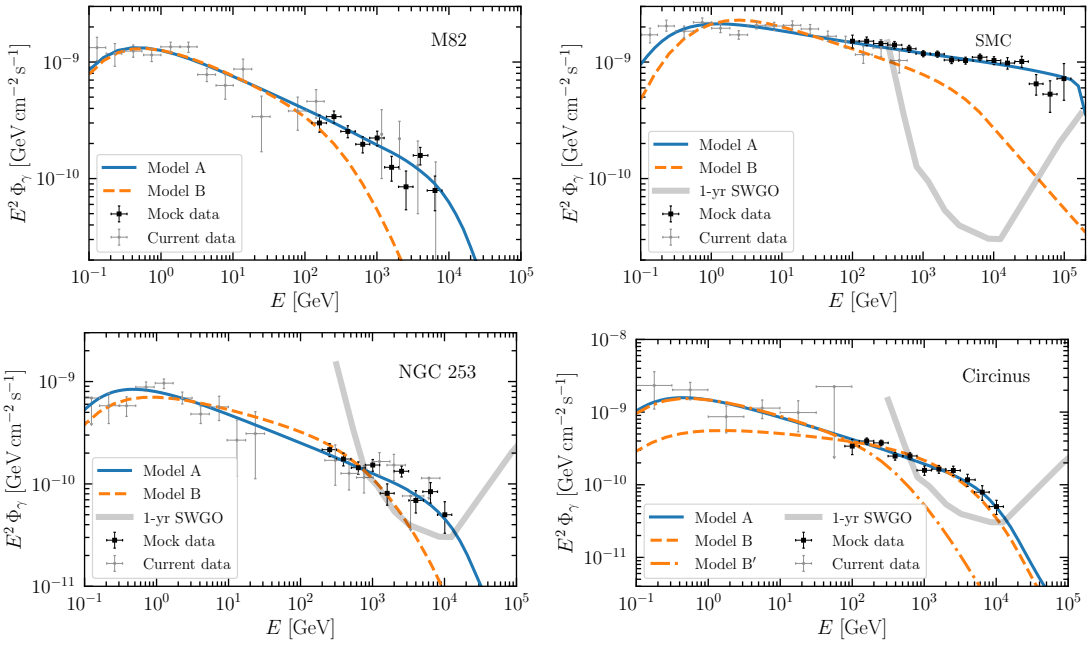

Figure 5.4: Spectral energy distributions of the most brightest sources compared to current (grey points) and one realization of CTA mock data (black points). The blue solid (orange dashed) lines show the best-fit scenario in case of model A (model B) of CR transport. For Circinus galaxy (bottom right panel), dashed-dotted orange line shows the best-fit SED for model B according to current data only. When present, grey curve represents the 1-year SWGO sensitivity to point-like sources in the Southern hemisphere [197].

models. The p-value is simply given by

$$p = \int_{\chi^2_{\rm min}}^{\infty} f_k(x)\,{\rm d}x \tag{5.11}$$

where $\chi^2_{\rm min} = -2\ln\left[\max \mathcal{L}_{\rm B}(\dot{M}_*, \Gamma)\right]$ and $f_k(x)$ is the probability distribution function of a chi-square with k degree of freedom. For each source, k is given by total number of data points (current and mock data) minus two (number of free parameters). On the other hand, the Bayes factor is computed as

$$\mathcal{B} = \frac{\int_{(\dot{M}_*,\,\Gamma)} \mathcal{L}_{\rm A}({\rm SED}|\dot{M}_*,\,\Gamma)\;{\rm d}\dot{M}_*\;{\rm d}\Gamma}{\int_{(\dot{M}_*,\,\Gamma)} \mathcal{L}_{\rm B}({\rm SED}|\dot{M}_*,\,\Gamma)\;{\rm d}\dot{M}_*\;{\rm d}\Gamma} \tag{5.12}$$

where $\mathcal{L}_{\rm A}$ and $\mathcal{L}_{\rm A}$ are the likelihood functions for model A and B, respectively. We note that the two integrals are performed over the same two-dimensional phase space given by the uniform priors on $\dot{M}_*$ and Γ. For each source, we therefore obtain a distribution of expected p-values and Bayes factors given the different mock data sets.

In Tab. 5.2 we summarise the results of the above-describe forecast analysis. In particular, we report the mean values of the distributions of p-value and Bayes factor along with the

Table 5.2: Results of the forecast analysis for the CTA telescope. For the four brightest sources, we report the mean p-values for model B and the mean Bayes factors for the two models corresponding to the distributions of 10^4 CTA mock data sets, along with the ones deduced by current data. The columns 95% and 68% show the one-side intervals of expected p-values and Bayes factors corresponding to that confidence level.

	p-value				Bayes factor, $\mathcal{B}$			
		Mock data				Mock data		
Source	Current data	95%	68%	Mean	Current data	95%	68%	Mean
SMC	4.3×10^{-10}	9.1×10^{-33}	4.4×10^{-35}	2.4×10^{-36}	5.8×10^{10}	1.4×10^{29}	6.6×10^{30}	2.8×10^{31}
M82	2.3×10^{-2}	3.8×10^{-4}	6.9×10^{-6}	3.8×10^{-7}	5.6×10^{2}	1.3×10^{3}	1.7×10^{6}	4.3×10^{7}
NGC 253	1.5×10^{-2}	4.2×10^{-4}	6.9×10^{-6}	3.5×10^{-6}	2.5×10^{2}	3.4×10^{5}	4.9×10^{8}	1.3×10^{10}
Circinus	4.1×10^{-1}	7.2×10^{-2}	1.3×10^{-2}	3.2×10^{-3}	1.0	8.3×10^{1}	2.5×10^{3}	1.0×10^{4}

corresponding values deduced with current data only. Moreover, we report the 68% and 95% one-sided intervals of the two distributions. As can be seen in the table, current data strongly disfavour model B for the SMC source. For other sources, we find that with future CTA observations model B might be excluded at more than 2σ according to the expected small p-values. Furthermore, large Bayes factors are expected in favour of model A. Interestingly, even though NGC 253 is slightly less luminous than M82 , the p-values and the Bayes factors are of the same order of magnitude (or even stronger) than for M 82. This is due to the fact that the effective area for the CTA south is expected to be bigger than CTA north, leading to a higher number of signal events expected in the detector (as well as a better sensitivity). Therefore, our results point out that CTA will be able to firmly discriminate between the two models of CR transport within the gamma-ray resolved SFGs and SBGs. In the next section, we evaluate the role of the astrophysical uncertainties on the environmental parameters for the forecast for the CTA telescope. We conclude this section by pointing out that CTA and SWGO will also quantitatively test the hadronic production of SMC, giving more indirect constraints on cosmic-ray transport mechanisms, assessing if its SED is entirely given by diffuse hadronic interactions or if there is a non-negligible contamination from point-like emissions such as Pulsar Wind Nebulae (PWN) and SNRs.

5.6 Impact of source uncertainties on mock data generation

In this section, we investigate how the mock data generation for the CTA telescope is affected by the current uncertainties on the source parameters. Such uncertainties are simply defined by the posterior distribution in Eq. (4.3) that is obtained with current gamma-ray data. Differently from the analysis presented in previous section (Sec. 5.5), for each source we produce mock data by sampling the star formation rate and the spectral index from the posterior distribution of model A, namely $(\dot{M}_*, \Gamma) \sim p_{\rm A}(\dot{M}_*, \Gamma|{\rm SED})$. These parameters determine the gamma-ray flux

$\Phi_{\gamma,\mathrm{A}}$ which is then employed to compute the expected number of signal events n_{signal} according to Eq. (5.8). This time, we consider the observed number of events simply as $n_{\mathrm{obs}} = n_{\mathrm{signal}} + n_{\mathrm{bkg}}$ and estimate the empirical $\widetilde{\mathrm{SED}}$ directly from n_{signal} (see Eq. (5.9)). As before, the uncertainty on the reconstructed SEDs is deduced from the Poisson uncertainty on the mock measurements n_{obs}. In this way, for each source we produce $\mathcal{O}(10^4)$ mock data sets which are analyzed assuming model A and model B. Indeed, we compute the p-values to test model B and the Bayes factors to compare the two models.

The results of this analysis are reported in Tab. 5.3. These findings are notably more restrictive compared to the previous case. This is primarily because, for M82, NGC 253, and SMC, the variability of the fit provided by Model A is minimal. Consequently, the predictions of Model A sharply contrast with those of Model B. In particular, for M82 and NGC 253, the mean Bayes factors are respectively of the order of 10^{23} and 10^9, which are much greater than the values obtained through the Poisson generation in Sec 5.5. Correspondingly, the rejection p-values are lower than the Poissonian mock data. In fact, for SMC, the average p-value is given by 2.0×10^{-38}, which is 2 order of magnitudes lower than the one provided by Poissonian mock data. The only exception is Circinus for which we just, currently, have six data points making its posterior distribution quite unconstrained. In this case, we obtain similar results for the two different approaches to mock data generation. We show this in Fig. 5.5 where in the top (bottom) panel we compare the distributions of for p-values (Bayes factors) for the two mock datasets. We also highlight the mean and the 95% C.L. values with dashed and dot-dashed lines, respectively, as well as the current values with collected gamma-ray data (solid lines). Even though the width of the distributions for the Poisson uncertainty and the source uncertainty are similar in this case, the distribution for latter case is peaked at higher values of Bayes factor. Therefore, it is conservative to consider only the Poisson uncertainty, as we do in the previous section.

5.7 Impact of the Uncertainty of Astrophysical Parameters

In this section, we scrutinize the impact on the results of the analysis presented in the previous section coming from the uncertainties on the source physical parameters. These might play a key role in model B which features a non-trivial calorimetric fraction ($F_{\mathrm{cal}}(E)$) as a function of the energy. Therefore, it is reasonable to check whether our results depend on the assumptions that the morphological parameters of local sources (e.g. h, n_{ISM}, and σ_g) are known and scale in a precise way with the star formation rate. In particular, Eq. (4.1) might be not exactly representative for all sources. For these reasons, for the four brightest sources we perform a

Table 5.3: Results of the CTA forecast analysis once the mock data are generated according the source posterior distribution in Eq. (4.3) obtained with current data. As in Tab. 5.2, we report the 95%, 68% and mean p-values testing model B as well as the Bayes factors comparing model A with model B.

Mock data		Source			
		SMC	M82	NGC 253	Circinus
p-value	95%	2.0×10^{-28}	2.8×10^{-5}	8.0×10^{-9}	2.2×10^{-1}
	68%	1.7×10^{-34}	9.4×10^{-6}	2.5×10^{-9}	4.8×10^{-2}
	Mean	1.0×10^{-38}	1.8×10^{-6}	5.7×10^{-10}	2.2×10^{-2}
$\mathcal{B}$	95%	1.7×10^{29}	1.8×10^{19}	1.4×10^{6}	3.5×10^{1}
	68%	1.2×10^{31}	1.2×10^{21}	1.1×10^{8}	6.0×10^{3}
	Mean	2.4×10^{33}	1.6×10^{23}	3.8×10^{9}	2.0×10^{4}

Table 5.4: Results of the forecast analysis for the CTA telescope, considering the uncertainty on the structural parameters of the sources for model B.

	p-value				Bayes factor, $\mathcal{B}$			
		Mock data				Mock data		
Source	Current data	95%	68%	Mean	Current data	95%	68%	Mean
SMC	5.7×10^{-6}	3.6×10^{-19}	6.3×10^{-22}	2.7×10^{-23}	1.8×10^{12}	4.0×10^{13}	3.2×10^{18}	1.3×10^{20}
M82	1.2×10^{-2}	6.7×10^{-3}	8.8×10^{-4}	1.1×10^{-4}	1.3×10^{3}	2.0×10^{4}	6.5×10^{5}	1.6×10^{7}
NGC 253	3.4×10^{-2}	4.2×10^{-2}	6.6×10^{-3}	1.2×10^{-3}	1.5×10^{3}	6.6×10^{1}	2.2×10^{3}	1.8×10^{4}
Circinus	4.7×10^{-2}	1.5×10^{-1}	3.4×10^{-2}	1.2×10^{-2}	1.2	4.1×10^{1}	1.4×10^{3}	3.3×10^{3}

similar analysis on current and mock data by taking 5 free and independent parameters for model B: Γ, $\dot{M}_*$, $n_{\rm ISM}$, σ_g, and h. For all the parameters, we consider uniform priors. For Γ and $\dot{M}_*$, we make use of the same priors as in previous section. For the SBN height h, we consider the range $70 - 150\,{\rm pc}$ (an uncertainty of a factor of 2), being consistent with [131, 195]. For the velocity dispersion σ_g, we take $25 - 50\,{\rm kms}^{-1}$ (an uncertainty of a factor of 2). Finally, for the gas density $n_{\rm ISM}$, we consider $\mathcal{O}(10)$ variations: for Circinus and NGC 253 in the range $10 - 200\,{\rm cm}^{-3}$, for M82 in the range $30 - 300\,{\rm cm}^{-3}$, and for for SMC in the range $1 - 20\,{\rm cm}^{-3}$. We summarise the main results in Tab. 5.4. These are obtained for only 100 mock datasets since the 5-parameter fitting procedure is highly time consuming. As can been seen by comparing with Tab. 5.2, the p-values (Bayes factors) increase (reduce) by a few orders of magnitudes. Nonetheless, even in this case, we find p-values $\lesssim 0.1$ (Bayes factor $\gtrsim 10$) for 95% of the mock data sets generated under model A. Therefore the conclusions derived in the previous sections remain unchanged. This is a crucial point which, from one hand, underlines once again the importance for future measurements (despite all the possible uncertainties) and, from the other, remarks the intrinsic difference from the calorimetric fractions of models A and B.

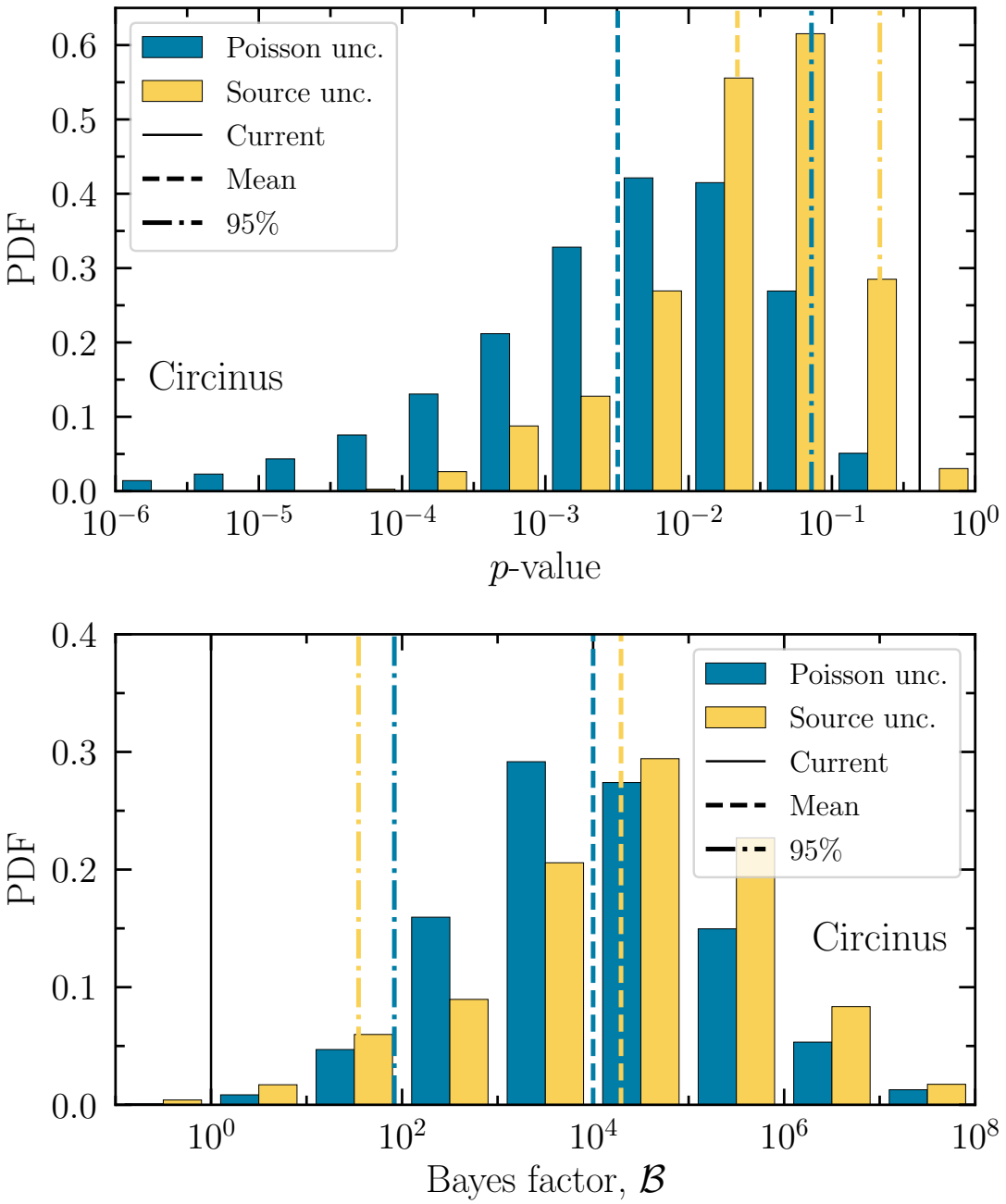

Figure 5.5: Distributions of p-values (top panel) and Bayes factors (bottom panel) obtained by generating CTA mock data according to a Poisson distribution (blue color) and to the posterior distribution of source parameters (yellow color). The vertical lines show both the current value (solid lines) with collected data, and the mean (dotted lines) and 95% (dot-dashed) values corresponding to the mock distributions.

5.8 From Point Sources to Diffuse Fluxes

The observation of nearby galaxies provides valuable constraints on the parameters which define their point-like emissions. Furthermore, as we presented in the previous sections, these observa-

tions also provide precious indirect information on the CR transport inside this kind of sources. As a result, this might have an impact on the diffuse emission of these sources. In this section, equipped with point-like spectrum information, we can evaluate the cumulative diffuse gamma-ray and neutrino fluxes correlated to unresolved SFGs and SBGs emission. In this section, we do not consider model B ([195], model B [131]), since it is inadequate at ultra-high energies, thereby making unreliable the comparison with IceCube neutrino observations. For this reason, we only consider model A, with the aim of refining our previous calculation provided in chapter 3, taking into account the spectral variability of SBGs as obtained in the present source-by-source analysis.

We carry this calculation out by adopting a similar approach to the one described in chapter 3. In particular, this approach exploits the fact that when model A is considered for good reservoirs, the neutrino and gamma-ray fluxes do not depend on the configuration details of the SBN (e.g. the dimension of the starburst region $R_{\rm SBN}$ or the interstellar medium density $n_{\rm ISM}$), but rather on the star formation rate $\dot{M}_*$ and the spectral index Γ. Therefore, we can consider a prototype galaxy (M82) to set the astrophysical parameters, and then linearly scale with the star formation rate the fluxes of a generic source, which take the expression [32]

$$\Phi_{\gamma,\nu}(E,z|\dot{M}_*,\Gamma) = \frac{\dot{M}_*}{\dot{M}_*^{\rm M82}}\Phi_{\gamma,\nu}(E,z|\dot{M}_*^{\rm M82},\Gamma) \tag{5.13}$$

Then, the diffuse gamma-ray and neutrino flux can be obtained as

$$\begin{aligned}\Phi_{\gamma,\nu}^{\rm diff}(E) = \int_0^{4.2} {\rm d}z \int_{\dot{M}_{*,\rm min}}^{\infty} {\rm d}\log\dot{M}_* \, \frac{c\, d_c(z)^2}{H(z)} \\ \times \mathcal{S}_{\rm SFR}(z,\dot{M}_*)\left\langle \Phi_{\gamma,\nu}\big(E,z|\dot{M}_*,\,\Gamma\big)\right\rangle_\Gamma\end{aligned} \tag{5.14}$$

where we integrate over the whole SFGs and SBGs population in redshift z and star formation rate $\dot{M}_*$, for which we consider the modified Schecter function $\mathcal{S}_{\rm SFR}(z,\dot{M}_*)$ reported by [32]. Such a quantity has been obtained by fitting in the redshift interval $0 \leq z \leq 4.2$ the IR+UV data of a Herschel Source sample [148] after subtracting the AGN contamination [149]. For the cosmological Hubble parameter $H(z) = H_0\sqrt{\Omega_M(1+z)^3+\Omega_\Lambda}$ we take $H_0 = 67.74$ km s^{-1}Mpc^{-1}, $\Omega_M = 0.31$ and $\Omega_\Lambda = 0.69$, and $d_c(z)$ denotes the comoving distance. Finally, $\langle\Phi_{\nu,\gamma}\rangle_\Gamma$ is the emitted neutrino and gamma-ray fluxes averaged over the distribution of allowed spectral indexes, namely

$$\left\langle \Phi_{\gamma,\nu}\big(E,z|\dot{M}_*,\,\Gamma\big)\right\rangle_\Gamma = \int \Phi_{\gamma,\nu}\big(E,z|\dot{M}_*,\,\Gamma\big)\, p_{\rm obs}(\Gamma)\,{\rm d}\Gamma \tag{5.15}$$

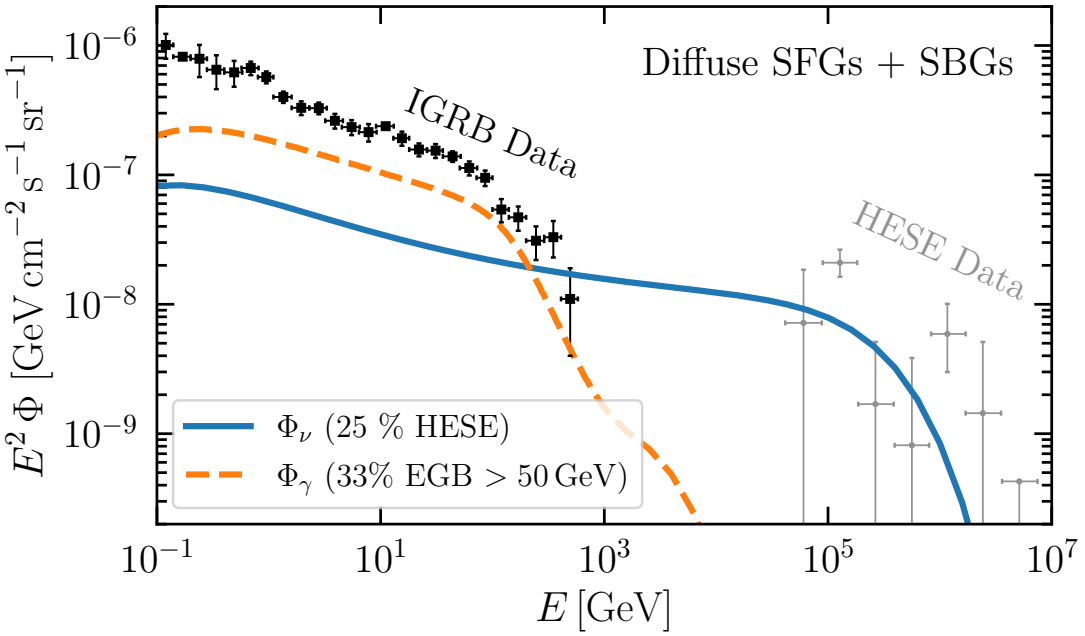

Figure 5.6: Diffuse neutrino (solid blue line) and gamma-ray (dashed orange line) flux from SFGs and SBGs predicted by model A for the CR transport. The contribution from electromagnetic cascades is also included. The data points correspond to the Fermi-LAT IGRB measurements [199] and the IceCube HESE ones per neutrino flavour [5].

The main differences between the present calculation and the one in chapter 3 (see also [52]) are threefold. Firstly, we take a different spectral index distribution $p_{\rm obs}(\Gamma)$, directly stemming from the Γ values inferred by gamma-ray point-like data and reported in Tab. 5.1 (take a look also at Tab. 4.2). This makes our estimates highly consistent with each other since the same CR transport model is used for point-like and diffuse analysis. In particular, we consider the spectral index distribution to be a Gaussian distribution with mean value of ($\Gamma_{\rm mean} = 4.36$) and standard deviation standard ($\sigma = 0.2$). Secondly, we do not set by hand a lower limit for the SFR above which SBGs and SFGs are considered as good calorimeters. Indeed, as summarised by Eq. (5.1), the sources which are dominated by either advection or diffusion losses naturally have their calorimetric fraction approaching zero, thus giving a negligible contribution to the diffuse fluxes. Therefore, we integrate from a minimum SFR $\dot{M}_{*,\rm min} = 0.038$ M$_\odot$yr^{-1} according to our point-like analysis. Thirdly, we do not consider a free normalization for the diffuse flux, which is instead directly predicted under the aforementioned assumptions. Before showing our main results, we would like to stress that the plausibility of this method resides in the fact that, as demonstrated also by Ref. [195], the majority of the contribution comes from sources which have a high star formation rate $\dot{M}_* \gtrsim 1\,{\rm M}_\odot\,{\rm yr}^{-1}$, for which the calorimetric approach is reasonably justified.

Indeed, in our approach, the low-SFR sources ($\dot{M}_* \lesssim 1\,\mathrm{M}_\odot\,\mathrm{yr}^{-1}$) contribute for less than 15%. This means that our calculation might slightly overestimate the diffuse contribution, although this does not sensibly affect our result. Fig. 5.6 shows the diffuse gamma-ray and neutrino fluxes compared with the Isotropic Gamma-Ray Background (IGRB) [199] and IceCube HESE [5] data, respectively. The gamma-ray flux takes also into account the electromagnetic cascade contribution, calculated with the γ-Cascade public code [114], although their contribution is more or less negligible since the overall spectrum is softer than E^{-2}. We find a gamma-ray flux similar to previous estimates [32, 52, 193]. In particular, we predict the SFGs and SBGs to provide an important contribution to the IGRB. Nevertheless, differently from the results of Refs. [84, 195], our prediction is consistent within 1σ uncertainties given with the non-blazar limits [12, 13, 85, 198], since it corresponds to 33% of the total EGB integrated above 50 GeV. This is highly significant since our result is obtained without any fine-tuning of parameters. Furthermore, as far as the neutrino production is concerned, we predict a flux which can explain a considerable fraction of the IceCube observations. Through the IceCube effective area, we find that our model produces 25 HESE events with energy higher than 30 TeV after 7.5 years of data-taking. This corresponds to roughly 25% of the totality of the HESE observed by the IceCube collaboration. Hence, differently from [195], we find a significantly higher neutrino contribution without violating the diffuse gamma-ray constraints. Overall, these results highlight the importance in constraining the properties of CR transport inside SFGs and SBGs in order to better assess their contribution to the diffuse emission measurements. Indeed, if CRs with $E \gtrsim 1\,\mathrm{TeV}$ escape from the sources, then their contribution to the diffuse emission might be significant scaled down (specially for neutrinos). Nonetheless, for the moment, the diffuse data cannot be used to discriminate between the two CR models due to partially unknown origin of diffuse neutrinos and gamma-rays.

5.9 Conclusions

In this chapter, we have investigated phemonelogically the consequences of two different models ((advection-dominated) model A [31] and (diffusion-dominated) model B [131]) for cosmic-ray transport within the cores of starforming and starburst galaxies. We have shown that current point-like observations by Fermi-LAT, VERITAS and H.E.S.S. gamma-ray telescopes already prefer model A, especially for the brightest sources SMC, M82 and NGC 253. Then, we have performed a forecast analysis for the CTA telescope which will potentially observe the gamma-ray emission from nearby galaxies at higher energies. Interestingly, we have found that future

CTA observations have the potential to firmly discriminate between model A and model B, providing the latter a highly-suppressed emission above few TeVs. We emphasize that in the Southern hemisphere a crucial role will be also played by the upcoming SWGO telescope thanks to a larger field of view and a longer duty-cycle compared to CTA. The comparison between the two models depends crucially on the hadronic production above ~ 1 TeV, which is present in model A and suppressed in model B due to diffusion. Since this hadronic production generally follows a power-law spectrum, the results we obtain are roughly independent of the details of the models (e.g. choice of the astrophysical parameters), and are mainly determined by the spectral index, normalization, and maximal cosmic-ray energy, which we obtain from current gamma-ray data on star-forming galaxies. Finally, we have employed the information inferred by the local gamma-ray observations to consistently and robustly estimate the diffuse gamma-ray and neutrinos emission from the whole population of starforming and starburst galaxies. We have found that model A predicts a 25% contribution of these sources to the IceCube HESE data, in agreement with the gamma-ray limits on the non-blazar component. This result confirms that cosmic reservoirs are of paramount importance for the description of high-energy diffuse neutrino observations, even though they cannot explain the whole astrophysical flux observed.

Chapter 6

Probing Dark-Matter Proton Interactions using Cosmic Reservoirs

In the previous chapter, we have analysed how the SBG gamma-ray data might be used to distinguish between different CR transport models, arriving to the conclusion that current data slight prefer model A, which predicts power-law gamma-ray spectrum with CR timescale mostly dominated by energy-independent timescales. In this chapter, we make use of model A in order to constrain Dark-Matter proton interactions using SBGs observations. This chapter is based on our analysis published in [200].

6.1 Introduction

The existence of Dark Matter (DM) is a milestone of the cosmological standard model [201]. However, its nature has not been identified yet [202–205]. Astrophysical and cosmological observations reveal that galaxies, including the Milky Way (MW), posses a halo of non-relativistic DM particles [37, 38, 206–208]. This has allowed direct-detection experiments to place powerful limits on the properties of DM particles which may elastically scatter off target nuclei (see [205] for a recent review). However, due to poor sensitivity at low nuclear recoil energies, such searches are typically limited to DM masses higher than 1 GeV, leaving sub-GeV DM largely unexplored by direct measurements. To probe such light DM particles, novel approaches are required in

addition to standard astrophysical [206, 207, 209–212], cosmological[213–218], and collider [219] searches. Ref. [220] proposed one such approach, pointing out that the spectrum of MW Cosmic-Rays (CRs) can be altered by DM-CR elastic interactions. Soon after, Ref.s [221, 222] showed that this interaction produces Boosted Dark Matter (BDM) particles, which can then be probed in direct-detection experiments due to their large energies (see Ref.s [223–249] for other BDM studies).

Up until now, the impact of DM-CR interaction has been mainly analyzed in the context of our own Galaxy (few exceptions are Ref. [224, 250–252]). However, CRs suffer a larger effect in environments which confine CRs for long times, so that they traverse through the DM halo longer. Therefore, in this chapter we propose to use *cosmic reservoirs*, namely sources which confine cosmic-rays, as a probe of DM-CR interactions. We focus on the nuclei of starburst galaxies (hereafter denoted as SBNi), which confine CRs [31, 52, 163] for $\sim 10^5$ years even at energies as large as 100 TeV. While these CRs cannot be directly observed, they produce gamma-rays and neutrinos via hadronic collisions [20, 21, 31, 32, 52, 163, 189]. Therefore, DM-CR interaction can distort the CR spectrum, and in turn the gamma-ray flux observed from SBNi (see Fig. 6.2). Here we show that the gamma-ray data from two nearby starburst galaxies, M82 and NGC 253, do not exhibit such a distortion, allowing us to bound the DM-CR cross section at the level of 10^{-34} cm^2 for DM with 10 KeV masses, as shown in Fig. 6.4. The bounds can be substantially improved with a better knowledge of the gamma-ray flux at energies 0.1–10 TeV. We show that the future Cherenkov Telescope Array (CTA) [26] will be able to strengthen these bounds by as much as two orders of magnitude.

6.2 Dark Matter Distribution inside SBNi

The DM-CR scattering rate depends on the DM (hereafter called χ) density distribution, which is pretty uncertain in the central cores of galaxies [253–255]. All we know is that galaxies are embedded in a DM halo. A benchmark parameterization is the Navarro-Frenk-White (NFW) distribution [256]

$$\rho_\chi(r) = \frac{\rho_s}{r/r_s\,(1+r/r_s)^2} \tag{6.1}$$

which is a function of the radial distance r from the SBN center. The scale radius r_s and the normalization ρ_s can be expressed through the concentration parameter $c_{200} = r_{200}/r_s$ and the mass M_{200} enclosed in a sphere of radius r_{200}, which is defined as the distance at which the mean DM density is 200 times the critical Universe density ρ_c. In fact, the mass enclosed with

a certain radius r_{200} can be expressed as:

$$M_{200} = \int_0^{r_{200}} 4\pi\rho_\chi(r)r^2 dr = 4\pi\rho_0 r_s^3 \left[\ln\left(\frac{r_{200}+r_s}{r_s}\right) - \frac{r_{200}}{r_s+r_{200}}\right] \tag{6.2}$$

Another parameterization is the so called Burkert profile [257]:

$$\rho_{DM}(r) = \frac{\rho_0 r_s^3}{(r+r_s)(r^2+r_s^2)} \tag{6.3}$$

Also for this density profile, we can parameterize it in terms of M_{200} and c_{200}. M_{200} and c_{200} are not measured, so we can only use the results from simulations. In particular, Ref.s [37–39] have shown that $7 \leq c_{200} \leq 12$ and $10^{10} \leq M_{200}/\mathrm{M}_\odot \leq 10^{12}$ describe pretty well the Dark Matter halo of local SBGs, such as M 82 and NGC 253. As benchmark cases in the following analysis we use $c_{200} = 7$ for both sources, $M_{200} = 10^{12}\,\mathrm{M}_\odot$ for M82 and $M_{200} = 3\times10^{11}\,\mathrm{M}_\odot$ for NGC 253 [37–39].

Fig. 6.1 shows the DM density distribution for both benchmark cases. In particular, the

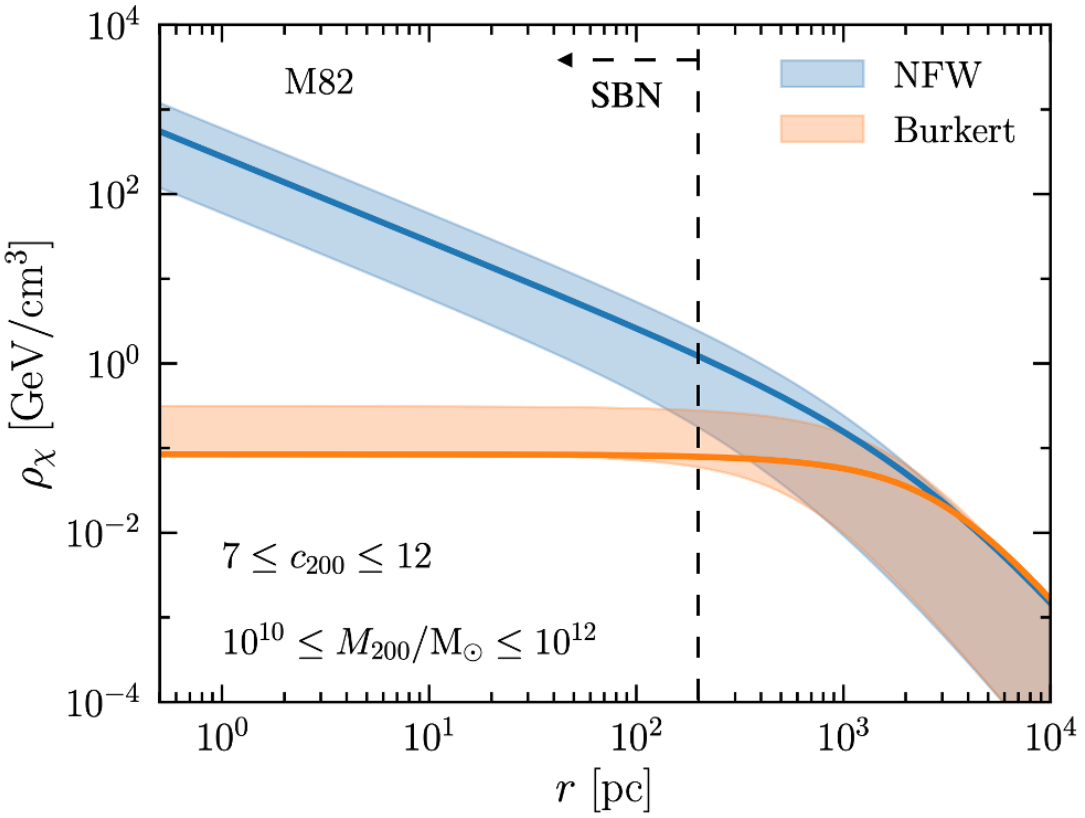

Figure 6.1: DM energy density as a function of r. The Blue band corresponds to the NFW profile, while the orange one corresponds to the Burkert profile. The vertical line correspond to the dimension R of a typical starburst nucleus $R = 200\,\mathrm{pc}$.

blue band corresponds to the NFW profile and the orange one corresponds to the Burkert one. The main difference between the Burkert and NFW profiles is the fact the that the former is not divergent at $r = 0$, leading to a different average density within the SBN. The figure also shows the value corresponding to $r = R_{\rm SBN} = 200\,{\rm pc}$ which corresponds to the benchmark value considered also in previous chapters (see also [31, 32, 163, 189]). The uncertainty on the DM halo impacts the rate of DM-proton interactions, thereby leading to uncertainty on the possible constraints on the DM-proton cross section $\sigma_{\chi p}$. In the next sections, we are going to show that this uncertainty leads to at most one order of magnitude uncertainty in the results.

6.3 DM-proton scatterings inside SBNi

If nucleons are coupled to DM, CRs confined in the SBN are trapped for such a long time that they can collide with DM. Elastic DM-CR scatterings cause an additional energy-loss in Eq. (3.3), competing with the others for sufficiently large DM-proton cross sections:

$$\tau_{\chi p}^{\rm el} = \left[-\frac{1}{E} \left(\frac{{\rm d}E}{{\rm d}t} \right)_{\chi p} \right]^{-1} , \tag{6.4}$$

with

$$\left(\frac{{\rm d}E}{{\rm d}t} \right)_{\chi p} = \frac{\rho_\chi}{m_\chi} \int_0^{T_\chi^{\rm max}} {\rm d}T_\chi \, T_\chi \frac{{\rm d}\sigma_{\rm el}}{{\rm d}T_\chi} , \tag{6.5}$$

where m_χ is the DM mass, ρ_χ is the spherically-symmetric DM density within the SBN, and ${\rm d}\sigma_{\rm el}/{\rm d}T_\chi$ is the differential elastic DM-proton cross section as a function of the final DM kinetic energy T_χ. The maximal allowed value $T_\chi^{\rm max}$ for T_χ in a collision with a proton with kinetic energy $T = E - m_p$ is

$$T_\chi^{\rm max} = \frac{2T^2 + 4m_p T}{m_\chi} \left[\left(1 + \frac{m_p}{m_\chi} \right)^2 + \frac{2T}{m_\chi} \right]^{-1} . \tag{6.6}$$

The differential cross section depends on the properties of the DM particle as well as on the DM-proton interaction. For definiteness, we consider Dirac fermion DM particles interacting with protons via a scalar mediator with a mass much larger than the transfer momentum $q^2 = 2m_\chi T_\chi$. This last assumption allows us to evaluate the cross section just in term of a single free parameter. Differently from Ref.s [220, 224], that assume a constant cross section with a flat spectrum in

recoil energy, for $T_\chi \leq T_\chi^{\max}$ we have [223]

$$\frac{\mathrm{d}\sigma_{\mathrm{el}}}{\mathrm{d}T_\chi} = \frac{\sigma_{\chi p}}{T_\chi^{\max}} \frac{F_p^2(q^2)}{16\,\mu_{\chi p}^2\,s}\,(q^2+4m_p^2)(q^2+4m_\chi^2)\,, \tag{6.7}$$

where $\sigma_{\chi p}$ is the DM-proton cross section at zero center-of-mass momentum, $\mu_{\chi p}$ is the reduced mass of χ and proton, and $s = m_\chi^2 + m_p^2 + 2Em_\chi$ is center-of-mass energy. The quantity F_p is the proton form factor [258]

$$F_p(q^2) = \left(\frac{1}{1+q^2/\Lambda^2}\right)^2 \quad \text{with} \quad \Lambda = 0.770\,\mathrm{GeV}\,. \tag{6.8}$$

At energies much higher than $m_p^2/2m_\chi$, DM-CR scatterings become inelastic, breaking the proton and producing additional gamma-rays from the pion decay [259]. We model this process via a simple semi-analytic approximation similar to Ref.s [237, 260, 261]: we assume the DM-CR inelastic cross section to follow the neutrino-nucleon one and rescale it to match the DM-CR cross section in the elastic regime. In this way, the inelastic cross section (σ_{inel}) is totally defined by means of $\sigma_{\chi p}$ in Eq. (6.7). The timescale for energy loss from inelastic DM-CR collision is

$$\tau_{\chi p}^{\mathrm{inel}} = \left(\kappa\,\sigma_{\mathrm{inel}}\,\frac{\rho_\chi}{m_\chi}\right)^{-1}\,, \tag{6.9}$$

where κ is the inelasticity of the process, assumed to be 0.5 as for inelastic proton-proton collisions. In the next section, we describe how we evaluate the gamma-ray emissivity also in case of DM-p interactions.

6.4 Evaluating the gamma-ray spectrum

In this section, we evaluate the gamma-ray spectrum considering also the DM-p interactions. The presence of exotic interactions between χ and protons make the timescale radius-dependent (dependent on the distance from the center of the SBN). Therefore, in order to obtain the gamma-ray spectrum, we firstly compute Eq. 3.3 for each r. Then, we can compute the pion production rate each r via (see chapter 3 and App. A for details):

$$q_\pi^{pp}(E_\pi, r) = \frac{n_{\mathrm{ISM}}}{k_\pi}\sigma_{pp}\left(m_p + \frac{E_\pi}{k_\pi}\right) n_p\left(m_p + \frac{E_\pi}{k_\pi}, r\right)\,, \tag{6.10}$$

Regarding the gamma-ray emissions from inelastic DM-proton collisions, we consider the

pion production to follow the proton-proton collisions

$$q_\pi^{\chi p}(E_\pi, r) = \frac{\rho_\chi(r)}{m_\chi\, k_\pi}\, \sigma_{\rm inel}\left(m_p + \frac{E_\pi}{k_\pi}\right) n_p\left(m_p + \frac{E_\pi}{k_\pi}, r\right). \tag{6.11}$$

The emissivity of photons coming from neutral pion decay is

$$Q_\pi(E, r) = 2\int_{E+m_\pi^2/4E}^{\infty} \frac{q_\pi^{pp}(E_\pi, r) + q_\pi^{\chi p}(E_\pi, r)}{\sqrt{E_\pi^2 - m_\pi^2}}\, {\rm d}E_\pi\,. \tag{6.12}$$

Finally, the total gamma-ray flux at Earth can be then computed as

$$\Phi_\gamma(E, z) = \frac{{\rm Abs}(E(1+z))\, e^{-\tau_{\gamma\,\gamma}(E,z)}}{4\pi\, d_c(z)^2} \int_{V_{\rm SBN}} Q_{\rm tot}(E(1+z), r)\, {\rm d}V\,, \tag{6.13}$$

where $Q_{\rm tot}(E, r)$ corresponds to the sum over all the contributions (bremsstrahlung + Inverse Compton + pion-decay photons), $d_c(z)$ is the comoving distance between the source and the Earth, and the integral is performed over the SBN volume.

It is important to notice that, as long as the DM-proton interaction timescales are not competitive with respect to the others ($\tau_{\chi p}^{\rm inel}$, $\tau_{\chi p}^{\rm el} \gg \tau_{\rm loss}, \tau_{\rm adv}$), the integration in Eq. (6.13) results to be just a multiplication of the total production rate ($Q_{\rm tot}$) and the SBN volume ($V_{\rm SBN}$). In the opposite scenario, when elastic χp collisions dominate ($\tau_{\chi p}^{\rm el} \ll \tau_{\rm loss}, \tau_{\rm adv}$), we have that protons mostly escape from the SBN and the gamma-ray spectrum becomes

$$\Phi_\gamma \propto \int Q_\pi(r)\, {\rm d}V \propto \int \frac{Q_p(p, r)\, \tau_{\chi p}^{\rm el,eff}(r)\, {\rm d}V}{V} \propto \int \frac{\rho_\chi^{-1}(r)\, {\rm d}V}{V}\,, \tag{6.14}$$

where the first passage is due to the fact that the dominant contribution comes from the pion decay. Eq. (6.14) shows that the gamma-ray spectrum only depend on the average DM density inside the SBN rather than the actual DM profile. In the regime where $\tau_{{\rm inel},\chi p}$ dominates over the others, the SBN starts being totally calorimetric. In this scenario the pion production, which is dominated by $q_\pi^{\chi p}(E_\pi, r)$ (see Eq. (6.11)), is just directly proportional to Q_p, therefore independent of ρ_χ and m_χ. As a result, the gamma-ray spectrum is independent on ρ_χ as well as the environmental parameters e.g. $R_{\rm SBN}$, $v_{\rm wind}$, $n_{\rm ISM}$ ($\Phi_\gamma \propto Q(p)$). All of this is crucial because it sets the behaviour of eventual contraints for light DM particles from SBNi. In particular, they do not depend on the details of the DM profile, but rather the mean density which the profile induce inside the SBN. In the next sections, we describe the phenomenological implications of these exotic interactions and how we can use current data to set strict upper limits.

6.5 Observable Features on the Gamma-ray Spectrum.

The additional energy loss from elastic DM-CR interactions cause a suppression in the CR, and therefore in the gamma-ray spectrum, whereas the inelastic DM-CR production can replenish the gamma-ray spectrum at higher energies. These effects are visible in Fig. 6.2 which represents the case of M82 source.

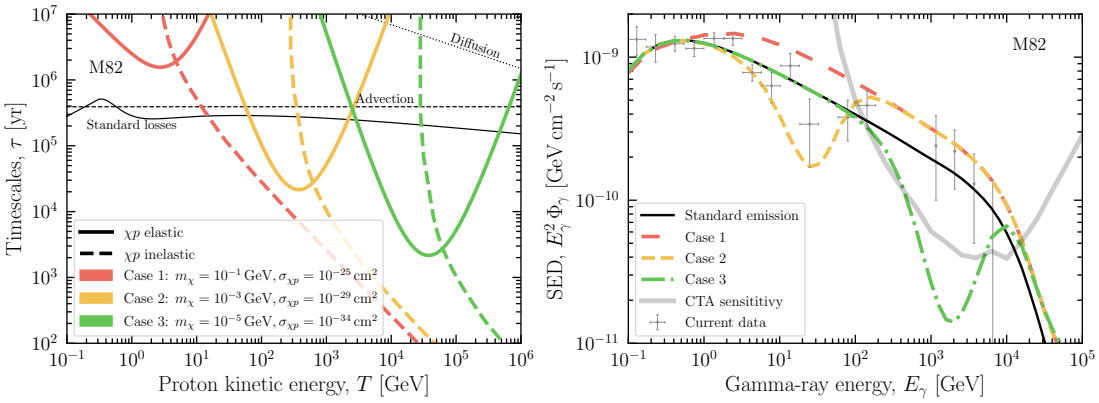

Figure 6.2: **Left panel.** Comparison between the proton timescales within M82 as a function of the proton kinetic energy T. The continuous, dashed and dotted black lines represent the standard losses, advection and diffusion timescales, respectively. The colored continuous (dashed) lines correspond to the elastic (inelastic) for three different cases. **Right panel.** The expected gamma-ray fluxes from M82 compared to current data [19, 262] and CTA sensitivity [26]. Analogously to the left panel, the black color line corresponds to the standard case (without DM-CR interactions), while the colored lines to the three different choices of (m_χ, $\sigma_{\chi p}$).

The left panel shows the DM-CR energy-loss timescales ($\tau_{\chi p}^{\rm el}$ and $\tau_{\chi p}^{\rm inel}$), averaged within the SBN volume, in comparison with the standard timescales. At low CR energies, $T \ll E_{\rm dip}^p = m_p^2/(2m_\chi)$, $\tau_{\chi p}^{\rm el} \simeq 3m_p^4/2\rho_\chi\sigma_{\chi p}T^3$ rapidly decreases with the CR kinetic energy. At high CR energies, elastic scattering becomes progressively unlikely compared with the inelastic one, so $\tau_{\chi p}^{\rm el} \simeq 128 m_\chi^6 T^3/\rho_\chi\sigma_{\chi p}\Lambda^8 \ln(Tm_\chi/2m_p^2)$ increases with the CR kinetic energy. Elastic DM-CR scattering thus can cause a dip in the CR spectrum at an energy $E_{\rm dip}^p \simeq m_p^2/2m_\chi$, due to protons being pushed to lower energies. Above the dip, inelastic DM-CR scattering becomes the dominant source of CR energy loss. In each scattering the CR energy is reprocessed in gamma-rays, leading to a new calorimetric regime in which the gamma-ray spectrum again follows the CR injection power-law spectrum.

The right panel of Fig. 6.2 shows the resulting gamma-ray spectrum, evidencing the dips corresponding to different masses m_χ due to elastic DM-CR scattering at an energy $E_{\rm dip}^\gamma \simeq 0.1 E_{\rm dip}^p$ – since gamma-rays carry on average 10% of the parent CR energy – and the higher-energy power-law behavior of the gamma-rays from inelastic DM-CR scattering. The latter can

exceed the gamma-rays produced in the standard proton-proton dominated regime (black line), in which the calorimetry is only partial due to competition with advective escape. In fact, in the standard case without DM-CR interactions, only a fraction $\tau_{\rm loss}^{\rm eff}/(\tau_{\rm loss}^{\rm eff}+\tau_{\rm adv}) \sim 40-50\%$ of the protons lose all of their energy to gamma-rays, where $\tau_{\rm loss}^{\rm eff} = \tau_{\rm loss}/(\Gamma-1)$ is the effective timescale for energy losses which provided a slightly more precise solution to the CR transport equation (see App. A for more details). However, we emphasize that the normalization of the gamma-ray spectrum after the dip also depends on the assumed inelasticity, which by rigor should be determined from the specific DM-quark coupling. Nevertheless, this has no significant impact on the bounds we derive, which essentially depend only on the behavior in the dip region and therefore on the elastic DM-CR scattering. Moreover, it is worth noticing that leptonic processes are completely subdominant in SBNi and cannot reduce the amplitude of the dip. We also show in Fig. 6.3, in the same way as for M82, the comparison between the standard timescales and elastic and inelastic χp timescales (left panel) for three different cases for $(m_\chi, \sigma_{\chi p})$. The corresponding fluxes are shown in the right panel. The spectral features are similar to the ones of M82.

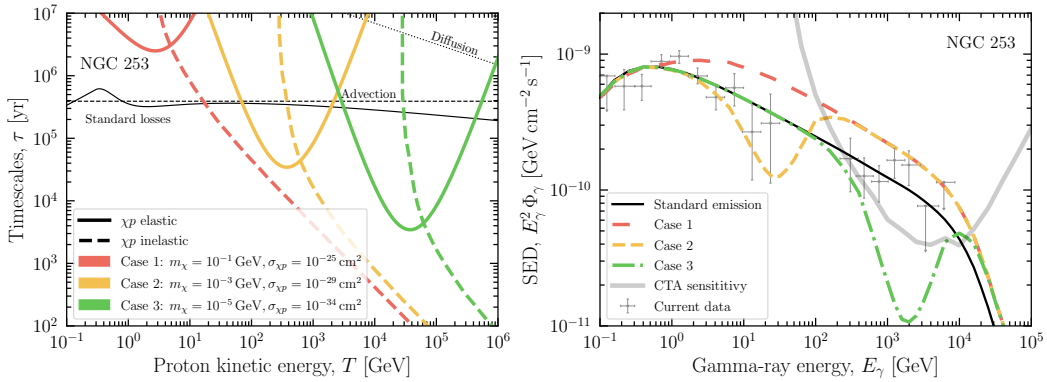

Figure 6.3: **Left panel.** Comparison between the proton timescales within NGC 253 as a function of the proton kinetic energy T. The continuous, dashed and dotted black lines represent the standard losses, advection and diffusion timescales, respectively. The colored continuous (dashed) lines correspond to the elastic (inelastic) for three different cases. **Right panel.** The expected gamma-ray fluxes from NGC 253 compared to current data [19, 49] and CTA sensitivity [26]. Analogously to the left panel, the black color line corresponds to the standard case (without DM-CR interactions), while the colored lines to the three different choices of $(m_\chi,\, \sigma_{\chi p})$.

6.6 Statistical Analysis and Discussion

Along with the previous chapters, we analyze GeV-TeV data for both M82 and NGC 253. All data-sets show a gamma-ray production up to TeV, with no hint of a break. Therefore, they

strongly constrain DM-CR interactions.

To obtain these bounds, we follow previous chapters, using the following likelihood:

$$\mathcal{L}(m_\chi, \sigma_{\chi p}, \theta) = e^{-\frac{1}{2}\sum_i \left(\frac{\mathrm{SED}_i - E_i^2 \Phi_\gamma(E_i|m_\chi, \sigma_{\chi p}, \theta)}{\sigma_i}\right)^2}, \tag{6.15}$$

where SED_i is the measured spectral energy distribution data, E_i and σ_i are respectively the centered energy bin value and the uncertainty on the data, and i runs over the number of data points. Finally, $\Phi_\gamma(E_i|m_\chi, \sigma_{\chi p}, \theta)$ is the gamma-ray flux, where θ represents the astrophysical nuisance parameters which are: $\dot{M}_*$, Γ, $R_{\rm SBN}$, $v_{\rm wind}$, $n_{\rm ISM}$, with $n_{\rm ISM}$. Following last chapter, we consider realistic linear priors for these parameters in order to take into account the astrophysical uncertainties on the structural properties of M82 and NGC 253. ab. 6.1 summarizes all the priors for both sources. For $\dot{M}^*$ and Γ, we impose similar priors as in the previous chapter, namely a range $[1, 3]$ for Γ and consistency within a factor 3 with respect to the ones inferred through IR and UV observations [20] for the star formation rate. For the dimension of the nuclei $R_{\rm SBN}$, we account for a variation of a factor 2 with respect to the value expected for SBN circumnuclear region [31, 32, 44, 45]. The range for the wind velocity is fixed according to the recent analyses [21, 30–32, 122]. Finally, for the gas density $n_{\rm ISM}$, the two sources require different priors according to the empirical Kennicut relation [44–46].

Source	$\dot{M}_*$ [$\mathrm{M_\odot\,yr^{-1}}$]	Γ	$n_{\rm ISM}$ [$\mathrm{cm^{-3}}$]	$R_{\rm SBN}$ [pc]	$v_{\rm wind}$ [$\mathrm{km\,s^{-1}}$]
M82	$[3, 30]$	$[1, 3]$	$[100, 400]$	$[100, 400]$	$[200, 1000]$
NGC 253	$[1.4, 17]$	$[1, 3]$	$[70, 280]$	$[100, 400]$	$[200, 1000]$

Table 6.1: Linear priors on the astrophysical nuisance parameters for the two sources adopted in the present analysis.

In order to obtain bounds on the DM-CR cross section, from the marginalized chi-squared $\chi^2(m_\chi, \sigma_{\chi p}) = -2 \ln \max_\theta \mathcal{L}(m_\chi, \sigma_{\chi p}, \theta)$ we define the test statistic $\Delta\chi^2 = \chi^2(m_\chi, \sigma_{\chi p}) - \chi^2(m_\chi, 0)$, comparing with the zero interaction case. We set bounds at 5σ confidence level by requiring $\Delta\chi^2 = 23.6$, since in the hypothesis of a DM signature the test statistic is distributed as a half-chi-squared variable.

Fig. 6.4 summarizes the constraints we find on $\sigma_{\chi p}$ as a function of m_χ, both for the case of M82 and NGC 253. The bounds flatten out for $m_\chi \lesssim 1$ keV, since lighter masses cause a dip at $E^\gamma_{\rm dip} \gtrsim 50$ TeV, where gamma-rays cannot be observed due to attenuation on extragalactic background light. NGC 253 leads to significantly better bounds at low masses due to the larger number of data points in the TeV region. Indeed, the main limitation from present-day data is the limited statistics in the $1 - 10$ TeV window. To quantify this, we perform a forecast analysis

for the CTA telescope [26], for both sources CTA will dramatically improve the gamma-ray measurements in this energy region, as already shown in previous chapter. We generate 50 mock data sets following the procedure explained in Sec. 5.5 and we obtain the projected bounds for each sample. Fig. 6.4 shows the mean values of these bounds (see next section for further details). CTA will strengthen the constraints up to two orders of magnitude for NGC 253 and five orders of magnitude for M82 in the low-mass region. We emphasize that constraining DM-CR scattering using starburst galaxies has the additional advantage that different galaxies can be used to make the results more robust, and the bounds from different sources can be combined to provide more stringent exclusions on the DM properties.

Our bounds are complementary to the direct-detection of boosted DM, whose bounds exhibit a ceiling due to the atmosphere attenuation of the BDM flux. Our bounds also look significantly stronger than the ones placed in Ref. [220] by searching for distortions of the Milky-Way CR spectrum due to DM-CR scattering, while for $m_\chi \lesssim 1\,\mathrm{MeV}$ they are comparable with the ones derived from the non-observation of BDM particles from DM-CR interactions in blazars [224]. However, the limits [220, 224] have been both obtained assuming an energy-independent DM-CR cross section, whereas we include the typical $\sigma_{\chi p} \propto E^2$ behavior due to a massive mediator, and a flat distribution for the DM recoil energy. Naively, since our bounds primarily come from CRs around 10 TeV energies in the low-mass range, whereas $\sigma_{\chi p}$ is defined at a center-of-mass energy of order GeVs, they are stronger than the ones in Ref. [220] by about 10^8 just because of the different cross section behavior. However, the difference in the recoil energy distribution also leads to a completely different shape for the bounds. For this reason, a comprehensive comparison would require a re-evaluation of their results, which is beyond the scope of this thesis.

Differently from the Milky Way [260], in SBNi the inelastic DM-CR scatterings are also less observationally interesting, since they just replace the proton-proton scatterings in making CRs lose their energy to gamma-rays. However, bounds based on inelastic scattering in the Milky Way are strongly dependent on how the differential cross section for gamma-ray production is modeled, which in turn requires a specific choice of the quark-DM coupling. Furthermore, these bounds are applicable only at large enough DM masses, where the cosmic-rays kinetic energy exceed the pion production threshold. Our bounds instead depend essentially on the elastic scattering, which requires no threshold condition, and therefore are robust against these uncertainties.

Concerning the blazar-BDM bounds, we also emphasize that they rely on the existence of a

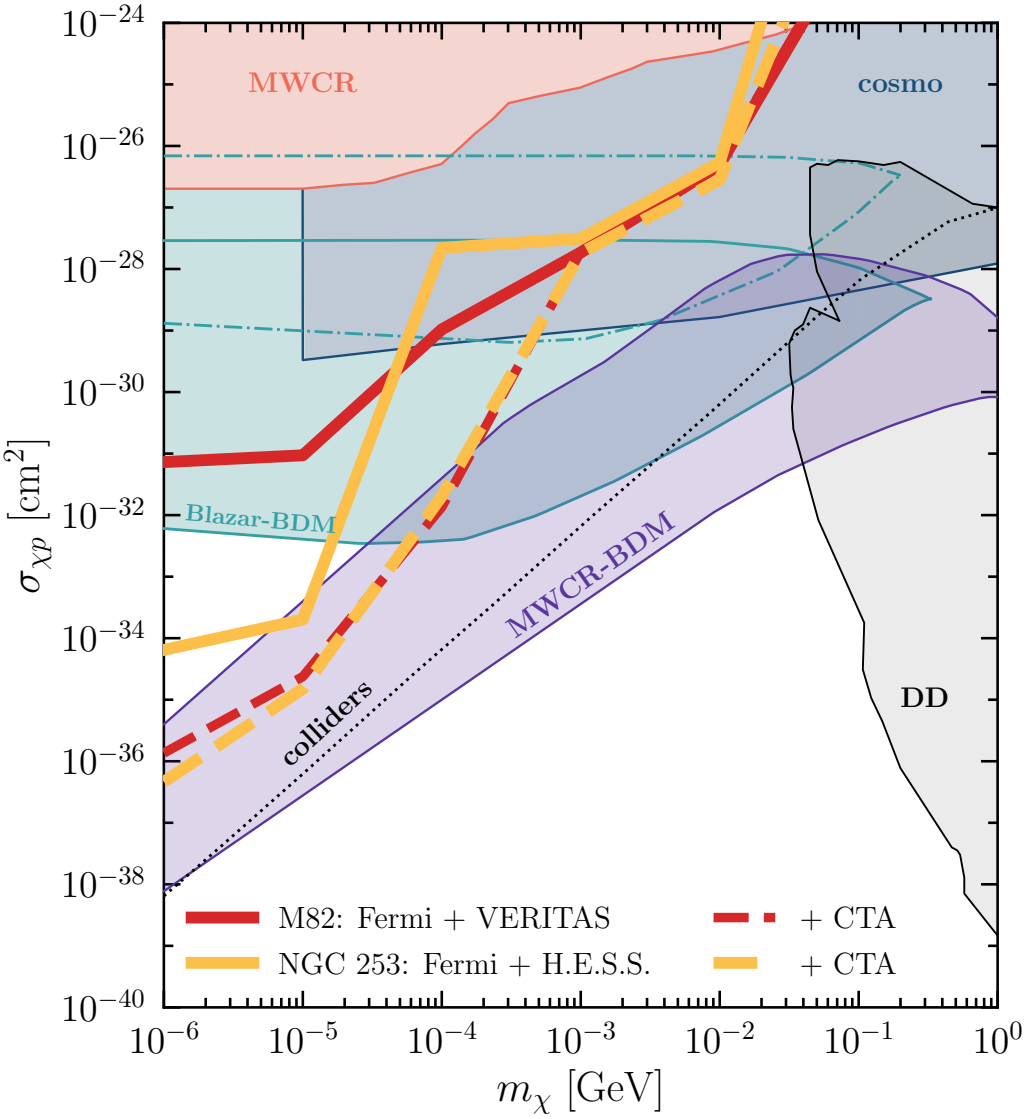

Figure 6.4: Constraints at 5σ on DM-proton cross section placed by means of current (thick solid lines) and future CTA (thick dashed lines) data for M82 (red color) and NGC 253 (yellow color) galaxies. For comparison, the constraints from cosmological observations [213–216], direct-detection experiments [263–273], colliders [219], Milky-Way Cosmic-Rays (MWCR) [220], Boosted Dark Matter from the blazar BL Lac (Blazar-BDM) with MiniBooNE (1) and XENON1T (2) detectors [224] are reported. For the Blazar-BDM limits, the regions delimited by dashed and solid lines correspond to different DM distributions around the BL Lac.

DM spike close to the central black hole. This is first of all impacted by the possibility of DM annihilation in the spike, as shown by Ref. [224]. Furthermore, the steepness of the DM profile in the spike itself is subject of debate [274–278], and these bounds may weaken considerably if the spike is less cuspy. On the other hand, our limits are pretty robust against astrophysical uncertainties, since they only rely on the existence of a CR power-law spectrum in SBNi, which is confirmed by gamma-ray data.

In Fig. 6.4, the region above the dotted line is excluded by trackless jet searches at LHC, as pointed out by Ref. [219]. However, this bound itself should possess a ceiling, since, if the particles interact too strongly, they do not reach the hadronic calorimeter. Since the size of the tracker and electromagnetic calorimeter is of the same order of magnitude as the hadronic calorimeter, we do not expect the collider limits to hold much more than an order of magnitude above the dotted line in Fig. 6.4.

Further, additional constraints could be placed by supernova observations [279–281], though to our knowledge no such bound exists in the literature for DM coupled to nucleons alone.

Finally, we briefly discuss the perspectives offered by neutrino astronomy. Neutrinos are in principle able to probe an energy range even higher than the gamma-ray one, since they travel unimpeded. Therefore, they could provide more stringent bounds in the low-mass region. The possibility of observing starburst galaxies as point sources at neutrino telescopes has been recently studied in Ref. [163]. If the neutrino spectrum from one starburst galaxies is measured with a sufficiently good precision, precious knowledge will be gained on this mass region. We leave this possibility open for a future work. Furthermore, if the primary source of the diffuse neutrino flux is established to be hadronic production in SBNi, the absence of dips in the flux can also be used to constrain the DM-CR cross section. The present large uncertainties on the diffuse energy spectrum, and on the astrophysical origin of these neutrinos, make this possibility interesting only for future perspectives.

6.7 CTA Mock data Generation and Forecast

In this section, we analyze the forecast bounds obtained for the CTA telescope. In particular, we simulate 50 mock data sets under the hypothesis of no DM-CR interactions, making them representative of the variability for future CTA data (due to the fact that the analysis is highly time-consuming, we cannot generate more mock datasets). For each data sample we perform the same statistical analysis detailed in the previous sections and obtain projected bounds. Fig. 6.5 shows the band of the constraints obtained for CTA from all of the data samples; the width of the bands quantifies the variability of the obtained bounds due to the Poisson fluctuations in the detected photons. This variability can reach up to more than an order of magnitude for M82, but stays within less than an order of magnitude for NGC 253. This is due to a larger expected number of events, considering that CTA south is expected to have a higher effective area than CTA north (as already emphasized in the previous chapters).

We also show as black lines reference minimum theoretical bounds, obtained requiring that

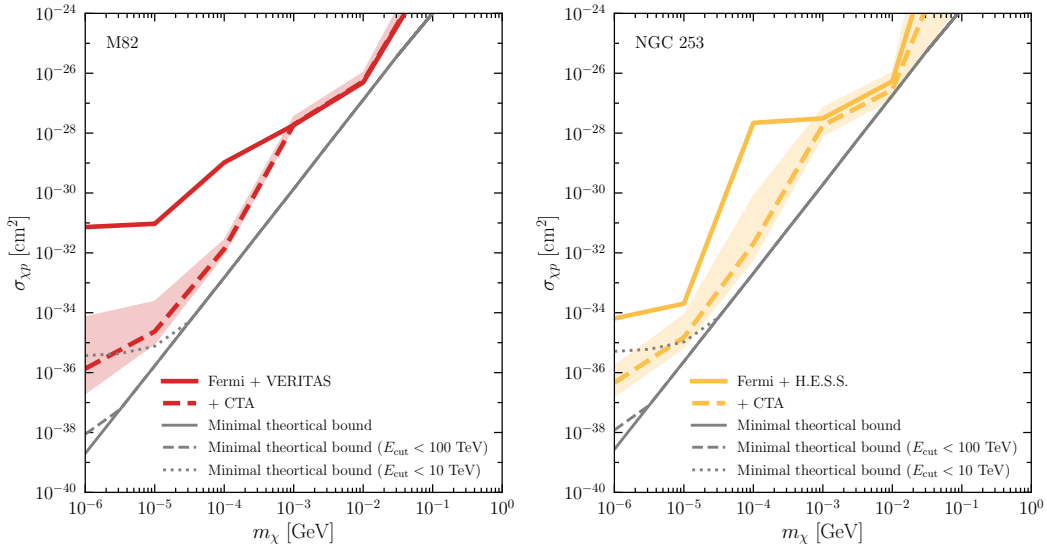

Figure 6.5: Comparison between the current constraints (solid lines) and the future ones (shaded bands) for the CTA telescope [26] in case of M82 (left panel) and NGC 253 (right panel). The dashed lines represent the average bounds imposed through current and CTA mock data. The black lines represent the minimal theoretical bounds reachable through SBN according to Eq. (6.16).

the expected number of DM-CR scatterings in the range below a cut energy $E < E_{\rm cut}$ is larger than 1, namely

$$\min_{E<E_{\rm cut}} \left[\tau_{\chi p}^{\rm el,eff} \left(\frac{1}{\tau_{\rm esc}} + \frac{1}{\tau_{\rm loss}^{\rm eff}} \right) \right] = 1 \,. \tag{6.16}$$

This means that the flux below the cut energy suffers by distortions smaller than 50%, and therefore cannot be constrained. The cut energy is meant to simulate the energy range accessible by gamma-ray experiments; for example, present gamma-ray data for M82 and NGC 253 are known up to a gamma-ray energy of about 1 TeV, which are hadronically produced by protons with energy of about 10 TeV. We show these theoretical bounds for the three choices $E_{\rm cut} =$ 10 TeV, 100 TeV, and arbitrarily large $E_{\rm cut}$. CTA closely approaches the minimum theoretical bound, but this argument shows that there is still space for improvement in the bounds with an increased precision of the experiment in the gamma-ray energy range below 10 TeV. All in all, this clearly demonstrate the potentiality for SBN to be complementary tools to collider for constraining DM particle properties.

6.8 Constraints Dependence on the Dark Matter Profile

In this section, we quantify how the constraints vary along different DM profiles as well as within the uncertainty on the DM halo parameters. Fig. 6.6 shows the constraints bands for M82 (on

the left) and NGC 253 (on the right) in case of the Burkert profile (orange band) and the NFW one (blue band). The bands represent the uncertainty due to the different values for c_{200} and M_{200} within the ranges $[7, 12]$ and $[10^{10}, 10^{12}]$ $M_\odot$, respectively. Under the same values for

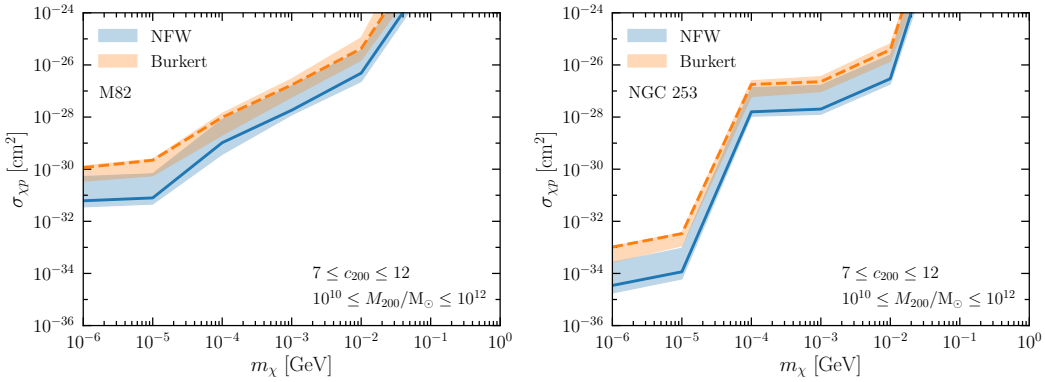

Figure 6.6: Dependence of the current DM constraints on the halo parameters c_{200} and M_{200} for the NFW (blue band) and Burkert (orange band) profiles, in case of M82 (left panel) and NGC 253 (right panel).

(c_{200}, M_{200}), the bounds imposed using a Burkert profile are usually a factor of 20 weaker than the ones with the NFW profile. The dependence of the constraints on the DM halo parameters is also of one order of magnitude. Hence, we can estimate the variability of the bounds combining the uncertainties from the profile and its parameters to be about two orders of magnitude.

6.9 Conclusions

In this chapter, we have studied the phenomenology arising from scattering between high-energy protons and DM particles inside SBNi. Current data can already exclude DM-CR interaction down to $\sigma_{\chi p} \lesssim 10^{-34}\,\mathrm{cm}^2$ for $m_\chi \lesssim 10^{-6}\,\mathrm{GeV}$. We have also obtained projected bounds from the future CTA, showing that it will improve the DM-CR constraints down to $\sigma_{\chi p} \sim 10^{-37} - 10^{-36}\,\mathrm{cm}^2$. Therefore, due to their nature of cosmic-rays reservoirs, starburst galaxies could play a significant role in investigating sub-GeV DM candidates, probing a region in between cosmological and collider bounds.

Chapter 7

Probing Galactic Star-forming Environments: Constraining the Neutrino Emission of Galactic Source Populations

In the previous chapters, we studied the gamma-ray and neutrino emission from Star-forming and Starburst Galaxies and exploited the gamma-ray data to also perform Cosmic-ray transport and beyond standard model studies. In this chapter, on the other hand, we are going to study the capability of current neutrino telescopes to constrain a galactic source populations. The chapter is based on our work published on [282].

7.1 Introduction

Galactic sources such as SNRs are expected to power CRs with energies up to a few PeVs; see *e.g.* Refs. [283–285] for recent reviews. This hypothesis can be indirectly probed by searching for the emission of γ-rays and neutrinos associated with the collisions of CRs with gas in the vicinity of their sources. Indeed, γ-ray observatories have detected a plethora of Galactic γ-ray sources [286–289] as well as extended diffuse emission [290–294], which can be attributed, in part, to the presence of accelerated CRs. However, the interpretation of these observations require a careful modeling of photon absorption processes as well as the inclusion of alternative

production processes involving energetic leptons.

In a recent study [6], the IceCube experiment reported the first observation of high-energy neutrino emission from the Galactic plane (GP) with a significance of $\sim 4.5\sigma$. The result is based on a fit of neutrino emission templates derived from models of CR propagation and interaction in the Milky Way [61, 290]. The templates are characterised by different spectra. The Fermi-LAT π^0 template [290] is characterised by a homogeneous $E^{-2.7}$ spectrum, while the KRA$_\gamma$ model [61] is characterised by an average harder spectrum ($E^{-2.5}$). Nonetheless, The best-fit normalization of the angular-integrated per-flavor neutrino flux is at the level of $E_\nu^2\Phi \simeq 2{\cdot}10^{-8}$ GeVcm^{-2}s^{-1} at a neutrino energy $E_\nu = 100$ TeV and marginally consistent with the different model predictions; see *e.g.* Ref. [61]. Fig. 7.1 summarizes the IceCube's results. In particular, it shows the spectral

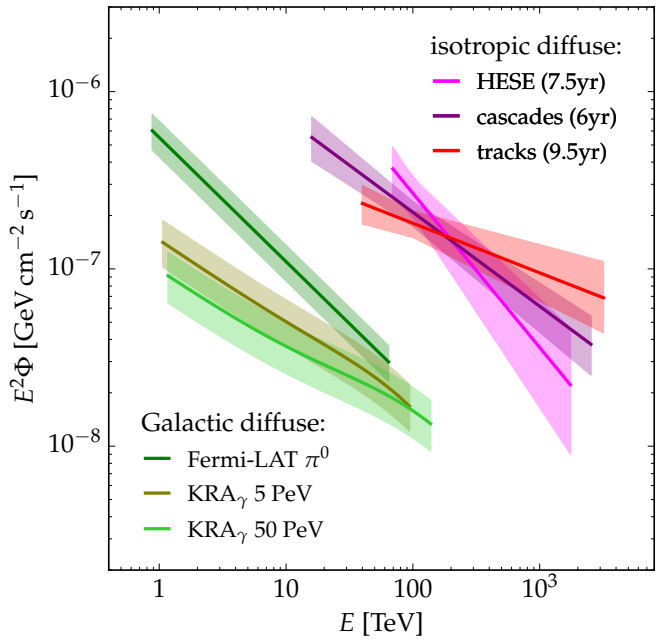

Figure 7.1: Summary of IceCube's observations of isotropic and Galactic diffuse neutrino emission. The plot shows the angular-integrated diffuse flux Φ of isotropic emission (red bands: HESE [5], cascades [295] & tracks [10]) and Galactic emission (green bands: Fermi-LAT π^0 [199] and KRA$_\gamma$ [61, 296]). The spectra are indicated by the best-fit spectrum (solid line) and the 1σ uncertainty range (shaded range).

energy distributions of isotropic diffuse emissions ("HESE" [5], "cascades" [295] and "tracks" [10]) as well as the results of Galactic diffuse emission (Fermi-LAT π^0 [199] and KRA$_\gamma$ [61]). The fluxes are integrated over solid angle for this comparison. The angular-integrated Galactic flux at 100 TeV is at the level of $\sim 10\%$ of the isotropic flux level. However, the Galactic diffuse flux is dominating over the isotropic emission along the Galactic Plane.

An important feature, in order to pint point the origin of the galactic neutrino emission,

it is the analysis of the spatial distribution of the data. Indeed, a true diffuse emission would follow the gas distribution because only those positions would be characterized by neutrino production. On the other hand, quasi-diffuse emission from a galactic source population would be characterised by several luminous spots in the sky very near to the galactic middle plane.

On this regard, the IceCube analysis [6] is based on a selection of cascade events, *i.e.* events with compact Cherenkov-light features following from a cascade of secondary short-ranged particles (see next chapter for more details about the cascade-like neutrino events). Since these events have a relatively high angular uncertainty of typically 7°, the analysis has a limited ability to resolve degree-scale emission from individual neutrino sources.

In this chapter, we study the contribution of unresolved Galactic neutrino sources to the Galactic diffuse flux [297–304]. Analogous to the case of Galactic TeV γ-ray sources [180, 305, 306], the relative contribution of unresolved sources to the Galactic diffuse emission is expected to increase with energy due to the relatively soft emission from CRs in the interstellar medium [61, 297, 300, 301, 303, 307–314]. We present here a novel model-independent formalism that parameterizes the (quasi-)diffuse Galactic emission in terms of the effective source surface density and neutrino luminosity, motivated by previous work on extragalactic neutrino populations, *e.g.* Refs. [315–317]. We show that IceCube's limited discovery potential for individual neutrino sources – in particular for extended Galactic sources – allows a strong contribution of unresolved sources to the Galactic diffuse flux at 100 TeV. The upcoming KM3NeT ARCA [27, 318] and the planned IceCube-Gen2 [319, 320] have the potential to probe this hypothesis; specially from rare Galactic CR PeVatrons, such as hypernova remnants and young massive stellar clusters.

7.2 The Quasi-Diffuse Emission from a Galactic Source Population

Analogously to the diffuse spectrum of SBGs studied in previous chapters, the expected quasi-diffuse (QD) flux of unresolved Galactic neutrino sources depends on their spatial distribution as well as the variability of their emission spectra. For sake of simplicity, we consider that neutrino sources are standard candles with a fixed luminosity following a power-law per-flavor neutrino spectrum $Q_\nu \propto E_\nu^{-\gamma}$ (units of $\mathrm{GeV}^{-1}\,\mathrm{s}^{-1}$) in the TeV-PeV energy range. We leave a spectral index blending and a luminosity distribution for future investigations.

The combined QD flux ϕ_{QD} (units of $\mathrm{GeV}^{-1}\,\mathrm{cm}^{-2}\,\mathrm{s}^{-1}$) from sources situated at distance D

from the Earth along the line of sight $\mathbf{n}(\Omega)$ is then given via the integral:

$$\phi_{\rm QD}(E_\nu, \Omega) = \frac{Q_\nu(E_\nu)}{4\pi} \int_0^\infty dD \rho(\mathbf{r}_\odot + D\mathbf{n}(\Omega)) \,, \tag{7.1}$$

where $\rho(\mathbf{r})$ is the source density and $\mathbf{r}_\odot$ represents the location of the solar system in the GP with distance $r_\odot \simeq 8.5$ kpc to the Galactic Center (GC). Figure 7.2 shows our relative location with respect to the GC, Galactic arms and nearby candidate neutrino sources, including pulsar wind nebulae (PWNe), supernova remnants (SNRs), and young massive stellar clusters (YMSCs).

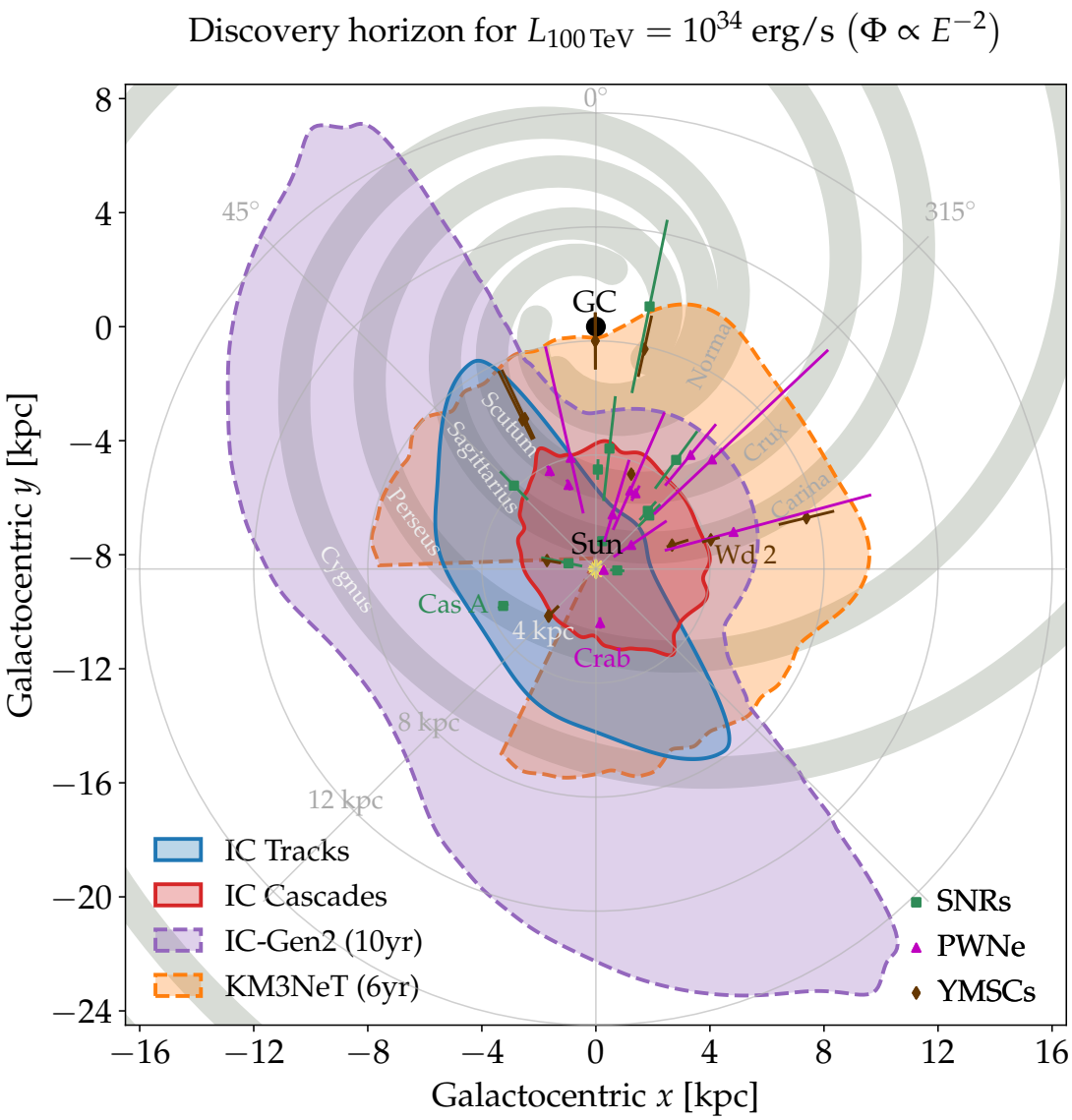

Figure 7.2: IceCube's detection horizon for Galactic neutrino sources with an E^{-2} emission spectrum ("IC Tracks" [321] and "IC Cascades" [6]) and the expected reach of KM3NeT [318] and the proposed IceCube-Gen2 facility [319, 320] assuming a monochromatic neutrino luminosity $L_{100\,\rm TeV} = 10^{34}$ erg/s. We indicate the location of Galactic arms [322] and nearby candidate neutrino sources.

7.2.1 Source Distribution

In order to characterize the galactic source distribution, we take into account several templates. We firstly consider an azimuthally-symmetric distribution of the form $\rho(\mathbf{r}) = \overline{\rho}(r)\exp(-|z|/\lambda)$, where λ represents the vertical half-width of the source distribution and $\overline{\rho}(r)$ the radial distribution at $z = 0$ (z represents the height respect to the galactic plane). The source distribution becomes effectively two-dimensional for large distances ($D \geq \lambda$). For the distribution along the galactic middle plane, we use:

$$\overline{\rho}(r) = \rho_{\odot}\left(\frac{r}{r_{\odot}}\right)^{\alpha} e^{-\beta(r/r_{\odot}-1)}\,, \tag{7.2}$$

where $\rho_{\odot}$ represents the (azimuthally averaged) local density in the solar neighbourhood at a distance $r_{\odot} \simeq 8.5$ kpc from the Galactic center. Our benchmark source distribution follows that of SNRs analyzed in Ref. [323] with best-fit values $\alpha = 1.09$, $\beta = 3.87$ and a vertical scale height $\lambda = 83\,\mathrm{pc}$. We also consider a distribution following the Galactic arm structure, because the sources of neutrino emission might be affected by the denser regions in our galaxy, thereby following its arm structure [180]. As our benchmark model we choose the 4-arm spiral model provided in Ref. [322] with the parametrization:

$$\rho(r,\phi,z) \equiv \overline{\rho}(r)\sum_i w_i \frac{e^{\kappa\cos(\phi-\phi_i(r))}}{I_0(\kappa)} e^{-\frac{z^2}{2\sigma_z^2}}\,, \tag{7.3}$$

where $\phi_i(r) \equiv \ln(r/a_i)/\beta_i$, $R = 2.9$ kpc, $\sigma_z = 0.07$ kpc, $\kappa = 29.1$, and the parameters a_i, β_i and w_i are given in Table 7.1.

Spiral Arm	β_i	a_i	w_i
Sagittarius-Carina	0.242	0.246	0.178
Scutum-Crux	0.279	0.608	0.280
Norma-Cygnus	0.249	0.449	0.357
Perseus	0.240	0.378	0.185

Table 7.1: Parameters of the Galactic spiral arms in Eq. (7.3) based on Ref. [322] with names following the common naming conventions. The relative weights w_i of the arms are normalized so that $\sum_i w_i = 1$.

This model uses a Galactocentric coordinate systems where the Solar system is located at $x_{\odot} = 0$ and $y_{\odot} = 8.5$ kpc for $x \equiv r\cos(\phi)$ and $y \equiv r\sin(\phi)$. Note that the parametrization (7.3) deviates from that of Ref. [322] that uses a Gaussian distributions in azimuthal angle ϕ. Our version (7.3) makes use of normalized von Mises distributions that are approximately Gaussian

in the limit of small widths $\kappa^{-1/2}$. Our normalization of Eq. (7.3) ensures that:

$$\frac{1}{2\pi}\int_0^{2\pi} \mathrm{d}\phi\rho(r,\phi,0) = \rho(r)\,, \tag{7.4}$$

regardless of the width of the Galactic arms. Note that the 4-arm spiral in Eq. (7.3) uses a Galactocentric coordinate system with $x = r\cos(\phi)$ and $y = r\sin(\phi)$ where the location of the Solar System at $x_\odot = 0$ and $y_\odot = 8.5$ kpc. Note that for the visualizations in Figures 7.2 we use a rotated coordinated system so that the Solar System appears at $x_\odot = 0$ and $y_\odot = -8.5$ kpc. Fig. 7.3 shows the 4-arm spiral distribution given by the parametrization of Eq. 7.3. With this

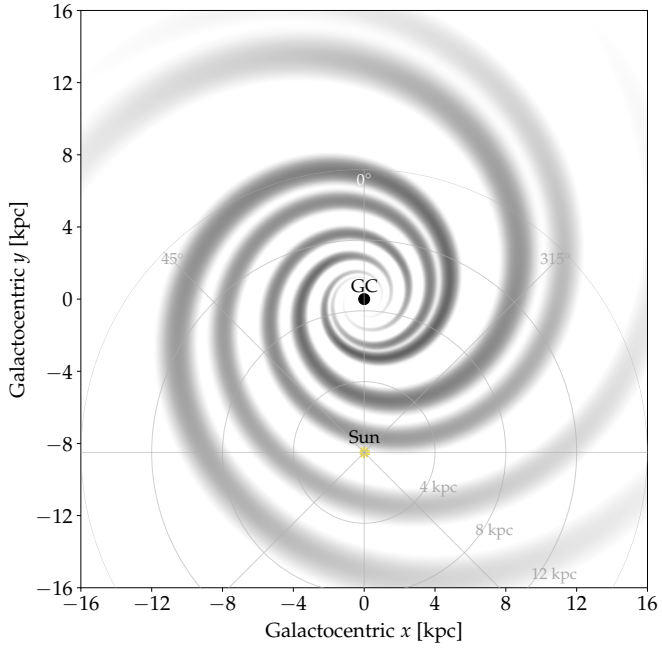

Figure 7.3: The 4-arm spiral parametrization of Eq. (7.3) superimposed over the radial SNR distribution from Ref. [323]. Note that for this visualization we rotated the Galactic coordinate system so that the Solar system appears at $x_\odot = 0$ and $y_\odot = -8.5$ kpc.

formalism, the angular-integrated quasi-diffuse flux can be parametrized as:

$$\Phi_{\rm QD}(E_\nu) \equiv \int d\Omega\phi_{\rm QD}(E_\nu,\Omega) = Q_\nu(E_\nu)\Sigma_\odot\xi_{\rm gal}\,, \tag{7.5}$$

where Ω is the solid angle and we introduced the local source surface density $\Sigma_\odot \equiv 2\lambda\rho(r_\odot)$ and

the dimensionless $\mathcal{O}(1)$ parameter, which we refer as galactic form factor:

$$\xi_{\rm gal} \equiv \frac{1}{4\pi\Sigma_\odot} \int d\Omega \int_0^\infty dD \rho(\mathbf{r}_\odot + D\mathbf{n}(\Omega)) \,. \tag{7.6}$$

where for the azimuthally-independent benchmark, we find $\xi_{\rm gal} \simeq 3$. We have investigated the dependence of our results by varying α and β in Eq. (7.2) within $[0, 2]$ and $[1, 4]$, respectively, for $\lambda = 0.1$ kpc. We find that for this set of parameters the Galactic form factor varies only within $2.6 \lesssim \xi_{\rm gal} \lesssim 4.1$. For the azimuthally-dependent template, we find that the Galactic form factor remains within $1.3 \lesssim \xi_{\rm gal} \lesssim 2.9$, indicating robustness of our results and showing that this formalism is almost indepedent on the template considered.

7.2.2 Difference in the Templates

Before discussing limits on galactic source population, here, we discuss the spatial difference in the templates we use here for this analysis. In particular, Fig. 7.4 shows the different spatial

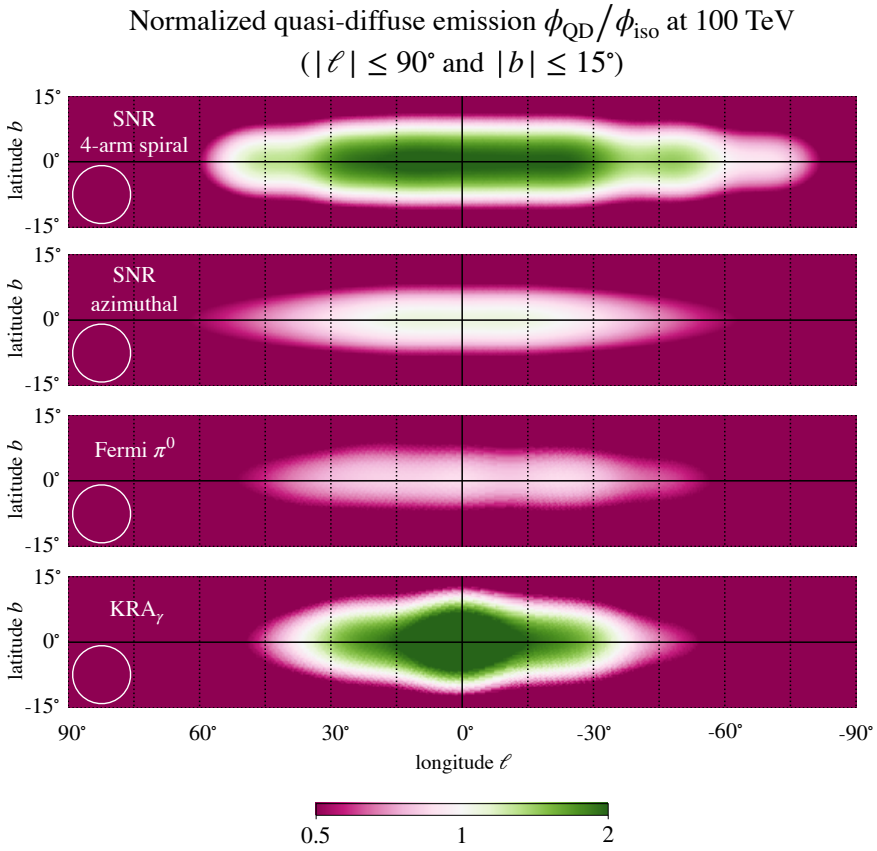

Figure 7.4: Comparison of diffuse and quasi-diffuse emission templates from the inner Galaxy. The template is smoothed over a Gaussian kernel with FWHM= 14° (white circle) corresponding to typical angular resolution of 7° of IceCube's cascade

templates of the diffuse and quasi-diffuse emission templates. The predicted emission templates are smeared out using a Gaussian kernel with full-width half maximum of 14° using `HealPix` tools [324, 325], in order to account for the limited angular resolution of the IceCube analysis [6]. In particular, from top to bottom, the spatial distribution of the Galactic emission (normalised to the isotropic flux level at 100 TeV)) for the 4-spiral arm distribution (Eq. 7.3), the SNR-azimuthal distribution (Eq. 7.2), the Fermi-LAT π^0 template [199], and the KRA_γ template [61]. All these templates predict an enhanced neutrino emission towards the inner galaxy, with some variation in morphology and flux level. As already pointed out in Ref. [6], the similarity of these templates makes the disentanglement of Galactic diffuse models challenging. However, the galactic flux dominates over the isotropic emission along the galactic plane.

7.3 Contribution of Unresolved Sourced to the Diffuse Galactic Emission

Having decided the source distribution, in this section, we study the contribution of unresolved sources with hard emission spectra ($\gamma = 2$) which can contribute significantly to the soft Galactic diffuse spectrum ($\gamma \simeq 2.5 - 2.7$) at the highest energies. As a pivot energy we choose $E_\nu = 100$ TeV where IceCube's best-fit Galactic diffuse flux is at the level of $E_\nu^2 \Phi \simeq 2 \cdot 10^{-8}$ GeVcm^{-2}s^{-1} independent of the Galactic emission models considered in Ref. [6] (see also Fig. 7.1). Fig. 7.5 shows the source populations in terms of the monochromatic neutrino luminosity at 100 TeV defined as:

$$L_{100\,\mathrm{TeV}} \equiv [E_\nu^2 Q_\nu(E_\nu)]_{E_\nu = 100\,\mathrm{TeV}}\,, \tag{7.7}$$

and the local source surface density $\Sigma_\odot$. The green lines show the combinations of $L_{100\,\mathrm{TeV}}$ and $\Sigma_\odot$ that contribute to the observed angular-integrated Galactic neutrino emission at 100 TeV at levels of 1%, 10% and 100%.

The non-observation of individual Galactic neutrino sources by IceCube implies a limit on the Galactic source surface density $\Sigma_\odot$ and luminosity $L_{100\ \mathrm{TeV}}$. We make use of IceCube's discovery potential (DP) Φ_{DP} (units of GeV^{-1} cm^{-2} s^{-1}) for point-like neutrino sources using track [321] and cascade events [6] that strongly depend on neutrino energy E_ν and source declination δ. For a given source luminosity $L_{100\,\mathrm{TeV}}$ these discovery potentials define a declination-dependent

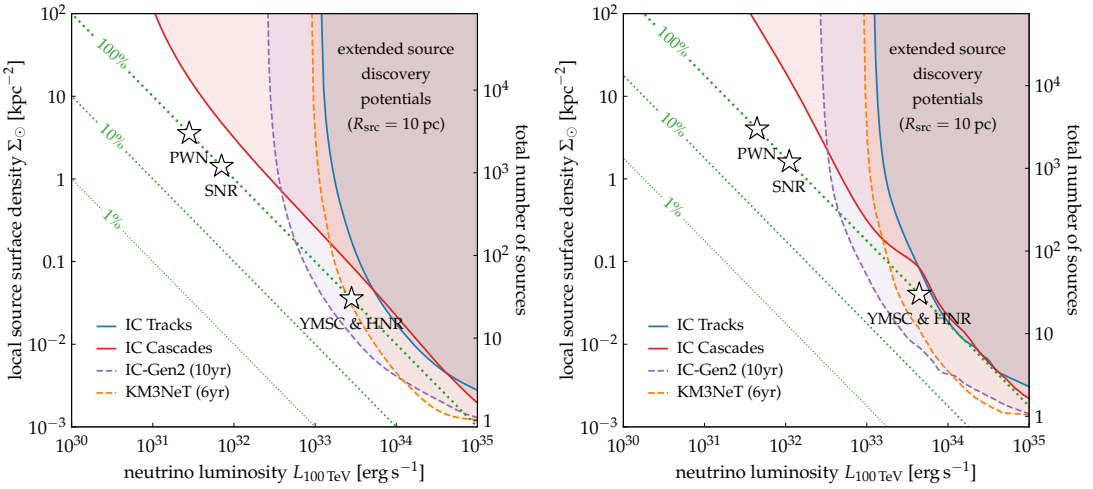

Figure 7.5: The **Left** panel shows the comparison of the Galactic diffuse neutrino emission to the effective local surface density and luminosity of Galactic neutrino source populations for the azimuthally-independent density. The green dashed lines show the contributions in terms of the observed angular-integrated neutrino flux at 100 TeV. The solid contours indicate populations where bright sources with an extension of $R_{\mathrm{src}} = 10$ pc should have been discovered in IceCube's point-source studies ("IC Tracks" [321] and "IC Cascades" [6]). The dashed contours show the expected reach of KM3NeT [318, 326] and the proposed IceCube-Gen2 facility [319, 320]. We also indicate the required luminosity of pulsar wind nebulae (PWNe), supernova remnants (SNRs), hypernovae remnants (HNRs) and young massive star clusters (YMSCs) to saturate the diffuse emission at 100 TeV. The **right** panel shows the same things for the 4-arm distribution.

discovery horizon of the form:

$$D_{\mathrm{max}}(\delta) \equiv \sqrt{\frac{L_{100\,\mathrm{TeV}}}{4\pi[E_\nu^2 \Phi_{\mathrm{DP}}(E_\nu, \delta)]_{E_\nu = 100\,\mathrm{TeV}}}}\,. \tag{7.8}$$

Figure 7.2 shows this horizon for Galactic sources for two IceCube analyses ("IC Tracks" [321] and "IC Cascades" [6]) and a monochromatic neutrino luminosity $L_{100\,\mathrm{TeV}} = 10^{34}$ erg s^{-1} as thick solid contours (this value is set as a benchmark case for visualization purposes. Indeed, the expected neutrino luminosity of unresolved sources is lower; see below for further details.) We also indicate nearby potential neutrino sources from three source classes: SNRs and PWNe from the catalog search of Ref. [6] and a list of nearby YMSCs [327–330] (see below for details). The point-source DP of track events shows a particularly strong dependence on Galactic longitude related to the huge background of atmosheric muons produced by CR interactions above the detector (southern hemisphere). Due to IceCube's location at the South Pole, where the zenith angle θ is degenerate with declination δ as $\theta = \delta + \pi/2$, this background affects the DP for sources in the Northern Sky, including sources in the direction of the GC. In contrast, the point-source DP of cascade events used in the study [6] has a reduced background rate (because of the containment cut which predominantly cut the background of atmospheric muons and neutrinos),

leading to a more uniform coverage in terms of declination. Note that the discovery horizons shown in Fig. 7.2 assume point-like sources and have to be corrected for the enlarged angular extension of nearby sources, as explained in Sec. 4.5. Assuming an (effective) source radius $R_{\rm src}$ and distance $D > R_{\rm src}$, the source angular radius becomes $\sigma_{\rm src} = \sin^{-1}(R_{\rm src}/D)$. We assume then that the DP of extended sources can be approximated as:

$$\Phi_{\rm DP}(E_\nu, \delta, \sigma_{\rm src}) \simeq \sqrt{\frac{\sigma^2_{\rm PSF} + \sigma^2_{\rm src}}{\sigma^2_{\rm PSF}}}\, \Phi_{\rm DP}(E_\nu, \delta)\,, \tag{7.9}$$

where $\sigma_{\rm PSF}$ is the size of the point-spread function (PSF); see *e.g.* Ref. [180]. For definiteness, we assume $\sigma_{\rm PSF} \simeq 0.2^\circ$ ($\sigma_{\rm PSF} \simeq 7^\circ$) for track (cascade) events, as benchmark cases. We emphasize that the angular resolution is dependent on the source declination and neutrino energy, but at 100 TeV, the IceCube median angular resolution is very near to 0.2° as quoted by Ref. [321]. Regarding the cascade angular resolution, we use the ICeCube-quoted value of 7° in [6]. The expected number $N_{\rm obs}$ of observed sources can be written as:

$$N_{\rm obs} = \int d\Omega \int_{R_{\rm src}}^{D_{\rm max}(\delta)} dD D^2 \rho(\mathbf{r}_\odot + D\mathbf{n}(\Omega))\,, \tag{7.10}$$

where $D_{\rm max}(\delta)$ accounts for the scaled DP of Eq. (7.9). So far, no Galactic neutrino point or extended sources have been identified, which implies an upper limit $N_{\rm obs} \lesssim 1$. Figure 7.5 shows the corresponding exclusion limits of neutrino sources using IC tracks (solid blue contour) and IC cascades (solid red contour), for both considered density templates. In particular, the left panel corresponds to the case azimuthally-independent, while the right one reports the 4-arm distribution. For this particular result, we assume that sources have an extension of $R_{\rm src} = 10$ pc (a typical value for a SNR), which significantly degrades the point-source DP of IC tracks.

Interestingly, IceCube's current source DPs are not sufficient to exclude a 100% contribution to the Galactic diffuse flux over a wide range of source surface densities and luminosities. This statement also holds for point-like sources, *e.g.* assuming $\sigma_{\rm src} \ll \sigma_{\rm PSF}$ (see the following sections for details), even though further constrained could be imposed from gamma-ray observations (see for instance [331]), which we leave for future investigations. On this regard, we emphasize that the measured diffuse galactic neutrino flux by IceCube is consistent with the flux level inferred by gamma-ray observatories in the TeV$-$PeV range, such as Tibet and LHAASO [6]. Therefore, even if, at $E_\nu \sim 100\,$TeV, the galactic neutrino flux was dominated by unresolved sources, their neutrino flux would not exceed the corresponding gamma-ray data at those energies.

Figure 7.2 also shows the expected discovery horizon for KM3NeT/ARCA [27] as well as the

planned IceCube-Gen2 [319, 320] for the same benchmark luminosity. For consistency, we assume that these planned detectors have the same $\sim 0.2^\circ$ angular resolution as used for IC tracks in Eq. 7.9. We emphasize that such a value is very near to the expected angular resolution of both detectors at $E_\nu \simeq 100\,\mathrm{TeV}$ [320, 332]. For instance, the expected median KM3NeT angular resolution is $\sim 0.15^\circ$ [332] and the angular resolution of IceCube-Gen2 to be $\lesssim 0.5^\circ$ above 10 TeV.

Using track events, optical Cherenkov telescopes in the Northern Hemisphere are expected to have an enhanced discovery horizon for sources towards the GC. Notably, a recent analysis by ANTARES [333] finds a hint for TeV neutrino emission from the Galactic Ridge, although with weak significance and consistent with earlier upper limits [334]. The expected exclusion contours of KM3NeT and IceCube-Gen2 are shown in Fig. 7.5 as dashed lines. These detectors will be able to probe the contribution of rare but powerful Galactic sources if they dominate ($> 50\%$) the diffuse emission at 100 TeV as long as the source extension is limited to about 10 pc. We notice that the IceCube and IceCube-Gen2 contours in Fig. 7.5 are horizontally separated by a factor 5, consistent with the fact that the IceCube-Gen2 is expected to be five times better than IceCube [319] (see also chapter 4).

It is also important to notice that, in order to be conservative, the KM3NeT DP from Ref. [318] shown in Fig. 7.2 excludes the region $\delta \gtrsim 50^\circ$ which is only visible above the horizon [27, 318]. The reason is due to the fact that the DP has been evaluated only considering upgoing tracks, for which the visibility harshly drops to zero at high declinations [318], leading to a worsening of the DP. However, similar to IceCube, future event selections of KM3NeT (e.g. down-going tracks) are also expected to probe neutrino sources via high-energy track events at high declination angles. Likewise, KM3NeT is also expected to have a good sensitivity and angular resolution to cascade events [27]; see also Ref. [304]. Similarly, IceCube-Gen2 is also expected to improve the detection prospects of Galactic neutrino sources with the inclusions of cascade events as well as by a surface veto for atmospheric background events [319].

7.3.1 Stacking Search and Candidate Neutrino Sources

In Ref. [6], IceCube also searches for the combined neutrino emission from three catalogs of SNRs, PWNe, and unidentified γ-ray sources. Each catalog comprises 12 local γ-ray sources with most promising expectations for neutrino emission under the hypothesis of correlated γ-ray and neutrino production from CR interactions. Assuming an equal weight for each source, the IceCube analysis finds an excess of more than 3σ from each of these catalog; however, as already pointed out in Ref. [6], it is not possible to interpret these results as independent evidence of

neutrino sources due to the spatial overlap with the Galactic diffuse emission templates combined with the limited angular resolution of the cascade data. Tab. 7.2 lists the catalogs of SNRs and PWNe that were analyzed in terms of their combined neutrino emission in Ref. [6]. The table shows the sources ordered by increasing Galactic longitude ℓ and with their estimated distance $D_{\rm min} < D < D_{\rm max}$. For sources with no available distance uncertainties, we estimate the uncertainty from the most probable source location D as $D^{\rm min} = D/2$ and $D^{\rm max} = 2D$, following the approach of Ref. [287]. For sake of completeness, the bottom rows of Tab. 7.2 also list the nearby YMSCs [327–330] shown in Fig. 7.2.

Since the distance of these sources is quite uncertain, we assume a flat prior on the distance, $f(D) = (D_i^{\rm max} - D_i^{\rm min})^{-1}$. Therefore, we can evaluate the flux of a single source as:

$$E^2\Phi = \int_{D_i^{\rm min}}^{D_i^{\rm max}} dD f(D) \frac{L_{100\,\rm TeV}}{4\pi D^2} = \frac{L_{100\,\rm TeV}}{4\pi D_i^{\rm min} D_i^{\rm max}}\,. \tag{7.11}$$

We notice that for sources which have no distance uncertainty, Eq. 7.11 provides just the expression $E^2\Phi = L_{100\,\rm TeV}/4\pi D^2$. Using this approach, the upper limits on the combined emission $\Phi^{90\%\rm UL}$ can be written as

$$L_{100\,\rm TeV} < E^2\Phi_{\rm stack}^{90\%\rm UL} \left[\sum_{i=1}^{N_{\rm cat}} \frac{1}{4\pi D_i^{\rm min} D_i^{\rm max}}\right]^{-1}\,. \tag{7.12}$$

Note that the location of a particular SNR candidate (HESS J1614-518) (see Tab. 7.2) is unkwown. Therefore, we exclude this source in the sum of Eq. 7.12, which provides a conservative upper limit on $L_{100\,\rm TeV}$ for SNRs. We will therefore consider in the following the per-flavor upper limits of IceCube's catalog stacking searches to derive bounds on the monochromatic neutrino luminosity of SNRs and PWNe. At the 90% confidence level, the combined flux is limited to $E_\nu^2\Phi_{\rm stack}^{90\%\rm UL} \simeq 9.0 \cdot 10^{-9}\,\rm GeV\,cm^{-2}\,s^{-1}$ for the SNR catalog and $E_\nu^2\Phi_{\rm stack}^{90\%\rm UL} \simeq 9.5 \cdot 10^{-9}\,\rm GeV\,cm^{-2}\,s^{-1}$ for PWNe. As a result, we obtain limits on the neutrino luminosity of $L_{100\,\rm TeV} < 3.7 \cdot 10^{32}\,\rm erg\,s^{-1}$ for SNRs and $L_{100\,\rm TeV} < 1.2 \cdot 10^{32}\,\rm erg\,s^{-1}$ for PWNe.

In the following, we discuss the astrophysical consequences of our analysis. Let us begin by estimating the expected neutrino flux level provided by diffuse CRs colliding with gas. The energy-loss timescale for hadronic collisions can be written as $\tau_{pp} = \left(k\sigma_{pp} c n_{gas}\right)^{-1} \simeq 50\,\rm Myr\,(n_{gas}/1cm^3)$ (see Eq. A.15 for more details), where we have used $\sigma_{pp} = 4 \cdot 10^{-26}\,\rm cm^2$ for reference and $n_{gas} = 1\,\rm cm^{-3}$ as a gas density (notice that the gas density in the Milky Way is typically $\sim$ two orders of magnitudes lower than the typical ISM density in SBNi). The local

CR density is $E^2 n_{\rm CR}(E) \simeq 7.5 \cdot 10^{-10} (E/{\rm GeV})^{-0.7}\ {\rm GeV\,cm^{-3}}$ for CRs in the GeV-PeV energy region [336]. From $n_{\rm CR}(E)$, we can determine the CR spectrum ($N_{\rm CR}$) (units of ${\rm GeV}^{-1}$) by assuming that they are homogeneously (and predominantly) concentrated along the galactic plane ($|z| \lesssim \lambda = 100\,{\rm pc}$). Therefore, we can write $\Sigma_\odot N_{CR} \simeq 2\lambda n_{CR}$, with $\lambda \simeq 100\,{\rm pc}$. Consequently, the neutrino flux is expected to inherit the soft spectrum of local CRs with $Q_\nu \propto E_\nu^{-2.7}$. Indeed, we can estimate the per-flavour neutrino spectral production rate (units of ${\rm GeV}^{-1}\,{\rm s}^{-1}$) using the multi-messenger relations [3]

$$E_\nu^2 Q_\nu \simeq (1/6)\tau_{\rm pp}^{-1} \Big[E^2 N_{\rm CR} \Big]_{\rm E_{CR}=20E_\nu} \tag{7.13}$$

Considering a pivotal energy of ${\rm E}_\nu = 100\,{\rm TeV}$ (corresponding to ${\rm E_{CR}} = {\rm E}_\nu/0.05 = 2\,{\rm PeV}$), we arrive at $\Sigma_\odot L_{100\,{\rm TeV}} \simeq 4 \cdot 10^{31}\,{\rm erg\,s^{-1}\,kpc^{-2}}$ which yields an angular-integrated diffuse flux of (see Eq. 7.5):

$$E_\nu^2 \Phi_{\rm MW} \simeq 8 \cdot 10^{-9} \left(\frac{\xi_{\rm gal}}{3} \right) \left(\frac{E_\nu}{100\ {\rm TeV}} \right)^{-0.7} \frac{\rm GeV}{\rm cm^2 s}\,. \tag{7.14}$$

This estimate is indeed in the vicinity of the flux level inferred by IceCube (see Fig. 7.1), indicating the strong contribution of Galactic diffuse emission to the signal.

7.3.2 SNRs

QD neutrino emission associated with CR interactions near or within their sources is expected to follow the hard emission spectrum $Q_\nu \propto E_\nu^{-2}$ of freshly accelerated CRs. SNRs have been argued to supply the bulk of Galactic CRs below the CR *knee* [337, 338]. By the end of the Sedov-Taylor phase, a significant energy fraction $\epsilon_{\rm CR}$ of the initial SN ejecta energy of $E_{\rm SN}$ could be transferred to CRs via diffusive shock acceleration (DSA) [339–343]. Considering $N_{\rm CR} \propto E^{-2}$, we can normalize the spectrum:

$$\int_{E_0}^{E_1} E N_{CR}(E) dE = \xi E_{\rm SN} \tag{7.15}$$

therefore the normalization factor is $\chi = 1/ln(E_1/E_0)$. Assuming $E_0 = 1\,{\rm GeV}$ and $E_1 = 1\,{\rm PeV}$, we obtain $\chi \simeq 0.07$ and $E^2 N_{\rm CR} \simeq \xi\chi E_{\rm SN}$. We can estimate the neutrino luminosity using the above-mentioned multi-messenger relation: $L_{100\,{\rm TeV}} \simeq \xi 10^{34} (E_{\rm SN}/10^{51}{\rm erg})\,{\rm erg\,s^{-1}}$. Interestingly, the upper limit (7.12) from the SNR catalog search limits the CR acceleration efficiency to a level of about 5% of the benchmark values for the chosen source parameters. CR

acceleration remains effective until the onset of the radiative phase at time [344]

$$\tau_{\rm RP} \simeq 4 \cdot 10^4\,{\rm yr} \left(\frac{E_{\rm SN}}{10^{51}\,{\rm erg}}\right)^{4/17} \left(\frac{n_{\rm gas}}{1\,{\rm cm}^{-3}}\right)^{-9/17} \tag{7.16}$$

We can then estimate the number of active SNRs from the local SN rate of $R_{\rm SN} \sim 0.03\ {\rm yr}^{-1}$ as $\mathcal{N}_{\rm SNR} \simeq R_{\rm SN} t_{\rm RP} \simeq 1200$ [297], which corresponds to a local surface source density of $\Sigma_\odot \simeq 1.6\ {\rm kpc}^{-2}$. Based on this surface density we can estimate that $L_{100\,\rm TeV} \simeq 6 \cdot 10^{31}\,{\rm erg\,s}^{-1}$ would be sufficient to saturate the diffuse flux, as can be seen in Fig. 7.5. This is consistent with above estimate of the neutrino luminosity for moderate CR acceleration efficiencies. This demonstrate that theoretically SNRs can produce the totality of the measured galactic neutrino flux level. We stress that in this approximated approach the SNRs are way below the calorimetric limit, since the calorimetric fraction can be approximated as $\tau_{\rm RP}/\tau_{pp} \ll 1$. However, it is important to stress that the production of 100 TeV neutrinos is a challenge for the standard DSA theory (see for instance [283–285]), since they should be able to accelerate CR up to PeVs energies. The acceleration conditions are expected to be more favorable for powerful (yet rare) core collapse SNe (hypernovae). In fact, for these sources $E_{SN} \simeq 10^{52}\,{\rm erg}$ [115, 345]. The rate of these hypernovae is $\sim 1 - 2\%$ of the SN rate [346–348] corresponding to about $\mathcal{N}_{\rm HNR} \simeq 30$ active hypernova remnants (HNRs) and a local surface source density of $\Sigma_\odot \simeq 0.04\ {\rm kpc}^{-2}$. The required luminosity to saturate the diffuse flux becomes now $L_{100\,\rm TeV} \simeq 2.5 \cdot 10^{33}\,{\rm erg\,s}^{-1}$ as shown in Fig. 7.5 and consistent with our earlier estimate for moderate CR acceleration efficiencies of a few percent.

7.3.3 PWN

There is a general consensus in ascribing the observed multiwavelength radiation from PWNe to leptonic mechanisms [349]. However, protons could also be extracted from the surface of spinning neutron stars and accelerated up to very high energies [350]. They could then be confined for a long time in a region surrounding the nebula, often referred to as a TeV halo, characterized by reduced diffusion [351]. The total number of γ-ray emitting PWNe in the Galaxy can be estimated from the SN rate $R_{\rm SN}$ and the lifetime $t_{\rm PWN} \lesssim 10^5\,{\rm yr}$ as $\mathcal{N}_{\rm PWN} \simeq R_{\rm SN} t_{\rm PWN} \simeq 3000$ [352], corresponding to a local surface density of $\Sigma_\odot \simeq 3.6\,{\rm kpc}^{-2}$. The corresponding neutrino luminosity required to saturate the diffuse flux becomes $L_{100\,\rm TeV} \simeq 2.8 \cdot 10^{31}\,{\rm erg\,s}^{-1}$ as shown in Fig. 7.5. Considering an initial spin-down power L_0 we estimate the time-integrated CR spectrum as $E^2 N_{\rm CR} \simeq \xi \eta t_{\rm PWN} L_0 \simeq \xi 2 \cdot 10^{50}\,{\rm erg}$ where ξ is the conversion efficiency of spin-down power into

CRs. The neutrino luminosity can now be estimated as $L_{100\mathrm{TeV}} \simeq (1/6) t_{\mathrm{pp}}^{-1} (t_{\mathrm{diff}}/t_{\mathrm{PWN}}) E^2 N_{\mathrm{CR}} \simeq \xi\ 3 \cdot 10^{32} \mathrm{erg\,s^{-1}}$, where we estimate $t_{\mathrm{diff}} \simeq 10^3\,\mathrm{yr}$ as the timescale of diffusive PeV CR escape from the PWN. Therefore, considering high CR acceleration efficiencies, it is feasible that PWNe can contribute substantially to the Galactic diffuse flux.

7.3.4 YMSCs

YMSCs are another class of promising candidate CR PeVatrons [353]. They are often defined as compact stellar aggregates characterized by a cluster mass $\gtrsim 10^4\,\mathrm{M_\odot}$ and a relatively young age $t_{\mathrm{YMSC}} \sim 1 - 10\,\mathrm{Myr}$ [354]. YMSCs can sustain powerful winds of kinetic luminosity $L_{\mathrm{kin}} \sim 10^{38} - 10^{39}\,\mathrm{erg\,s^{-1}}$ where CRs can be efficiently accelerated at the wind termination shock [353]. In addition, SNe can dominate the CR injection power 5−10 Myr after the cluster formation [355]. The local number density of YMSCs can be estimated from the local star formation rate density $\sim 5000\,\mathrm{M_\odot\,Myr^{-1}\,kpc^{-2}}$. Assuming that about 10% of stars end up in bound star clusters and that YMSCs contribute about 10% to the overall star cluster luminosity function (see Ref. [354] for details) it is possible to estimate the YMSC surface density as $\Sigma_\odot \sim 0.02 - 0.2\,\mathrm{kpc^{-2}}$ for which one can expect diffusive shock acceleration at the wind termination shock to be the dominant acceleration mechanism. For $\Sigma_\odot \simeq 0.04\,\mathrm{kpc^{-2}}$, that we also used in our previous estimate for HNRs, we see that the luminosity required to saturate the diffuse flux becomes $L_{100\,\mathrm{TeV}} \simeq 2.5 \cdot 10^{33}\,\mathrm{erg\,s^{-1}}$ as shown in Fig. 7.5. Using this value, we obtain that the total neutrino flux of the YMSC catalogue in Tab. 7.2 is $E_\nu^2 \Phi_{\mathrm{tot}}^{\mathrm{YMSC}} \lesssim 1.6 \cdot 10^{-8}\,\mathrm{GeV\,cm^{-2}\,s^{-1}}$. We can estimate the time-integrated CR spectrum as $E^2 N_{\mathrm{CR}} = \xi \chi t_{\mathrm{YMSC}} L_{\mathrm{kin}} \simeq \xi 2 \cdot 10^{51}$ erg for typical YMSC conditions, by using CR acceleration in the wind termination. The neutrino luminosity can now be estimated as $L_{100\mathrm{TeV}} \simeq (1/6) t_{\mathrm{pp}}^{-1} E^2 N_{\mathrm{CR}} \simeq \xi\ 3 \cdot 10^{34}\ \mathrm{erg\,s^{-1}}$, where we assumed $n_{\mathrm{gas}} \simeq 0.1\,\mathrm{cm^3}$ as the average gas density in the shocked wind region. Also in this case, for high CR acceleration efficiencies, it is possible for YMSC to saturate the diffuse galactic flux level.

7.4 Impact of the Extension of the Sources

In this section, we show the impact of the source extension over the limits on the galactic source population. In fact, in the previous sections, we have considered an extension of $R_{\mathrm{src}} = 10$ pc as a benchmark value to estimate the scaling of point-like discovery potentials for extended Galactic sources. However, the discovery horizon of Galactic sources depends strongly on this assump-

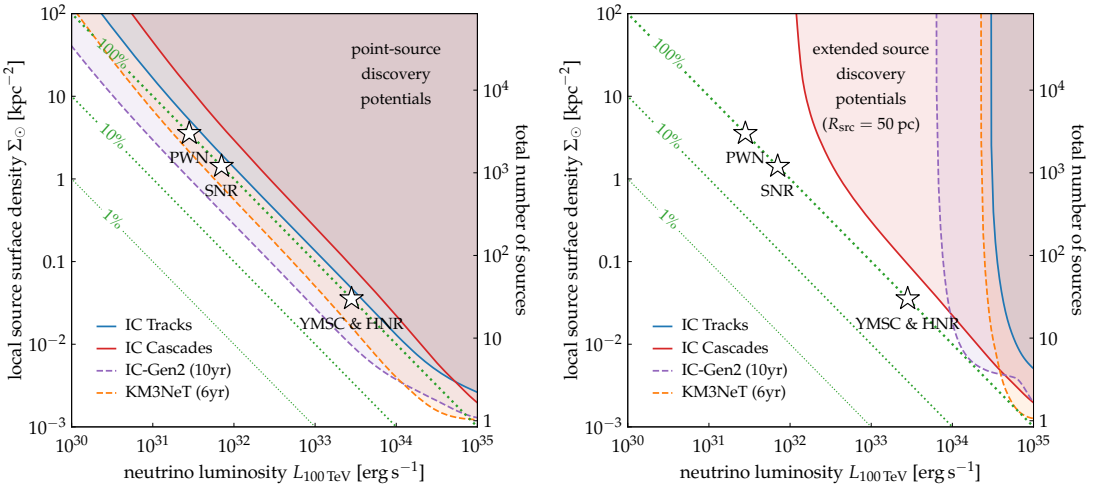

Figure 7.6: Same as Fig. 7.5 but considering the discovery potential for point-like sources (left plot) and for sources with a 50 pc radius (right plot).

tion. As an illustration (here we just consider the azimuthally-independent source distribution), Fig. 7.6 shows the exclusion limits of Galactic populations (as compared to Fig. 7.5) for point-like sources (left panel) and sources with a radius of $R_{\mathrm{src}} = 50$ pc, typical for YMSCs [356] and also an average value for the radius of a Pulsar TeV Halo, which can extend up to $\sim 100\,\mathrm{pc}$ [357]. Indeed, identifying PeVatrons of large extension will be challenging for the upcoming detectors, even though dedicated multi-messengers analyses might improve the discovery prospects. Note that the sources extension is less relevant for cascades-based analyses of Ref. [6] due to the large intrinsic angular uncertainty of event reconstructions in IceCube. We also emphasize that in a more realistic scenario sources will have different sizes and this could impact the limits as well. For instance, if local sources have a reduced radius with respect to sources near the Galactic center, this might well lead limits very near to the point-like case shown in Fig. 7.6.

7.5 Conclusions

In this chapter, we have studied the possible contribution of galactic sources to the galactic diffuse neutrino emission. In particular, we have developed a model-independent formalism to describe the QD emission of different galactic source templates. We have discussed the expected quasi-diffuse flux of unresolved source in a model-independent way by considering the average surface source density and luminosity of Galactic source populations. We have shown that our results are robust against variations of Galactic source distributions along the Galactic plane. We have shown that the combined contribution of the sources can be dominant at 100 TeV, which is

also consistent with the non-observation of individual galactic neutrino source, for the moment. Indeed, due to IceCube's limited angular resolution of cascade events, the spatial morphology of QD emission is practically indistinguishable from diffuse emission from CR interactions in the ISM. Future observations of Galactic neutrino sources will allow us to improve our methods, *e.g.* by modeling sources via their luminosity function and their variability of source spectra. We have also introduced the concept of discovery horizon for individual galactic neutrino sources of high-energy neutrino telescopes. We have utilized the IceCube's point-source DPs for E^{-2} source spectra. We accounted for source extensions by rescaling the PS DPs with the source solid angle, which is a good approximation for background-dominated data. However, we emphasize that realistic source spectra might be characterised by breaks or cutoffs at 100 TeV (due to the limited maximal energy reachable by CRs). Only dedicated analysis (by IceCube) will be able to provide us with more realistic discovery horizons.

Despite all of this, even in the most optimistic conditions of unbroken power-law emission and negligible source extension, IceCube's discovery horizon for Galactic sources is presently insufficient to exclude a dominant QD emission of Galactic sources at 100 TeV (see Fig. 7.6). This scenario might also be constrained by gamma-ray data, but we will explore additional constraints arising from a combined analysis of gamma-ray and neutrino data in future studies.

We have also estimated the prospects for the upcoming KM3NeT/ARCA [27] detector and the planned IceCube-Gen2 to probe galactic QD emission. We have found that for fiducial source radius of 10 pc, the most promising targets for future studies are HNRs and YMSCs. We have also found that it will be hard to discover spatially- bigger pevatrons due to the worsening of the DPs for the extension (see also [304] for other details), although KM3NeT/ARCA is expected to have a good DP for neutrino-cascade events which are expected to be less dependent of the source sizes due to an intrinsic greater angular uncertainty [27] (see [304] for details about searches of galactic pevatrons using neutrino-cascade events).

SNR Catalog of Ref. [6]

Source name	ℓ [°]	$D^{\min}$ [kpc]	$D^{\max}$ [kpc]
HESS J1912+101	44.5	3.4	4.8
Gamma Cygni	78.2	0.49	1.96
Cassiopeia A	111.7	3.3	3.7
Vela Junior	266.2	0.5	1
RCW 86	315.1	2.1	3.2
HESS J1457-593	318.2	2.3	3.17
SNR G323.7-01.0	323.6	3.5	6
HESS J1614-518	331.5	-	-
RX J1713.7-3946	347.3	0.9	1.1
CTB 37A	348.4	6.3	12.5
HESS J1731-347	353.5	2.4	6.1
HESS J1745-303	358.8	3.13	3.85

PWN Catalog of Ref. [6]

Source name	ℓ [°]	$D^{\min}$ [kpc]	$D^{\max}$ [kpc]
HESS J1813-178	12.8	2	8
HESS J1825-137	18.0	2.9	3.3
HESS J1837-069	25.2	3.6	4
Crab nebula	184.5	1.7	2.1
Vela X	263.3	0.25	0.3
HESS J1026-582	285.1	2.5	10
HESS J1303-631	304.2	0.75	3
Kookaburra	313.3	2.8	11.2
MSH 15-52	320.3	3.8	6.6
HESS J1616-508	332.3	2.7	3.3
HESS J1632-478	336.3	1.5	6
HESS J1708-443	343.1	1	4

List of YMSCs shown in Fig. 7.2

Source name	ℓ [°]	$D^{\min}$ [kpc]	$D^{\max}$ [kpc]
Arches	0.1	7	9
Quintuplet	0.2	7	9
RSGC01	25.3	5.05	7.73
RSGC02	26.2	5.05	7.74
Cygnus OB2	80.2	1.24	1.94
h Per (NGC 869)	134.6	1.84	2.44
χ Per (NGC 884)	135.0	1.84	2.44
NGC 3603	283.7	6.6	8.6
Westerlund 2	284.3	3.84	4.48
Trumpler 14	287.4	2.6	3.4
Westerlund 1	339.6	3.54	3.72
DBS2003 179	347.6	6.9	9.1

Table 7.2: List of SNRs and PWNe studied in Ref. [6] in ascending Galactic longitude ℓ. The distance range is taken from Ref. [335]. For sources where only an approximate distance D is provided, we follow the approach of Ref. [287] with $D^{\min} = D/2$ and $D^{\max} = 2D$. Also listed are nearby YMSCs [327–330] indicated in Fig. 7.2.

Chapter 8

Details on the Cherenkov Neutrino Telescopes

In this chapter, we discuss details about the neutrino interactions and telescopes in order to clarify details used in the previous chapters which are especially discuss in the following one.

8.1 Neutrino Interactions

Neutrinos only interact with matter through the weak interaction. Indeed, the neutrino ν_{l} (of a given flavour l) interaction with a target nucleon N are (see [358, 359] for details)

$$\begin{aligned} \text{CC: } \nu_{\mathrm{l}} + \mathrm{N} &\xrightarrow{\mathrm{W}^{\pm}} \mathrm{l} + \mathrm{X} \\ \text{NC: } \nu_{\mathrm{l}} + \mathrm{N} &\xrightarrow{\mathrm{Z}^{0}} \nu_{\mathrm{l}} + \mathrm{X} \end{aligned} \tag{8.1}$$

where l is the corresponding lepton to the neutrino flavour (electron, muon, tau) and X represents the hadronic cascade resulting after the interaction. The difference between the interaction is that the first one is mediated by the boson $\mathrm{W}^{\pm}$ and the second one by Z^{0}. Interactions mediated by $\mathrm{W}^{\pm}$ are also referred as charged-current CC interactions, while the the interactions mediated by Z^{0} are also called neutral-charged interactions [358]. For example, at very high energies ($10^{16}\,\mathrm{eV} \lesssim \mathrm{E}_{\nu} \lesssim 10^{21}\,\mathrm{eV}$), the cross-sections can be approximated by (see [360] for more details)

$$\sigma^{\mathrm{CC}}_{\nu\,\mathrm{N}} = 5.53 \cdot 10^{-36} \left(\frac{E_{\nu}}{1\,\mathrm{GeV}} \right)^{\alpha} \tag{8.2}$$

and

$$\sigma^{\mathrm{NC}}_{\nu\,\mathrm{N}} = 2.31 \cdot 10^{-36} \left(\frac{E_\nu}{1\,\mathrm{GeV}} \right)^{\alpha} \tag{8.3}$$

with $\alpha \simeq 0.363$ [360]. Even though Eqs.8.2 and 8.3 do not represent the νN cross section on the total energy range, they show that CC interactions are more probable than NC [358]. As we will see below, the different interaction channels lead to different kind of hadronic showers, consequently leading to different observable topologies in the events recorded by a neutrino telescope.

8.2 Cherenkov Light

The hadronic shower produced because of the interaction between nucleons and neutrinos mostly release relativistic particles, which are able to induce Cherenkov radiation into the material [358] (see also [361] for further details). When a charged particle passes through a material with a velocity $v > c/n$, where c/n is the light velocity in the medium (n is the refractive index of the medium), it polarises the medium, producing a dipole momentum along its trajectory [358]. The medium reacts by emitting electrons in order to restore equilibrium and therefore emit photons, the so called Cherenkov photons, coherently and with fronts in a specific directions forming a cone angle with the lepton initial direction of motion [358]

$$\cos(\theta_{\mathrm{C}}) = \frac{1}{\beta \mathrm{n}} \tag{8.4}$$

where $\beta = v/c$. For relativistic particles $\beta \simeq 1$, $\theta_{\mathrm{C}} = 42.7°$ for sea water ($n = 1.36$) and $\theta_{\mathrm{C}} = 40.7°$ for ice ($n = 1.32$) (the refractive index refers to the visible light wavelengths, where these materials are transparent to light) [358]. The number of photon emitted by the material per unit of particle travelled length x and wavelength λ is [358]

$$\frac{d^2N}{dxd\lambda} = \frac{2\pi\alpha Z^2}{\lambda^2}\left(1 - \frac{1}{\beta^2 n^2(\lambda)}\right) \simeq \frac{2\pi\alpha Z^2}{\lambda^2}\left(1 - \frac{1}{n^2(\lambda)}\right) \tag{8.5}$$

where α is the fine-structure constant, Z is the charge of the particle and the last passage of Eq. 8.5 holds in the ultra-relativistic regime $\beta \simeq 1$. Eq. 8.5 demonstrates that radiation with lower wavelengths are mostly emitted. Therefore, neutrino telescopes are constructed to be especially sensitive to the blue and UV light [358].

8.3 Light Propagation in the Medium

When the Cherenkov light propagates through the medium, it gets absorbed and scattered by it [358, 359]. This sets quantitative upper limit on the distance between optical sensors of a neutrino telescope[359]. From a quantitative point of view, we can define the absorption coefficient $\mathrm{a}(\lambda)$, the scattering coefficient $\mathrm{b}(\lambda)$ and also the attenuation coefficient $\mathrm{c}(\lambda) = \mathrm{a}(\lambda) + \mathrm{b}(\lambda)$[358]. The light intensity propagating through the medium (in general ice or water) is [358, 359]

$$\mathrm{I_i(x,\lambda) = I_0(\lambda)(\lambda)e^{-x/L_i(\lambda)}} \tag{8.6}$$

where x is the length of the path of the light in the medium, i runs over absorption, scattering and attenuation and the $L_i(\lambda)$ represents the corresponding lenght defined as $(\mathrm{L_a}(\lambda) = \mathrm{a^{-1}}(\lambda), \mathrm{L_b}(\lambda) = \mathrm{b^{-1}}(\lambda), \mathrm{L_c}(\lambda) = \mathrm{c^{-1}}(\lambda))$ [358]. From these definitions, we can see that [359]

$$\frac{1}{\mathrm{L_c}(\lambda)} = \frac{1}{\mathrm{L_a}(\lambda)} + \frac{1}{\mathrm{L_b}(\lambda)} \tag{8.7}$$

Another important quantity is the effective scattering length, which takes into account the scattering angle between the initial direction of light and the scattered light [358]:

$$\mathrm{L_b^{eff}}(\lambda) \simeq \frac{\mathrm{L_b}(\lambda)}{1 - < \cos(\theta) >} \tag{8.8}$$

where $< \cos(\theta) >$ is the average scattering angle cosine. For $350\,\mathrm{nm} \lesssim \lambda \lesssim 550\,\mathrm{nm}$, $\mathrm{L_b}(\lambda) \simeq 100\,\mathrm{m}$ and $\mathrm{L_b}(\lambda) \simeq 70\,\mathrm{m}$ respectively for polar ice and sea water [359]. This means that under the same instrumented volume, the effective volume of a telescope would be higher in the ice, because photons travel longer distances before getting absorbed [358]. By contrast, the effective scattering length is higher in ice than in sea water, leading to a greater degradation in the angular resolution in ice [358].

8.4 Event Topology for a Neutrino Telescope

As mentioned above, different neutrino interactions lead to different topology in the events observable by neutrino telescopes. They are in general divided in several categories [358, 359]:

- Track-like events
- Cascade or Shower events

- Double-bang events

Track-like or simply tracks events are mostly generated by ν_μ in CC interactions [358]. In fact, the outgoing muon produced by the interaction might propagate for several meters, depending on the energy (few meters for $E_\nu \sim 1\,\text{GeV}$ and kilometers for $E_\nu \gtrsim 1\,\text{TeV}$ [358]), producing a long track in the detector before decaying in electrons [358]. This event topology is particularly important when it comes to detecting point-like astrophysical neutrino sources, since the track generally allows for a good reconstruction of the muon direction and, consequently, the direction of the parent neutrino [358]. Indeed, the angle between the initial neutrino direction and the muon direction is given by [358, 359] (see also [362] for other details)

$$\theta_{\mu\nu} \leq \frac{0.6^\circ}{\sqrt{\frac{E_\nu}{1\,\text{TeV}}}} \tag{8.9}$$

Eq. 8.9 is fundamental for a neutrino telescope, since it shows that neutrinos can be traced back by muons. Furthermore, since neutrinos are not electrically charged, they trace back to the source which has emitted it [362]. This is also the same concept used for photons in *conventional* astronomy. On the other hand, since muons propagate for long distances, only a small fraction releases its energy in the detector, leading to a very poor energy resolution for the track channel.

Since at the ground level, the atmospheric muon flux exceed the flux of atmospheric neutrinos by a factor of 10^{11}, neutrino telescopes are deployed underwater or under-ice in order to harshly reduce the contamination of atmospheric muons (see next chapter for further details about this) [359]. Nonetheless, this is not sufficient to suppress all the muons. Indeed, their flux exceed the atmospheric muon flux induced by atmospheric neutrinos by 5 order of magnitudes even at 3000 m of depth [359]. As a result, the technique used to further reduce their contamination is using the Earth as a shield for muons, taking into account only the upgoing events [27, 318, 359]. The upgoing events– events which comes from below the detector– are the ones moving upward in the orientation of the detector [359], so in practice, they are the events which has to pass through the Earth before arriving into the detector; thereby, they have a higher probability of interactions with particles before reaching it. This makes sure that most of the muons observed at the detector are given by neutrino interactions. However, as we will see below, many down-going muons are mis-reconstructed as up-going, leading to a contamination in the track event sample. Cascade or shower events are generated by the hadronic and electromagnetic showers of particle which emit an almost spherical short-range light pattern [358]. They are produced by all-flavour neutrinos in NC interactions as well as by electron neutrinos in CC interactions.

For instance, when a neutrino interact via NC interactions, they produce an hadronic shower which is characterised by a small-range particle and a sizeable part of the parent neutrino energy is deposited into the detector [358]. The point is that the outgoing neutrino (produced after the interaction of the incoming neutrino)carry itself a part of the in-going energy making it hard to estimate it in this channel [358]. By contrast, when an electron neutrino interact via CC interaction, both an hadronic and electromagnetic cascades are produced. In fact, electrons release their energy through bremsstrahlung at the interaction vertex and the two showers allow for a very good reconstruction of the neutrino energy. However, the showers, since they have a few meters of extension, do not allow for a good reconstruction of the initial neutrino direction, leading to a harsh angular resolution [358] (see [362] and Refs. therein for further details). For this reason, the cascade channel is useful in order to study the diffuse emission of sources, where it is not crucial to discriminate the direction of astrophysical neutrino sources. In fact, as we will see better in the next chapter, the way in order to overcome the background issue, is to use the contained events, namely the events which interaction within the instrumented volume of the detector. This eliminates most of the background, preserving most of the good-quality showers events. Double-bang events are the ones generated by ν_τ via CC interactions. In particular, the τ lepton produced decay right after the interaction producing an electron or muon (with a branching ratio BR = 35%) and into hadrons (with a branching ratio BR = 65%). In case of production of a muon, a track is observed; otherwise a cascade is observed [358]. In particular, for energies $2\,\mathrm{PeV} \lesssim \mathrm{E}_\nu \lesssim 20\,\mathrm{PeV}$ of the primary neutrino, both cascades are observable and these events are called double-bangs [358]. In other energy ranges, the probability of observing the second cascade is very low and in general these events are called lollipops [358].

8.5 The KM3NeT Project

The KM3-scale Neutrino Telescope [27, 358] or simply the KM3NeT project is a research infrastructure which will feature the next generation of Cherenkov Neutrino telescope in the Mediterranean sea. It will be constituted of two neutrino telescopes: **ORCA** (Oscillation Research with Cosmic in the Abyss) [27, 358, 359] is designed in order to probe fundamental neutrino physics such as oscillation neutrino parameters and neutrino mass hierarchy, studying astrophysical and atmospheric neutrinos with energies $1\,\mathrm{MeV} \lesssim \mathrm{E}_\nu \lesssim 100\,\mathrm{GeV}$ [27]. Its location is $42°48'\,\mathrm{N}\,06°02'\,\mathrm{E}$, namely about 40 Km offshore from Toulon (France), at a depth $\sim 2500\,\mathrm{m}$ [27]. **ARCA** (Astroparticle Research with Cosmic in the Abyss [27, 358, 359]) is designed in order to probe high-energy neutrinos from $100\,\mathrm{GeV} \lesssim \mathrm{E}_\nu \lesssim 100\,\mathrm{PeV}$. It is currently under construction

at the location $36°16'\,\mathrm{N}\,16°06'\,\mathrm{E}$, at $\sim 100\,\mathrm{Km}$ offshore Sicily (Porto Palo di Capo Passero) at a depth of $\sim 3500\,\mathrm{m}$ [27]. The detector will consist of arrays of Digital Optical Modules (DOMs), which are pressure-resistant spheres, containing 31 PMTs with 3-inch photocatode diameter [27, 359]. The DOMs are being arranged in detection units (DUs), vertical strings anchored on the sea floor. Each DU consists of 18 DOMs [27, 358, 359]. Even though, the physics target is different, both ARCA and ORCA will share the same technology. The main difference will be the spatial configuration of the detectors: the horizontal distance between each DU will be 90 m for ARCA and 20 m for ORCA, the vertical distance between each DOM will be 36 m for ARCA and 9 m for ORCA. Finally, the lowest DOM will be 70 m above the seabed for ARCA and 30 m for ORCA (see [27] for details). At the time of writing, there are 21 lines taking data for ARCA and 18 for ORCA, already working and taking actual data.

8.6 Building Blocks

The KM3NeT detectors can be visualised as three dimensional arrays of DUs (or simply strings) [359]. These arrays are also denominated as building blocks. When completed, ARCA will be constituted of two building blocks, while ORCA by only one [27]. The main parameters which describe the array and modify the properties of the detector are: *1)* the number of strings, *2)* the vertical distance between DOMs, *3)* the horizontal distance between strings, it 4) the number of DOMs for each string [359]. Here, focusing only on the KM3NeT/ARCA detector, we report, following Ref. [359], a simulation study on the number of neutrino events expected from the galactic source SNR RXJ1713.7-3943 has been carried out for several values of the water absorption length [363] (see also [359]). In particular, Fig. 8.1 shows the number of expected events for 1 year of data taking from RXJ1713.7-3943 as a function of the number of strings, on the left, and of the number of DOMs, on the right. Furthermore, the color scheme corresponds to different scaling factors applied to the absorption length of seawater [363].

Fig. 8.1 also demonstrates that the optimum configuration is obtained for $\sim$ 115 strings and $\sim$ 18 DOM for each string, confirming the number reported in the previous section [363]. Therefore, the definition of building block is the minimal detector configuration which maximize the efficiency [359].

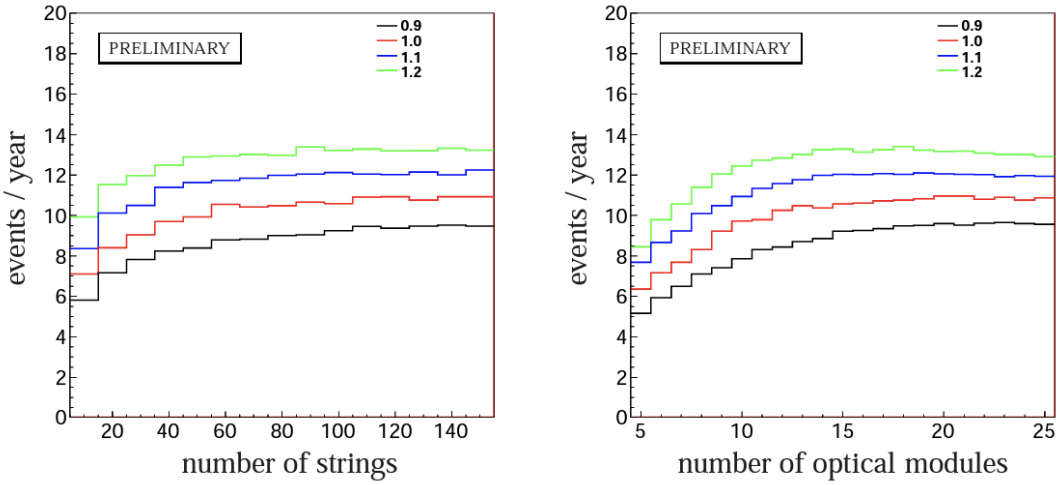

Figure 8.1: **Left**: The expected rate of signal events from the RXJ1713.7-3943 source as a function of the number of strings (DUs). **Left**: The expected rate of signal events from the RXJ1713.7-3943 source as a function of the number of the DOMs. For both images, the color scheme corresponds to different scaling factors applied to the absorption length of seawater [363]. Images taken from the open-access Ref. [363]. These images have been also shown by Ref. [359].

8.7 Background Characterization

One of the aim for a neutrino detector is to discover an excess of astrophysical neutrino events over the background events. The background events for an optical neutrino telescope is comprised by background light produced by natural radioactivity as well as byproducts of interactions of CRs with the Earth atmosphere [27, 359].

8.7.1 Natural Radioactivity

Natural radioactivity can be presented in the sea. Indeed, there could be emission of Cherenkov light produced by the propagation of charged particles after the decay particular elements in the water [359]. The most abundant element is ^{40}K, which predominantly (Branching ratio $\simeq 89\%$) decays into [359]:

$$^{40}K \rightarrow {}^{40}Ca + e^{-} + \bar{\nu}_{e^-} \tag{8.10}$$

the energy of the electrons produced by the reaction 8.10 is sufficient to produce Cherenkov light in the sea water [359]. Another reaction for ^{40}K is given by the electron capture phenomenon (branching ratio $\simeq 11\%$) [359]:

$$^{40}K + e^{-} \rightarrow {}^{40}Ar + \nu_e + \gamma \tag{8.11}$$

The photon produced has a energy distribution peaking at $E_\gamma \simeq 1.46\,\mathrm{MeV}$, thereby it might induce the production of electrons (due to Compton scattering) above the threshold to produce Cherenkov light inside the water [359]. Another source of background is the light emitted by biological organisms inside the water (also called bio-luminescence) [359]. The contribution given by bio luminescence light can be divided in two categories [359]:

- Contribution from small bacteria: duration of days
- Contribution from large-size organisms: burst activity of duration $\sim 1\,\mathrm{s}$

The first category produce a steady and almost homogeneous rate for the photomultiplier count [359]. On the other hand, the contribution from larger organisms are expected to be spatially localized as well as have a smaller time duration, although they are expected to provide a higher contribution to the background rate [359]. Therefore, the two components due to the bio luminescence produce two different impact in the data taking. In order to quantitatively assess the presence of organisms able to produce bioluminiscence, several experiments have been conducted several in situ. In particular, sea water has been retrieved for different values of depth at Capo Passero (KM3NeT/ARCA construction site). Below $\simeq 2500\,\mathrm{m}$, no luminescent bacteria have been found [359].

8.7.2 Physical Background

The main component to the physical background of a Cherenkov neutrino telescope is given by the byproducts of the interactions between CRs with the Earth atmosphere. Indeed, as analyzed in the previous chapters, when a proton interact with matter, they produce many particles, such as pions and kaons, which in turn decay in neutrinos. Therefore, these interactions, extended air showers, are bound to produce an overwhelming background of neutrinos, also called atmospheric neutrinos [27, 318, 359, 364]. The atmospheric neutrino flux is usually divided in two components: the conventional component and the prompt one [365]. The conventional component is given by the neutrinos produced by the consequent decays of pions π and kaons K, in a similar way as analysed for the SBG neutrino component in the previous chapters. On the other hand, the prompt component is given by neutrinos produced by the decay of heavy hadrons [365]. This component is mainly given by the decay of charmed heavy mesons [365, 366]. This component is dominant at high energies, since the decay length for π, K becomes effectively lower than their path length in the atmosphere [366]. As a consequence, the contribution of the decay short-lived hadrons becomes evident [366]. The conventional component is calculated according to Ref.

[367]. The prompt component is modelled through Ref. [366]. For both fluxes, we apply a knee correction [368] (see also [326] for further details). In general, the expected atmospheric flux behaves as a power-law flux with a very soft spectral index $\gamma \sim 3.7$ [367]. Therefore, testing the hypothesis of an astrophysical neutrino signal above an atmospheric neutrino background generally exploits that the signal consists of an harder spectrum ($\gamma \sim 2 - 2.2$) [27, 318, 326]. Another crucial component to the background events is given by atmospheric muons. In fact, in extended air showers, muons are mostly producing collimated, hence forming the so called muon bundles [318]. These muons are expected to arrive almost simultaneously, with a very small spread time $\sim$ 1 ns [369]. We simulate atmospheric muons through MUPAGE [369, 370], which parameterizes the expected muon flux underwater as a function of the distance to the shower [369]. As we emphasized above, the background of atmospheric muon is rejected through the Earth shielding. However, many muons get reconstructed as upgoing even though down-going, mimicking neutrino interactions [369]. This process of mis-reconstruction impacts at least $\sim 40\%$ of down-going muons [369].

8.8 KM3NeT Monte Carlo Simulation Pipeline

Monte Carlo (MC) simulations are tools used in order to quantify the properties of a neutrino detector. In this section, we outline the simulation pipeline used for the KM3NeT detector which is also employed in the next chapter to evaluate its quasi-differential sensitivity. The simulation are carried out assuming the nominal geometry expected from the two ARCA building blocks (BBs) (see [27] for other details about the detector geometry). Furthermore, simulations consider the two BBs as independent. Therefore, simulations are performed on KM3NeT/ARCA 115 and then the number of events is simply multiplied by 2 [27]. The first step of the simulations is to generate each particle which could generate an observable signature in the detector. Then, it is important to simulate the interaction between the particles and the medium, and consequently, simulate the Cherenkov light propagation in the seawater, the produced signal, . Finally, the detector response is calculated, trigger and event reconstruction. See [27, 358, 359, 371] for more details. In this section, we outline the simulation tools and pipeline used in the KM3NeT Collaboration and which we are going to use in the next chapter in order to evaluate its sensitivity.

8.8.1 Event Generation

In this section, we describe the event generation in the simulation pipeline. Firstly, we are going to describe the neutrino event generation and then we turn to the atmospheric muon generation.

Neutrino Generation

In order to fully generate neutrino events, we start from their direction, the energy and the position [371]. In order to do this, the detector active volume is modelled as a cylinder surrounding the instrumented volume [27, 358, 359, 371]. This cylinder is also referred as *can* and it can be visualized in Fig. 8.2. In particular, the *can* is represented as a yellow cylinder anchored to the

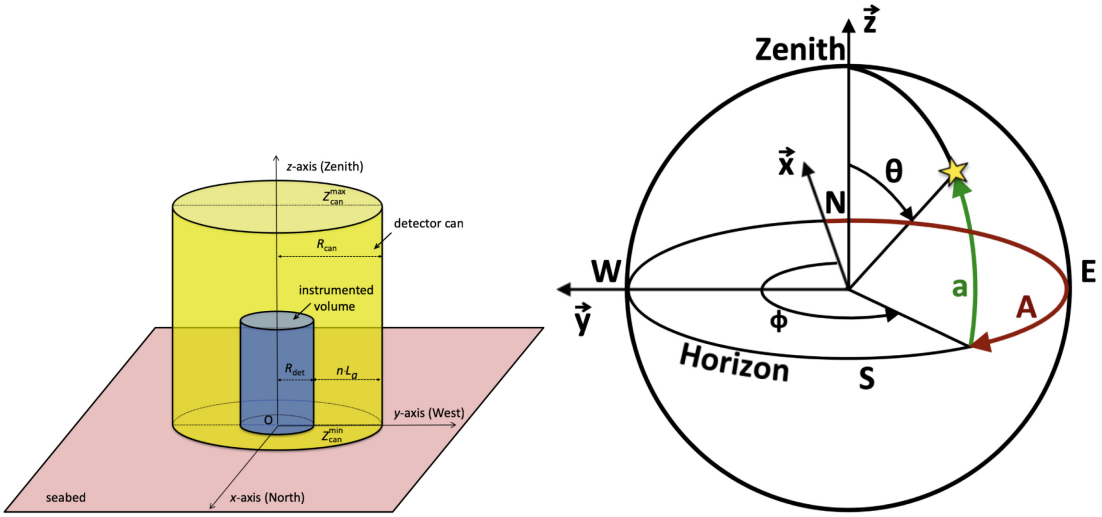

Figure 8.2: **Left:**The can (yellow cylinder) surrounding the instrumented volume of the detector (blue cylinder). The can is anchored to the seabed. The image also shows the orientation of the frame of reference for the event simulation (see [371] for more details). **Right**: The Cartesian frame of reference used in gSeaGen for simulations of neutrino-induced events. The figure also shows the source altitude a, its azimuth angle A and their relation with the angles θ and θ, defining the arrival direction of neutrinos. Both images have been taken from the open-access Ref. [371]. Similar images reported also in [358, 359].

seabed. The instrumented volume of the detector is shown as a blue cylinder. The code used in order to generate neutrino-related interactions is gSeaGen [371]. Only the events leading to Cherenkov light in the can are registered and considered in the output files [371]. For instance, only events occurring inside the *can* or producing a muon reaching the can surface are taken in account [371]. In this sense, the *can* may be considered as an horizon for the light emitted by the neutrino interactions [371]. The right panel of Fig. 8.2 reports the Cartesian frame of reference used in the code for the simulations. In particular, the z-axis is defined to point toward the local zenith, x-axis points north and y-axis points west in order to form a right-handed frame (see

[371] for more details). The neutrino direction is defined through two angles θ and ϕ. These angles are related to the altitude a and the zenith A of the source [371]

$$\begin{aligned} \theta &= \frac{\pi}{2} - \mathrm{a} \\ \phi &= 2\pi - \mathrm{A} \end{aligned} \tag{8.12}$$

In the case of diffuse neutrino simulations, θ and ϕ are randomly extracted by an isotropic distribution and then the neutrino direction cosines can be evaluated with [371]

$$\begin{cases} \mathrm{n_x} = -\sin(\theta) \cdot \cos(\phi) \\ \mathrm{n_y} = -\sin(\theta) \cdot \sin(\phi) \\ \mathrm{n_z} = -\cos(\theta) \end{cases} \tag{8.13}$$

In case of point-like neutrino source emission simulation, θ and ϕ are generated along the apparent trajectory of the source in the sky due to the Earth's rotation, using the equatorial coordinates of the source and the geographical coordinates of the detector (see [371] for more details).

The position of neutrinos (the interaction vertexes) is generated by means of a circular surface with radius $\mathrm{R_T}$ [371]. This generation area is tangent to a sphere centered at the can with a radius $\mathrm{R_L}$. This radius represent the diagonal of the interaction volume (be careful that the generation area is always outside of the interaction volume). Finally, the generation area radius can be related to the detector diagonal through [371]

$$\mathrm{R_T} = \frac{\mathrm{D}}{2} + 100\,\mathrm{m} \tag{8.14}$$

Neutrinos are generated following a power-law spectrum $E^{-\gamma}$ by binning the energy spectrum in log(E). In particular, the number of neutrinos can be determined in each bin through [371]

$$\mathrm{N_i} = \mathrm{N_{tot}} \frac{\int_{\mathrm{E^i_{min}}}^{\mathrm{E^i_{max}}} \mathrm{E}^{-\gamma} \mathrm{dE}}{\int_{\mathrm{E_{min}}}^{\mathrm{E_{max}}} \mathrm{E}^{-\gamma} \mathrm{dE}} \tag{8.15}$$

where $\mathrm{N_{tot}}$ is the total number of neutrinos from $\mathrm{E_{min}}$ and $\mathrm{E_{max}}$ [371].

After generating this information, it is important to simulate the neutrino interactions in the medium [371], either the rock or water. For instance, for upgoing neutrino events, the Earth absorption effect has to be taken into account in order to correctly estimate the number of events

in the detector. The probability for a neutrino to pass through without interacting is given by [27, 358, 359, 371]

$$\mathrm{P_{Earth,cos(\theta)}} = \mathrm{e}^{-\mathrm{N_A}\sigma(\mathrm{E})\rho_{\mathrm{l}}(\theta)} \tag{8.16}$$

where $\mathrm{N_A}$ is the Avogadro number, $\sigma(E)$ is the neutrino cross section and finally $\rho_l(\theta)$ is the effective column density [358, 371]. The effective column density is [371]

$$\rho_l(\theta) = \int_L \rho_{\mathrm{Earth}}(l)dl \tag{8.17}$$

in practice is the total column density which the neutrino encounters during its path in the Earth.

The power of MC simulations is also that even if neutrino are generated from a particular energy spectrum, they can be re-weighted to change it [359] (see also [358, 371]). For example, it is possible to generate atmospheric and cosmic neutrinos with the same set of parameters and then re-weight the spectra with the corresponding MC weight to obtain the correct spectra [358]. This is an important tool also to minimize the quantity of information needed to perform these simulations. The idea is to define a MC generation weight with [359]

$$\mathrm{W_{evt}} = \frac{\Phi(\mathrm{E},\theta,\phi)}{\Phi_{\mathrm{gen}}(\mathrm{E},\theta,\phi)} \tag{8.18}$$

where $\Phi(E,\theta,\phi)$ is the model flux needed to simulate and $\Phi_{\mathrm{gen}}(E,\theta,\phi)$ is the generation flux. The generation flux can be reconstructed by the number of simulated neutrinos arriving in the detector. In fact, it is possible to define a MC generation weight is defined as [358, 371] (see also [27, 359])

$$\mathrm{W_{gen}} = \frac{\mathrm{V_{gen}t_{gen}I_\theta I_E E^\gamma}\sigma(\mathrm{E_\nu})\rho\mathrm{N_A P_{Earth}}}{\mathrm{N_{tot}}} \tag{8.19}$$

where $\mathrm{I} = \int_{\mathrm{E_{min}}}^{\mathrm{E_{max}}} \mathrm{E}^\gamma \mathrm{dE}$ [358], $\mathrm{I}_\theta = 2\pi(\cos\theta|_{\mathrm{max}} - \cos\theta|_{\mathrm{min}})$ for diffuse emission and $\mathrm{I}_\theta = 1$ for point-like emission [358, 371]. $\mathrm{T_{gen}}$ is the simulated lifetime. $\mathrm{V_{gen}}$ is the generation volume, namely the volume. Finally, $\mathrm{N_{tot}}$ is the total number of generated events [359, 371]. $\mathrm{w_{gen}}$ represents the inverse of the generation flux $\Phi_{\mathrm{gen}}(E,\theta,\phi)$. Therefore, we have that the final event simulation is [358, 359, 371]

$$\mathrm{w_{evt}} = \mathrm{w_{gen}}\Phi(\mathrm{E},\theta,\phi) \tag{8.20}$$

In this way it is possible to obtain different neutrino spectra from the same generated neutrino

flux.

Atmospheric Muon Generation

For atmospheric muons, as outlined in the previous section, the code used is MUPAGE [369, 370]. In particular, such a code allows for strongly reducing computation time, which is fundamental especially for a very huge detector like ARCA [359]. The code describes the angular and energy spectrum of muons with depths between 1500 m and 5000 m below the sea level and with zenith angles below 85° [359], using parametric formulae to describe the muon flux [370]. The parametric formulae have been obtained through MC simulations of the shower propagation in the atmosphere through the HEMAS [372] code [370]. MUPAGE assumes that all muon bundles are parallel to the particle shower axis and that they arrive at the same time to the plane perpendicular to the axis. the lifetime considered is the time interval in which a flux of N muons is produced in nature [359] (see [369, 370] for more details). We simulate muon bundle energies with threshold of 10 TeV and 50 TeV in order have sufficient coverage in the high-energy regime [27].

8.8.2 Detector Response: Effective Area

An important parameter which both describes the detector response and it is essential to quantify a neutrino telescope sensitivity is the effective area [27, 373]. The effective area is defined as the area such that all the neutrinos, in a specific energy range, crossing it would be detected [359, 373]. Therefore, given a neutrino telescope with an given effective area $\mathrm{A_{eff}(E_\nu)}$ and a point-like neutrino spectrum $\mathrm{d^2\phi(E_\nu)/dEd\Omega}$, the rate of neutrino events detected by the neutrino telescope can be written [27, 359, 373]

$$\frac{\mathrm{N_\nu}}{\mathrm{T}} = \int_{\Delta E} \frac{d^2\phi(E_\nu)}{\mathrm{dEd\Omega}} \mathrm{A_{eff}(E)dEd\Omega} \tag{8.21}$$

In other words, the effective area represents the efficiency of the detector such as the incident neutrinos it can reconstruct [359]. Indeed, it can be evaluated as [27]

$$\mathrm{A_{eff}(E_\nu)} = \frac{\mathrm{R_{trig}(E_\nu)}}{\phi(\mathrm{E_\nu})} \tag{8.22}$$

where $\mathrm{R_{trig}(E_\nu)}$ is the rate of detector particle at trigger level [27] measured in $[\mathrm{s^{-1}\,GeV^{-1}}]$. On the other hand, the neutrino flux ϕ is measured in $[\mathrm{s^{-1}\,GeV^{-1}\,cm^2}]$ (In case of diffuse flux emission, both $\mathrm{R_{trig}(E_\nu)}$ and ϕ are solid-angle integrated [27]). As a result, $\mathrm{A_{eff}(E_\nu)}$ has the

physical dimensions of a surface [m^2]. Therefore, depending on the analysis performed, neutrino telescopes can have different effective areas depending on the event selection. For instance, the effective area strongly depends on the neutrino (and anti-neutrino) cross section and the geometry of the detector. Eq. 8.22 can also be rewritten in terms of *effective volume* and the probability of interaction for a neutrino as [359]

$$\mathrm{A_{eff}(E_\nu) = V_{eff}(E_\nu, \theta)\sigma(E_\nu) \cdot \rho N_A P_{Earth}(E_\nu, \theta)} \tag{8.23}$$

where $V_{\mathrm{eff}}(\mathrm{E}_\nu, \theta)$ is the effective volume, namely the generation volume scaled with the reconstructed neutrino events [359]:

$$\mathrm{V_{eff}(E_\nu) = \frac{N_{rec}(E_\nu)}{N_{gen}(E_\nu)} V_{gen}} \tag{8.24}$$

Eq. 8.24 shows that the effective volume depend on the detector response and consequently, it is also dependent on the event selection performed on the neutrino events. The behaviour of the effective area is usually of an energy-increasing function with a plateaux at higher energies were the signal start to saturate the detector [359].

8.8.3 KM3NeT/ARCA Event Reconstruction

In this section, we briefly report the event reconstruction algorithms for tracks and cascades for the KM3NeT/ARCA telescope, following Ref. [374]. Firstly, The reconstruction algorithms are based on the maximum likelihood methods [374] in order to quantitatively calculate the direction, energy and the interaction vertex of neutrinos.

For the track events, the reconstruction algorithm is called Jgandalf [358] and it uses a maximization in more steps [358, 374]. In particular, the first step– also referred as a prefit– perform linear fits to several subsets of hits [358]. Such subsets are selected randomly in order to remove the optical background and the prefit is performed on all the permutations of the hits [358]. This prefit neglects scattering and dispersion of light and it is performed with a grid of 1° [374, 375] and it provides a set of 12 best-fit track directions [358]. Then, the second fit exploits the following likelihood [27, 374]

$$\mathcal{L} = \prod_{\mathrm{hitPMTs}} \frac{\delta \mathrm{P}}{\delta \mathrm{t}}(\rho_i, \theta_i, \phi_i, \Delta \mathrm{t}, \mathrm{E}) \tag{8.25}$$

where $\frac{\delta \mathrm{P}}{\delta t}$ is the PDF which provides the expected scattered light from the Cherenkov radiation

and energy loss of a muon [374]. This PDF takes into account the quantum efficiency of the PMTs as well as the fact that the light collected by the PMTS is strictly related to the muon energy [27, 374]. It is a function of five parameters (see [27, 374] for more details): *1)* ρi, the distance between the nearest muon track and the PMT, *2)* the PMT orientation angles ϕ_i, ϕ_i, *3)* E is the muon energy and finally *4)* Δt, namely the time difference between the expected and the measured hit[1] time according to the Cherenkov hypothesis. From this maximum likelihood, it possible to extract very important information such as the energy and angular resolution for the track events, where the angular resolution is defined as the median angular distance between the reconstructed muon track and the true energy direction from MC simulations [359]. By contrast, the energy resolution is defined as the median value of the energy bias [332, 374]

$$\Delta E_{\mathrm{bias}} = 100\% \left(\frac{\mathrm{E_{rec}}}{\mathrm{E_{vis}}} - 1 \right) \tag{8.26}$$

where $\mathrm{E_{rec}}$ is the reconstructed energy, while E_{vis} is the true energy of neutrinos from MC simulations, namely the neutrino energy generated from the MC simulation. For the full KM3NeT/ARCA detector (ARCA 230), the expected medium angular resolution is $\sim 0.25°$ at 10 TeV and it is $\lesssim 0.15°$ for $E \geq 100\,\mathrm{TeV}$ [374]. By contrast, the energy resolution is of the order of $\sim 50\%$ [332, 374].

The shower reconstruction algorithm is called AAshowerfit [358, 376] and it also uses a fit performed in more steps [374, 375]. For the shower reconstruction, firstly only the coincident hits on the same DOM within 20 ns [374] are selected. Then, the vertex position and time is found by minimising [374]

$$\mathrm{M} = \sum_{\mathrm{i}} \sqrt{1 + (\Delta \mathrm{t_i})} \tag{8.27}$$

where Δt_i is the time difference between the measured hit and the expected hit assuming a spherical light pattern from the vertex and i runs over the hits [374]. The final fit maximizes the following likelihood function exploiting the hit/no hit information [374, 375]

$$\log(\mathcal{L}) = \sum_{\mathrm{i} \in \mathrm{no\,hit\,PMTs}} \log(\mathrm{P_i^{no\,hit\,PMTS}}) + \sum_{\mathrm{i} \in \mathrm{hit\,PMTs}} \log(1 - \mathrm{P_i^{no\,hit\,PMTS}}) \tag{8.28}$$

where $P_i^{\mathrm{no\,hit\,PMTS}}$ is [374, 375]

$$\mathrm{P_i^{no\,hit\,PMTS}} = \mathrm{e}^{-\mu_{\mathrm{sig}} - \mathrm{R_{back}} \cdot \mathrm{T}} \tag{8.29}$$

[1] A *hit* in a Cherenkov neutrino telescope is the detection of Cherenkov photons

with $\mu_{\rm sig}$ being the signal photons expected on PMTs and $\mathrm{R_{back}}$ is the background rate in a given time window T [374, 375]. The performance of AAshowerfit results in a very good energy resolution which can reach values of the order of 5% [375]. On the other hand, the angular resolution is of the order of 2° at 10 TeV and of the order of $\sim 1^\circ$ above $E \gtrsim 100$ TeV [332, 374].

Chapter 9

KM3NeT/ARCA Differential Sensitivity

In this chapter, we study the capability of KM3NeT/ARCA to discriminate diffuse and point-like neutrino spectra. In particular, we aim at determining both the energy-integrated and energy-dependent expectations for the full KM3NeT/ARCA detector, in order to understand if the upcoming detector can effectively trace TeV neutrinos from SBGs. Indeed, as explained in the previous chapter, the enhanced angular resolution will enable to probe both point and extended emission from astrophysical sources especially in the southern hemisphere (see also the previous chapter 7 for the discovery horizon for the galactic plane). This chapter is based on the analysis performed and presented several times at several conferences on behalf of the KM3NeT collaboration (see [377–379] for the proceedings).

9.1 Sensitivity and Discovery Potential for a Neutrino Telescope

In this section, we describe the concepts of the sensitivity and discovery potential for a neutrino telescope. These quantities are in general derived through the instrument response functions of the detector and they allow for quantitative assessment of the capability of a neutrino telescope to disentangle an astrophysical neutrino signal above the background expectations [358, 359]. In order to compute the sensitivity and discovery potential, we start from the fact that a neutrino telescope observes a set of events for which energy, time and direction of arrival get reconstructed

[358]. As a result, the data can be used in order to test different hypotheses [358]: 1) H_0: data only consist of background events (atmospheric neutrinos + atmospheric muons). 2) H_1: data consistent of background events + signal events. Therefore, we can define the test statistics TS as [358]

$$\mathrm{TS} = \log\left(\frac{\mathcal{L}(\mathrm{data}, H_1)}{\mathcal{L}(\mathrm{data}, H_0)}\right) \tag{9.1}$$

The higher value for the TS, the higher the probability of the data being inconsistent with the background-only (H_0) hypothesis. In order to write a likelihood function ($\mathcal{L}$), the background and signal PDFs (from Monte Carlo simulations) are exploited. In the next section, we define the precise likelihood framework used in order to define the exact TS used.

9.2 Binned Likelihood Framework

The likelihood in this chapter is chosen following the approach of Ref. [380]. Indeed, we define the likelihood as

$$\mathcal{L} = \prod_i P(n_i, \lambda \cdot \mu_s^i + \mu_b^i) \tag{9.2}$$

where $P(n, \mu)$ is the Poisson probability distribution (PDF) of observing n events with an expected mean value of μ. μ_s is the expected number of signal events, while μ_b is the expected number of background events. i generally runs over reconstructed variables. For the following, we bin the likelihood in reconstructed energy for diffuse analysis and reconstructed energy as well as cone angle for point-like analysis (see below for further details). Finally, λ is the signal strength which physically represents a free normalization for the signal. In order to estimate the sensitivity and the discovery potential of the detector, Monte Carlo simulations are used in order to quantify the expected number of signal and background. We simulate real data-sets by means of pseudo-experiments (PEs) generations [358]. The procedure consists of randomly generating events following the PDFs of signal and background and then evaluate the TS for each PE. The TS can be evaluated as

$$\mathrm{TS} = \frac{\mathcal{L}(\tilde{\lambda})}{\mathcal{L}(\lambda = 0)} \tag{9.3}$$

where $\tilde{\lambda}$ is the signal strength value which maximizes the likelihood for a given PE. We also account for the fact that, generally, Eq. 9.3 provides TS = 0 (It physically represents the situation that the background-only hypothesis dominates over the signal+ background hypothesis).

Indeed, we allow for negative $\tilde{\lambda}$ values for the likelihood maximization, leading us to TS > 0.

9.3 Sensitivity and Discovery Potential Definition

The TS distributions can be determined for several λ values and they can be used to set the capability of the experiment. Indeed, we can define the 90% C.L. sensitivity as well as the model discovery potential (MDP). The sensitivity of the experiment, in our analysis, is a quantity which is used to impose "a median" upper-limit on the expected astrophysical signal flux, in the hypothesis no signal excess is found in the data. From a quantitative point of view, the sensitivity is defined as the value of signal strength λ_{90} for which

$$\int_{\mathrm{TS_m}}^{+\infty} d(\mathrm{TS}|\lambda_{90})\mathrm{dTS} = 90\% \tag{9.4}$$

where TS_m is the median distribution in the null hypothesis (only background) and $d(\mathrm{TS}|\lambda_{90})$ is the PDF distribution for the TS for a given λ_{90} value. λ_{90} is generally referred as a Model Rejection Factor (MRF), because if it is lower than 1 then the telescope is able to put a constrain on the theoretical expectations; otherwise, it will take more time. In other words, the sensitivity is defined as the signal strength for which 90% of the signal is above the median of the background-only distribution [380]. The MDP (at 5σ) is defined as the minimum flux needed for a discovery at 5σ level in the 50% of the cases. From a quantitative point of view [358]:

$$\int_{\mathrm{TS}_{5\sigma}}^{+\infty} d(\mathrm{TS}|\lambda_{5\sigma})\mathrm{dTS} = 50\% \tag{9.5}$$

where $\mathrm{TS}_{5\sigma}$ is the TS threshold corresponding to a 5σ significance in the background-only (H_0) hypothesis. This value is calculated using the one-sided Gaussian approximation [318, 359]. In other words, we consider $\mathrm{TS}_{5\sigma}$ given by

$$\mathrm{TS}_{5\sigma} = \int_{\mu+5\sigma}^{+\infty} \mathrm{f_{Gau}(x|\mu,\sigma)dx} \tag{9.6}$$

where $f_{\mathrm{Gau}}(x|\mu,\sigma)$ is a Gaussian PDF given μ and σ respectively as a mean value and the standard deviation. $\mathrm{TS}_{5\sigma} = 2.85 \cdot 10^{-7}$ [359]. Values obtained through Eq. 9.6 are totally independent on μ. Indeed, they are only dependent on the significance, in other words the number of sigmas needed for the discovery. The final sensitivity can be expressed as

$$\phi_{90}(E) = \lambda_{90}\phi_s(E) \tag{9.7}$$

while the MDP as

$$\phi_{5\sigma}(E) = \lambda_{5\sigma}\phi_s(E) \tag{9.8}$$

where $\phi_s(E)$ is the signal flux injected in the simulations corresponding to $\lambda = 1$. The resulting sensitivity (MDP) is totally independent on the normalization of the assumed signal spectrum. On the other hand, the sensitivity and MDP are only dependent on the capability of the detector to disentangle between H_0 and H_1 hypotheses. Thereby, they crucially depend on the spectral assumption given by the signal hypothesis. For instance, an hard power-law ($\gamma \simeq 2$) spectrum will produce a much better sensitivity than a soft power-law ($\gamma \simeq 3$) (see for instance Fig. 2 of Ref. [50]). The physical reason is due to the fact that a soft signal spectrum is characterised by an energy distribution similar to the energy distribution of atmospheric neutrinos, leading to a worsening of the capability of disentangling the two hypotheses.

9.4 Quasi-Differential Sensitivity (and MDP)

In the previous section, we have quantitatively defined how to compute the sensitivity and the MDP. Their dependency on the assumed spectrum make them model-dependent, thereby they do not capture the capability of a neutrino telescope to constrain a generic astrophysical neutrino signal. In this thesis, we are interested in considering model-independent limits; hence, we take into account the so called quasi-differential sensitivity and MDP [50, 380]. In order to compute the quasi-differential limits, we divide the signal in true-energy bins, injecting for each bin a E^{-2} spectrum. In this way, we can determine the sensitivity for each energy bin. The quasi-differential sensitivity (and MDP) can be represented as an energy-dependent piece-wise function. The physical meaning of representing the expectations of a neutrino telescope with quasi-differential limits is manifold. Firstly, as emphasized above, they are model-independent, therefore they can be evaluated even when it is not clear which is the expectations from a particular astrophysical source or even when the expectations of a source are only known in a particular energy range (see below for more details about this). Secondly, they highlight the energy range where a telescope is most sensitive to when a diffuse or a point-like signal is considered. Nonetheless, there is a strict connection between the quasi-differential limits and the limits introduced in the previous section (hereafter, we refer to them as energy-integrated limits, or simply integrated limits). Indeed, the MRF is inversely proportional to the expected

signal events [377–379, 381]. Therefore, for the integrated MRF, we can write

$$\lambda_{90}^{\text{int}} \propto \mathrm{n_s}^{-1} = \frac{1}{\sum_{\mathrm{i}} \mathrm{n_s^i}} \propto \frac{1}{\sum_{\mathrm{i}} (\lambda_{90}^{\mathrm{i}})^{-1}} \tag{9.9}$$

where i runs over the energy signal bins and λ_{90}^{i} is the MRF for each energy signal bin. Eq. 9.9 points out that, from a numerical point of view, the integrated MRF is always smaller than each differential MRF. In fact, the price to pay to work with quasi-differential limits, is to work under the same background rate with a smaller number of signal events than the energy-integrated case. Let us also comment on the reason why these kind of limits are also called quasi-differential limits and not simply differential limits. From a theoretical point of view, one would like to have the smallest energy bins possible, because the differential limits should represent the limits at a given energy [382]. However, a real telescope is limited by the event statistics, which prevents us from choosing very small energy bins. Indeed, the dimensions of the bins are generally given by a trade-off between not having statistics-related problems (enlarging the bins) and not choosing a too large bins in order to lose the energy dependency of the sensitivity. For the following, we choose, following what IceCube has already presented [383], half-decade width energy bins for the signal. Finally, we also comment on the reason why we chose to inject signal of E^{-2} rather than other energy spectra, if the differential limits are independent on the energy spectrum. The reason is that the finite dimension of the signal energy bins allows for a mild fluctuations of the number and the distribution of the signal event for different spectral energy distributions. As a result, the MRF would slightly fluctuate for different energy spectra, leading to a non-completely spectrum independent limits (this is also another reason why the energy bins cannot be chosen to be arbitrary large). This slightly limits the physical interpretation of the quasi-differential limits. Indeed, the final meaning would that if a flux has a higher SED for an entire sensitivity bin, then it can be constrained if no neutrino excess is found in the data.

9.5 Diffuse Flux Analysis

In this section, we evaluate the differential sensitivity for KM3NeT/ARCA for a diffuse flux (see [379, 384] for more details). We evaluate the sensitivity for both track-like and cascade-like events.

9.5.1 Track-like Selection

Here, we report the rationale for selecting good quality upgoing tracks. Firstly, we consider some preliminary cuts on the reconstructed events in order to reject "bad-quality" events:

- Negative reconstructed energy ($E_{rec} < 0$);
- Negative reconstructed track length;
- Negative likelihood of the *JGandalf*-reconstructed solution;

Further cuts are required to pass through the preselection chain:

- The error calculated for the fit reconstruction (referred as β_0) should be positive ($\beta_0 > 0$);
- The events should be reconstructed by JGandalf.

These cuts are performed in order to remove all events with unphysical properties. Then, only events with reconstructed zenith angle (zenith angle with respect to the detector) $\theta \leq 100°$ are considered in order to reduce the contamination of atmospheric muons. As above-mentioned, this selection is not enough to reduce the background rate because of the high rate of mis-reconstructed muons in the track sample. Hence, we need further cuts to reduce their contamination. The quasi-final selection chain is obtained by optimising the signal/background ratio (considering a E^{-2} spectrum for the signal):

- Track length > 300 meters,
- The logarithm of the likelihood reconstruction fit $\log_{10}(\text{Lik}) > 1.4$,
- The angular error on the track fit: $log_{10}(\beta_0) < 1.8$,
- If the neutrino energy is $log_{10}() < 4.5$, $log_{10}(npe) > 0$ (the logarithm of the number-of-photo-electron (**npe**) should be more than 0),
- If $log_{10}(Energy) < 4.5$ (neutrino energy true), $log_{10}(Nhits) > 0.5$ (the logarithm of the number-of-hits ($Nhits$) should be more than 0.5).

Tab. 9.5.1 reports the number of events after the selection chain.

Finally, a dedicated boosted decision tree [385] has been developed to reject the mis-reconstructed atmospheric muons (see also [378]). This kind of algorithm is based on machine-learning techniques, so it needs to be trained with test data-sets. For instance, this kind of algorithms take

Selection	Atm. muons	Atm. neutrinos	signal (E^{-2})
JGandalf reconstructed	39389988.	79139.2	1380.8
Up-going cut ($\theta < 100°$)	263816.23	58505.4	843.8
Quality cut	98745.6	51380.8	722.7

Table 9.1: The number of events for background (first and second column) and signal (third column), after the up-going and quality selections. All neutrino flavours are included.

Variable	Description
Lik	Likelihood from track reconstruction algorithm (JGandalf)
Track length	The distance between first and last hits in metres
$n.hits$	Number of hits used by JGandalf algorithm
npe	Number of photo-electrons along the whole track
β_0	Angular error fit calculated by JGandalf
ToT	Sum of the ToT for hits used for the track reconstruction
$cos(\theta_z)$	Cosine of Zenith reconstructed by JGandalf

Table 9.2: Sample list of variables (JGandalf algorithm) used to train the BDT machine learning: an Adaptive Boost training was performed.

in input reconstructed variables and allow for a better separation between the signal and background events with respect to ordinary variable cuts [384]. The training is performed in order to reject the remaining mis-reconstructed atmospheric muons in the sample (since there is no difference between an atmospheric neutrino and an astrophysical neutrino, there is no algorithm able to reduce the amount of such background with respect to the signal [378]). Several variables were used to train the BDT, see e.g. Tab. 9.2. Finally, a selection is performed over the BDT score value. Indeed, events classified as signal-like have a BDT value close to 1, on the contrary the events classified as background-like have a value close to -1. The majority of the ν_μ and $\bar{\nu_\mu}$ (cosmic and atmospheric) interacting through CC have been classified as signal, while the other neutrino flavours and atmospheric muons as background. The selection applied for the BDT score is (see also Fig. 9.1):

- For the events with $80° < \theta < 100°$ (the so called horizontal events), the cut was BDT $>$ 0.9.
- Events with $\theta < 80°$ (up-going events), BDT > 0.4.

Finally, after the BDT cut, the final sample of upgoing track-like events is obtained (Tab. 9.3 shows the number of events for the final selection).

Fig. 9.2 reports the reconstructed energy distribution, on the left before applying the selection chain, and on the right, after the preselection and the BDT scores cuts applied.

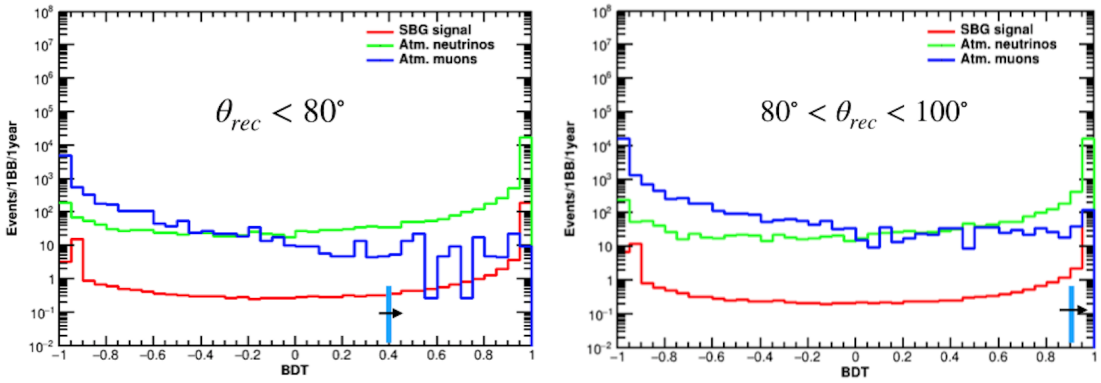

Figure 9.1: **Left**: The BDT score distribution for the up-going class. The BDT score cut chosen is 0.4. **Right**: The BDT score distribution for the horizontal events. In this case, a stronger cut ($BDT > 0.9$) is applied to remove the atmospheric muons.

Selection	Atm. muons	Atm. neutrinos	signal (E^{-2})
JGandalf reconstructed	39389988.	79139.2	1380.8
Up-going cut ($\theta < 100°$)	263816.23	58505.4	843.8
Quality cut	98745.6	51380.8	722.7
BDT cut	389.0	42510.1	456

Table 9.3: Number of events (1yr and 1BB) (background and signal) which passed several steps of the selection chain. From top to bottom: the JGandalf reconstruction, the up-going cut $\theta \leq 100°$, the quality cut and finally the whole selection chain. The entire selection chain rejected significantly the atmospheric muons: from the initial $3.9 \cdot 10^7$ (first row) to 389 (last row) events considered in the all energy range (1year/1BB).

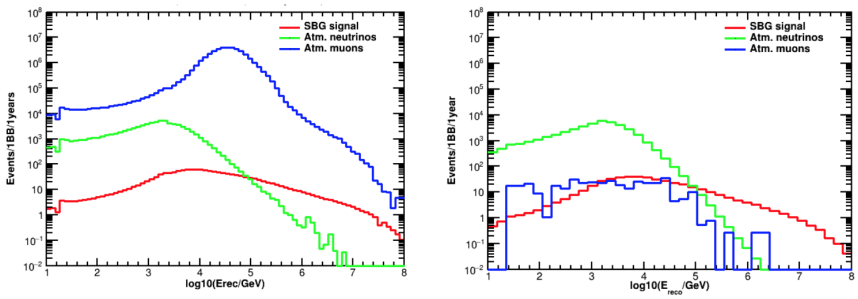

Figure 9.2: **Left**:The energy JGandalf distribution before to apply the selection chain. The background is referred in green (atmospheric neutrinos) and blue (atmospheric muons) line, instead the SBG diffuse signal is reported with the red line. **Right**: The final track-like sample after the quality cut and BDT selection.

9.5.2 All-Sky Cascade Selection

In this section we summarize the selection performed to select good-quality cascades (see [379] for further details). Differently from the tracks, we consider all-sly cascades, so the final sample of cascades is not spatially homogeneous with the track sample. We begin by excluding all the events which passed the track-like selection discussed in the previous section: in other words,

we make sure to exclude good-quality tracks from the sample ($N_{reco} - N_{Track}$). Assuming an instrumented volume of the detector as a cylinder, only the events with the vertex reconstructed by *AAshowerfit* within the instrumented volume were selected (see Fig. 9.3):

- Defining z_{det} as the detector height. Only events with $z_{det} < 650$ m are considered for the cascade selection.
- Considering R_{det} ($\sqrt{x^2 + y^2}$) as the detector radius. A selection was performed considering only events with $R_{det} < 600$ m.

where x, y, z are the coordinates of the AAshowerfit reconstructed vertex of the events. Using

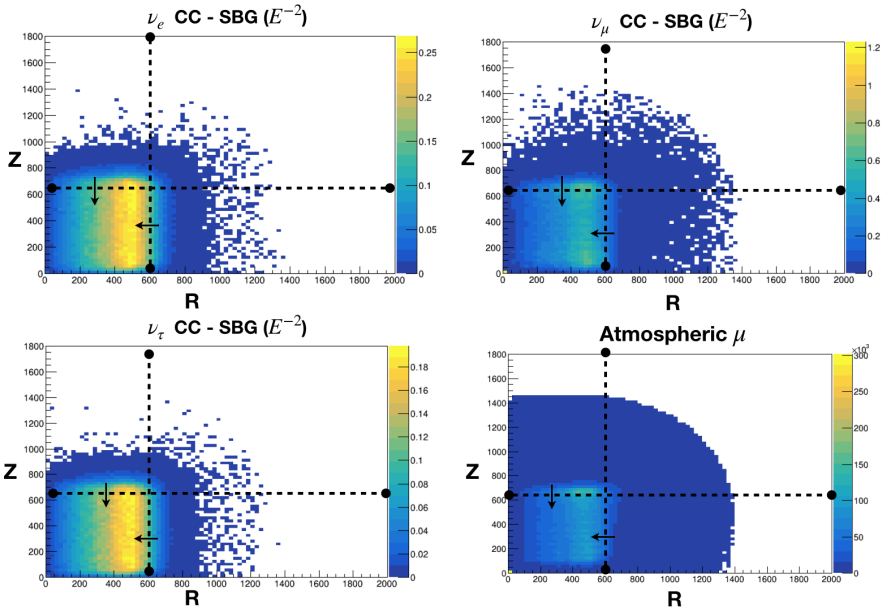

Figure 9.3: The z_{det} and R_{det} AAshowerfit for the ν_e CC (top left), ν_μ CC (top right), ν_τ CC (bottom left) and atmospheric muons. The arrows indicate the region selected for the contained shower.

the sample of the contained events, a pre-selection mainly with the reconstruction variables was applied, as described following:

- Len < 300 m, variable related to *JGandalf*.
- Considering the Likelihood and number of hits used by the *AAshowerfit* reconstruction, a combination of these variables was implemented to achieve a good sample of cascade-like events. The selection was: $\mathcal{L} < -500$ and $n_{\text{hits}} > 400$.

After that, in a similar manner as for the track-like selection, a dedicated BDT (referred as BDT_{casc}) is optimised to classify well reconstructed cascade. Using the BDT_{casc} score, considering different region of sky (cosine of Zenith by AAshowerfit) the following selection was applied

(as for the BDT_{track}, values of $\mathrm{BDT_{casc}}$ close to 1 means that the event was classified as a good cascade):

- If $\cos(\theta) > 0.6$, $\mathrm{BDT_{casc}} > -1.1$
- If $0.2 < \cos(\theta) < 0.6, \mathrm{BDT_{casc}} > -0.9$
- If $-0.2 < \cos(\theta) < 0.2, \mathrm{BDT_{casc}} > -0.8$
- If $-0.6 < \cos(\theta) < -0.2, \mathrm{BDT_{casc}} > 0.8$
- If $\cos(\theta) < -0.6$, $\mathrm{BDT_{casc}} > 1.1$

In order to remove the atmospheric muons, for the downgoing events, a strong cut was performed using the BDT_{casc} ($\cos(\theta) < -0.6$, $\mathrm{BDT_{casc}} > 1.1$).

Selection	Atm. muons	Atm. neutrinos	signal (E^{-2})
Contaiment events	29303257.	31981.5	743.1
Quality cut *AAshowerfit*	389871.11	4460.0	311.4
BDT_{casc} cut full sky	103.9	913.1	61.3

Table 9.4: The total number of events (1 year and 1 BB) for background and signal after the shower-like selection chain. In this table are reported different BDT_{casc} final cut applied in this diffuse analysis.

Selection	ν_μ CC	ν_μ NC	ν_e CC	ν_e NC	ν_τ CC	ν_τ NC
Containment events	336.4	39.3	166.8	39.2	122.0	39.2
$\mathrm{BDT_{casc}}$ cut full sky	8.2	4.6	23.1	4.5	16.1	4.5

Table 9.5: Event rate (1 yr and 1 BB) for each neutrino flavour after respectively the event containment and the full event chain.

9.5.3 Addressing Statistics Problems

Figs. 9.2 and 9.4 clearly show that after the whole selection chains (both for tracks and cascades), the atmospheric muon energy distribution is affected by statistics problems. This might well impact the sensitivity calculation since it crucially depends on the expected background rate (see e.g. Eq. 9.2). In order to overcome this issue, we fit the cumulative atmospheric muon distributions and use the best-fit functions in order to evaluate the background rate in the likelihood. We report the utilized fit for each case. Before continuing discussing the fit, we report how we pass from the MC cumulative distribution to the MC *differential* distribution

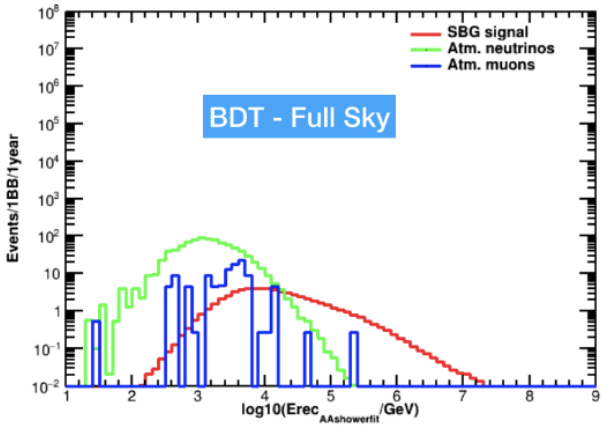

Figure 9.4: The AAshowerfit (reconstructed) energy distribution after the whole cascade selection. Blue line represents atmospheric muons, green line represents atmospheric neutrinos, red line represents the signal.

where we show the number of events in each "bin" (a range of x). We know that $N(> x)$ is given by

$$N(> x) = \int_x^9 \frac{dN}{dx} dx \tag{9.10}$$

where $\frac{dN}{dx}$ can be considered a continuous PDF distribution for muons. Fitting data from Fig. 9.5, we can calculate $N(> x)$. As a result, we can evaluate $\frac{dN}{dx}$ as

$$\frac{dN}{dx} = -\frac{dN(> x)}{dx} \tag{9.11}$$

and then we can evaluate the number of muons in a bin $\in [x_1, x_2]$ is given by

$$N(x_1 < x < x_2) = \int_{x_1}^{x_2} \frac{dN}{dx} dx \tag{9.12}$$

As a result, by fitting the cumulative muon distribution we can evaluate the number of muons for each reconstructed energy bin.

Track-like Event Fit

Here, we summarize the results for the cumulative Gaussian as a function for fitting the muon distribution (we normalized the cumulative function to 1).

The expression is:

$$N(> x) = 1 - \frac{1}{\sqrt{2\pi}\sigma} \int_{-\infty}^{x} e^{-\frac{(t-\mu)^2}{2\sigma^2}} dt \tag{9.13}$$

The best fit values are $\mu = 3.30 \pm 0.02$ and $\sigma = 1.05 \pm 0.03$. The reduced chi squared $\chi^2 = 4.6 \cdot 10^{-4}$. χ^2 is calculated by summing over the square of the "fit residuals" and then divide the sum by the number of degrees of freedom (the number of data minus the number of free parameters). Fig 9.5 shows the comparison between the cumulative distribution and the best fit scenario.

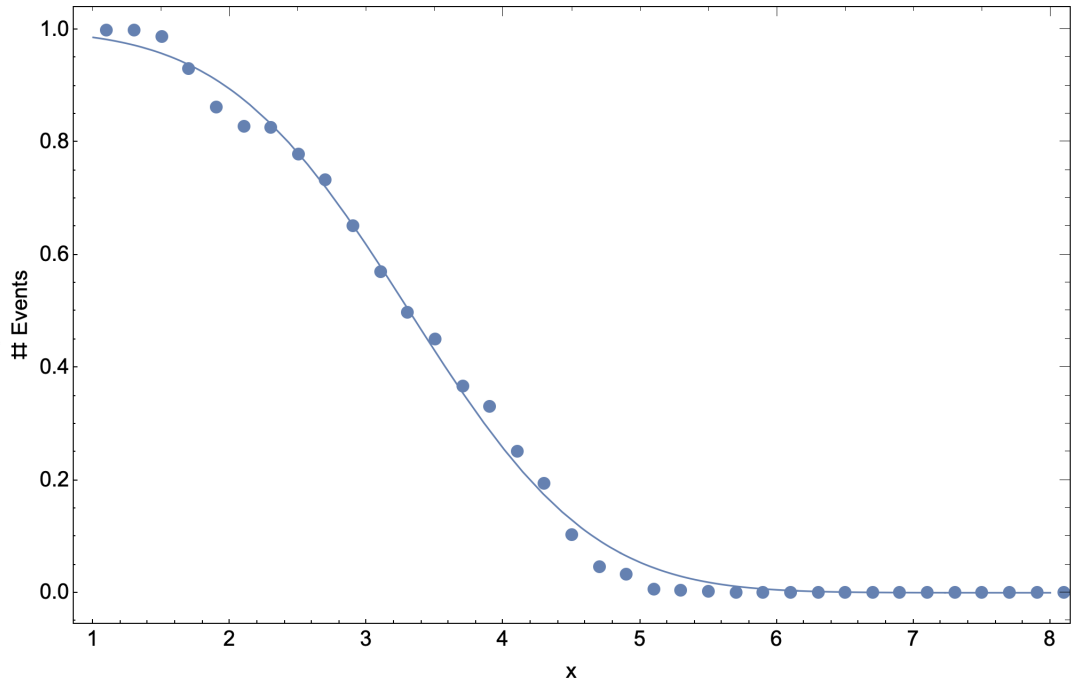

Figure 9.5: Gaussian best fits compared with the cumulative distribution data.

In Fig. 9.6, we also report the comparison between the pure MC distribution and then one obtained after using the best-fit function.

Fig. 9.6 shows that the background rate produced by the best-fit function is conservative with respect to the pure Monte Carlo distribution.

Cascade-like Event Fit

Here, we summarize the fit performed for cascades. The expression is given by:

$$N(>x;\mu,\sigma) = 1 - \int_{-\infty}^{x} \frac{\Gamma(\frac{\nu+1}{2})}{\sqrt{\nu\pi}\sigma\Gamma(\frac{\nu}{2})} \left(1 + \frac{(t-\mu)^2}{\nu\sigma^2}\right)^{-\frac{\nu+1}{2}} dt$$

Here, we summarize the results for the t-student distribution. As for the track-like events, we fix $\nu = 3$. The best-fit values are: $\mu = 3.55 \pm 0.02$ and $\sigma = 0.29 \pm 0.02$. The reduced chi squared is $\chi = 9 \cdot 10^{-4}$. Fig. 9.7 shows the comparison between the best-fit function and the

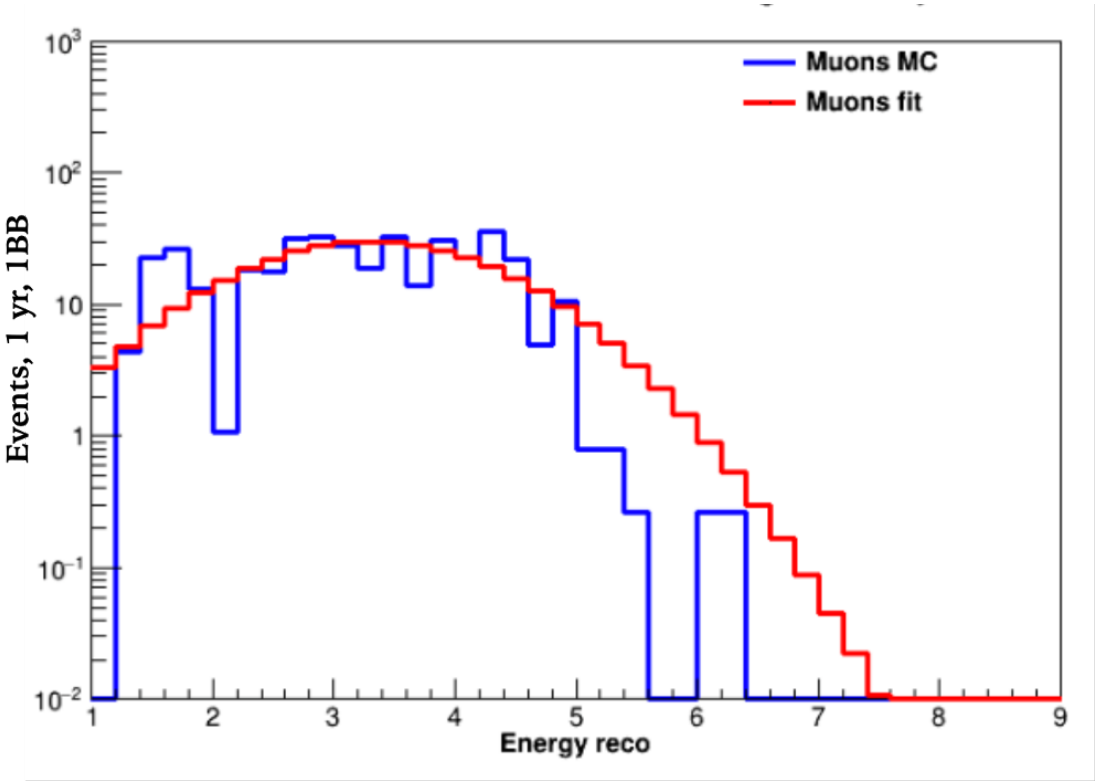

Figure 9.6: Comparison between the "MC" distribution for the muons given by the pure MC (blu histogram) and the one given by the best fit scenario of the cumulative distribution using a gaussian distribution. This refers to the number of events for 1 yr and 1 BB.

cumulative muon distribution for cascades. Finally, Fig. 9.8 shows the comparison between the corresponding Monte Carlo distributions.

9.5.4 Results

Equipped with the track and cascade event selection, we can evaluate the 90% C.L. quasi-differential sensitivity. We utilize $5 \cdot 10^4$ PEs. Fig. 9.9 shows the quasi-differential sensitivity after 10 years of operation for 2BB, on the left for upgoing tracks, and on the right for all-sky cascades. The sensitivities refer to one flavour of neutrinos + antineutrinos. They are compared with the corresponding IceCube measured spectra. In particular, the track sensitivity is compared with the 9.5 yr through-going muon flux [10] and the cascade sensitivity is compared with the 6 yr cascade flux [295]. The results are highly significant for several reasons. Firstly, the track sensitivity peaks (it is minimum) around 1 PeV, where there is a significant contribution from horizontal events. By contrast, the cascade sensitivity peaks at $\sim$ 100 TeV, since the containment requirement harshly reduces the amount of signal events above this energy. For

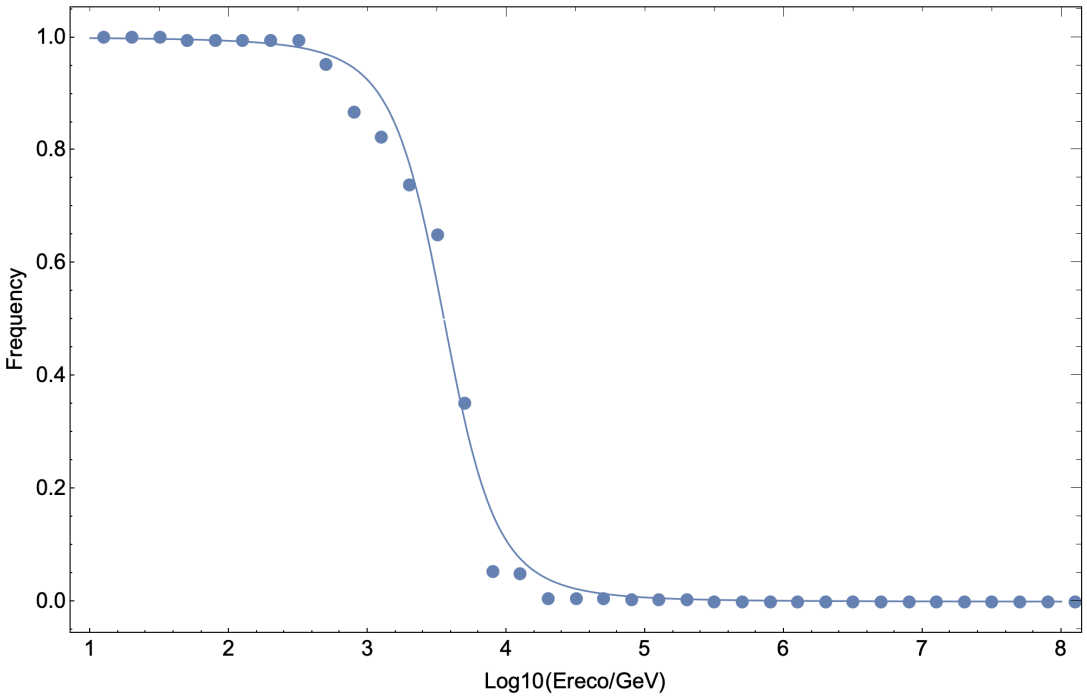

Figure 9.7: Tstudent best fits compared with the cumulative distribution data for cascades.

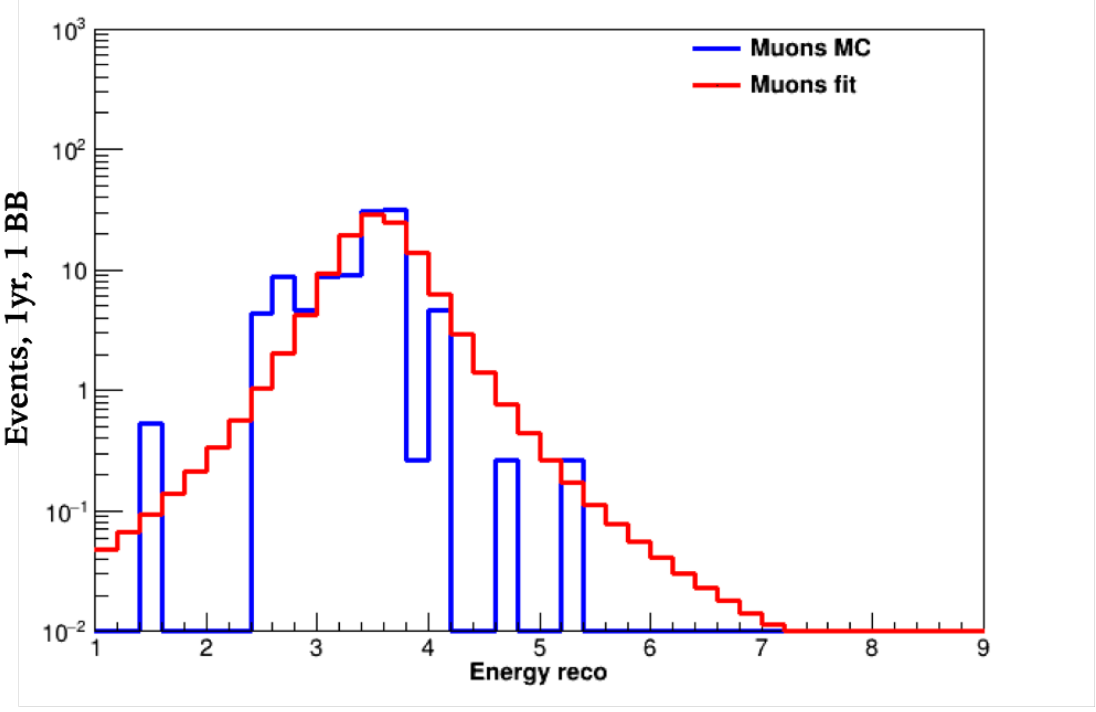

Figure 9.8: Comparison between the MC distributions for the cascades (after the selection chain described and the BDT). The blue histogram represents the pure MC distribution and the red one refers to the t-student distribution.

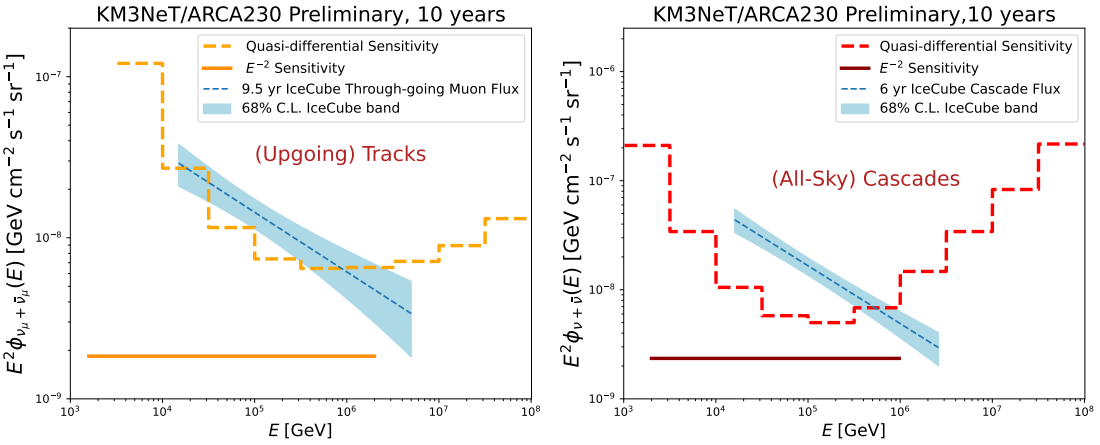

Figure 9.9: **Left**: 90% C.L. Quasi-differential sensitivity (per neutrino flavour) for KM3NeT/ARCA after 10 years of operation and 2BB for a diffuse spectrum for upgoing tracks (dashed orange line). The continuous orange line shows the integrated sensitivity for a E^{-2} diffuse spectrum. The sensitivity is compared with the corresponding 9.5 yr diffuse spectrum measurement by the IceCube Collaboration in the through-going muon channel [10]. **right**: 90% C.L. quasi-differential sensitivity (per neutrino flavour) for KM3NeT/ARCA after 10 years of operation and 2BB for a diffuse spectrum for the all-sky contained cascades (dashed red line). The integrated sensitivity for a E^{-2} diffuse spectrum is shown with the continuous dark red line. The sensitivity is compared with the corresponding 6 yr cascade flux measured by the IceCube collaboration [295].

this very reason, at high energies tracks result in a better sensitivity than cascades; while, at low energies, the sensitivity is better for cascades due to a reduced background rate. Indeed, the containment cut mostly reduces muon neutrinos which are the most dominant channel within atmospheric neutrinos, leading to a very good sensitivity at low energy. This makes the cascade channel very good for diffuse or quasi-diffuse flux studies [6]. Another reason why the result is important is due to it sets the potential of KM3NeT/ARCA to constrain a diffuse spectrum outside the energy ranges where the IceCube has measured it. Indeed, the spectrum is not well known below $\sim 10 - 15$ TeV and above ~ 1 PeV. Therefore, it is crucial to understand if it can be extrapolated also for lower energies as well as if it changes its shape. Indeed, as highlighted in Chapter 3, there is some tension between the diffuse gamma-ray and neutrino data due to the electromagnetic cascade contribution (see also [386] for a recent analysis).

Fig. 9.9 also show, for reference, the integrated sensitivities for a E^{-2}, which for convention are shown in the 90% range where the signal is concentrated. As emphasized in Sec. 9.3, the integrated sensitivities stand below the corresponding quasi-differential ones. Another physical way to interpret this is result is that the integrated sensitivity exploits the information of the energy dependence of the signal spectrum, while the quasi-differential sensitivity can be regarded as *blind* sensitivity without any signal information. Therefore, a flux standing between the integrated and quasi-differential sensitivity is a flux which can be constrained by the experiment

but it will be impossible to disentangle which energy range has contributed the most to the sensitivity. We end this section by highlighting that future event selection, able to further reduce the background rate, will further reduce the sensitivity of the KM3NeT/ARCA detector.

9.6 Point-Like Flux Analysis

In this section, we study the quasi-differential sensitivity expected by the Full KM3NeT/ARCA detector for point-like and extended sources emissions. In order to study emission from specific sources, it is important to exploit the fact that, in case a source emits neutrinos, those will be clustered throughout the nominal position of the source. Therefore, in the likelihood formalism (Eq. 9.2), we also bin the likelihood in cone angle α bins (the angular distance of an event to the nominal position of the source). Therefore, we test the compatibility of pseudo data with the signal + background hypotheses by means of 2D histograms (see also [318, 332] or even [387]). For the reconstructed energy, we consider the $[1, 8]$ range for $\log(\mathrm{E_{rec}})$, while $[0, 5^\circ]$ ($[0, 15^\circ]$) for α for tracks (cascades). In order to quantify the signal and background rate in each bin, we make use of the same event selection as we explained in the diffuse analysis. The main point is that we need to weight the signal distributions in order to account for the hypothesis of a source emitting neutrinos. We do it by means of the Point-Spread-Function (PSF) of the detector, which represents the PDF of a neutrino event to be reconstructed at an angular distance α with respect to the generation position. We can write the distribution of the number of signal events as [326]

$$\frac{dN_{i,c}}{d\Omega d\log(\mathrm{E_{rec}})} = \sum_{\mathrm{f}} \int dE \frac{dP_{\mathrm{fc}}}{d\Omega \log(\mathrm{E_{rec}})} A^{\mathrm{fc}}_{\mathrm{eff}}(E, \theta) \phi_s(E) \tag{9.14}$$

where f runs over the flavours and c over the interaction channels. $A^{\mathrm{fc}}_{\mathrm{eff}}(E, \theta)$ is the declination-dependent effective area which depends on the true energy(see the previous chapter) and zenith angle. The declination-dependent effective area is calculated by averaging over the right ascension

$$\mathrm{A_{eff}}(\mathrm{E}, \delta) = \frac{1}{2\pi} \int_0^{2\pi} \mathrm{A_{eff}}(\mathrm{E}, \theta(\delta, \mathrm{r}))\mathrm{dr} \tag{9.15}$$

this also allows for a better estimates of the background rate around the source position, accounting for the declination band of the source limiting statistics-related problems or a underestimation of the background rate. $\frac{dP_{\mathrm{fc}}}{d\Omega \log(\mathrm{E_{rec}})}$ is a PDF taking into account both the energy

and angular resolution of the experiment. In particular, it is considered to be factorised

$$\frac{dP_{\rm fc}}{d\Omega \log(\mathrm{E_{rec}})} = \frac{dP_{\rm fc}}{d\Omega} \cdot \frac{dP_{\rm fc}}{\mathrm{dlog(E_{rec})}} \tag{9.16}$$

where the first term represent the energy-dependent PSF and the second term describes the energy resolution. The PSF can be rewritten in terms of the cone angle α, by using $\mathrm{d}\Omega = 2\pi\sin(\alpha)\mathrm{d}\alpha$. Therefore, we can write

$$\frac{dP_{\rm fc}}{d\Omega \log(\mathrm{E_{rec}})} = \frac{dP_{\rm fc}}{d\alpha} \cdot \frac{dP_{\rm fc}}{\mathrm{dlog(E_{rec})}} \frac{\mathrm{d}\alpha}{\mathrm{d}\Omega} = \frac{dP_{\rm fc}}{d\alpha} \cdot \frac{dP_{\rm fc}}{\mathrm{dlog(E_{rec})}} \frac{1}{2\pi\sin(\alpha)} \tag{9.17}$$

In order to address the problem of the extension of a source, the PSF is smeared out with a Gaussian kernel in order to account for an extension greater than the angular resolution of the experiment (the angular resolution is defined as the median of the PSF) [27, 326, 388]. Fig. 9.10 shows an example for the 2D distributions for signal and background (considering the track channel). In particular, it reports the expected signal (left) and background (right) events in

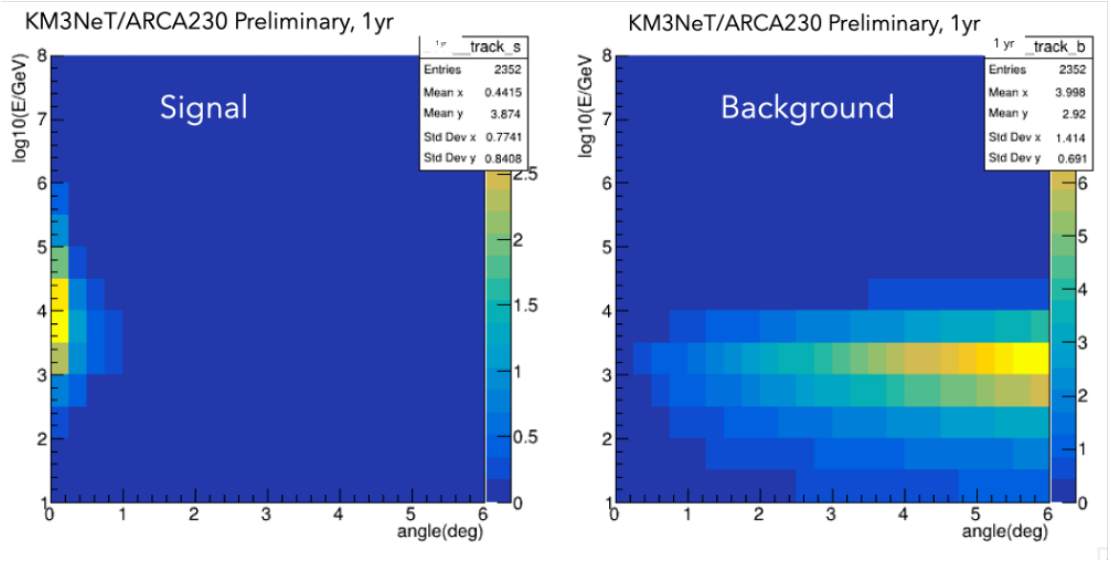

Figure 9.10: **Left:** The expected Signal event distribution distribution for the Small Magellanic Cloud (SMC) after 1 year of data taking. **Right:** The expected background event distribution (muons + neutrinos) for SMC after 1 year of data taking.

the direction of SMC (simulated as an extended source of radius $r = 0.5°$) after one year of data taking of ARCA230. It is evident that the signal events clusters around the source and this fact can be exploited in the likelihood analysis in order to obtain cutting-edge limits.

9.6.1 Focus On Local Starburst Galaxies

In this section, we report the results for point-like sensitivity expectations for particular SBGs. Indeed, following Chapter 4, we focus on the SMC, Circinus Galaxy and NGC 1068. We report the results separately for each source.

9.6.2 The Small Magellanic Cloud

SMC, as analysed in Chapter 4, exhibits a hard gamma-ray spectrum up to 1 TeV [19]. We showed that its star-forming activity is consistent with the stable gamma-ray spectrum of the source, in other words the gamma-ray spectrum can be powered 100% from diffuse hadronic collisions [163]. It is located at equatorial coordinates of $(-72.83°, 13.18°)$ [19], where the first coordinate is the equatorial declination and the second one is the equatorial right ascension. KM3NeT/ARCA is expected to have full visibility at those declinations [318], thereby having the potential to constrain such an hadronic scenario. We simulate the source as disk of radius $r = 0.5°$, encompassing a total extension of $\sim 1°$, consistent with the angular extension measured by Fermi-LAT observations [19]. We compare the expectations with the model we used in chapter 4.

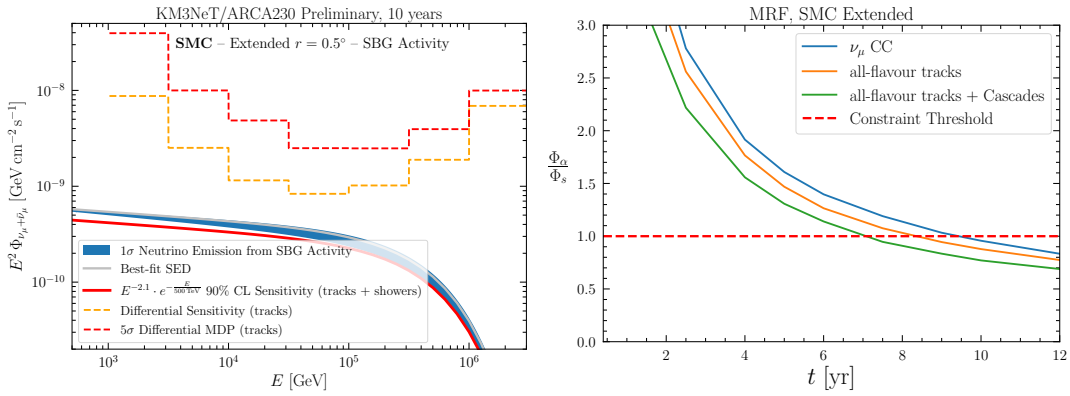

Figure 9.11: **Left**: 1σ Neutrino emission expectations (blue band) compared with the integrated sensitivity (red line) and the quasi-differential sensitivity (dashed orange line) and the quasi-differential 5σ MDP (dashed red line). **Right**: MRF as a function of the KM3NeT/ARCA operation time, for different samples: $\nu_\mu + \bar{\nu}_\mu$ CC (blue line), all-flavour tracks (orange line), all-flavour tracks + cascades (green line).

Fig. 9.11 shows our results for SMC. In particular, in the left panel, we compare the 1σ neutrino expectation flux (obtained through the posterior distribution of the analysis described in Chapter 4) with the integrated sensitivity (red line) and the quasi-differential sensitivity (dashed orange line) and the quasi-differential 5σ MDP (dashed red line). The expected sensitivities are shown for an lifetime of 10 yr of 2BB. In the right panel, we show the integrated MRF as a

function of the operation time. We show the case of $\nu_\mu + \bar{\nu}_\mu$ CC (blue line), all-flavour tracks (orange line), all-flavour tracks + cascades (green line). Interestingly, after 7.5 yr of data taking, the model put forward in chapter 4 can be at least constrained at 90% C.L. (not exactly point-like but with its extension). This confirms that even considering the extension of the source, KM3NeT/ARCA will be able to constrain the total hadronic scenario from this source. Fig. 9.11 represents the case discussed in Sec. 9.5.4, where the expected flux stands in between the integrated sensitivity and the quasi-differential one. Indeed, we expect the detector to be able to put a constrain on the scenario without disentangling its spectral energy distribution (SED).

9.6.3 Circinus Galaxy

Here, we analyze the sensitivity for the Circinus Galaxy. It is situated at 4 Mpc away from the Earth [20]. Along with the star-forming activity, it has also AGN activity. Indeed, it is also classified as a Seyfert galaxy [389]. Therefore, it might well be a perfect target for future observations for the KM3NeT/ARCA.

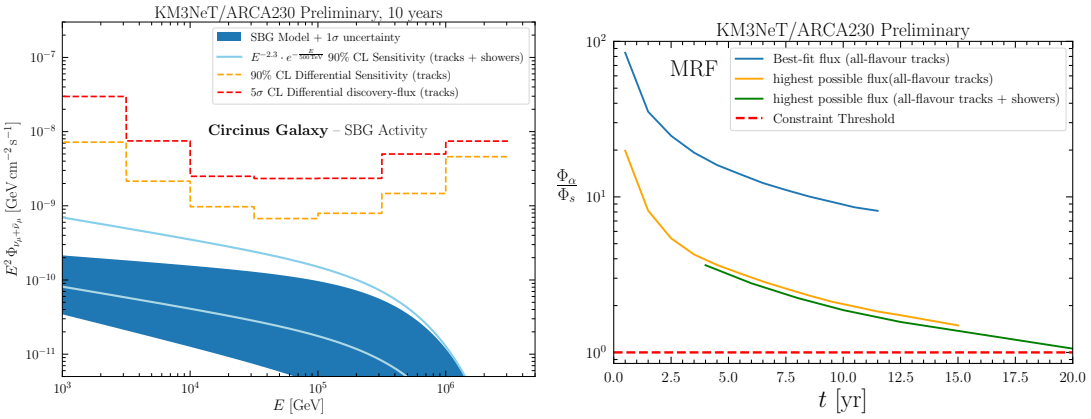

Figure 9.12: **Left**: 1σ Neutrino emission expectations (blue band) compared with the quasi-differential sensitivity (orange line). **Right**: MRF as a function of the KM3NeT/ARCA operation time, for different spectra: the blue line represents the case of the best-fit theoretical SED. The orange and the green lines refer to the upper limit spectrum. The orange line refers to the all-flavour track and the green line to all-flavour tracks + cascades.

Fig. 9.12 shows the results for Circinus galaxy in the same fashion as for SMC. In particular, on the left we compare the 1σ neutrino expectations (see Chapter 4 for more details) with the quasi-differential sensitivity after 10yr and 2BB (orange dashed line) as well as the quasi-differential 5σ MDP (dashed red line) and the integrated sensitivity for the best-fit SED of the source (light blue line). The right plot shows the integrated MRF as a function of time for different cases. The blue line refers to the best-fit Circinus flux for the all-flavour tracks. The orange and green lines refer to the upper-limit flux of the source (the highest possible flux at

1σ): the orange line refers to the all-flavour tracks, while the green one to the all-flavour tracks + cascades. This source is characterised by a lower flux with respect to SMC (see also Fig. 4.1), therefore the expectations are less promising. Differently from Fig. 4.1, the sensitivity takes into account the actual flux of the source, in particular the high-energy cut-off, which makes it hard to produce a competitive integrated upper limit. Nonetheless, after $\sim$ 20 yr of data taking, the upper limit of the source can be constrained. We emphasize that this source might be characterised by an hot-corona activity due to the presence of the AGN in its core [173]. Indeed, The authors of Ref. [173] has evaluated an expected neutrino spectrum which can be as high as $E^2\phi_{\nu_\mu+\bar{\nu}_\mu} \simeq 10^{-8}\,\mathrm{GeV\,cm^{-2}\,s^{-1}}$, thereby a neutrino flux which is higher than the expected quasi-differential sensitivity. This unequivocally demonstrates that KM3NeT/ARCA will test such hadronic scenarios, either discovering or challenging the hot-corona paradigm.

9.6.4 NGC 1068

Here, we analyze also NGC 1068. In Sec. 4.6, we have shown that the SBG activity of the source is consistent with its gamma-ray spectrum, but the neutrino spectrum observed by IceCube cannot be explained this kind of activity.

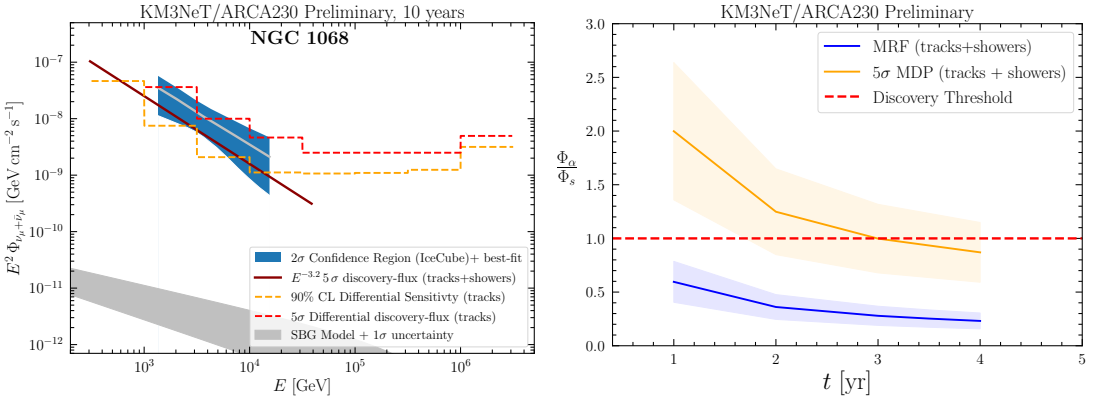

Figure 9.13: **Left**: The quasi-differential sensitivity (orange line), the quasi-differential 5σ MDP (Red line) and the integrated 5σ MDP for a $E^{-3.2}$ spectrum (dark red line) compared with the 2σ IceCube C.L. measured region [60] and the 1σ Neutrino expectations (already shown in Fig. 4.3). **Right**: integrated MRF and 5σ MDP as functions of the operation time for the full KM3NeT/ARCA. The bands corresponds to the uncertainty on the normalization to the spectrum measured by IceCube [60].

Fig. 9.13 shows, on the left, the quasi-differential sensitivity (dashed orange line), the quasi differential 5σ MDP (dashed red line) and the integrated 5σ MDP for a $E^{-3.2}$ spectrum (dark red line) (best-fit spectrum measured by ICeCube [60]) after 10 yr of operation for 2BB compared with the 2σ C.L. region measured by ICeCube [60]. The gray band represents the 1σ flux region

expected from SBG activity. On the right, the integrated MRF and MDP for the IceCube best-fit flux is shown as a function of time. The corresponding blue and orange bands represent the uncertainty on the IceCube measured normalization of the spectrum [60]. The results show that within 3yr of operation, the full KM3NeT/ARCA detector will be able to strenghten IceCube's discovery. We emphasize that the shape of NGC 1068 spectrum outside the energy range $\sim [1 - 15]$TeV [60] is not well constrained, therefore the differential limits clarify the potentiality of KM3NeT/ARCA to further constrain the property of this source.

9.6.5 Impact of the Source Extension

Here, we quantify the impact of the source extension on the quasi-differential sensitivity. In particular, we evaluate the differential limits for SMC simulating it also as a point-like source.

Fig. 9.14 shows the comparison between the quasi-differential sensitivity for SMC between the case of no-extension and the extension of $r = 0.5°$.

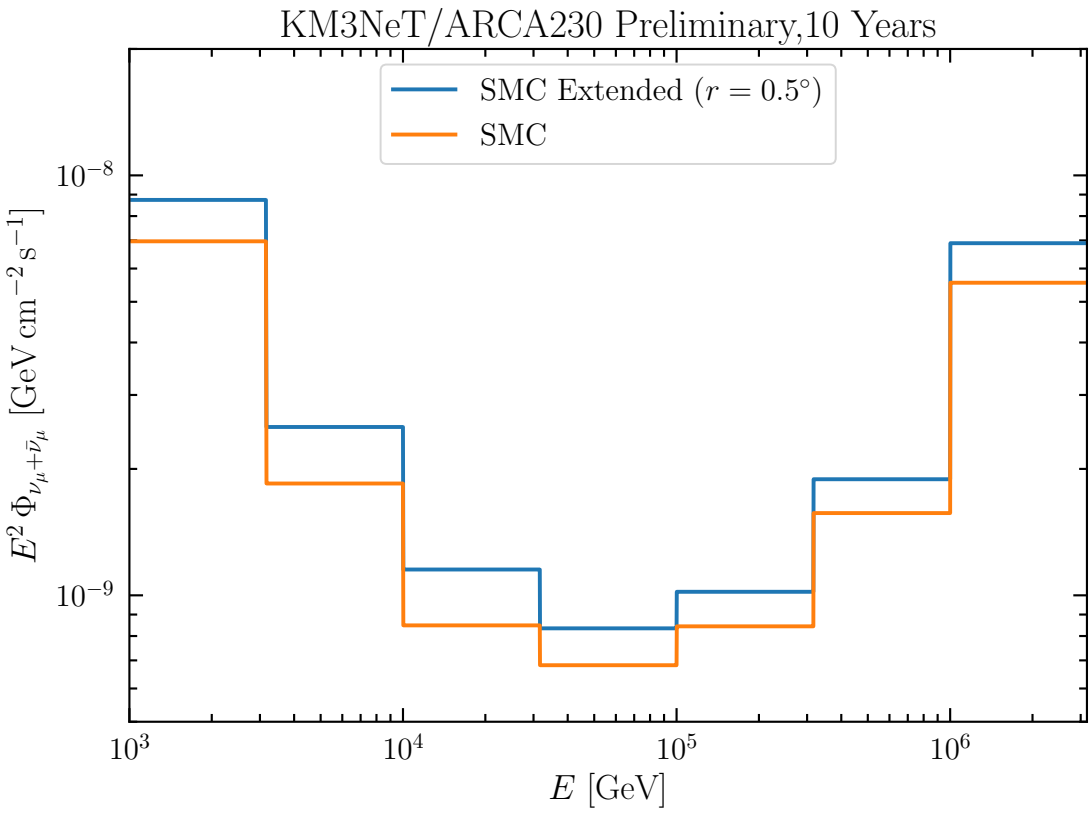

Figure 9.14: Comparison between the quasi-differential sensitivity for different extension. The orange line corresponds to the point-like case and the blue line to $r = 0.5°$ case.

The extension considered of SMC makes the sensitivity worse of $\sim 30\%$ than the point-like

case.

9.7 Conclusions

In this chapter, we have introduced, for the first time, the quasi-differential sensitivity for the KM3NeT/ARCA both for diffuse and point-like (extended) sources. In particular, we have analyzed if (consistently with what theoretically predicted in chapter 4) KM3NeT/ARCA can trace TeV neutrino from SFGs and SBGs. We have found through a binned-maximum-likelihood method that KM3NeT/ARCA is bound to probe, after $\sim 8\,\mathrm{yr}$ of full operation time, neutrino emission from local SFGs, potentially linking star-forming activity with high-energy neutrino production. The detector is also expected to discriminate between SBG and AGN activity from local Seyfert Galaxies, such as Circinus Galaxy. We also emphasize that with further (improved) event selection, the sensitivity and the discovery potential of the experiment is going to improve. For instance, selecting also down-going track events might improve the sensitivity for declinations $\delta \gtrsim 50^{\circ}$. Finally, we also comment on the fact that future sensitivities might also depend on the statistical treatment of the data. In fact, we have used of a binned-likelihood method but also a unbinned likelihood method could have been possible [358, 359].

Chapter 10

Conclusions

In this thesis, an extensive study on the non-thermal emission from star-forming environments (galactic and extra galactic) has been performed in a multi-messenger framework. Regarding the extra galactic star-forming environments, we have applied a leaky-box model in order to describe the CR transport inside SBNi and we exploited such a model to quantify the gamma-ray and neutrino emissions of SBGs. We have introduced a new evidence-based spectral index blending which demonstrated to leave the diffuse gamma-ray unperturbed, while making the neutrino expectations higher, potentially reducing the tension between the diffuse extra-galactic gamma-ray and neutrino observations. In fact, we demonstrated that SBGs, in this new scenario, can explain up to 40% of the HESE flux measured by the ICeCube collaboration. We also evaluated the neutrino budget of local SBGs and SFGs, exploiting the strict connection between IR luminosity and the SFR, and we have found that KM3NeT/ARCA has the potential to trace TeV neutrinos from these sources, especially if situated in the southern hemisphere. Therefore, we expect the future neutrino telescopes to be able to trace the star formation rate shedding more light also on topics related to role of SFR in galaxy formation. We also presented, for the first time, a dedicated KM3NeT analyses evaluating the quasi-differential limits for the upcoming experiment, both for a diffuse and point-like emissions and compare them to the expected SEDs of local SBGs. We have also performed a forecast analysis for the future CTA telescope, demonstrating its capability of setting strict constraints on the CR transport mechanisms inside SBNi. We have also exploited such forecasts to perform a beyond standard model study. In particular, we have utilized gamma-ray data from M 82 and NGC 253 to strongly constrain DM-p interactions showing that current data constrain $\sigma_{\chi p} \sim 10^{-34}\,\mathrm{cm}^2$ for $m_\chi \lesssim 10^{-6}\,\mathrm{GeV}$. We have shown that CTA will improve such bounds up to ~ 2 orders of magnitude.

Finally, we have also studied, in light of the new IceCube discovery of neutrinos emitted from the Milky Way, the neutrino emission from galactic source populations, introducing the concept of discovery horizon for high-energy neutrino telescopes. Unfortunately, current neutrino telescopes (IceCube) cannot discriminate true diffuse emission from a quasi-diffuse emission from a template of point-like (extended) sources, because of a limited angular resolution. However, KM3NeT/ARCA and IceCube Gen2 are going to probe the contribution of these potential pevatrons (especially HNRs and YMSCs) if they dominate ($> 50\%$) the diffuse emission at 100 TeV as long as the source extension is limited to about 10 pc. On this regard, we emphasize that it will be hard to discover spatially-bigger pevatrons due to the worsening of the DPs for the extension, although the KM3NeT/ARCA cascades are expected to be less dependent of the source sizes and therefore perfect for future studies on this topic.

Bibliography

[1] I. V. Dorman and L. I. Dorman. How cosmic rays were discovered and why they received this misnomer. *Adv. Space Res.*, 53:1388–1404, 2014. doi: 10.1016/j.asr.2013.04.022.

[2] Thomas K. Gaisser, Todor Stanev, and Serap Tilav. Cosmic Ray Energy Spectrum from Measurements of Air Showers. *Front. Phys. (Beijing)*, 8:748–758, 2013. doi: 10.1007/s11467-013-0319-7.

[3] Ofelia Pisanti. Astrophysical neutrinos: theory. *Journal of Physics: Conference Series*, 1263:012004, Jun 2019. ISSN 1742-6596. doi: 10.1088/1742-6596/1263/1/012004. URL http://dx.doi.org/10.1088/1742-6596/1263/1/012004.

[4] M. Ackermann, M. Ajello, W. B. Atwood, L. Baldini, and Ballet et al. Fermi-LAT Observations of the Diffuse γ-Ray Emission: Implications for Cosmic Rays and the Interstellar Medium. , 750(1):3, May 2012. doi: 10.1088/0004-637X/750/1/3.

[5] R. Abbasi et al. The IceCube high-energy starting event sample: Description and flux characterization with 7.5 years of data. *Phys. Rev. D*, 104:022002, 2021. doi: 10.1103/PhysRevD.104.022002.

[6] R. Abbasi et al. Observation of high-energy neutrinos from the Galactic plane. *Science*, 380(6652):1338–1343, 2023. doi: 10.1126/science.adc9818.

[7] M. Ackermann et al. The spectrum of isotropic diffuse gamma-ray emission between 100 MeV and 820 GeV. *Astrophys. J.*, 799:86, 2015. doi: 10.1088/0004-637X/799/1/86.

[8] Austin Schneider. Characterization of the Astrophysical Diffuse Neutrino Flux with IceCube High-Energy Starting Events. *PoS*, ICRC2019:1004, 2020. doi: 10.22323/1.358.1004.

[9] M.G. Aartsen et al. Characteristics of the diffuse astrophysical electron and tau neutrino flux with six years of IceCube high energy cascade data. *Phys. Rev. Lett.*, 125:121104, 2020. doi: 10.1103/PhysRevLett.125.121104.

[10] R. Abbasi et al. Improved Characterization of the Astrophysical Muon–neutrino Flux with 9.5 Years of IceCube Data. *Astrophys. J.*, 928(1):50, 2022. doi: 10.3847/1538-4357/ac4d29.

[11] M. Ajello et al. The Origin of the Extragalactic Gamma-Ray Background and Implications for Dark-Matter Annihilation. *Astrophys. J. Lett.*, 800(2):L27, 2015. doi: 10.1088/2041-8205/800/2/L27.

[12] M. Ackermann et al. Resolving the Extragalactic γ-Ray Background above 50 GeV with the Fermi Large Area Telescope. *Phys. Rev. Lett.*, 116(15):151105, 2016. doi: 10.1103/PhysRevLett.116.151105.

[13] Mariangela Lisanti, Siddharth Mishra-Sharma, Lina Necib, and Benjamin R. Safdi. Deciphering Contributions to the Extragalactic Gamma-Ray Background from 2 GeV to 2 TeV. *Astrophys. J.*, 832(2):117, 2016. doi: 10.3847/0004-637X/832/2/117.

[14] M.G. Aartsen et al. The contribution of Fermi-2LAC blazars to the diffuse TeV-PeV neutrino flux. *Astrophys. J.*, 835(1):45, 2017. doi: 10.3847/1538-4357/835/1/45.

[15] Dan Hooper, Tim Linden, and Abby Vieregg. Active Galactic Nuclei and the Origin of IceCube's Diffuse Neutrino Flux. *JCAP*, 02:012, 2019. doi: 10.1088/1475-7516/2019/02/012.

[16] Chengchao Yuan, Kohta Murase, and Peter Mészáros. Complementarity of Stacking and Multiplet Constraints on the Blazar Contribution to the Cumulative High-Energy Neutrino Intensity. *Astrophys. J.*, 890:25, 2020. doi: 10.3847/1538-4357/ab65ea.

[17] Daniel Smith, Dan Hooper, and Abigail Vieregg. Revisiting AGN as the source of IceCube's diffuse neutrino flux. *JCAP*, 03:031, 2021. doi: 10.1088/1475-7516/2021/03/031.

[18] Todd A. Thompson, Eliot Quataert, Eli Waxman, Norman Murray, and Crystal L. Martin. Magnetic fields in starburst galaxies and the origin of the fir-radio correlation. *Astrophys. J.*, 645:186–198, 2006. doi: 10.1086/504035.

[19] M. Ajello, M. Di Mauro, V.S. Paliya, and S. Garrappa. The γ-ray Emission of Star-Forming Galaxies. *Astrophys. J.*, 894(2):88, 2020. doi: 10.3847/1538-4357/ab86a6.

[20] P. Kornecki, L. J. Pellizza, S. del Palacio, A. L. Müller, J. F. Albacete-Colombo, and G. E. Romero. γ-ray/infrared luminosity correlation of star-forming galaxies. *Astron. Astrophys.*, 641:A147, 2020. doi: 10.1051/0004-6361/202038428.

[21] P. Kornecki, E. Peretti, S. del Palacio, P. Benaglia, and L. J. Pellizza. Exploring the physics behind the non-thermal emission from star-forming galaxies detected in γ rays. *Astron. Astrophys.*, 657:A49, 2022. doi: 10.1051/0004-6361/202141295.

[22] VERITAS Collaboration, V. A. Acciari, E. Aliu, T. Arlen, T. Aune, and Bautista et al. A connection between star formation activity and cosmic rays in the starburst galaxy M82. , 462(7274):770–772, December 2009. doi: 10.1038/nature08557.

[23] H. E. S. S. Collaboration, H. Abdalla, F. Aharonian, F. Ait Benkhali, E. O. Angüner, and Arakawa et al. The starburst galaxy NGC 253 revisited by H.E.S.S. and Fermi-LAT. , 617:A73, September 2018. doi: 10.1051/0004-6361/201833202.

[24] A. Abdul Halim et al. Constraining the sources of ultra-high-energy cosmic rays across and above the ankle with the spectrum and composition data measured at the Pierre Auger Observatory. *JCAP*, 05:024, 2023. doi: 10.1088/1475-7516/2023/05/024.

[25] Pedro Abreu et al. Arrival Directions of Cosmic Rays above 32 EeV from Phase One of the Pierre Auger Observatory. *Astrophys. J.*, 935(2):170, 2022. doi: 10.3847/1538-4357/ac7d4e.

[26] B. S. Acharya et al. *Science with the Cherenkov Telescope Array*. WSP, 11 2018. ISBN 978-981-327-008-4. doi: 10.1142/10986.

[27] S. Adrian-Martinez et al. Letter of intent for KM3NeT 2.0. *J. Phys. G*, 43(8):084001, 2016. doi: 10.1088/0954-3899/43/8/084001.

[28] Robert C. Kennicutt, Jr. and Neal J. Evans, II. Star Formation in the Milky Way and Nearby Galaxies. *Ann. Rev. Astron. Astrophys.*, 50:531–608, 2012. doi: 10.1146/annurev-astro-081811-125610.

[29] Ivana Orlitova. Starburst galaxies. *arXiv e-prints*, art. arXiv:2012.12378, December 2020. doi: 10.48550/arXiv.2012.12378.

[30] Enrico Peretti, Giovanni Morlino, Pasquale Blasi, and Pierre Cristofari. Particle acceleration and multimessenger emission from starburst-driven galactic winds. *Mon. Not. Roy. Astron. Soc.*, 511(1):1336–1348, 2022. doi: 10.1093/mnras/stac084.

[31] Enrico Peretti, Pasquale Blasi, Felix Aharonian, and Giovanni Morlino. Cosmic ray transport and radiative processes in nuclei of starburst galaxies. *Mon. Not. Roy. Astron. Soc.*, 487(1):168–180, 2019. doi: 10.1093/mnras/stz1161.

[32] Enrico Peretti, Pasquale Blasi, Felix Aharonian, Giovanni Morlino, and Pierre Cristofari. Contribution of starburst nuclei to the diffuse gamma-ray and neutrino flux. *Mon. Not. Roy. Astron. Soc.*, 493(4), 2020. doi: 10.1093/mnras/staa698.

[33] Neal J. Evans, Jeong-Gyu Kim, and Eve C. Ostriker. Slow Star Formation in the Milky Way: Theory Meets Observations. , 929(1):L18, April 2022. doi: 10.3847/2041-8213/ac6427.

[34] F. Mannucci, R. Maiolino, G. Cresci, M. Della Valle, L. Vanzi, F. Ghinassi, V. D. Ivanov, N. M. Nagar, and A. Alonso-Herrero. The infrared supernova rate in starburst galaxies. , 401:519–530, April 2003. doi: 10.1051/0004-6361:20030198.

[35] Daniela Calzetti. Star Formation Rate Indicators. In Jesús Falcón-Barroso and Johan H. Knapen, editors, *Secular Evolution of Galaxies*, page 419. 2013. doi: 10.48550/arXiv.1208.2997.

[36] Cai-Na Hao, Robert C. Kennicutt, Benjamin D. Johnson, Daniela Calzetti, Daniel A. Dale, and John Moustakas. Dust-corrected Star Formation Rates of Galaxies. II. Combinations of Ultraviolet and Infrared Tracers. , 741(2):124, November 2011. doi: 10.1088/0004-637X/741/2/124.

[37] Maria Werhahn, Christoph Pfrommer, Philipp Girichidis, and Georg Winner. Cosmic rays and non-thermal emission in simulated galaxies. II. γ-ray maps, spectra and the far infrared-γ-ray relation. 5 2021. doi: 10.1093/mnras/stab1325.

[38] Maria Werhahn, Christoph Pfrommer, Philipp Girichidis, Ewald Puchwein, and Rüdiger Pakmor. Cosmic rays and non-thermal emission in simulated galaxies − I. Electron and proton spectra compared to Voyager-1 data. *Mon. Not. Roy. Astron. Soc.*, 505(3):3273–3294, 2021. doi: 10.1093/mnras/stab1324.

[39] Maria Werhahn, Christoph Pfrommer, and Philipp Girichidis. Cosmic rays and non-thermal emission in simulated galaxies: III. probing cosmic ray calorimetry with radio spectra and the FIR-radio correlation. 5 2021.

[40] Eric F. Bell. Estimating Star Formation Rates from Infrared and Radio Luminosities: The Origin of the Radio-Infrared Correlation. , 586(2):794–813, April 2003. doi: 10.1086/367829.

[41] Yu Gao and Philip M. Solomon. The Star Formation Rate and Dense Molecular Gas in Galaxies. , 606(1):271–290, May 2004. doi: 10.1086/382999.

[42] J. Dreyer, J. K. Becker, and W. Rhode. Neutrinos from Starburst-Galaxies: A source stacking analysis of AMANDA II and IceCube data. *Astrophys. Space Sci. Trans.*, 7:7–10, 2011. doi: 10.5194/astra-7-7-2011.

[43] Adam Onus, Mark R. Krumholz, and Christoph Federrath. Numerical calibration of the HCN-star formation correlation. , 479(2):1702–1710, September 2018. doi: 10.1093/mnras/sty1662.

[44] Jr. Kennicutt, Robert C. The Global Schmidt law in star forming galaxies. *Astrophys. J.*, 498:541, 1998. doi: 10.1086/305588.

[45] Jr. Kennicutt, Robert C. Star formation in galaxies along the Hubble sequence. *Ann. Rev. Astron. Astrophys.*, 36:189–231, 1998. doi: 10.1146/annurev.astro.36.1.189.

[46] Robert C. Kennicutt and Mithi A. C. De Los Reyes. Revisiting the integrated star formation law. ii. starbursts and the combined global schmidt law. *The Astrophysical Journal*, 908(1):61, Feb 2021. ISSN 1538-4357. doi: 10.3847/1538-4357/abd3a2. URL http://dx.doi.org/10.3847/1538-4357/abd3a2.

[47] Maarten Schmidt. The Rate of Star Formation. , 129:243, March 1959. doi: 10.1086/146614.

[48] Maarten Schmidt. The Rate of Star Formation. II. The Rate of Formation of Stars of Different Mass. , 137:758, April 1963. doi: 10.1086/147553.

[49] H. Abdalla et al. The starburst galaxy NGC 253 revisited by H.E.S.S. and Fermi-LAT. *Astron. Astrophys.*, 617:A73, 2018. doi: 10.1051/0004-6361/201833202.

[50] R. Abbasi et al. Search for High-energy Neutrinos from Ultraluminous Infrared Galaxies with IceCube. *Astrophys. J.*, 926(1):59, 2022. doi: 10.3847/1538-4357/ac3cb6.

[51] Yunchuan Xiang, Qingquan Jiang, and Xiaofei Lan. Fermi-LAT Detection of a New Starburst Galaxy Candidate: IRAS 13052-5711. *Astrophys. J.*, 953(1):95, 2023. doi: 10.3847/1538-4357/ace166.

[52] Antonio Ambrosone, Marco Chianese, Damiano F. G. Fiorillo, Antonio Marinelli, Gennaro Miele, and Ofelia Pisanti. Starburst galaxies strike back: a multi-messenger analysis with

Fermi-LAT and IceCube data. *Mon. Not. Roy. Astron. Soc.*, 503(3):4032–4049, 2021. doi: 10.1093/mnras/stab659.

[53] M.G. Aartsen et al. Evidence for High-Energy Extraterrestrial Neutrinos at the IceCube Detector. *Science*, 342:1242856, 2013. doi: 10.1126/science.1242856.

[54] M.G. Aartsen et al. First observation of PeV-energy neutrinos with IceCube. *Phys. Rev. Lett.*, 111:021103, 2013. doi: 10.1103/PhysRevLett.111.021103.

[55] M.G. Aartsen et al. Observation and Characterization of a Cosmic Muon Neutrino Flux from the Northern Hemisphere using six years of IceCube data. *Astrophys. J.*, 833(1):3, 2016. doi: 10.3847/0004-637X/833/1/3.

[56] M.G. Aartsen et al. The IceCube Neutrino Observatory - Contributions to ICRC 2017 Part II: Properties of the Atmospheric and Astrophysical Neutrino Flux. *preprint (1710.01191)*, 10 2017.

[57] J. Stettner. Measurement of the Diffuse Astrophysical Muon-Neutrino Spectrum with Ten Years of IceCube Data. *PoS*, ICRC2019:1017, 2020. doi: 10.22323/1.358.1017.

[58] M.G. Aartsen et al. Multimessenger observations of a flaring blazar coincident with high-energy neutrino IceCube-170922A. *Science*, 361(6398):eaat1378, 2018. doi: 10.1126/science.aat1378.

[59] M.G. Aartsen et al. Neutrino emission from the direction of the blazar TXS 0506+056 prior to the IceCube-170922A alert. *Science*, 361(6398):147–151, 2018. doi: 10.1126/science.aat2890.

[60] R. Abbasi et al. Evidence for neutrino emission from the nearby active galaxy NGC 1068. *Science*, 378(6619):538–543, 2022. doi: 10.1126/science.abg3395.

[61] Daniele Gaggero, Dario Grasso, Antonio Marinelli, Alfredo Urbano, and Mauro Valli. The gamma-ray and neutrino sky: A consistent picture of Fermi-LAT, Milagro, and IceCube results. *Astrophys. J. Lett.*, 815(2):L25, 2015. doi: 10.1088/2041-8205/815/2/L25.

[62] Peter B. Denton, Danny Marfatia, and Thomas J. Weiler. The Galactic Contribution to IceCube's Astrophysical Neutrino Flux. *JCAP*, 08:033, 2017. doi: 10.1088/1475-7516/2017/08/033.

[63] A. Albert et al. New constraints on all flavor Galactic diffuse neutrino emission with the ANTARES telescope. *Phys. Rev. D*, 96(6):062001, 2017. doi: 10.1103/PhysRevD.96.062001.

[64] A. Albert et al. Joint Constraints on Galactic Diffuse Neutrino Emission from the ANTARES and IceCube Neutrino Telescopes. *Astrophys. J. Lett.*, 868(2):L20, 2018. doi: 10.3847/2041-8213/aaeecf.

[65] M.G. Aartsen et al. Search for Sources of Astrophysical Neutrinos Using Seven Years of IceCube Cascade Events. *Astrophys. J.*, 886:12, 2019. doi: 10.3847/1538-4357/ab4ae2.

[66] A. Keivani et al. A Multimessenger Picture of the Flaring Blazar TXS 0506+056: implications for High-Energy Neutrino Emission and Cosmic Ray Acceleration. *Astrophys. J.*, 864(1):84, 2018. doi: 10.3847/1538-4357/aad59a.

[67] M. Cerruti, A. Zech, C. Boisson, G. Emery, S. Inoue, and J.-P. Lenain. Leptohadronic single-zone models for the electromagnetic and neutrino emission of TXS 0506+056. *Mon. Not. Roy. Astron. Soc.*, 483(1):L12–L16, 2019. doi: 10.1093/mnrasl/sly210.

[68] P. Padovani, P. Giommi, E. Resconi, T. Glauch, B. Arsioli, N. Sahakyan, and M. Huber. Dissecting the region around IceCube-170922A: the blazar TXS 0506+056 as the first cosmic neutrino source. *Mon. Not. Roy. Astron. Soc.*, 480(1):192–203, 2018. doi: 10.1093/mnras/sty1852.

[69] Shan Gao, Anatoli Fedynitch, Walter Winter, and Martin Pohl. Modelling the coincident observation of a high-energy neutrino and a bright blazar flare. *Nature Astron.*, 3(1):88–92, 2019. doi: 10.1038/s41550-018-0610-1.

[70] Xavier Rodrigues, Shan Gao, Anatoli Fedynitch, Andrea Palladino, and Walter Winter. Leptohadronic Blazar Models Applied to the 2014–2015 Flare of TXS 0506+056. *Astrophys. J. Lett.*, 874(2):L29, 2019. doi: 10.3847/2041-8213/ab1267.

[71] Andrea Palladino, Xavier Rodrigues, Shan Gao, and Walter Winter. Interpretation of the diffuse astrophysical neutrino flux in terms of the blazar sequence. *Astrophys. J.*, 871(1):41, 2019. doi: 10.3847/1538-4357/aaf507.

[72] A. V. Plavin, Y. Y. Kovalev, Y. A. Kovalev, and S. V. Troitsky. Directional association of TeV to PeV astrophysical neutrinos with radio blazars. *Astrophys. J.*, 908:157, 2021. doi: 10.3847/1538-4357/abceb8.

[73] S. Adrian-Martinez et al. The First Combined Search for Neutrino Point-sources in the Southern Hemisphere With the Antares and Icecube Neutrino Telescopes. *Astrophys. J.*, 823(1):65, 2016. doi: 10.3847/0004-637X/823/1/65.

[74] M.G. Aartsen et al. All-sky Search for Time-integrated Neutrino Emission from Astrophysical Sources with 7 yr of IceCube Data. *Astrophys. J.*, 835(2):151, 2017. doi: 10.3847/1538-4357/835/2/151.

[75] M.G. Aartsen et al. Search for steady point-like sources in the astrophysical muon neutrino flux with 8 years of IceCube data. *Eur. Phys. J. C*, 79(3):234, 2019. doi: 10.1140/epjc/s10052-019-6680-0.

[76] M.G. Aartsen et al. Time-Integrated Neutrino Source Searches with 10 Years of IceCube Data. *Phys. Rev. Lett.*, 124(5):051103, 2020. doi: 10.1103/PhysRevLett.124.051103.

[77] A. Albert et al. ANTARES and IceCube Combined Search for Neutrino Point-like and Extended Sources in the Southern Sky. *Astrophys. J.*, 892:92, 2020. doi: 10.3847/1538-4357/ab7afb.

[78] Eli Waxman and John N. Bahcall. High-energy neutrinos from cosmological gamma-ray burst fireballs. *Phys. Rev. Lett.*, 78:2292–2295, 1997. doi: 10.1103/PhysRevLett.78.2292.

[79] R. Abbasi et al. An absence of neutrinos associated with cosmic-ray acceleration in γ-ray bursts. *Nature*, 484:351–353, 2012. doi: 10.1038/nature11068.

[80] M.G. Aartsen et al. An All-Sky Search for Three Flavors of Neutrinos from Gamma-Ray Bursts with the IceCube Neutrino Observatory. *Astrophys. J.*, 824(2):115, 2016. doi: 10.3847/0004-637X/824/2/115.

[81] M.G. Aartsen et al. Extending the search for muon neutrinos coincident with gamma-ray bursts in IceCube data. *Astrophys. J.*, 843(2):112, 2017. doi: 10.3847/1538-4357/aa7569.

[82] M.G. Aartsen et al. Constraints on minute-scale transient astrophysical neutrino sources. *Phys. Rev. Lett.*, 122(5):051102, 2019. doi: 10.1103/PhysRevLett.122.051102.

[83] Kohta Murase, Markus Ahlers, and Brian C. Lacki. Testing the Hadronuclear Origin of PeV Neutrinos Observed with IceCube. *Phys. Rev. D*, 88(12):121301, 2013. doi: 10.1103/PhysRevD.88.121301.

[84] Irene Tamborra, Shin'ichiro Ando, and Kohta Murase. Star-forming galaxies as the origin of diffuse high-energy backgrounds: Gamma-ray and neutrino connections, and implications for starburst history. *JCAP*, 09:043, 2014. doi: 10.1088/1475-7516/2014/09/043.

[85] Keith Bechtol, Markus Ahlers, Mattia Di Mauro, Marco Ajello, and Justin Vandenbroucke. Evidence against star-forming galaxies as the dominant source of IceCube neutrinos. *Astrophys. J.*, 836(1):47, 2017. doi: 10.3847/1538-4357/836/1/47.

[86] Abraham Loeb and Eli Waxman. The Cumulative background of high energy neutrinos from starburst galaxies. *JCAP*, 05:003, 2006. doi: 10.1088/1475-7516/2006/05/003.

[87] Marco Chianese, Gennaro Miele, Stefano Morisi, and Edoardo Vitagliano. Low energy IceCube data and a possible Dark Matter related excess. *Phys. Lett. B*, 757:251–256, 2016. doi: 10.1016/j.physletb.2016.03.084.

[88] Andrea Palladino and Francesco Vissani. Extragalactic plus Galactic model for IceCube neutrino events. *Astrophys. J.*, 826(2):185, 2016. doi: 10.3847/0004-637X/826/2/185.

[89] Andrea Palladino, Maurizio Spurio, and Francesco Vissani. On the IceCube spectral anomaly. *JCAP*, 12:045, 2016. doi: 10.1088/1475-7516/2016/12/045.

[90] Marco Chianese, Rosa Mele, Gennaro Miele, Pasquale Migliozzi, and Stefano Morisi. Use of ANTARES and IceCube Data to Constrain a Single Power-law Neutrino Flux. *Astrophys. J.*, 851(1):36, 2017. doi: 10.3847/1538-4357/aa97e6.

[91] Xiao-Chuan Chang, Ruo-Yu Liu, and Xiang-Yu Wang. How far are the sources of IceCube neutrinos? Constraints from the diffuse TeV gamma-ray background. *Astrophys. J.*, 825: 148, 2016. doi: 10.3847/0004-637X/825/2/148.

[92] Di Xiao, Peter Mészáros, Kohta Murase, and Zi-gao Dai. Revisiting the Contributions of Supernova and Hypernova Remnants to the Diffuse High-energy Backgrounds: Constraints on Very High Redshift Injection. *Astrophys. J.*, 826(2):133, 2016. doi: 10.3847/0004-637X/826/2/133.

[93] Takahiro Sudoh, Tomonori Totani, and Norita Kawanaka. High-energy gamma-ray and neutrino production in star-forming galaxies across cosmic time: Difficulties in explaining the IceCube data. *Publ. Astron. Soc. Jap.*, 70(3), 2018. doi: 10.1093/pasj/psy039.

[94] Antonio Capanema, Arman Esmaili, and Kohta Murase. New constraints on the origin of medium-energy neutrinos observed by IceCube. *Phys. Rev. D*, 101(10):103012, 2020. doi: 10.1103/PhysRevD.101.103012.

[95] Antonio Capanema, Arman Esmaili, and Pasquale Dario Serpico. Where do IceCube neutrinos come from? Hints from the diffuse gamma-ray flux. *JCAP*, 02:037, 2021. doi: 10.1088/1475-7516/2021/02/037.

[96] Kohta Murase, Dafne Guetta, and Markus Ahlers. Hidden Cosmic-Ray Accelerators as an Origin of TeV-PeV Cosmic Neutrinos. *Phys. Rev. Lett.*, 116(7):071101, 2016. doi: 10.1103/PhysRevLett.116.071101.

[97] Kohta Murase and Kunihito Ioka. TeV–PeV Neutrinos from Low-Power Gamma-Ray Burst Jets inside Stars. *Phys. Rev. Lett.*, 111(12):121102, 2013. doi: 10.1103/PhysRevLett.111.121102.

[98] Shigeo S. Kimura, Kohta Murase, and Kenji Toma. Neutrino and Cosmic-Ray Emission and Cumulative Background from Radiatively Inefficient Accretion Flows in Low-Luminosity Active Galactic Nuclei. *Astrophys. J.*, 806:159, 2015. doi: 10.1088/0004-637X/806/2/159.

[99] Irene Tamborra and Shin'ichiro Ando. Diffuse emission of high-energy neutrinos from gamma-ray burst fireballs. *JCAP*, 09:036, 2015. doi: 10.1088/1475-7516/2015/9/036.

[100] Irene Tamborra and Shin'ichiro Ando. Inspecting the supernova–gamma-ray-burst connection with high-energy neutrinos. *Phys. Rev. D*, 93(5):053010, 2016. doi: 10.1103/PhysRevD.93.053010.

[101] Nicholas Senno, Kohta Murase, and Peter Meszaros. Choked Jets and Low-Luminosity Gamma-Ray Bursts as Hidden Neutrino Sources. *Phys. Rev. D*, 93(8):083003, 2016. doi: 10.1103/PhysRevD.93.083003.

[102] Peter B. Denton and Irene Tamborra. Exploring the Properties of Choked Gamma-ray Bursts with IceCube's High-energy Neutrinos. *Astrophys. J.*, 855(1):37, 2018. doi: 10.3847/1538-4357/aaab4a.

[103] Peter B. Denton and Irene Tamborra. The Bright and Choked Gamma-Ray Burst Contribution to the IceCube and ANTARES Low-Energy Excess. *JCAP*, 04:058, 2018. doi: 10.1088/1475-7516/2018/04/058.

[104] Peter B. Denton and Irene Tamborra. Invisible Neutrino Decay Could Resolve IceCube's Track and Cascade Tension. *Phys. Rev. Lett.*, 121(12):121802, 2018. doi: 10.1103/PhysRevLett.121.121802.

[105] Asli Abdullahi and Peter B. Denton. Visible Decay of Astrophysical Neutrinos at IceCube. *Phys. Rev. D*, 102(2):023018, 2020. doi: 10.1103/PhysRevD.102.023018.

[106] M. Chianese, G. Miele, and S. Morisi. Dark Matter interpretation of low energy IceCube MESE excess. *JCAP*, 01:007, 2017. doi: 10.1088/1475-7516/2017/01/007.

[107] Marco Chianese, Gennaro Miele, and Stefano Morisi. Interpreting IceCube 6-year HESE data as an evidence for hundred TeV decaying Dark Matter. *Phys. Lett. B*, 773:591–595, 2017. doi: 10.1016/j.physletb.2017.09.016.

[108] Marco Chianese, Gennaro Miele, Stefano Morisi, and Eduardo Peinado. Neutrinophilic Dark Matter in the epoch of IceCube and Fermi-LAT. *JCAP*, 12:016, 2018. doi: 10.1088/1475-7516/2018/12/016.

[109] Atri Bhattacharya, Arman Esmaili, Sergio Palomares-Ruiz, and Ina Sarcevic. Update on decaying and annihilating heavy dark matter with the 6-year IceCube HESE data. *JCAP*, 05:051, 2019. doi: 10.1088/1475-7516/2019/05/051.

[110] Marco Chianese, Damiano F.G. Fiorillo, Gennaro Miele, Stefano Morisi, and Ofelia Pisanti. Decaying dark matter at IceCube and its signature on High Energy gamma experiments. *JCAP*, 11:046, 2019. doi: 10.1088/1475-7516/2019/11/046.

[111] Ariane Dekker, Marco Chianese, and Shin'ichiro Ando. Probing dark matter signals in neutrino telescopes through angular power spectrum. *JCAP*, 09:007, 2020. doi: 10.1088/1475-7516/2020/09/007.

[112] Kenny C.Y. Ng et al. Sensitivities of KM3NeT on decaying dark matter. *preprint (2007.03692)*, 7 2020.

[113] Andrea Palladino, Anatoli Fedynitch, Rasmus W. Rasmussen, and Andrew M. Taylor. IceCube Neutrinos from Hadronically Powered Gamma-Ray Galaxies. *JCAP*, 09:004, 2019. doi: 10.1088/1475-7516/2019/09/004.

[114] Carlos Blanco. γ-cascade: a simple program to compute cosmological gamma-ray propagation. *JCAP*, 01:013, 2019. doi: 10.1088/1475-7516/2019/01/013.

[115] Lyubov G. Sveshnikova. The knee in galactic cosmic ray spectrum and variety in supernovae. *Astron. Astrophys.*, 409:799–808, 2003. doi: 10.1051/0004-6361:20030909.

[116] Charles D. Dermer, Kohta Murase, and Yoshiyuki Inoue. Photopion Production in Black-Hole Jets and Flat-Spectrum Radio Quasars as PeV Neutrino Sources. *JHEAp*, 3-4:29–40, 2014. doi: 10.1016/j.jheap.2014.09.001.

[117] Luis A. Anchordoqui, Thomas C. Paul, Luiz H. M. da Silva, Diego F. Torres, and Brian J. Vlcek. What IceCube data tell us about neutrino emission from star-forming galaxies (so far). *Phys. Rev. D*, 89(12):127304, 2014. doi: 10.1103/PhysRevD.89.127304.

[118] Kimberly Emig, Cecilia Lunardini, and Rogier Windhorst. Do high energy astrophysical neutrinos trace star formation? *JCAP*, 12:029, 2015. doi: 10.1088/1475-7516/2015/12/029.

[119] Reetanjali Moharana and Soebur Razzaque. Angular correlation between IceCube high-energy starting events and starburst sources. *JCAP*, 12:021, 2016. doi: 10.1088/1475-7516/2016/12/021.

[120] Cecilia Lunardini, Gregory S. Vance, Kimberly L. Emig, and Rogier A. Windhorst. Are starburst galaxies a common source of high energy neutrinos and cosmic rays? *JCAP*, 10:073, 2019. doi: 10.1088/1475-7516/2019/10/073.

[121] Cesar Rojas-Bravo and Miguel Araya. Search for gamma-ray emission from star-forming galaxies with Fermi LAT. *Mon. Not. Roy. Astron. Soc.*, 463(1):1068–1073, 2016. doi: 10.1093/mnras/stw2059.

[122] R.A. Chevalier and Andrew W. Clegg. Wind from a starburst galaxy nucleus. *Nature*, 317:44, 1985. doi: 10.1038/317044a0.

[123] Vladimir N. Zirakashvili and H.J. Voelk. Simple model of the outflow from starburst galaxies: application to radio observations. *Astrophys. J.*, 636:140–148, 2005. doi: 10.1086/497900.

[124] Timothy A. D. Paglione, Alan P. Marscher, James M. Jackson, and David L. Bertsch. Diffuse Gamma-Ray Emission from the Starburst Galaxy NGC 253. *Astrophys. J.*, 460:295, March 1996. doi: 10.1086/176969.

[125] Diego F. Torres. Theoretical modelling of the diffuse emission of gamma-rays from extreme regions of star formation. The Case of Arp 220. *Astrophys. J.*, 617:966–986, 2004. doi: 10.1086/425415.

[126] M. Persic, Y. Rephaeli, and Y. Arieli. Vhe emission from m82. 2008.

[127] Y. Rephaeli, Y. Arieli, and M. Persic. High Energy Emission from the Starburst Galaxy NGC253. *Mon. Not. Roy. Astron. Soc.*, 401:423, 2010. doi: 10.1111/j.1365-2966.2009.15661.x.

[128] Brian C. Lacki and Todd A. Thompson. Diffuse Hard X-ray Emission in Starburst Galaxies as Synchrotron from Very High Energy Electrons. *Astrophys. J.*, 762:29, 2013. doi: 10.1088/0004-637X/762/1/29.

[129] Tova M. Yoast-Hull, John E. Everett, J.S. Gallagher, and Ellen G. Zweibel. Winds, Clumps, and Interacting Cosmic Rays in M82. *Astrophys. J.*, 768:53, 2013. doi: 10.1088/0004-637X/768/1/53.

[130] Xilu Wang and Brian D. Fields. Are Starburst Galaxies Proton Calorimeters? *Mon. Not. Roy. Astron. Soc.*, 474(3):4073–4088, 2018. doi: 10.1093/mnras/stx2917.

[131] Mark R. Krumholz, Roland M. Crocker, Siyao Xu, A. Lazarian, M.T. Rosevear, and Jasper Bedwell-Wilson. Cosmic ray transport in starburst galaxies. *Mon. Not. Roy. Astron. Soc.*, 493(2):2817–2833, 2020. doi: 10.1093/mnras/staa493.

[132] Ji-Hoon Ha, Dongsu Ryu, and Hyesung Kang. Modeling of Cosmic-Ray Production and Transport and Estimation of Gamma-Ray and Neutrino Emissions in Starburst Galaxies. *Astrophys. J.*, 907(1):26, 2021. doi: 10.3847/1538-4357/abd247.

[133] Eduardo M. Gutiérrez, Gustavo E. Romero, and Florencia L. Vieyro. Cosmic rays from the nearby starburst galaxy NGC 253: the effect of a low luminosity active galactic nucleus. *Mon. Not. Roy. Astron. Soc.*, 494(2):2109–2116, 2020. doi: 10.1093/mnras/staa811.

[134] Robert H. Kraichnan. Inertial-Range Spectrum of Hydromagnetic Turbulence. *Phys. Fluids*, 8:1385–1387, 1965. doi: 10.1063/1.1761412.

[135] S.R. Kelner, Felex A. Aharonian, and V.V. Bugayov. Energy spectra of gamma-rays, electrons and neutrinos produced at proton-proton interactions in the very high energy regime. *Phys. Rev. D*, 74:034018, 2006. doi: 10.1103/PhysRevD.74.034018. [Erratum: Phys.Rev.D 79, 039901 (2009)].

[136] Alberto Franceschini and Giulia Rodighiero. The extragalactic background light revisited and the cosmic photon-photon opacity. *Astron. Astrophys.*, 603:A34, 2017. doi: 10.1051/0004-6361/201629684.

[137] Franceschini, Alberto and Rodighiero, Giulia. The extragalactic background light revisited and the cosmic photon-photon opacity (corrigendum). *A&A*, 614:C1, 2018. doi: 10.1051/0004-6361/201629684e. URL https://doi.org/10.1051/0004-6361/201629684e.

[138] Pierre Cristofari, Pasquale Blasi, and Elena Amato. The low rate of Galactic pevatrons. *Astroparticle Physics*, 123:102492, December 2020. doi: 10.1016/j.astropartphys.2020.102492.

[139] A. Abramowski et al. Acceleration of petaelectronvolt protons in the Galactic Centre. *Nature*, 531:476, 2016. doi: 10.1038/nature17147.

[140] A.U. Abeysekara et al. Multiple Galactic Sources with Emission Above 56 TeV Detected by HAWC. *Phys. Rev. Lett.*, 124(2):021102, 2020. doi: 10.1103/PhysRevLett.124.021102.

[141] Ana Laura Müller, Gustavo E. Romero, and Markus Roth. High-energy processes in starburst-driven winds. *Mon. Not. Roy. Astron. Soc.*, 496(2):2474–2481, 2020. doi: 10.1093/mnras/staa1720.

[142] Gustavo E. Romero, Ana Laura Müller, and Markus Roth. Particle acceleration in the superwinds of starburst galaxies. *Astron. Astrophys.*, 616:A57, 2018. doi: 10.1051/0004-6361/201832666.

[143] Luis Alfredo Anchordoqui. Acceleration of ultrahigh-energy cosmic rays in starburst superwinds. *Phys. Rev. D*, 97(6):063010, 2018. doi: 10.1103/PhysRevD.97.063010.

[144] Pasquale Blasi, Richard I. Epstein, and Angela V. Olinto. Ultrahigh-energy cosmic rays from young neutron star winds. *Astrophys. J. Lett.*, 533:L123, 2000. doi: 10.1086/312626.

[145] Jonathan Arons. Magnetars in the metagalaxy: an origin for ultrahigh-energy cosmic rays in the nearby universe. *Astrophys. J.*, 589:871–892, 2003. doi: 10.1086/374776.

[146] Eli Waxman. Cosmological gamma-ray bursts and the highest energy cosmic rays. *Phys. Rev. Lett.*, 75:386–389, 1995. doi: 10.1103/PhysRevLett.75.386.

[147] Glennys R. Farrar and Andrei Gruzinov. Giant AGN Flares and Cosmic Ray Bursts. *Astrophys. J.*, 693:329–332, 2009. doi: 10.1088/0004-637X/693/1/329.

[148] C. Gruppioni et al. The Herschel PEP/HerMES Luminosity Function. I: Probing the Evolution of PACS selected Galaxies to z 4. *Mon. Not. Roy. Astron. Soc.*, 432:23, 2013. doi: 10.1093/mnras/stt308.

[149] I. Delvecchio et al. Tracing the cosmic growth of supermassive black holes to z $\sim$ 3 with Herschel. *Mon. Not. Roy. Astron. Soc.*, 439(3):2736–2754, 2014. doi: 10.1093/mnras/stu130.

[150] G. Rodighiero, E. Daddi, I. Baronchelli, A. Cimatti, and A. et al. Renzini. The Lesser Role of Starbursts in Star Formation at z = 2. , 739(2):L40, October 2011. doi: 10.1088/2041-8205/739/2/L40.

[151] S. Abdollahi et al. *Fermi* Large Area Telescope Fourth Source Catalog. *Astrophys. J. Suppl.*, 247(1):33, 2020. doi: 10.3847/1538-4365/ab6bcb.

[152] G. Ghisellini, C. Righi, L. Costamante, and F. Tavecchio. The Fermi blazar sequence. *Mon. Not. Roy. Astron. Soc.*, 469(1):255–266, 2017. doi: 10.1093/mnras/stx806.

[153] Kohta Murase, Yoshiyuki Inoue, and Charles D. Dermer. Diffuse Neutrino Intensity from the Inner Jets of Active Galactic Nuclei: Impacts of External Photon Fields and the Blazar Sequence. *Phys. Rev. D*, 90(2):023007, 2014. doi: 10.1103/PhysRevD.90.023007.

[154] B. Theodore Zhang and Zhuo Li. Constraints on cosmic ray loading and PeV neutrino production in blazars. *JCAP*, 03:024, 2017. doi: 10.1088/1475-7516/2017/03/024.

[155] Yoshiyuki Inoue. Contribution of the Gamma-ray Loud Radio Galaxies Core Emissions to the Cosmic MeV and GeV Gamma-Ray Background Radiation. *Astrophys. J.*, 733:66, 2011. doi: 10.1088/0004-637X/733/1/66.

[156] M. Di Mauro, F. Calore, F. Donato, M. Ajello, and L. Latronico. Diffuse γ-ray emission from misaligned active galactic nuclei. *Astrophys. J.*, 780:161, 2014. doi: 10.1088/0004-637X/780/2/161.

[157] Nissim Fraija and Antonio Marinelli. Neutrino, Γ-ray, and Cosmic-ray Fluxes From the Core of the Closest Radio Galaxies. *Astrophys. J.*, 830(2):81, 2016. doi: 10.3847/0004-637X/830/2/81.

[158] Carlos Blanco and Dan Hooper. High-Energy Gamma Rays and Neutrinos from Nearby Radio Galaxies. *JCAP*, 12:017, 2017. doi: 10.1088/1475-7516/2017/12/017.

[159] S. Adrian-Martinez et al. Letter of intent for KM3NeT 2.0. *J. Phys. G*, 43(8):084001, 2016. doi: 10.1088/0954-3899/43/8/084001.

[160] Bair Shoibonov. Baikal-GVD - the Next Generation Neutrino Telescope in Lake Baikal. *J. Phys. Conf. Ser.*, 1263(1):012005, 2019. doi: 10.1088/1742-6596/1263/1/012005.

[161] M. Agostini et al. The Pacific Ocean Neutrino Experiment. *Nature Astron.*, 4(10):913–915, 2020. doi: 10.1038/s41550-020-1182-4.

[162] M.G. Aartsen et al. IceCube-Gen2: The Window to the Extreme Universe. *preprint (2008.04323)*, 8 2020.

[163] Antonio Ambrosone, Marco Chianese, Damiano F. G. Fiorillo, Antonio Marinelli, and Gennaro Miele. Could Nearby Star-forming Galaxies Light Up the Pointlike Neutrino Sky? *Astrophys. J. Lett.*, 919(2):L32, 2021. doi: 10.3847/2041-8213/ac25ff.

[164] A. K. Inoue, H. Hirashita, and H. Kamaya. Conversion law of infrared luminosity to star formation rate for galaxies. *Publ. Astron. Soc. Jap.*, 52:539, 2000. doi: 10.1093/pasj/52.3.539.

[165] Hiroyuki Hirashita, Veronique Buat, and Akio K. Inoue. Star formation rate in galaxies from uv, ir, and h-alpha estimators. *Astron. Astrophys.*, 410:83–100, 2003. doi: 10.1051/0004-6361:20031144.

[166] Fang-Ting Yuan, Tsutomu T. Takeuchi, Véronique Buat, Sébastien Heinis, Elodie Giovannoli, Katsuhiro L. Murata, Jorge Iglesias-Páramo, and Denis Burgarella. AKARI/IRC Broadband Mid-Infrared Data as an Indicator of the Star-Formation Rate. , 63:1207–1217, December 2011. doi: 10.1093/pasj/63.6.1207.

[167] A. Alonso-Herrero et al. Uncovering the deeply embedded AGN activity in the nuclear regions of the interacting galaxy Arp299. *Astrophys. J. Lett.*, 779:L14, 2013. doi: 10.1088/2041-8205/779/1/L14.

[168] Tova M. Yoast-Hull, John S. Gallagher, Susanne Aalto, and Eskil Varenius. γ-Ray emission from Arp 220: indications of an active galactic nucleus. *Mon. Not. Roy. Astron. Soc.*, 469 (1):L89–L93, 2017. doi: 10.1093/mnrasl/slx054.

[169] Xiao-Lei Guo, Yu-Liang Xin, Neng-Hui Liao, and Yi-Zhong Fan. Circinus Galaxy Revisted with 10 Years of Fermi-LAT Data. 5 2019. doi: 10.3847/1538-4357/ab44ba.

[170] Yoshiyuki Inoue, Dmitry Khangulyan, and Akihiro Doi. On the Origin of High-energy Neutrinos from NGC 1068: The Role of Nonthermal Coronal Activity. *Astrophys. J. Lett.*, 891(2):L33, 2020. doi: 10.3847/2041-8213/ab7661.

[171] Kohta Murase, Shigeo S. Kimura, and Peter Meszaros. Hidden Cores of Active Galactic Nuclei as the Origin of Medium-Energy Neutrinos: Critical Tests with the MeV Gamma-Ray Connection. *Phys. Rev. Lett.*, 125(1):011101, 2020. doi: 10.1103/PhysRevLett.125.011101.

[172] Yun-chuan Xiang, Jun-hao Deng, and Ze-jun Jiang. The Likely Counterpart to γ-Ray Excess from The Northwest Region of Arp 220. 5 2021.

[173] Ali Kheirandish, Kohta Murase, and Shigeo S. Kimura. High-Energy Neutrinos from Magnetized Coronae of Active Galactic Nuclei and Prospects for Identification of Seyfert Galaxies and Quasars in Neutrino Telescopes. 2 2021.

[174] Brent Groves, Michael A. Dopita, Ralph S. Sutherland, Lisa J. Kewley, Jörg Fischera, Claus Leitherer, Bernhard Brandl, and Wil van Breugel. Modeling the pan-spectral energy distribution of starburst galaxies. IV. the controlling parameters of the starburst SED. *The Astrophysical Journal Supplement Series*, 176(2):438–456, jun 2008. doi: 10.1086/528711. URL https://doi.org/10.1086/528711.

[175] Alberto D. Bolatto, Adam K. Leroy, Katherine Jameson, Eve Ostriker, Karl Gordon, Brandon Lawton, Snežana Stanimirović, Frank P. Israel, Suzanne C. Madden, Sacha Hony, Karin M. Sandstrom, Caroline Bot, Mónica Rubio, P. Frank Winkler, Julia Roman-Duval, Jacco Th. van Loon, Joana M. Oliveira, and Rémy Indebetouw. THE STATE OF THE GAS AND THE RELATION BETWEEN GAS AND STAR FORMATION AT LOW METALLICITY: THE SMALL MAGELLANIC CLOUD. *The Astrophysical Journal*, 741(1):12, oct 2011. doi: 10.1088/0004-637x/741/1/12. URL https://doi.org/10.1088/0004-637x/741/1/12.

[176] B.-Q. For, B. S. Koribalski, and T. H. Jarrett. Gas and star formation in the circinus galaxy. *Monthly Notices of the Royal Astronomical Society*, 425(3):1934–1950, Aug 2012. ISSN 0035-8711. doi: 10.1111/j.1365-2966.2012.21416.x. URL http://dx.doi.org/10.1111/j.1365-2966.2012.21416.x.

[177] S. Rahmani, S. Lianou, and P. Barmby. Star formation laws in the Andromeda galaxy: gas, stars, metals and the surface density of star formation. *Monthly Notices of the Royal*

Astronomical Society, 456(4):4128–4144, 01 2016. ISSN 0035-8711. doi: 10.1093/mnras/stv2951. URL https://doi.org/10.1093/mnras/stv2951.

[178] Luis A. Anchordoqui, John F. Krizmanic, and Floyd W. Stecker. High-Energy Neutrinos from NGC 1068. 2 2021.

[179] S. Aiello et al. Sensitivity of the KM3NeT/ARCA neutrino telescope to point-like neutrino sources. *Astropart. Phys.*, 111:100–110, 2019. doi: 10.1016/j.astropartphys.2019.04.002.

[180] Constantin Steppa and Kathrin Egberts. Modelling the Galactic very-high-energy γ-ray source population. *Astron. Astrophys.*, 643:A137, 2020. doi: 10.1051/0004-6361/202038172.

[181] Björn Eichmann, Foteini Oikonomou, Silvia Salvatore, Ralf-Jürgen Dettmar, and Julia Becker Tjus. Solving the Multimessenger Puzzle of the AGN-starburst Composite Galaxy NGC 1068. *Astrophys. J.*, 939(1):43, 2022. doi: 10.3847/1538-4357/ac9588.

[182] R. R. J. Antonucci and J. S. Miller. Spectropolarimetry and the nature of NGC 1068. *Astrophys. J.*, 297:621–732, 1985. doi: 10.1086/163559.

[183] Jack F. Gallimore, David J. Axon, Christopher P. O'Dea, Stefi A. Baum, and Alan Pedlar. A survey of kiloparsec-scale radio outflows in radio-quiet active galactic nuclei. *The Astronomical Journal*, 132(2):546, jun 2006. doi: 10.1086/504593. URL https://dx.doi.org/10.1086/504593.

[184] Tomonari Michiyama, Yoshiyuki Inoue, Akihiro Doi, and Dmitry Khangulyan. ALMA Detection of Parsec-scale Blobs at the Head of a Kiloparsec-scale Jet in the Nearby Seyfert Galaxy NGC 1068. *Astrophys. J. Lett.*, 936(1):L1, 2022. doi: 10.3847/2041-8213/ac8935.

[185] Misaki Mizumoto, Takuma Izumi, and Kotaro Kohno. Kinetic energy transfer from x-ray ultrafast outflows to millimeter/submillimeter cold molecular outflows in seyfert galaxies. *The Astrophysical Journal*, 871(2):156, jan 2019. doi: 10.3847/1538-4357/aaf814. URL https://dx.doi.org/10.3847/1538-4357/aaf814.

[186] Enrico Peretti, Alessandra Lamastra, Francesco Gabriele Saturni, Markus Ahlers, Pasquale Blasi, Giovanni Morlino, and Pierre Cristofari. Diffusive shock acceleration at EeV and associated multimessenger flux from ultra-fast outflows driven by Active Galactic Nuclei. 1 2023.

[187] V. A. Acciari et al. Constraints on gamma-ray and neutrino emission from NGC 1068 with the MAGIC telescopes. *Astrophys. J.*, 883:135, 2019. doi: 10.3847/1538-4357/ab3a51.

[188] A.D. Avrorin et al. Neutrino Telescope in Lake Baikal: Present and Future. *PoS*, ICRC2019:1011, 2020. doi: 10.22323/1.358.1011.

[189] Antonio Ambrosone, Marco Chianese, Damiano F G Fiorillo, Antonio Marinelli, and Gennaro Miele. Observable signatures of cosmic rays transport in Starburst Galaxies on gamma-ray and neutrino observations. *Monthly Notices of the Royal Astronomical Society*, 515(4):5389–5399, 07 2022. ISSN 0035-8711. doi: 10.1093/mnras/stac2133. URL `https://doi.org/10.1093/mnras/stac2133`.

[190] Naoya Shimono, Tomonori Totani, and Takahiro Sudoh. Prospects of newly detecting nearby star-forming galaxies by the Cherenkov Telescope Array. 3 2021.

[191] Yun-chuan Xiang, Ze-jun Jiang, and Yun-yong Tang. Evaluation of Hadronic Emission in Starburst Galaxies and Star-forming Galaxies. 5 2021.

[192] Ellis R. Owen, Khee-Gan Lee, and Albert K. H. Kong. Characterising the signatures of star-forming galaxies in the extra-galactic γ-ray background. 6 2021. doi: 10.1093/mnras/stab1707.

[193] Ellis R. Owen, Albert K. H. Kong, and Khee-Gan Lee. The extragalactic γ-ray background: imprints from the physical properties and evolution of star-forming galaxy populations. *Mon. Not. Roy. Astron. Soc.*, 513(2):2335–2348, 2022. doi: 10.1093/mnras/stac1079.

[194] Matt A. Roth, Mark R. Krumholz, Roland M. Crocker, and Todd A. Thompson. CONGRuENTS (COsmic-ray, Neutrino, Gamma-ray and Radio Non-Thermal Spectra). I. A predictive model for galactic non-thermal emission. 12 2022.

[195] Matt A. Roth, Mark R. Krumholz, Roland M. Crocker, and Silvia Celli. The diffuse γ-ray background is dominated by star-forming galaxies. *Nature*, 597(7876):341–344, 2021. doi: 10.1038/s41586-021-03802-x.

[196] A. Albert et al. Science Case for a Wide Field-of-View Very-High-Energy Gamma-Ray Observatory in the Southern Hemisphere. 2 2019.

[197] Jim Hinton. The Southern Wide-field Gamma-ray Observatory: Status and Prospects. *PoS*, ICRC2021:023, 2021. doi: 10.22323/1.395.0023.

[198] Shigeru Yoshida and Kohta Murase. Constraining photohadronic scenarios for the unified origin of IceCube neutrinos and ultrahigh-energy cosmic rays. *Phys. Rev. D*, 102(8):083023, 2020. doi: 10.1103/PhysRevD.102.083023.

[199] M. Ackermann et al. The spectrum of isotropic diffuse gamma-ray emission between 100 MeV and 820 GeV. *Astrophys. J.*, 799:86, 2015. doi: 10.1088/0004-637X/799/1/86.

[200] Antonio Ambrosone, Marco Chianese, Damiano F. G. Fiorillo, Antonio Marinelli, and Gennaro Miele. Starburst Nuclei as Light Dark Matter Laboratories. 10 2022.

[201] N. Aghanim et al. Planck 2018 results. VI. Cosmological parameters. *Astron. Astrophys.*, 641:A6, 2020. doi: 10.1051/0004-6361/201833910. [Erratum: Astron.Astrophys. 652, C4 (2021)].

[202] Gianfranco Bertone and Tim Tait, M. P. A new era in the search for dark matter. *Nature*, 562(7725):51–56, 2018. doi: 10.1038/s41586-018-0542-z.

[203] Felix Kahlhoefer. Review of LHC Dark Matter Searches. *Int. J. Mod. Phys. A*, 32(13): 1730006, 2017. doi: 10.1142/S0217751X1730006X.

[204] Carlos Pérez de los Heros. Status, Challenges and Directions in Indirect Dark Matter Searches. *Symmetry*, 12(10):1648, 2020. doi: 10.3390/sym12101648.

[205] Julien Billard et al. Direct detection of dark matter—APPEC committee report*. *Rept. Prog. Phys.*, 85(5):056201, 2022. doi: 10.1088/1361-6633/ac5754.

[206] Fabio Iocco, Miguel Pato, and Gianfranco Bertone. Evidence for dark matter in the inner Milky Way. *Nature Phys.*, 11:245–248, 2015. doi: 10.1038/nphys3237.

[207] Gianfranco Bertone and Dan Hooper. History of dark matter. *Rev. Mod. Phys.*, 90(4): 045002, 2018. doi: 10.1103/RevModPhys.90.045002.

[208] Paolo Salucci. The distribution of dark matter in galaxies. *Astron. Astrophys. Rev.*, 27 (1):2, 2019. doi: 10.1007/s00159-018-0113-1.

[209] Chiara Arina. Impact of cosmological and astrophysical constraints on dark matter simplified models. *Front. Astron. Space Sci.*, 5:30, 2018. doi: 10.3389/fspas.2018.00030.

[210] Eric Cotner and Alexander Kusenko. Astrophysical constraints on dark-matter Q-balls in the presence of baryon-violating operators. *Phys. Rev. D*, 94(12):123006, 2016. doi: 10.1103/PhysRevD.94.123006.

[211] Anne M. Green. Dark matter in astrophysics/cosmology. *SciPost Phys. Lect. Notes*, 37:1, 2022. doi: 10.21468/SciPostPhysLectNotes.37.

[212] Antonino Del Popolo. Dark matter and structure formation a review. *Astron. Rep.*, 51: 169–196, 2007. doi: 10.1134/S1063772907030018.

[213] Yacine Ali-Haïmoud, Jens Chluba, and Marc Kamionkowski. Constraints on Dark Matter Interactions with Standard Model Particles from Cosmic Microwave Background Spectral Distortions. *Phys. Rev. Lett.*, 115(7):071304, 2015. doi: 10.1103/PhysRevLett.115.071304.

[214] Vera Gluscevic and Kimberly K. Boddy. Constraints on Scattering of keV–TeV Dark Matter with Protons in the Early Universe. *Phys. Rev. Lett.*, 121(8):081301, 2018. doi: 10.1103/PhysRevLett.121.081301.

[215] Weishuang Linda Xu, Cora Dvorkin, and Andrew Chael. Probing sub-GeV Dark Matter-Baryon Scattering with Cosmological Observables. *Phys. Rev. D*, 97(10):103530, 2018. doi: 10.1103/PhysRevD.97.103530.

[216] Tracy R. Slatyer and Chih-Liang Wu. Early-universe constraints on dark matter-baryon scattering and their implications for a global 21 cm signal. *Phys. Rev. D*, 98:023013, Jul 2018. doi: 10.1103/PhysRevD.98.023013. URL `https://link.aps.org/doi/10.1103/PhysRevD.98.023013`.

[217] E. O. Nadler et al. Milky Way Satellite Census. III. Constraints on Dark Matter Properties from Observations of Milky Way Satellite Galaxies. *Phys. Rev. Lett.*, 126:091101, 2021. doi: 10.1103/PhysRevLett.126.091101.

[218] Keir K. Rogers, Cora Dvorkin, and Hiranya V. Peiris. Limits on the Light Dark Matter–Proton Cross Section from Cosmic Large-Scale Structure. *Phys. Rev. Lett.*, 128(17): 171301, 2022. doi: 10.1103/PhysRevLett.128.171301.

[219] N. Daci, Isabelle De Bruyn, S. Lowette, M. H. G. Tytgat, and B. Zaldivar. Simplified SIMPs and the LHC. *JHEP*, 11:108, 2015. doi: 10.1007/JHEP11(2015)108.

[220] Christopher V. Cappiello, Kenny C. Y. Ng, and John F. Beacom. Reverse Direct Detection: Cosmic Ray Scattering With Light Dark Matter. *Phys. Rev. D*, 99(6):063004, 2019. doi: 10.1103/PhysRevD.99.063004.

[221] Torsten Bringmann and Maxim Pospelov. Novel direct detection constraints on light dark matter. *Phys. Rev. Lett.*, 122(17):171801, 2019. doi: 10.1103/PhysRevLett.122.171801.

[222] Yohei Ema, Filippo Sala, and Ryosuke Sato. Light Dark Matter at Neutrino Experiments. *Phys. Rev. Lett.*, 122(18):181802, 2019. doi: 10.1103/PhysRevLett.122.181802.

[223] Yohei Ema, Filippo Sala, and Ryosuke Sato. Neutrino experiments probe hadrophilic light dark matter. *SciPost Phys.*, 10(3):072, 2021. doi: 10.21468/SciPostPhys.10.3.072.

[224] Jin-Wei Wang, Alessandro Granelli, and Piero Ullio. Direct Detection Constraints on Blazar-Boosted Dark Matter. *Phys. Rev. Lett.*, 128:221104, 2022. doi: 10.1103/PhysRevLett.128.221104.

[225] Alessandro Granelli, Piero Ullio, and Jin-Wei Wang. Blazar-boosted dark matter at Super-Kamiokande. *JCAP*, 07(07):013, 2022. doi: 10.1088/1475-7516/2022/07/013.

[226] Roberta Calabrese, Marco Chianese, Damiano F. G. Fiorillo, and Ninetta Saviano. Direct detection of light dark matter from evaporating primordial black holes. *Phys. Rev. D*, 105 (2):L021302, 2022. doi: 10.1103/PhysRevD.105.L021302.

[227] Roberta Calabrese, Marco Chianese, Damiano F. G. Fiorillo, and Ninetta Saviano. Electron scattering of light new particles from evaporating primordial black holes. *Phys. Rev. D*, 105(10):103024, 2022. doi: 10.1103/PhysRevD.105.103024.

[228] Kaustubh Agashe, Yanou Cui, Lina Necib, and Jesse Thaler. (In)direct Detection of Boosted Dark Matter. *JCAP*, 10:062, 2014. doi: 10.1088/1475-7516/2014/10/062.

[229] Gian F. Giudice, Doojin Kim, Jong-Chul Park, and Seodong Shin. Inelastic Boosted Dark Matter at Direct Detection Experiments. *Phys. Lett. B*, 780:543–552, 2018. doi: 10.1016/j.physletb.2018.03.043.

[230] Christopher V. Cappiello and John F. Beacom. Strong New Limits on Light Dark Matter from Neutrino Experiments. *Phys. Rev. D*, 100(10):103011, 2019. doi: 10.1103/PhysRevD.104.069901. [Erratum: Phys.Rev.D 104, 069901 (2021)].

[231] James Alvey, Miguel Campos, Malcolm Fairbairn, and Tevong You. Detecting Light Dark Matter via Inelastic Cosmic Ray Collisions. *Phys. Rev. Lett.*, 123:261802, 2019. doi: 10.1103/PhysRevLett.123.261802.

[232] James B. Dent, Bhaskar Dutta, Jayden L. Newstead, and Ian M. Shoemaker. Bounds on Cosmic Ray-Boosted Dark Matter in Simplified Models and its Corresponding Neutrino-Floor. *Phys. Rev. D*, 101(11):116007, 2020. doi: 10.1103/PhysRevD.101.116007.

[233] Joshua Berger, Yanou Cui, Mathew Graham, Lina Necib, Gianluca Petrillo, Dane Stocks, Yun-Tse Tsai, and Yue Zhao. Prospects for detecting boosted dark matter in DUNE through hadronic interactions. *Phys. Rev. D*, 103(9):095012, 2021. doi: 10.1103/PhysRevD.103.095012.

[234] Wenyu Wang, Lei Wu, Jin Min Yang, Hang Zhou, and Bin Zhu. Cosmic ray boosted sub-GeV gravitationally interacting dark matter in direct detection. *JHEP*, 12:072, 2020. doi: 10.1007/JHEP12(2020)072. [Erratum: JHEP 02, 052 (2021)].

[235] Gang Guo, Yue-Lin Sming Tsai, and Meng-Ru Wu. Probing cosmic-ray accelerated light dark matter with IceCube. *JCAP*, 10:049, 2020. doi: 10.1088/1475-7516/2020/10/049.

[236] Yongsoo Jho, Jong-Chul Park, Seong Chan Park, and Po-Yan Tseng. Leptonic New Force and Cosmic-ray Boosted Dark Matter for the XENON1T Excess. *Phys. Lett. B*, 811: 135863, 2020. doi: 10.1016/j.physletb.2020.135863.

[237] Gang Guo, Yue-Lin Sming Tsai, Meng-Ru Wu, and Qiang Yuan. Elastic and Inelastic Scattering of Cosmic-Rays on Sub-GeV Dark Matter. *Phys. Rev. D*, 102(10):103004, 2020. doi: 10.1103/PhysRevD.102.103004.

[238] James B. Dent, Bhaskar Dutta, Jayden L. Newstead, Ian M. Shoemaker, and Natalia Tapia Arellano. Present and future status of light dark matter models from cosmic-ray electron upscattering. *Phys. Rev. D*, 103:095015, 2021. doi: 10.1103/PhysRevD.103.095015.

[239] Nicole F. Bell, James B. Dent, Bhaskar Dutta, Sumit Ghosh, Jason Kumar, Jayden L. Newstead, and Ian M. Shoemaker. Cosmic-ray upscattered inelastic dark matter. *Phys. Rev. D*, 104:076020, 2021. doi: 10.1103/PhysRevD.104.076020.

[240] Jie-Cheng Feng, Xian-Wei Kang, Chih-Ting Lu, Yue-Lin Sming Tsai, and Feng-Shou Zhang. Revising inelastic dark matter direct detection by including the cosmic ray acceleration. *JHEP*, 04:080, 2022. doi: 10.1007/JHEP04(2022)080.

[241] Anirban Das and Manibrata Sen. Boosted dark matter from diffuse supernova neutrinos. *Phys. Rev. D*, 104(7):075029, 2021. doi: 10.1103/PhysRevD.104.075029.

[242] Chen Xia, Yan-Hao Xu, and Yu-Feng Zhou. Production and attenuation of cosmic-ray boosted dark matter. *JCAP*, 02(02):028, 2022. doi: 10.1088/1475-7516/2022/02/028.

[243] Chen Xia, Yan-Hao Xu, and Yu-Feng Zhou. Azimuthal asymmetry in cosmic-ray boosted dark matter flux. 6 2022.

[244] C. Kachulis et al. Search for Boosted Dark Matter Interacting With Electrons in Super-Kamiokande. *Phys. Rev. Lett.*, 120(22):221301, 2018. doi: 10.1103/PhysRevLett.120.221301.

[245] Kyrylo Bondarenko, Alexey Boyarsky, Torsten Bringmann, Marco Hufnagel, Kai Schmidt-Hoberg, and Anastasia Sokolenko. Direct detection and complementary constraints for sub-GeV dark matter. *JHEP*, 03:118, 2020. doi: 10.1007/JHEP03(2020)118.

[246] M. Andriamirado et al. Limits on sub-GeV dark matter from the PROSPECT reactor antineutrino experiment. *Phys. Rev. D*, 104(1):012009, 2021. doi: 10.1103/PhysRevD.104.012009.

[247] Xiangyi Cui et al. Search for Cosmic-Ray Boosted Sub-GeV Dark Matter at the PandaX-II Experiment. *Phys. Rev. Lett.*, 128(17):171801, 2022. doi: 10.1103/PhysRevLett.128.171801.

[248] R. Xu et al. Constraints on sub-GeV dark matter boosted by cosmic rays from the CDEX-10 experiment at the China Jinping Underground Laboratory. *Phys. Rev. D*, 106(5):052008, 2022. doi: 10.1103/PhysRevD.106.052008.

[249] Tarak Nath Maity and Ranjan Laha. Cosmic-ray boosted dark matter in Xe-based direct detection experiments. 10 2022.

[250] Francesc Ferrer, Gonzalo Herrera, and Alejandro Ibarra. New constraints on the dark matter-neutrino and dark matter-photon scattering cross sections from TXS 0506+056. 9 2022.

[251] Mikhail Gorchtein, Stefano Profumo, and Lorenzo Ubaldi. Erratum: Probing dark matter with active galactic nuclei jets [phys. rev. d 82, 083514 (2010)]. *Phys. Rev. D*, 84:069903, Sep 2011. doi: 10.1103/PhysRevD.84.069903. URL `https://link.aps.org/doi/10.1103/PhysRevD.84.069903`.

[252] Marina Cermeño, Céline Degrande, and Luca Mantani. Signatures of leptophilic t-channel dark matter from active galactic nuclei. *Phys. Rev. D*, 105(8):083019, 2022. doi: 10.1103/PhysRevD.105.083019.

[253] Maria Benito, Nicolas Bernal, Nassim Bozorgnia, Francesca Calore, and Fabio Iocco. Particle Dark Matter Constraints: the Effect of Galactic Uncertainties. *JCAP*, 02:007, 2017. doi: 10.1088/1475-7516/2017/02/007. [Erratum: JCAP 06, E01 (2018)].

[254] Maria Benito, Alessandro Cuoco, and Fabio Iocco. Handling the Uncertainties in the Galactic Dark Matter Distribution for Particle Dark Matter Searches. *JCAP*, 03:033, 2019. doi: 10.1088/1475-7516/2019/03/033.

[255] María Benito, Fabio Iocco, and Alessandro Cuoco. Uncertainties in the Galactic Dark Matter distribution: An update. *Phys. Dark Univ.*, 32:100826, 2021. doi: 10.1016/j.dark.2021.100826.

[256] Julio F. Navarro, Carlos S. Frenk, and Simon D. M. White. The Structure of cold dark matter halos. *Astrophys. J.*, 462:563–575, 1996. doi: 10.1086/177173.

[257] A. Burkert. The Structure of dark matter halos in dwarf galaxies. *Astrophys. J. Lett.*, 447: L25, 1995. doi: 10.1086/309560.

[258] I. Angeli. A consistent set of nuclear rms charge radii: properties of the radius surface R(N,Z). *Atom. Data Nucl. Data Tabl.*, 87(2):185–206, 2004. doi: 10.1016/j.adt.2004.04.002.

[259] James Alvey, Torsten Bringmann, and Helena Kolesova. No room to hide: implications of cosmic-ray upscattering for GeV-scale dark matter. 9 2022.

[260] Richard H. Cyburt, Brian D. Fields, Vasiliki Pavlidou, and Benjamin D. Wandelt. Constraining strong baryon dark matter interactions with primordial nucleosynthesis and cosmic rays. *Phys. Rev. D*, 65:123503, 2002. doi: 10.1103/PhysRevD.65.123503.

[261] Dan Hooper and Samuel D. McDermott. Robust Constraints and Novel Gamma-Ray Signatures of Dark Matter That Interacts Strongly With Nucleons. *Phys. Rev. D*, 97(11): 115006, 2018. doi: 10.1103/PhysRevD.97.115006.

[262] V. A. Acciari et al. A connection between star formation activity and cosmic rays in the starburst galaxy M 82. *Nature*, 462:770–772, 2009. doi: 10.1038/nature08557.

[263] Adrienne L. Erickcek, Paul J. Steinhardt, Dan McCammon, and Patrick C. McGuire. Constraints on the interactions between dark matter and baryons from the x-ray quantum calorimetry experiment. *Phys. Rev. D*, 76:042007, Aug 2007. doi: 10.1103/PhysRevD.76.042007. URL `https://link.aps.org/doi/10.1103/PhysRevD.76.042007`.

[264] A. Aguilar-Arevalo, D. Amidei, X. Bertou, M. Butner, and Cancelo et al. Search for low-mass wimps in a 0.6 kg day exposure of the damic experiment at snolab. *Phys. Rev. D*, 94:

082006, Oct 2016. doi: 10.1103/PhysRevD.94.082006. URL https://link.aps.org/doi/10.1103/PhysRevD.94.082006.

[265] G. Angloher et al. Results on light dark matter particles with a low-threshold CRESST-II detector. *Eur. Phys. J. C*, 76(1):25, 2016. doi: 10.1140/epjc/s10052-016-3877-3.

[266] Timon Emken and Chris Kouvaris. How blind are underground and surface detectors to strongly interacting Dark Matter? *Phys. Rev. D*, 97(11):115047, 2018. doi: 10.1103/PhysRevD.97.115047.

[267] E. Armengaud et al. Searching for low-mass dark matter particles with a massive Ge bolometer operated above-ground. *Phys. Rev. D*, 99(8):082003, 2019. doi: 10.1103/PhysRevD.99.082003.

[268] G. Angloher et al. Results on MeV-scale dark matter from a gram-scale cryogenic calorimeter operated above ground. *Eur. Phys. J. C*, 77(9):637, 2017. doi: 10.1140/epjc/s10052-017-5223-9.

[269] Chris Kouvaris and Josef Pradler. Probing sub-GeV Dark Matter with conventional detectors. *Phys. Rev. Lett.*, 118(3):031803, 2017. doi: 10.1103/PhysRevLett.118.031803.

[270] J. I. Collar. Search for a nonrelativistic component in the spectrum of cosmic rays at earth. *Phys. Rev. D*, 98:023005, Jul 2018. doi: 10.1103/PhysRevD.98.023005. URL https://link.aps.org/doi/10.1103/PhysRevD.98.023005.

[271] C. Awe, P. S. Barbeau, J. I. Collar, S. Hedges, and L. Li. Liquid scintillator response to proton recoils in the 10–100 keV range. *Phys. Rev. C*, 98(4):045802, 2018. doi: 10.1103/PhysRevC.98.045802.

[272] Matthew J. Dolan, Felix Kahlhoefer, and Christopher McCabe. Directly detecting sub-gev dark matter with electrons from nuclear scattering. *Phys. Rev. Lett.*, 121:101801, Sep 2018. doi: 10.1103/PhysRevLett.121.101801. URL https://link.aps.org/doi/10.1103/PhysRevLett.121.101801.

[273] M. Shafi Mahdawi and Glennys R. Farrar. Constraints on Dark Matter with a moderately large and velocity-dependent DM-nucleon cross-section. *JCAP*, 10:007, 2018. doi: 10.1088/1475-7516/2018/10/007.

[274] R. D. Blandford. Origin and evolution of massive black holes in galactic nuclei. *ASP Conf. Ser.*, 182:87, 1999.

[275] Piero Ullio, HongSheng Zhao, and Marc Kamionkowski. A Dark matter spike at the galactic center? *Phys. Rev. D*, 64:043504, 2001. doi: 10.1103/PhysRevD.64.043504.

[276] Paolo Gondolo and Joseph Silk. Dark matter annihilation at the galactic center. *Phys. Rev. Lett.*, 83:1719–1722, Aug 1999. doi: 10.1103/PhysRevLett.83.1719. URL `https://link.aps.org/doi/10.1103/PhysRevLett.83.1719`.

[277] Paolo Gondolo. Either neutralino dark matter or cuspy dark halos. *Phys. Lett. B*, 494: 181–186, 2000. doi: 10.1016/S0370-2693(00)01218-1.

[278] G. Bertone, G. Sigl, and J. Silk. Astrophysical limits on massive dark matter. *Mon. Not. Roy. Astron. Soc.*, 326:799–804, 2001. doi: 10.1046/j.1365-8711.2001.04650.x.

[279] Simon Knapen, Tongyan Lin, and Kathryn M. Zurek. Light Dark Matter: Models and Constraints. *Phys. Rev. D*, 96(11):115021, 2017. doi: 10.1103/PhysRevD.96.115021.

[280] Jae Hyeok Chang, Rouven Essig, and Samuel D. McDermott. Supernova 1987A Constraints on Sub-GeV Dark Sectors, Millicharged Particles, the QCD Axion, and an Axion-like Particle. *JHEP*, 09:051, 2018. doi: 10.1007/JHEP09(2018)051.

[281] William DeRocco, Peter W. Graham, Daniel Kasen, Gustavo Marques-Tavares, and Surjeet Rajendran. Supernova signals of light dark matter. *Phys. Rev. D*, 100(7):075018, 2019. doi: 10.1103/PhysRevD.100.075018.

[282] Antonio Ambrosone, Kathrine Mørch Groth, Enrico Peretti, and Markus Ahlers. Galactic Diffuse Neutrino Emission from Sources beyond the Discovery Horizon. 6 2023.

[283] Pasquale Blasi. The Origin of Galactic Cosmic Rays. *Astron. Astrophys. Rev.*, 21:70, 2013. doi: 10.1007/s00159-013-0070-7.

[284] Elena Amato and Pasquale Blasi. Cosmic ray transport in the Galaxy: A review. *Adv. Space Res.*, 62:2731–2749, 2018. doi: 10.1016/j.asr.2017.04.019.

[285] Stefano Gabici, Carmelo Evoli, Daniele Gaggero, Paolo Lipari, Philipp Mertsch, Elena Orlando, Andrew Strong, and Andrea Vittino. The origin of Galactic cosmic rays: challenges to the standard paradigm. *Int. J. Mod. Phys. D*, 28(15):1930022, 2019. doi: 10.1142/S0218271819300222.

[286] M. Ackermann et al. Search for Extended Sources in the Galactic Plane Using Six Years of *Fermi*-Large Area Telescope Pass 8 Data above 10 GeV. *Astrophys. J.*, 843(2):139, 2017. doi: 10.3847/1538-4357/aa775a.

[287] H. Abdalla et al. The H.E.S.S. Galactic plane survey. *Astron. Astrophys.*, 612:A1, 2018. doi: 10.1051/0004-6361/201732098.

[288] A. U. Abeysekara et al. Multiple Galactic Sources with Emission Above 56 TeV Detected by HAWC. *Phys. Rev. Lett.*, 124(2):021102, 2020. doi: 10.1103/PhysRevLett.124.021102.

[289] Zhen Cao et al. Ultrahigh-energy photons up to 1.4 petaelectronvolts from 12 γ-ray Galactic sources. *Nature*, 594(7861):33–36, 2021. doi: 10.1038/s41586-021-03498-z.

[290] M. Ackermann et al. Fermi-LAT Observations of the Diffuse Gamma-Ray Emission: Implications for Cosmic Rays and the Interstellar Medium. *Astrophys. J.*, 750:3, 2012. doi: 10.1088/0004-637X/750/1/3.

[291] M. Ajello et al. Fermi-LAT Observations of High-Energy γ-Ray Emission Toward the Galactic Center. *Astrophys. J.*, 819(1):44, 2016. doi: 10.3847/0004-637X/819/1/44.

[292] M. Amenomori et al. First Detection of sub-PeV Diffuse Gamma Rays from the Galactic Disk: Evidence for Ubiquitous Galactic Cosmic Rays beyond PeV Energies. *Phys. Rev. Lett.*, 126(14):141101, 2021. doi: 10.1103/PhysRevLett.126.141101.

[293] Shiping Zhao, R. Zhang, Y. Zhang, and Q. Yuan. Measurement of the diffuse gamma-ray emission from Galactic plane with LHAASO-KM2A. *PoS*, ICRC2021:859, 2021. doi: 10.22323/1.395.0859.

[294] Zhen Cao et al. Measurement of ultra-high-energy diffuse gamma-ray emission of the Galactic plane from 10 TeV to 1 PeV with LHAASO-KM2A. 5 2023.

[295] M. G. Aartsen et al. Characteristics of the diffuse astrophysical electron and tau neutrino flux with six years of IceCube high energy cascade data. *Phys. Rev. Lett.*, 125(12):121104, 2020. doi: 10.1103/PhysRevLett.125.121104.

[296] Daniele Gaggero, Dario Grasso, Antonio Marinelli, Alfredo Urbano, and Mauro Valli. KRAγ cosmic-ray diffusion models [Data set]. *Zenodo*, page https://doi.org/10.5281/zenodo.7070823, 2022. doi: 10.5281/zenodo.7070823.

[297] Markus Ahlers and Kohta Murase. Probing the Galactic Origin of the IceCube Excess with Gamma-Rays. *Phys. Rev. D*, 90(2):023010, 2014. doi: 10.1103/PhysRevD.90.023010.

[298] Matthias Mandelartz and Julia Becker Tjus. Prediction of the diffuse neutrino flux from cosmic ray interactions near supernova remnants. *Astropart. Phys.*, 65:80–100, 2015. doi: 10.1016/j.astropartphys.2014.12.002.

[299] Luis A. Anchordoqui, Haim Goldberg, Thomas C. Paul, Luiz H. M. da Silva, and Brian J. Vlcek. Estimating the contribution of Galactic sources to the diffuse neutrino flux. *Phys. Rev. D*, 90(12):123010, 2014. doi: 10.1103/PhysRevD.90.123010.

[300] Markus Ahlers, Yang Bai, Vernon Barger, and Ran Lu. Galactic neutrinos in the TeV to PeV range. *Phys. Rev. D*, 93(1):013009, 2016. doi: 10.1103/PhysRevD.93.013009.

[301] Ke Fang and Kohta Murase. Multimessenger Implications of Sub-PeV Diffuse Galactic Gamma-Ray Emission. *Astrophys. J.*, 919(2):93, 2021. doi: 10.3847/1538-4357/ac11f0.

[302] Takahiro Sudoh and John F. Beacom. Where are Milky Way's hadronic PeVatrons? *Phys. Rev. D*, 107(4):043002, 2023. doi: 10.1103/PhysRevD.107.043002.

[303] Georg Schwefer, Philipp Mertsch, and Christopher Wiebusch. Diffuse Emission of Galactic High-Energy Neutrinos from a Global Fit of Cosmic Rays. 11 2022.

[304] Takahiro Sudoh and John F. Beacom. Identifying Extended PeVatron Sources via Neutrino Shower Detection. 5 2023.

[305] Maddalena Cataldo, Giulia Pagliaroli, Vittoria Vecchiotti, and Francesco Lorenzo Villante. The TeV Gamma-Ray Luminosity of the Milky Way and the Contribution of H.E.S.S. Unresolved Sources to Very High Energy Diffuse Emission. *Astrophys. J.*, 904(2):85, 2020. doi: 10.3847/1538-4357/abc0ee.

[306] V. Vecchiotti, F. Zuccarini, F. L. Villante, and G. Pagliaroli. Unresolved Sources Naturally Contribute to PeV Gamma-Ray Diffuse Emission Observed by Tibet ASγ. *Astrophys. J.*, 928(1):19, 2022. doi: 10.3847/1538-4357/ac4df4.

[307] F. W. Stecker. Diffuse Fluxes of Cosmic High-Energy Neutrinos. *Astrophys. J.*, 228: 919–927, 1979. doi: 10.1086/156919.

[308] G. Domokos, B. Elliott, and S. Kovesi-Domokos. Cosmic neutrino production in the Milky Way. *J. Phys. G*, 19:899–912, 1993. doi: 10.1088/0954-3899/19/6/010.

[309] V. S. Berezinsky, T. K. Gaisser, F. Halzen, and Todor Stanev. Diffuse radiation from cosmic ray interactions in the galaxy. *Astropart. Phys.*, 1:281–288, 1993. doi: 10.1016/0927-6505(93)90014-5.

[310] G. Ingelman and M. Thunman. Particle production in the interstellar medium. 3 1996.

[311] Carmelo Evoli, Dario Grasso, and Luca Maccione. Diffuse Neutrino and Gamma-ray Emissions of the Galaxy above the TeV. *JCAP*, 06:003, 2007. doi: 10.1088/1475-7516/2007/06/003.

[312] A. Neronov, D. V. Semikoz, and C. Tchernin. PeV neutrinos from interactions of cosmic rays with the interstellar medium in the Galaxy. *Phys. Rev. D*, 89(10):103002, 2014. doi: 10.1103/PhysRevD.89.103002.

[313] Jagdish C. Joshi, Walter Winter, and Nayantara Gupta. How Many of the Observed Neutrino Events Can Be Described by Cosmic Ray Interactions in the Milky Way? *Mon. Not. Roy. Astron. Soc.*, 439(4):3414–3419, 2014. doi: 10.1093/mnras/stu189. [Erratum: Mon.Not.Roy.Astron.Soc. 446, 892 (2014)].

[314] M. Kachelrieß and S. Ostapchenko. Neutrino yield from Galactic cosmic rays. *Phys. Rev. D*, 90(8):083002, 2014. doi: 10.1103/PhysRevD.90.083002.

[315] Markus Ahlers and Francis Halzen. Pinpointing Extragalactic Neutrino Sources in Light of Recent IceCube Observations. *Phys. Rev. D*, 90(4):043005, 2014. doi: 10.1103/PhysRevD.90.043005.

[316] Kohta Murase and Eli Waxman. Constraining High-Energy Cosmic Neutrino Sources: Implications and Prospects. *Phys. Rev. D*, 94(10):103006, 2016. doi: 10.1103/PhysRevD.94.103006.

[317] Markus Ackermann et al. Astrophysics Uniquely Enabled by Observations of High-Energy Cosmic Neutrinos. *Bull. Am. Astron. Soc.*, 51:185, 2019.

[318] S. Aiello et al. Sensitivity of the KM3NeT/ARCA neutrino telescope to point-like neutrino sources. *Astropart. Phys.*, 111:100–110, 2019. doi: 10.1016/j.astropartphys.2019.04.002.

[319] M. G. Aartsen et al. IceCube-Gen2: the window to the extreme Universe. *J. Phys. G*, 48 (6):060501, 2021. doi: 10.1088/1361-6471/abbd48.

[320] R. Abbasi *et al.*, (IceCube-Gen2 Collaboration), *IceCube-Gen2 Technical Design: The IceCube-Gen2 Neutrino Observatory*. `http://icecube-gen2.wisc.edu/science/publications/TDR` (2023).

[321] M. G. Aartsen et al. Time-Integrated Neutrino Source Searches with 10 Years of IceCube Data. *Phys. Rev. Lett.*, 124(5):051103, 2020. doi: 10.1103/PhysRevLett.124.051103.

[322] Thomas Y. Steiman-Cameron, Mark Wolfire, and David Hollenbach. COBE and the Galactic Interstellar Medium: Geometry of the Spiral Arms from FIR Cooling Lines. *Astrophys. J.*, 722:1460–1473, 2010. doi: 10.1088/0004-637X/722/2/1460.

[323] D. A. Green. Constraints on the distribution of supernova remnants with Galactocentric radius. *Mon. Not. Roy. Astron. Soc.*, 454(2):1517–1524, 2015. doi: 10.1093/mnras/stv1885.

[324] K. M. Górski, E. Hivon, A. J. Banday, B. D. Wandelt, F. K. Hansen, M. Reinecke, and M. Bartelman. HEALPix - A Framework for high resolution discretization, and fast analysis of data distributed on the sphere. *Astrophys. J.*, 622:759–771, 2005. doi: 10.1086/427976.

[325] Andrea Zonca, Leo Singer, Daniel Lenz, Martin Reinecke, Cyrille Rosset, Eric Hivon, and Krzysztof Gorski. healpy: equal area pixelization and spherical harmonics transforms for data on the sphere in Python. *Journal of Open Source Software*, 4(35):1298, 2019. doi: 10.21105/joss.01298.

[326] Alfonso Garcia Soto et al. Sensitivity estimates for diffuse, point-like, and extended neutrino sources with KM3NeT/ARCA. *JINST*, 16(09):C09030, 2021. doi: 10.1088/1748-0221/16/09/C09030.

[327] S. Pfalzner. Universality of young cluster sequences. *Astron. Astrophys.*, 498:L37, 2009. doi: 10.1051/0004-6361/200912056.

[328] Esteban F. E. Morales, Friedrich Wyrowski, Frederic Schuller, and Karl M. Menten. Stellar clusters in the inner galaxy and their correlation with cold dust emission. *Astron. Astrophys.*, 560:A76, 2013. doi: 10.1051/0004-6361/201321626.

[329] N. V. Kharchenko, A. E. Piskunov, S. Roser, E. Schilbach, and Ralf-Dieter Scholz. Astrophysical parameters of Galactic open clusters. *Astron. Astrophys.*, 438:1163–1173, 2005. doi: 10.1051/0004-6361:20042523.

[330] Carlos A. Vargas Alvarez, Henry A. Kobulnicky, David R. Bradley, Sheila J. Kannappan, Mark A. Norris, Richard J. Cool, and Brendan P. Miller. The Distance to the Massive Galactic Cluster Westerlund 2 from a Spectroscopic and HST Photometric Study. *Astron. J.*, 145:125, 2013. doi: 10.1088/0004-6256/145/5/125.

[331] Vittoria Vecchiotti, Francesco L. Villante, and Giulia Pagliaroli. Unveiling the nature of galactic TeV sources with IceCube results. 7 2023.

[332] Thijs van Eeden. Astronomy potential of KM3NeT/ARCA230. *PoS*, ICRC2023:1075, 2023. doi: 10.22323/1.444.1075.

[333] A. Albert et al. Hint for a TeV neutrino emission from the Galactic Ridge with ANTARES. *Phys. Lett. B*, 841:137951, 2023. doi: 10.1016/j.physletb.2023.137951.

[334] A. Albert et al. Joint Constraints on Galactic Diffuse Neutrino Emission from the ANTARES and IceCube Neutrino Telescopes. *Astrophys. J. Lett.*, 868(2):L20, 2018. doi: 10.3847/2041-8213/aaeecf.

[335] Gilles Ferrand and Samar Safi-Harb. A Census of High-Energy Observations of Galactic Supernova Remnants. *Adv. Space Res.*, 49:1313–1319, 2012. doi: 10.1016/j.asr.2012.02.004.

[336] R. L. Workman et al. Review of Particle Physics. *PTEP*, 2022:083C01, 2022. doi: 10.1093/ptep/ptac097.

[337] W. Baade and F. Zwicky. On Super-Novae. *Proc. Nat. Acad. Sci.*, 20(5):254–259, 1934. doi: 10.1073/pnas.20.5.254.

[338] V. L. Ginzburg and S. I. Syrovatsky. Origin of Cosmic Rays. *Progress of Theoretical Physics Supplement*, 20:1–83, January 1961. doi: 10.1143/PTPS.20.1.

[339] G. F. Krymskii. A regular mechanism for the acceleration of charged particles on the front of a shock wave. *Akademiia Nauk SSSR Doklady*, 234:1306–1308, June 1977.

[340] R. D. Blandford and J. P. Ostriker. Particle Acceleration by Astrophysical Shocks. *Astrophys. J. Lett.*, 221:L29–L32, 1978. doi: 10.1086/182658.

[341] W. I. Axford, E. Leer, and G. Skadron. The Acceleration of Cosmic Rays by Shock Waves. In *15th International Cosmic Ray Conference*, page 132, 1977.

[342] A. R. Bell. The Acceleration of cosmic rays in shock fronts. I. *Mon. Not. Roy. Astron. Soc.*, 182:147–156, 1978.

[343] A. R. Bell. The acceleration of cosmic rays in shock fronts. II. *Mon. Not. Roy. Astron. Soc.*, 182:443–455, 1978.

[344] John M. Blondin, Eric B. Wright, Kazimierz J. Borkowski, and Stephen P. Reynolds. Transition to the Radiative Phase in Supernova Remnants. , 500(1):342–354, June 1998. doi: 10.1086/305708.

[345] Xiang-Yu Wang, Soebur Razzaque, Peter Meszaros, and Zi-Gao Dai. High-energy Cosmic Rays and Neutrinos from Semi-relativistic Hypernovae. *Phys. Rev. D*, 76:083009, 2007. doi: 10.1103/PhysRevD.76.083009.

[346] Dafne Guetta and Massimo Della Valle. On the Rates of Gamma Ray Bursts and Type Ib/c Supernovae. *Astrophys. J. Lett.*, 657:L73–L76, 2007. doi: 10.1086/511417.

[347] Iair Arcavi et al. Core-Collapse Supernovae from the Palomar Transient Factory: Indications for a Different Population in Dwarf Galaxies. *Astrophys. J.*, 721:777–784, 2010. doi: 10.1088/0004-637X/721/1/777.

[348] Pierre Cristofari, Pasquale Blasi, and Elena Amato. The low rate of Galactic pevatrons. *Astropart. Phys.*, 123:102492, 2020. doi: 10.1016/j.astropartphys.2020.102492.

[349] N. Bucciantini, J. Arons, and E. Amato. Modeling the spectral evolution of PWNe inside SNRs. *Mon. Not. Roy. Astron. Soc.*, 410:381, 2011. doi: 10.1111/j.1365-2966.2010.17449.x.

[350] Kumiko Kotera, Elena Amato, and Pasquale Blasi. The fate of ultrahigh energy nuclei in the immediate environment of young fast-rotating pulsars. *JCAP*, 08:026, 2015. doi: 10.1088/1475-7516/2015/08/026.

[351] Payel Mukhopadhyay and Tim Linden. Self-generated cosmic-ray turbulence can explain the morphology of TeV halos. *Phys. Rev. D*, 105(12):123008, 2022. doi: 10.1103/PhysRevD.105.123008.

[352] M. Fiori, B. Olmi, E. Amato, R. Bandiera, N. Bucciantini, L. Zampieri, and A. Burtovoi. Modelling the γ-ray pulsar wind nebulae population in our galaxy. *Mon. Not. Roy. Astron. Soc.*, 511(1):1439–1453, 2022. doi: 10.1093/mnras/stac019.

[353] G. Morlino, P. Blasi, E. Peretti, and P. Cristofari. Particle acceleration in winds of star clusters. *Mon. Not. Roy. Astron. Soc.*, 504(4):6096–6105, July 2021. doi: 10.1093/mnras/stab690.

[354] Simon Portegies Zwart, Steve McMillan, and Mark Gieles. Young massive star clusters. *Ann. Rev. Astron. Astrophys.*, 48:431–493, 2010. doi: 10.1146/annurev-astro-081309-130834.

[355] Thibault Vieu, Stefano Gabici, Vincent Tatischeff, and Sruthi Ravikularaman. Cosmic ray production in superbubbles. *Mon. Not. Roy. Astron. Soc.*, 512(1):1275–1293, 2022. doi: 10.1093/mnras/stac543.

[356] F. Aharonian et al. A deep spectromorphological study of the γ-ray emission surrounding the young massive stellar cluster Westerlund 1. *Astron. Astrophys.*, 666:A124, 2022. doi: 10.1051/0004-6361/202244323.

[357] Tim Linden, Katie Auchettl, Joseph Bramante, Ilias Cholis, Ke Fang, Dan Hooper, Tanvi Karwal, and Shirley Weishi Li. Using HAWC to discover invisible pulsars. *Phys. Rev. D*, 96(10):103016, 2017. doi: 10.1103/PhysRevD.96.103016.

[358] Giulia Illuminati. *Searches for cosmic neutrino sources with ANTARES, KM3NeT and IceCube and time calibration of ANTARES*. PhD thesis, U. Valencia (main), 2020.

[359] Agata Trovato. *Development of reconstruction algorithms for large volume neutrino telescopes and their application to the KM3NeT detector*. PhD thesis, Catania U., SSC, 2014.

[360] J. A. Formaggio and G. P. Zeller. From eV to EeV: Neutrino Cross Sections Across Energy Scales. *Rev. Mod. Phys.*, 84:1307–1341, 2012. doi: 10.1103/RevModPhys.84.1307.

[361] P. A. Čerenkov. Visible radiation produced by electrons moving in a medium with velocities exceeding that of light. *Phys. Rev.*, 52:378–379, Aug 1937. doi: 10.1103/PhysRev.52.378. URL `https://link.aps.org/doi/10.1103/PhysRev.52.378`.

[362] T. Chiarusi and M. Spurio. High-Energy Astrophysics with Neutrino Telescopes. *Eur. Phys. J. C*, 65:649–701, 2010. doi: 10.1140/epjc/s10052-009-1230-9.

[363] Maarten De Jong. Km3Net: Perspectives. *PoS*, NEUTEL2015:055, 2016. doi: 10.22323/1.244.0055.

[364] T. K. Gaisser. *Cosmic rays and particle physics*. 1990. ISBN 978-0-521-33931-5.

[365] Yu Seon Jeong, Atri Bhattacharya, Rikard Enberg, C. S. Kim, Mary Hall Reno, Ina Sarcevic, and Anna Stasto. Prompt atmospheric neutrino flux. *PoS*, ICHEP2016:083, 2016. doi: 10.22323/1.282.0083.

[366] Rikard Enberg, Mary Hall Reno, and Ina Sarcevic. Prompt neutrino fluxes from atmospheric charm. *Phys. Rev. D*, 78:043005, 2008. doi: 10.1103/PhysRevD.78.043005.

[367] Morihiro Honda, T. Kajita, K. Kasahara, S. Midorikawa, and T. Sanuki. Calculation of atmospheric neutrino flux using the interaction model calibrated with atmospheric muon data. *Phys. Rev. D*, 75:043006, 2007. doi: 10.1103/PhysRevD.75.043006.

[368] Thomas K. Gaisser. Spectrum of cosmic-ray nucleons, kaon production, and the atmospheric muon charge ratio. *Astroparticle Physics*, 35(12):801–806, July 2012. doi: 10.1016/j.astropartphys.2012.02.010.

[369] Y. Becherini, A. Margiotta, M. Sioli, and M. Spurio. A Parameterisation of single and multiple muons in the deep water or ice. *Astropart. Phys.*, 25:1–13, 2006. doi: 10.1016/j.astropartphys.2005.10.005.

[370] G. Carminati, A. Margiotta, and M. Spurio. Atmospheric MUons from PArametric formulas: A Fast GEnerator for neutrino telescopes (MUPAGE). *Comput. Phys. Commun.*, 179:915–923, 2008. doi: 10.1016/j.cpc.2008.07.014.

[371] S. Aiello, A. Albert, S. Alves Garre, Z. Aly, and Ameli et al. gSeaGen: The KM3NeT GENIE-based code for neutrino telescopes. *Computer Physics Communications*, 256: 107477, November 2020. doi: 10.1016/j.cpc.2020.107477.

[372] G. Battistoni, C. Forti, and J. Ranft. Study of the high-energy cosmic ray cascades using the dual parton model. *Astropart. Phys.*, 3:157–184, 1995. doi: 10.1016/0927-6505(94)00039-6.

[373] Gisela Anton. Neutrino Telescopes. *arXiv e-prints*, art. arXiv:2010.06012, October 2020. doi: 10.48550/arXiv.2010.06012.

[374] Thijs van Eeden. High energy neutrino reconstruction and selections with full KM3NeT/ARCA. *PoS*, ICRC2023:1074, 2023. doi: 10.22323/1.444.1074.

[375] Karel Melis, Aart Heijboer, and Maarten de Jong. KM3NeT/ARCA Event Reconstruction Algorithms. *PoS*, ICRC2017:950, 2018. doi: 10.22323/1.301.0950.

[376] Thijs van Eeden, Jordan Seneca, and Aart Heijboer. High-energy reconstruction for single and double cascades using the KM3NeT detector. *PoS*, ICRC2021:1089, 2021. doi: 10.22323/1.395.1089.

[377] Walid Idrissi Ibnsalih, Antonio Ambrosone, Antonio Marinelli, Gennaro Miele, Pasquale Migliozzi, Ofelia Pisanti, and Ankur Sharma. Expectations for the high-energy neutrino detection from starburst galaxies with KM3NeT/ARCA. *PoS*, ICRC2021:1168, 2021. doi: 10.22323/1.395.1168.

[378] Antonio Marinelli et al. KM3NeT/ARCA expectations in view of a novel multimessenger study of starburst galaxies. *JINST*, 16(12):C12016, 2021. doi: 10.1088/1748-0221/16/12/C12016.

[379] A. Ambrosone, W. I. Ibnsalih, A. Marinelli, G. Miele, P. Migliozzi, and M. R. Musone. KM3NeT/ARCA Sensitivity to Starburst Galaxies. *EPJ Web Conf.*, 280:03001, 2023. doi: 10.1051/epjconf/202328003001.

[380] M. G. Aartsen et al. Differential limit on the extremely-high-energy cosmic neutrino flux in the presence of astrophysical background from nine years of IceCube data. *Phys. Rev. D*, 98(6):062003, 2018. doi: 10.1103/PhysRevD.98.062003.

[381] Gary J. Feldman and Robert D. Cousins. A Unified approach to the classical statistical analysis of small signals. *Phys. Rev. D*, 57:3873–3889, 1998. doi: 10.1103/PhysRevD.57.3873.

[382] Pablo Correa Camiroaga. *Merging Neutrino Astronomywith the Extreme Infrared Sky: A Search for Cosmic Neutrinos from Ultra-Luminous Infrared Galaxies with the IceCube Observatory.* PhD thesis, Vrije Universiteit Brussel, 2022.

[383] M. G. Aartsen et al. Search for steady point-like sources in the astrophysical muon neutrino flux with 8 years of IceCube data. *Eur. Phys. J. C*, 79(3):234, 2019. doi: 10.1140/epjc/s10052-019-6680-0.

[384] Walid Idrissi Ibnsalih. *Study of Starburst galaxies observability though the KM3NeT/ARCA telescope and time calibration of detector units.* PhD thesis, Università degli studi della Campania Luigi Vanvitelli, 2023.

[385] Yann Coadou. Boosted decision trees. 3 2022. doi: 10.1142/9789811234033_0002.

[386] Ke Fang, John S. Gallagher, and Francis Halzen. The TeV Diffuse Cosmic Neutrino Spectrum and the Nature of Astrophysical Neutrino Sources. *Astrophys. J.*, 933(2):190, 2022. doi: 10.3847/1538-4357/ac7649.

[387] Rasa Muller, Aart Heijboer, and Thijs van Eeden. Search for cosmic neutrino point sources and extended sources with 6-8 lines of KM3NeT/ARCA. *PoS*, ICRC2023:1018, 2023. doi: 10.22323/1.444.1018.

[388] M. G. Aartsen et al. Search for Time-independent Neutrino Emission from Astrophysical Sources with 3 yr of IceCube Data. *Astrophys. J.*, 779:132, 2013. doi: 10.1088/0004-637X/779/2/132.

[389] R. Maiolino, A. Krabbe, N. Thatte, and R. Genzel. Seyfert activity and nuclear star formation in the circinus galaxy. *Astrophys. J.*, 493:650, 1998. doi: 10.1086/305150.

[390] V. L. Ginzburg and S. I. Syrovatskii. *The Origin of Cosmic Rays*. 1964.

[391] Thomas K. Gaisser, Ralph Engel, and Elisa Resconi. *Cosmic Rays and Particle Physics*. 2016.

[392] Andrew W. Strong, Igor V. Moskalenko, and Vladimir S. Ptuskin. Cosmic-ray propagation and interactions in the Galaxy. *Ann. Rev. Nucl. Part. Sci.*, 57:285–327, 2007. doi: 10.1146/annurev.nucl.57.090506.123011.

[393] Brian C. Lacki and Rainer Beck. The Equipartition Magnetic Field Formula in Starburst Galaxies: Accounting for Pionic Secondaries and Strong Energy Losses. *Mon. Not. Roy. Astron. Soc.*, 430:3171, 2013. doi: 10.1093/mnras/stt122.

[394] C. Gruppioni et al. Star Formation in Herschel's Monsters versus Semi-Analytic Models. *Mon. Not. Roy. Astron. Soc.*, 451(4):3419–3426, 2015. doi: 10.1093/mnras/stv1204.

Appendix A

The Leaky Box Model Approximation

In this appendix, we discuss the leaky box model approximation for SBGs as well as we report the expressions for the CR timescales used. The general transport equation for cosmic-rays can be written as [220, 390–392]:

$$\frac{dn(E)}{dt} - \nabla \cdot [D(E) \cdot \nabla n(E) + \mathbf{V} n(E)] + \frac{d}{dE}\big[\frac{dE}{dt} n(E)\big] = Q(E) + \sum_k \int_E^{+\infty} dE' \frac{d\sigma_k(E, E')}{dE} n_k(E') \tag{A.1}$$

where $N(E)$ represents the CR energy distribution inside the galaxy, $D(E)$ is the diffusion coefficient, $\mathbf{V}$ represents the advection velocity. $Q(E)$ is the injection term in the energy phase space and the last two terms in the right-hand side of the equation respectivelu represent the loss due to collisions with the interstellar medium and secondary CR production from spallation [220]. Eq. A.1 can be simplified in the case of SBGs, since their activity timescale is much larger than the timescales involved in the non-thermal emissions. We emphasize that p-p interactions are considered as cooling intercation and therefore encoded in the energy loss term. In fact, we can look for a steady-state solution. Secondly, since we are mostly interested in a small region inside the SBG (SBN), the diffusion coefficient can be considered non-positional dependent over the SBN, the equation can be simplified into [220, 393]:

$$Q(E) = \frac{d}{dE}\big[\frac{dE}{dt} N(E)\big] + \frac{N(E)}{\tau(E)} \tag{A.2}$$

where $\tau(E)$ takes into account both the escape timescale which is given by:

$$\tau_{\rm esc} = (\tau_{\rm adv}^{-1} + \tau_{\rm diff}^{-1}(E))^{-1} \tag{A.3}$$

Eq. A.2 is called leaky-box model equation since it physically represent the balance between the injection term with all the physical processes occurring in the source. Eq. A.2 can be further simplified considering the momentum phase space. Indeed, we have that

$$n(E) = 4\pi p^2 f(p) \frac{dp}{dE} \tag{A.4}$$

and also

$$Q(E) = 4\pi p^2 Q(p) \frac{dp}{dE} \tag{A.5}$$

inserting Eqs. A.4 and A.5 into Eq. 3.3, we can obtain the solutions of the CR equation into the momentum phase space. If the source is dominated by escaping phenomena, just like advection and diffusion, then

$$f(p) = \tau_{\rm esc} Q(p) \tag{A.6}$$

By contrast if the energy losses dominate we have that

$$f(p) = -\frac{\tau_{\rm loss}}{pE^2} \int p^2 Q(p) dp \tag{A.7}$$

For a power-law injection spectrum $Q(p) \propto p^{-\alpha}$, we have

$$f(p) = \frac{\tau_{\rm loss} p^2}{p^2 + m_p^2} \frac{Q(p)}{(\alpha - 3)} \simeq \tau_{\rm loss} \frac{Q(p)}{\Gamma - 1} = \tau_{\rm loss}^{\rm eff} Q(p) \tag{A.8}$$

where $\Gamma = \alpha - 2$ and the last passage is due to the fact we mostly focus on $p > m_p$. Therefore, Eq. A.5 can simplified into

$$f(p) = Q(p) \cdot \left(\frac{1}{\tau_{\rm adv}} + \frac{1}{\tau_{\rm diff}} + \frac{1}{\tau_{\rm loss}^{\rm eff}} \right)^{-1} \tag{A.9}$$

for $\Gamma \simeq 2$, Eq. A.9 can be further simplifed into

$$f(p) = Q(p) \cdot \left(\frac{1}{\tau_{\rm adv}} + \frac{1}{\tau_{\rm diff}} + \frac{1}{\tau_{\rm loss}} \right)^{-1} \tag{A.10}$$

which is the *original* leaky-box model equation. This equation has been extensively used in

literature [31, 32]. Eqs. A.9 and A.10 show that scaling the energy-loss timescale by a factor $(\Gamma - 1)^{-1}$ gives a slighlty more precise normalization factor than Eq. A.10. Nonetheless, the qualitative results do not change as already emphasized by Ref. [21], because in our case $\Gamma \simeq 2$.

A.1 Formulae for the Timescales

In this section, we report the formulae used for the proton and electrons timescales. Firstly, in order to describe the diffusion timescale, following Refs. [31, 32], we use a quasi-linear formalism to evaluate the diffusion coefficient $D(p)$:

$$D(p) = \frac{r_l(p)v(p)}{3 \cdot \mathcal{F}(k)} \tag{A.11}$$

where $v(p)$ is the particle velocity, $r_l(p)$ is the Larmor radius and $\mathcal{F}(k)$ is the normalized energy density per unit of logarithmic wave number k [31]. We use $\mathcal{F}(k) = k \cdot W(k)$, with $w(k) = w_0 \cdot (k/k_0)^{-d}$, with $k_0 = L_0^{-1}$, where L_0 is the coherence lenght, which is assumed to be $\simeq 1\,\mathrm{pc}$ [31, 32]. This value comes from the fact that we expect the interstellar medium to experience a high degree of turbulence of a length scale smaller than the radius of the SBN. Furthermore, we normalize $\mathcal{F}(k)$ requiring that

$$\int_{k_0}^{+\infty} w(k)dk = \left(\frac{\delta B}{B}\right)^2 = \eta_B \tag{A.12}$$

where η_B represents the degree of magnetic turbulence. We expect a high degree of magnetic turbulence, leading to $\eta_B \simeq 1$. We also choose a Kolmogorov-like scenario for diffusion by choosing $d = -5/3$. As stressed in the main text of the thesis, the actual walue for d is not particular important, since the role of diffusion in the CR transport inside SBNi is marginal. Finally, the diffusion timescale is

$$\tau_{\mathrm{diff}}(p) = \frac{R^2}{D(p)} \tag{A.13}$$

The energy loss timescale is given by

$$\frac{1}{\tau_{\mathrm{loss}}} = \sum_i \left(-\frac{1}{E}\frac{dE_i}{dt} \right) \tag{A.14}$$

where i runs over the considered processes. For protons we consider: proton-proton interactions,

ionization and Coulomb interaction. for the proton proton interaction

$$t_{pp} = \left(k \cdot n_{\rm ISM} \cdot c \cdot \sigma_{pp}(E)\right)^{-1} \tag{A.15}$$

where $k \simeq 0.5$ is the inelasticity factor, $n_{\rm ISM}$ is the interstellar medium density and $\sigma_{pp}(E)$ is the inelastic cross section [135] (see also [20]):

$$\sigma_{pp}(E) = (34.3 + 1.88L + 0.25L^2) \cdot \left[1 - \left(\frac{E_{\rm th}}{E}\right)^4\right]^2 \text{mb} \tag{A.16}$$

where $L = \text{Ln(E/TeV)}$ and $E_{\rm th} = 1.22 \cdot 10^{-3}\,\text{TeV}$ is the threshold energy for pion production. For the ionization energy rate, we use [31]:

$$(\frac{dE}{dt})_{\rm ion} \simeq 1.82 \cdot 10^{-7} n_{\rm ISM} \cdot (1 + 0.185\text{Ln}(\beta)\Theta(\beta - 0.01))\frac{2\beta^2}{10^{-6} + 2\beta^3}\,\text{eV}\,\text{s}^{-1} \tag{A.17}$$

where $\beta = v/c$ and $\Theta(x)$ is the step function. For the Coulomb energy loss term:

$$(\frac{dE}{dt})_{\rm cou} \simeq \frac{3.08 \cdot 10^{-7} n_e \beta^2}{\beta^3 + 2.34 \cdot 10^{-5}(T_e/(2.0 \cdot 10^6\,\text{K})^{1.5})}\Theta(\beta - 7.4 \cdot 10^{-4}(T_e/(2.0 \cdot 10^6\,\text{K})^{1.2})\,\text{eV}\,\text{s}^{-1} \tag{A.18}$$

where n_e and T_e plasma temperature and density, respectively [31] (we use the values from Ref. [31]). For the electrons, we account for synchrotron, inverse compton, bremsstrahlung, ionization processes. The synchrotron timescale is given by:

$$(\frac{dE}{dt}) = \frac{4}{3}\sigma_T \cdot c \cdot \gamma^2 \beta^2 U_B \tag{A.19}$$

where σ_T is the Thompson cross section, U_B is the magnetic energy density. The energy loss for inverse compton is

$$(\frac{dE}{dt})_{\rm IC} = \frac{3\sigma_T \cdot c \cdot m_e^2 c^4}{4}\int_0^\infty d\epsilon \frac{n(\epsilon)}{\epsilon}\int_0^1 dq \frac{\Lambda^2 q G(q,\Lambda)}{(1+\Lambda q)^3} \tag{A.20}$$

where $\Lambda = 4\epsilon \cdot E_e/(m_e^2 \cdot c^4)$ and $G(q,\Lambda)$ is [31]

$$G(q,\Lambda) = 2qlog(q) + (1+2q)(1-q) + \frac{(\Gamma q)^2(1-q)}{2(1+\Lambda q)} \tag{A.21}$$

The bremsstrahlung timescale is:

$$\tau_{\rm brem} = 4 \cdot 10^7 \left(\frac{n_{\rm ISM}}{cm^{-3}} \right)^{-1} \, {\rm yr} \tag{A.22}$$

While, for the ionization timescale is:

$$\tau_{\rm ion} \simeq 1.9 \cdot 10^9 \left(\frac{E}{100\,{\rm TeV}} \right) \left(\frac{n_{\rm ISM}}{250\,{\rm cm}^{-3}} \right)^{-1} \, {\rm yr} \tag{A.23}$$

A.2 Secondary Particle Production rate Formulae

In this section, we report the formulae for the computation of the secondary particle as evaluated in [135] and [31] which have been used for this work. Let us call $x = E_i/E_\pi$ and $r = 1 - \lambda = (m_\mu/m_\pi)^2$. The muonic neutrinos produced directly by the decay of the muon ($\pi \to \mu\,\nu_\mu$) is given by [31, 135]

$$f_{\nu_\mu^1}(x) = \frac{1}{\lambda}\Theta[\lambda - x] \tag{A.24}$$

while the electrons and the muonic neutrinos produced by muon decay $\mu \to \nu_\mu\,\bar{\nu}_e\,e$ can be described by the following functions [31, 135]

$$f_e(x) = f_{\nu_\mu^2}(x) = g_{\nu_\mu}(x)\Theta[x - r] + (h^{(1)}_{\nu_\mu}(x) + h^{(2)}_{\nu_\mu}(x))\Theta[r - x] \tag{A.25}$$

$g_{\nu_\mu(x)}$ is given by [31, 135]

$$g_{\nu_\mu}(x) = \frac{3 - 2r}{9(1 - r)^2}(9x^2 - 6 \cdot {\rm Ln(x)} - 4{\rm x}^3 - 5) \tag{A.26}$$

By constrast

$$h^{(1)}_{\nu_\mu}(x) = \frac{3 - 2r}{9(1 - r)^2}(9r^2 - 6{\rm Ln(r)} - 4{\rm r}^3 - 5) \tag{A.27}$$

and

$$h^{(2)}_{\nu_\mu}(x) = \frac{(1 + 2r)(r - x)}{9r^2}[9(r + x) - 4(r^2 + rx + x^2)] \tag{A.28}$$

For the electron neutrino (analogously to muonic neutrinos), we have that

$$f_{\nu_e}(x) = g_{\nu_e}(x)\Theta[x - r] + (h^{(1)}_{\nu_e}(x) + h^{(2)}_{\nu_e}(x))\Theta[r - x] \tag{A.29}$$

with

$$g_{\nu_e}(x) = \frac{2}{3(1-r)^2}[(1-x)(6(1-x)^2 + r(5+5x-4x^2)) + 6r\mathrm{Ln(x)}] \tag{A.30}$$

$$h^{(1)}_{\nu_e}(x) = \frac{2}{3(1-r)^2}[(1-r)(6-7r+11r^2-4r^3) + 6r\mathrm{Ln(r)}] \tag{A.31}$$

$$h^{(2)}_{\nu_e}(x) = \frac{2(r-x)}{3r^2}[7r^2 - 4r^3 + 7xr - 4xr^2 - 2x^2 - 4x^2r] \tag{A.32}$$

where for $x = 0$, $f_{\nu^2_\mu}(0) = 2.214$ and $f_{\nu_e}(0) = 2.367$ [135]. On the other hand, for $x \to 1$,

$$f_{\nu^2_\mu}(x) = \frac{2(3-2r)(1-x)^3}{3(1-r)^2} \tag{A.33}$$

and

$$f_{\nu_e}(x) = \frac{4(1-x)^3}{1-r} \tag{A.34}$$

Appendix B

On the Density of Starburst Galaxies

In this section, we report the actual density distribution we used for the diffuse gamma-ray and neutrino spectra. Following Ref. [32], we define a redshift-dependent modified Schechter function:

$$\Phi_{\rm SFR}(z,\psi) = \tilde{\Phi}(z)\left(\frac{\psi}{\tilde{\psi}(z)}\right)^{1-\tilde{\alpha}(z)} \times \exp\left[-\frac{1}{2\tilde{\sigma}^2(\mathrm{z})}\log^2\left(1+\frac{\psi}{\tilde{\psi}(\mathrm{z})}\right)\right] \tag{B.1}$$

where the SFR ψ is measured in $M_\odot\,\mathrm{yr}^{-1}$ and the parameters $\tilde{\Phi}(z)$, $\tilde{\psi}(z)$, $\tilde{\alpha}(z)$ and $\tilde{\sigma}(z)$ are obtained through the best fit of these function with the actual data provided by [148] (see [32] for further details). The best-fit parameters used are summarized in Tab. B.1.

z	$\tilde{\Phi}(z)(10^{-3}\,\mathrm{M}_\odot\,\mathrm{dex}^{-1})$	$\tilde{\psi}(z)$	$\tilde{\alpha}(z)$	$\tilde{\sigma}^2(z)(10^{-1})$
0.0-0.3	2.8	7	1.6	1.32
0.3-0.45	1.5	18	1.6	1.2
0.45-0.6	1.2	27	1.6	0.85
0.6 -0.8	1.5	34	1.6	0.8
0.8-1.0	1.2	32	1.6	1.5
1.0-1.2	1.05	36	1.6	1.8
1.2-1.7	1.7	37	1.6	1.7
1.7-2.0	0.9	65	1.6	1.2
2.0-2.5	0.35	170	1.6	1.2
2.5-3.0	0.15	240	1.6	1.8
3.0-4.2	0.0145	550	1.6	3.5

Table B.1: $\tilde{\psi}(z)$, $\tilde{\alpha}(z)$ and $\tilde{\sigma}(z)$ used for the Schecter function calculation

From the values reported in Tab. B.1, it is possible to compute the star formation rate

density:

$$\mathrm{SFRD(z)} = \int_{\log(\psi_{\mathrm{min}})}^{+\infty} \Phi_{\mathrm{SFR}}(\mathrm{z}, \psi) \cdot \psi \, \mathrm{d} \log(\psi) \tag{B.2}$$

where $\log(\psi_{\mathrm{min}}) = -1.5$ is the minimum star formation rate as in [32, 394].

z	SFRD $(\mathrm{M}_{\odot}\,\mathrm{yr}^{-1}\,\mathrm{Mpc}^{-3})$
0-0.3	0.025
0.3-0.45	0.034
0.45-0.6	0.037
0.6 -0.8	0.057
0.8-1.0	0.054
1.0-1.2	0.057
1.2-1.7	0.092
1.7-2.0	0.089
2.0-2.5	0.078
2.5-3.0	0.056
3.0-4.2	0.016

Table B.2: Values of the SFRD obtained following Ref. [32].

Tab. B.2 summarised the values obtained for the SFRD for each redshift bin. The values are consistent with the ones obtained by Ref. [394] (see also [32] for further details).

Appendix C

Profile likelihoods

Here, we collect the full set of likelihood contour plots for all the four parameters considered in the multi-messenger analyses of the Fermi-LAT EGB data with the IceCube 7.5-year HESE data (Figures C.1 for "blending" and C.2 for "M82 prototype" SBG models) and 6-year high-energy cascade data (Figures C.3 for "blending" and C.4 for "M82 prototype" SBG models).

C.1 Multi-messenger analysis without EM cascades

In this appendix, we present the results for the multi-messenger analyses once we do not take into account the production of secondary gamma-rays from the electromagnetic (EM) cascades for the SBG and blazars components. It is indeed important to characterize the impact of the EM cascades in obtaining the main results of the analysis. To this aim, we consider just the gamma-ray absorption on CMB+EBL for the SBG component modelled with the spectral index blending, and simply take the gamma-ray spectral energy distribution of blazars as reported by Ajello et al. [11]. Accordingly, we consider the following positional prior imposed on the contribution from resolved blazars [13] as

$$\chi^2_{\rm pos} = \left(\frac{N_{\rm Blazars} - 0.98}{0.11} \right)^2 , \tag{C.1}$$

which is fully consistent with the prior given by Ajello et al. [11]. In Figure C.5 we compare to data the 68.3% and 95.4% CL uncertainty bands for the SBG neutrino and gamma-ray fluxes. We find that the non-inclusion of the EM cascades generally allows for a larger normalization for the SBG component. Finally, in Figures C.6 and C.7 we show the full set of two-dimensional profile likelihoods obtained with the IceCube 7.5-year HESE and 6-year high-energy cascade

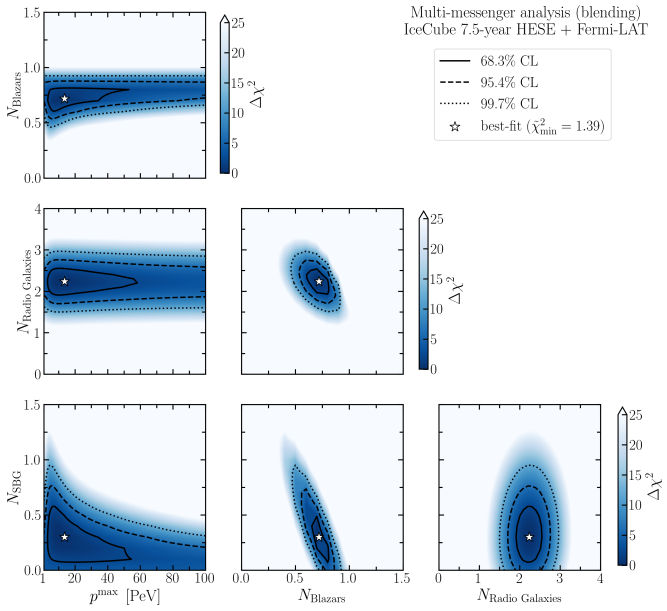

Figure C.1: Two-dimensional profile likelihood plots for the multi-messenger analysis of the IceCube 7.5-year HESE neutrino data and the Fermi-LAT EGB data using the blending modeling of SBGs.

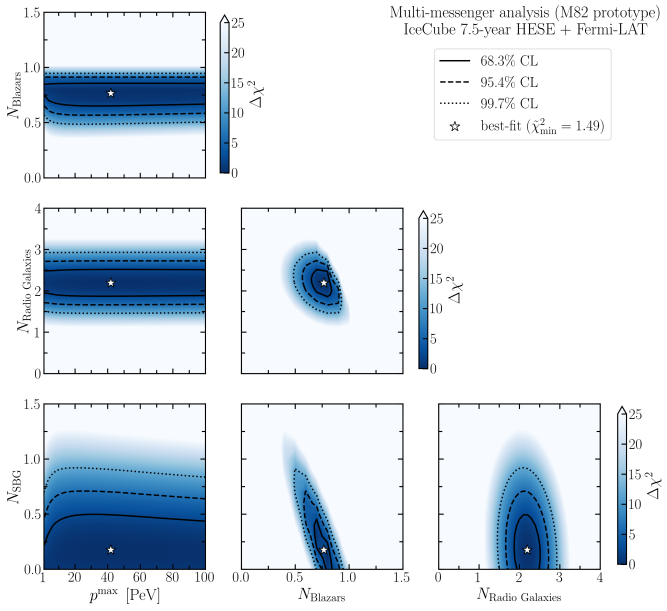

Figure C.2: Two-dimensional profile likelihood plots for the multi-messenger analysis of the IceCube 7.5-year HESE neutrino data and the Fermi-LAT EGB data using the M82 prototype for SBGs.

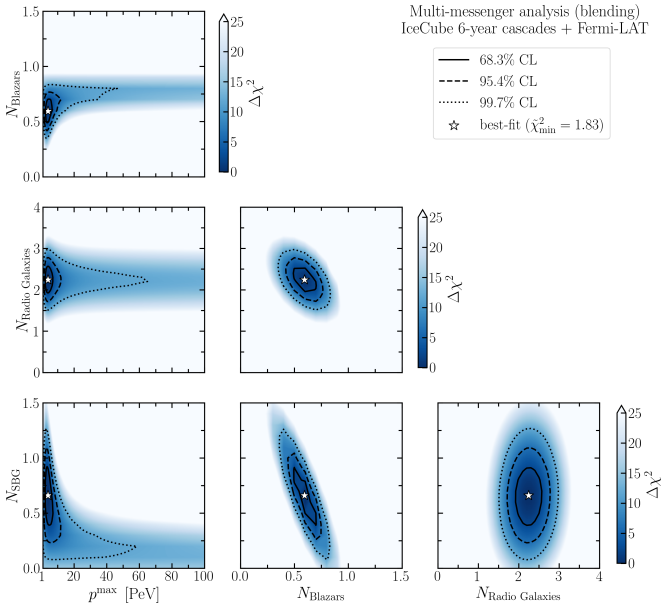

Figure C.3: Two-dimensional profile likelihood plots for the multi-messenger analysis of the IceCube 6-year cascades neutrino data and the Fermi-LAT EGB data using the blending modeling for SBGs.

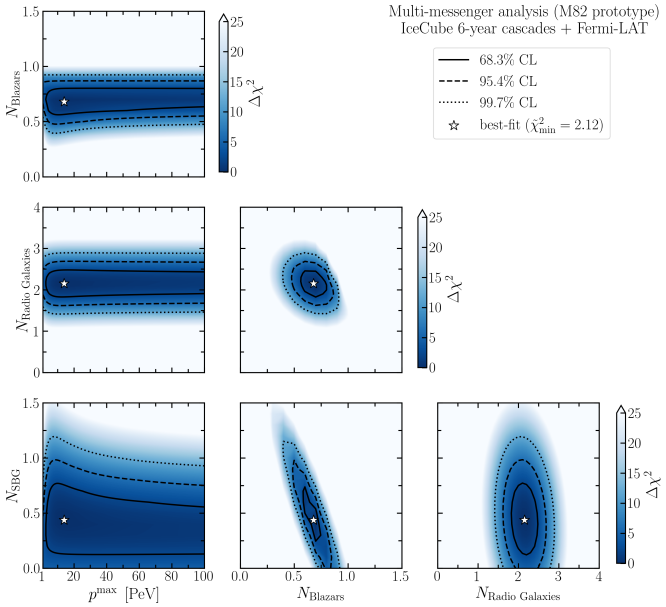

Figure C.4: Two-dimensional profile likelihood plots for the multi-messenger analysis of the IceCube 6-year cascades neutrino data and the Fermi-LAT EGB data using the M82 prototype modeling for SBGs.

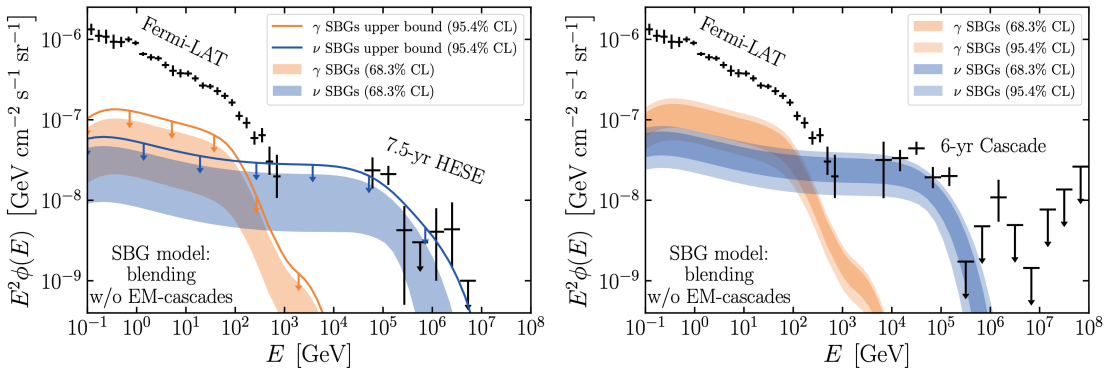

Figure C.5: Gamma-ray (orange) and single-flavour neutrino (blue) uncertainty bands at 68.3% CL (dark colors) and 95.4% CL (light colors) for the SBG component deduced by the multi-messenger analysis in case of data-driven blending of spectral indexes without the contribution of electromagnetic cascades. The left (right) plot corresponds to the multi-messenger analysis with IceCube 7.5-year HESE (6-year cascade) neutrino data. In the left plot, the solid lines correspond to upper bounds at 95.4% CL.

neutrino data, respectively.

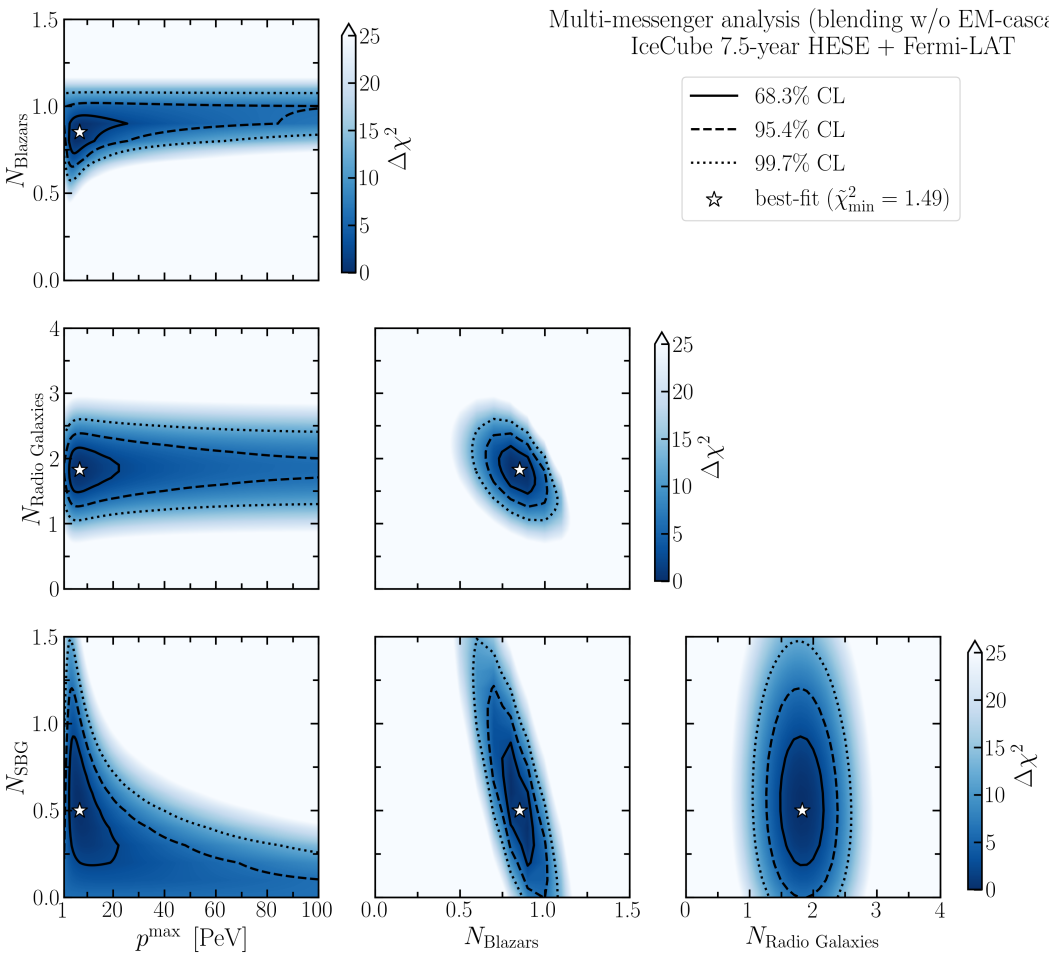

Figure C.6: Two-dimensional profile likelihood plots for the multi-messenger analysis of the IceCube 7.5-year HESE neutrino data and the Fermi-LAT EGB data using the blending modeling for SBGs without the contribution of electromagnetic cascades.

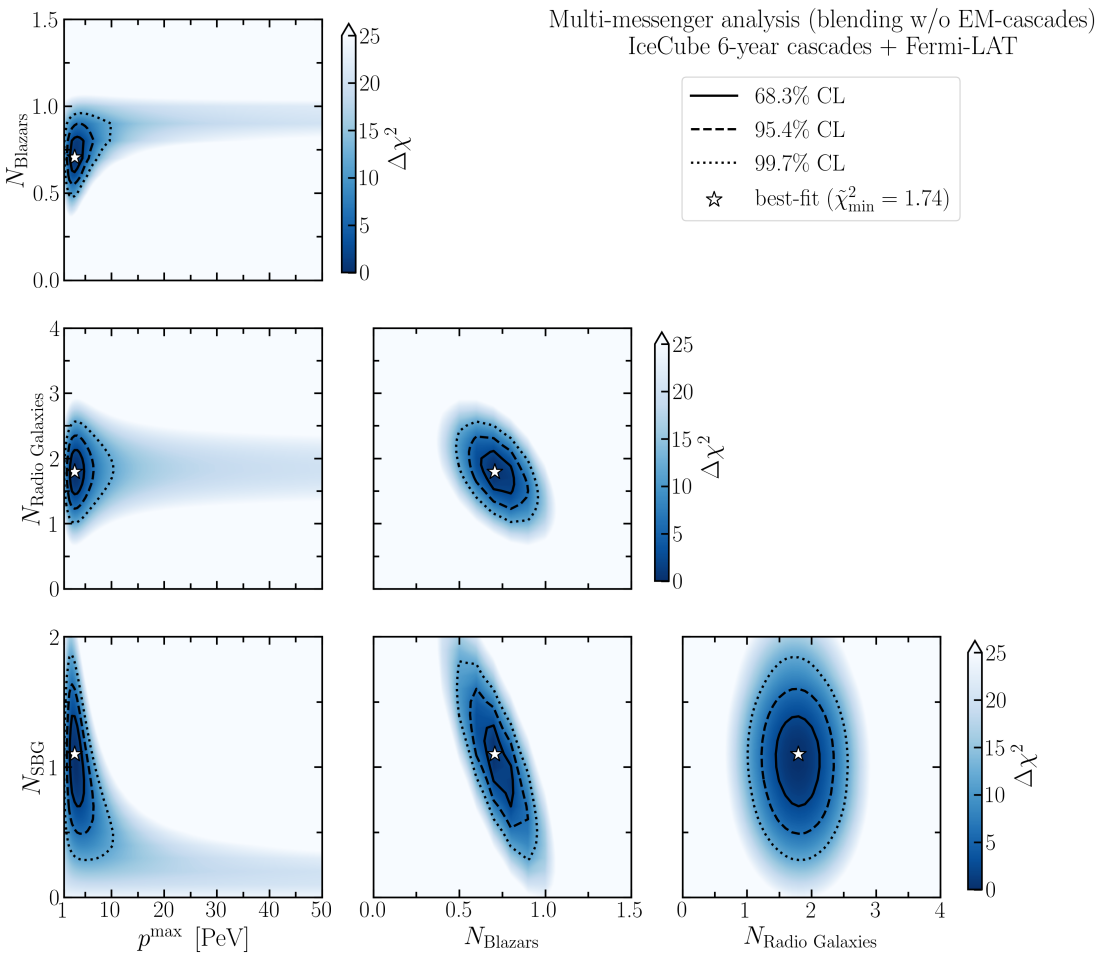

Figure C.7: Two-dimensional profile likelihood plots for the multi-messenger analysis of the IceCube 6-year high-energy cascade neutrino data and the Fermi-LAT EGB data using the blending modeling for SBGs without the contribution of electromagnetic cascades.